Arctic sea level and geostrophic flow:

from the development of a satellite-based pan-Arctic dataset to the study of the seasonality from satellite remote sensing and model output.

Dissertation submitted by

Francesca Doglioni

in partial fulfilment of the requirements
for the degree of

Doctor of Natural Sciences (Dr. rer. nat.)

to

Faculty 1
Physics and Electrical Engineering
University of Bremen

Colloquium: 14th of December 2023

Universität Bremen

ALFRED-WEGENER-INSTITUT
HELMHOLTZ-ZENTRUM FÜR POLAR- UND MEERESFORSCHUNG

1. Reviewer: Prof. Dr. Torsten Kanzow

2. Reviewer: Dr. Maren Walter

This dissertation was written at the Physical Oceanography section of the Alfred Wegener Institute, Helmholtz Centre for Polar and Marine Research, Bremerhaven.

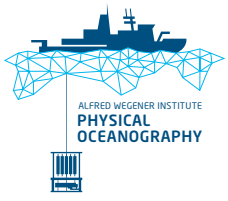

"Satellite altimetry is the most successful ocean experiment of all times."

— Walter Munk, speech for the US Commission on Ocean Policy, University of California, San Diego, April 2002

Abstract

The geographical and environmental conditions of the Arctic region make it one of the most remote, harsh and challenging regions on Earth to observe. Indeed, being covered by sea ice all year round, the Arctic Ocean is the least observed and therefore the most unknown component of the whole Arctic climate system. In particular, the sea ice cover hampers both the access by ships and the observations via remote sensing, thereby hindering long-term monitoring. Yet, the Arctic Ocean and the neighbouring Nordic Seas, play a crucial role in the cycling of fresh water and heat across the global ocean. Changes in the Arctic Ocean circulation have been induced by global warming, that modified the atmosphere-ice-ocean interface. Up to recent times, changes in the circulation in the ice-covered Arctic have been observed mainly via in-situ data (e.g., ship observations and moorings), which are sparse and mostly cover short periods of time. Strong seasonal biases make it difficult to integrate in-situ observations to provide a large-scale perspective on the variability and long-term changes. Since 2010, with the launch of the CryoSat-2 satellite altimetry mission and the development of techniques to process altimetry data from cracks in the ice, a new opportunity to observe the Arctic Ocean sea surface height and geostrophic surface circulation up to 88°N has opened. The overarching goal of my thesis was to investigate the state-of-the-art of satellite altimetry in the Arctic Ocean, and use altimetry data in combination with model simulations to provide a basin-scale assessment of seasonality of the Arctic sea surface height and geostrophic surface circulation, and its drivers.

Despite the availability of re-processed altimetry data in ice-covered regions, only few experimental gridded, multi-year datasets are available to date. Moreover, these products have been scarcely evaluated in terms of ocean velocity and it is not yet clear how they compare to each other. I therefore used observations from the ice-covered Arctic newly processed at the Alfred Wegener Institute, in combination with observations from the ice-free Arctic, to develop a new quality-controlled gridded pan-Arctic dataset of sea surface height and geostrophic surface velocity. The dataset, based on CryoSat-2 observations, extends up to 88°N and covers a period of 10 years (2011-2020). Both the sea surface height and the geostrophic velocity fields were evaluated in the ice-covered Arctic Ocean by comparison with in-situ data. Additionally, sea surface height was compared over the entire Arctic with an independent satellite altimetry product to evaluate the impact of different methodologies (source data, corrections, gridding) on the final product. This comparison showed that, while different methodologies do not prevent a generally good agreement between monthly fields (correlation coefficient higher than 0.7 over 85% of the domain), local differences between the two datasets can be attributed to different corrections applied. Results of the evaluation of the sea surface height fields against distributed hydrographic profiles data demonstrate that the mean field is consistent with known large-scale circulation patterns, and that these are also preserved in the transition between ice-covered and ice-free areas. Furthermore, monthly time series of sea surface height are compared to the sum of steric plus bottom pressure equivalent height from mooring data, showing a relatively good agreement (correlation coefficients larger than 0.5, with p-value lower than 0.06), with differences on a month-to-month basis due to the different sampling of mesoscale activity. Geostrophic velocity derived from the altimetry dataset were compared to near-surface velocity from a total of 26 moorings. Among these, two mooring arrays located across the Fram Strait and

the Laptev Sea continental slope observe the structure and variability of the Arctic Boundary Current at two locations. Comparison to data from the mooring arrays showed that the highest correlation was achieved when both satellite and in-situ data are averaged over 50-60 km across the slope current and intra-seasonal frequencies are removed. This allowed to establish that the altimetry dataset is able to resolve Arctic slope current variability at seasonal and longer time scales, over across-current scales of about 50-60 km.

Having demonstrated the capability of the altimetry dataset to resolve the Arctic slope currents seasonal variability, my second objective was to provide a basin-wide assessment of the large-scale variability and its drivers. This was achieved in the second part of my thesis using the gridded altimetry dataset in combination with model simulations. Large-scale seasonal patterns in both the sea surface height and geostrophic velocity fields were identified. These manifest in the form of out of phase sea level anomalies between the Eurasian shelf seas and the central deep basin, accompanied by a modulation of the geostrophic currents at the shelf break. As a result, slope currents are stronger in winter and weaker in summer along the entire Eurasian continental slope from the southern Norwegian coasts to the western Laptev Sea. By separating mass-related and density-related contributions to sea surface height seasonality in the model simulations, I was able to attribute the large scale pattern of shelf-basin decoupling to the mass contribution, therefore to cross-slope water mass transport. I then investigated the mechanisms regulating the cross-slope transport. While the wind field is in agreement with shoreward Ekman transport in winter and offshore transport in summer, a quantitative analysis of the equivalent height change over the shelf seas showed that this exceeds the observed sea surface height seasonal changes by one order of magnitude. The cross-slope transport is found to match the observed sea surface height seasonal changes when an additional compensatory cross-slope transport at depth, in geostrophic balance, is considered. Although the large-scale seasonal pattern was attributed in large part to mass-related variability, density-related changes were as prominent in confined regions, among them the Laptev Sea continental slope. By comparing the seasonal variability in the simulated vertical sections of velocity and density there, with the large-scale density-related and mass-related geostrophic velocity anomalies, I demonstrate how the latter can be complementary in identifying the character (barotropic mass-driven or baroclinic density-driven) and the origin of a shelf break current variability.

In conclusion the work presented in this thesis demonstrated the capability of satellite altimetry to provide a basin-wide assessment of the Arctic large-scale seasonal patterns of sea surface height and circulation, proving in particular to be a valid tool to investigate the drivers of the slope current seasonality.

Zusammenfassung

Ihre geographische Abgeschiedenheit und die harschen Umweltbedingungen machen die Arktis zu einer der rausten und abgelegensten Regionen der Erde. Tatsächlich ist der Arktische Ozean, welcher das gesamte Jahr über teilweise mit Meereis bedeckt ist, der am wenigsten vermessenste und somit unbekannteste Bestandteil des gesamten Arktischen Klimasystems. Insbesondere die Meereisbedeckung verhindert sowohl den ganzjährigen Zugang durch Schiffe, als auch die Beobachtung mittels Fernerkundung und erschwert somit die langfristige und lückenlose Beobachtung. Der Arktische Ozean, im Zusammenspiel mit dem benachbarten Europäischen Nordmeer, spielt jedoch eine entscheidende Rolle im globalen Kreislauf von Süßwasser und Wärme. Jüngste Veränderungen in der Ozeanzirkulation des Arktischen Ozeans wurden durch Anpassungen des Atmosphären-Ozean-Eis Systems an einen sich verändernden Gleichgewichtszustand, bedingt durch die anhaltende globale Klimaerwärmung, ausgelöst. Bis vor kurzem wurden Veränderungen in der Ozeanzirkulation in der eisbedeckten Arktis hauptsächlich anhand von In-situ-Daten beobachtet. Diese sind jedoch räumlich begrenzt verfügbar und decken meist nur kurze Zeiträume ab, was es schwierig macht, ein umfassendes Bild der Variabilität und deren langfristiger Veränderung zu liefern. Darüber hinaus erschweren die starken saisonalen Schwankungen des Arktischen Klimasystems das Zusammenführen von In-situ-Beobachtungen aus verschiedenen Jahren, was die Unsicherheit bei der Schätzung langfristiger Veränderungen erhöht. Seit 2010, mit dem Start der CryoSat-2-Satellitenaltimetriemission und der gleichzeitigen Entwicklung von neuen Methoden zur Verarbeitung von Altimetriedaten aus Spalten im Meereis, besteht eine neue Möglichkeit, die Auslenkung der Meeresoberfläche des Arktischen Ozeans und somit die geostrophische Oberflächenzirkulation bis 88°N geographischer Breite zu ermitteln. Das übergeordnete Ziel meiner Dissertation besteht darin, den Stand der Technik der Satellitenaltimetrie im Bereich des Arktischen Ozeans zu untersuchen und ferner Altimetriedaten in Kombination mit Modellsimulationen zu verwenden, um eine den gesamten Arktischen Ozean umfassenden Blick auf die Saisonalität der arktischen Meeresoberflächenhöhe und der geostrophischen Oberflächenströmungen sowie deren Antreiber zu erhalten.

Trotz der generellen Verfügbarkeit aufbereiteter Altimetriedaten in eisbedeckten Regionen sind bisher nur wenige experimentelle, gerasterte und zudem mehrjährige Datensätze der Meeresoberflächenhöhe und der geostrophischen Oberflächenzirkulation verfügbar. Darüber hinaus wurden diese Produkte kaum hinsichtlich der Meereisgeschwindigkeit bewertet. Zudem wurde ein umfassender Vergleich der bestehenden Produkte bisher nicht vorgenommen. Im ersten Teil meiner Dissertation verwende ich daher neu verarbeitete Beobachtungen aus der eisbedeckten Arktis in Kombination mit Beobachtungen aus der eisfreien Arktis, um einen neuen, panarktischen, qualitätskontrollierten und gerasterten Datensatz zu entwickeln, welcher die Meeresoberflächenhöhe sowie die geostrophische Oberflächengeschwindigkeit enthält. Dieser auf CryoSat-2-Beobachtungen basierende Datensatz erstreckt sich bis 88°N geographische Breite und deckt einen Zeitraum von 10 Jahren (2011-2020) ab. Sowohl die Meeresoberflächenhöhe als auch die geostrophischen Geschwindigkeitsfelder im eisbedeckten Arktischen Ozean werden durch Vergleich mit In-situ-Daten bewertet. Darüber hinaus werden die Felder der Meeresoberflächenhöhe in der gesamten Arktis mit einem unabhängigen Satelliten-Altimetrieprodukt verglichen, um die Auswirkungen verschiedener

Methoden (Quelldaten, Korrekturen, Rasterung) auf das Endprodukt zu bewerten. Die Ergebnisse des Vergleichs mit dem unabhängigen Satellitendatensatz zeigen, dass unterschiedliche Methoden eine allgemein gute Übereinstimmung liefern (Korrelationskoeffizient höher als 0,7 in mehr als 85% der untersuchten Region). Ferner zeigt sich jedoch, dass lokale Differenzen zwischen den beiden Datensätzen unterschiedlichen Korrekturen, die auf die Datensätze angewendet wurden, zugeschrieben werden können. Die Ergebnisse der Auswertung der Meeresoberflächenhöhe anhand räumlich und zeitlich verteilter hydrografischer Profile zeigen, dass das mittlere Feld mit bekannten großräumigen Zirkulationsmustern übereinstimmt und dass ein kongruenter Übergang zwischen eisbedeckten und eisfreien Gebieten gewährleistet ist.

Darüber hinaus werden monatliche Zeitreihen der Meeresoberflächenhöhe mit der Summe der sterischen und bodendruck-äquivalenten Höhe aus Verankerungsdaten abgeglichen, was eine zufriedenstellend Übereinstimmung zeigt (Korrelationskoeffizienten größer als 0,5, mit p-Wert kleiner als 0,06). Etwaige Unterschiede resultieren aus der variierenden mesoskaligen Aktivität von Monat zu Monat. Die geostrophische Geschwindigkeit im Altimetriedatensatz wird mit der oberflächennahen Geschwindigkeit von insgesamt 26 Messstationen verglichen. Unter diesen Messstationen erproben zwei Verankerungen in der Framstraße und am Kontinentalhang der Laptevsee an jeweils zwei Standorten die Struktur und Variabilität des Arktischen Randstroms. Ein Vergleich mit Daten aus den Verankerungen zeigt, dass die höchste Korrelation erreicht wird, wenn sowohl Satelliten- als auch In-situ-Daten über 50–60 km über den Randstrom gemittelt und intra-saisonale Frequenzen entfernt wurden. Dadurch konnte festgestellt werden, dass der Altimetriedatensatz in der Lage ist, die Strömungsvariabilität entlang der arktischen Kontinentalabhänge auf saisonalen und längeren Zeiträumen über räumliche Skalen von etwa 50–60 km aufzulösen.

Nach erfolgreicher Demonstration der Fähigkeit des Altimetriedatensatzes zur Auflösung der saisonalen Variabilität der arktischen Randströme, bestand das zweite Ziel dieser Arbeit darin, eine beckenumfassende Perspektive auf die großräumige Variabilität und ihre Antreiber zu erarbeiten. Dies wurde mit Hilfe des gerasterten Altimetriedatensatzes in Kombination mit Modellsimulationen erreicht. Es wurden großräumige saisonale Muster sowohl in der Meeresoberflächenhöhe als auch in den geostrophischen Geschwindigkeitsfeldern identifiziert. Diese manifestieren sich in Form von phasenverschobenen Meeresspiegelanomalien zwischen den eurasischen Schelfmeeren und dem zentralen arktischen Becken, einhergehend mit einer Modulation der geostrophischen Strömungen am Schelfrand. Resultierend daraus sind die Strömungen entlang des gesamten eurasischen Kontinentalabhangs von der südnorwegischen Küste bis zur westlichen Laptevsee im Winter verstärkt und im Sommer abgeschwächt. Durch die Aufspaltung in massenbezogenen und dichtebezogenen Beitrag zur Saisonalität der Meeresoberflächenhöhe in den Modellsimulationen konnte ich das großräumige Muster der Schelf-Becken-Entkopplung dem Massenbeitrag und damit dem Massenaustausch zwischen zentralen Becken und Schelfmeeren zuordnen. Anschließend habe ich die Mechanismen untersucht, die den genannten Massentransport regulieren. Während das Windfeld mit dem anlandig gerichteten Ekman-Transport im Winter und dem ablandig gerichteten Transport im Sommer qualitativ übereinstimmt, zeigte eine quantitative Analyse der äquivalenten Höhenänderung über den Schelfmeeren, dass diese die beobachteten saisonalen Änderungen der Meeresoberflächenhöhe um eine Größenordnung übersteigt. Es wurde zudem festgestellt, dass der Massenaustausch zwischen Schelfmeeren und arktischem Becken mit den beobachteten jahreszeitlichen Veränderungen der Meeresoberflächenhöhe übereinstimmt, wenn ein zusätzlicher kompensatorischer Transport in der Tiefe im geostrophischen Gleichgewicht berücksichtigt wird. Obwohl das großräumige saisonale Muster zu einem großen Teil auf massenbedingte Variabilität zurückzuführen ist, sind dichtebedingte Veränderungen in begrenzten Regionen, darunter am Kontinentalhang der Laptevsee, ebenso ausgeprägt. Durch den Vergleich der saisonalen Variabilität in den dort simulierten Geschwindigkeits- und Dichtefeldern mit den großräumigen dichte- und massenbezogenen geostrophischen Geschwindigkeitsanomalien zeige ich, wie letztere bei der Identifizierung des Ursprungs (barotrope massengetriebene oder barokline dichtgetriebene) komplementär sein können.

Zusammenfassend demonstrierte ich die Fähigkeit der Satellitenaltimetrie, ein beckenweites Bild der großräumigen, saisonalen Muster der Meeresoberflächenhöhe und -zirkulation in der Arktis zu liefern. Inbesondere erwies sich diese als wirksames Instrument zur Untersuchung der Säsonalität der Randströmungen und zur Identifizierung ihrer Antreiber.

Contents

Chapter 1

Introduction

The Arctic Ocean is a high-latitude ice-covered ocean surrounded by continents (Fig. 1.1). It is composed by wide shelf seas at its periphery, which enclose almost completely three deep interconnected basins covering the northernmost latitudes. The central deep basins are connected on the Eurasian side to the subpolar Nordic Seas via the deep Fram Strait (maximum depth of about 2500 m). The system formed by the central Arctic Ocean and the Nordic Seas is called the Arctic Mediterranean. The exchange of heat and freshwater between the global ocean and the Arctic Mediterranean is one of the key processes that contribute to maintain the global ocean conveyor belt (Buckley and Marshall, 2016). These are exchanged thanks to a complex system of currents that connect the two and reaches deep into the central Arctic. Warm Atlantic Water flows into the Arctic Mediterranean, where it is modified by cooling and mixing with ambient water, to flow out as dense North Atlantic Deep Water (Dickson and Brown, 1994). This water forms when modified Atlantic water is subject to deep convection in the Nordic seas and sinks to the bottom (Brakstad et al., 2023, e.g.,), feeding the lower limb of the Atlantic Meridional Ocean Circulation. Furthermore, fresh and cold Polar Water is exported from the Arctic in the surface layer, overlying the modified Atlantic Water. This water mass influences the stratification of the water column in regions of deep convection, in turn affecting the formation of deep waters, whose production might be reduced in the future due to the expected increase in fresh water export (e.g. Böning et al., 2016; Rhein et al., 2018; de Steur et al., 2018).

In the past decades, the Arctic Ocean circulation system have been directly and indirectly affected by climate change. Warming of surface air temperature is occurring exceptionally rapidly in the Arctic (e.g., Overland and Wang, 2018), an effect commonly referred to as Arctic Amplification (e.g., Serreze et al., 2009). Alterations of the ice cover, due to a warmer atmosphere, affects the atmosphere-ice-ocean interface (Zhang et al., 2008; Martin et al., 2014; Armitage et al., 2020; Sumata et al., 2022), thereby directly modifying the atmospheric forcing of ice drift and ocean currents (Rampal et al., 2009; Spreen et al., 2011; Armitage et al., 2017). Furthermore, higher temperatures influence the availability of liquid fresh water from sea-ice melt and river runoff (Proshutinsky et al., 2009; Morison et al., 2012; Rabe et al., 2014; Wang et al., 2018a; Proshutinsky et al., 2019), whose distribution in turn determines the sea level field and the associated geostrophic circulation (Timmermans et al., 2011; Giles et al., 2012; Xiao et al., 2020; Wang et al., 2020). Despite the fact that changes in the Arctic climate have a strong impact on the global climate, this is to date one of the most remote and scarcely observed regions on Earth. Particularly, its harsh environmental conditions pose several challenges to long-term monitoring.

Indeed the Arctic Ocean, which can only be accessed by ships breaking through its ice cover, is the most unknown component of the whole Arctic climate system. Access to this ocean via ship is hampered by highly dynamic sea ice. This very same reason makes deployments and recovering of seafloor-based or ice-tethered instruments a never ending challenge. In-situ monitoring of the Arctic Ocean circulation has been initiated

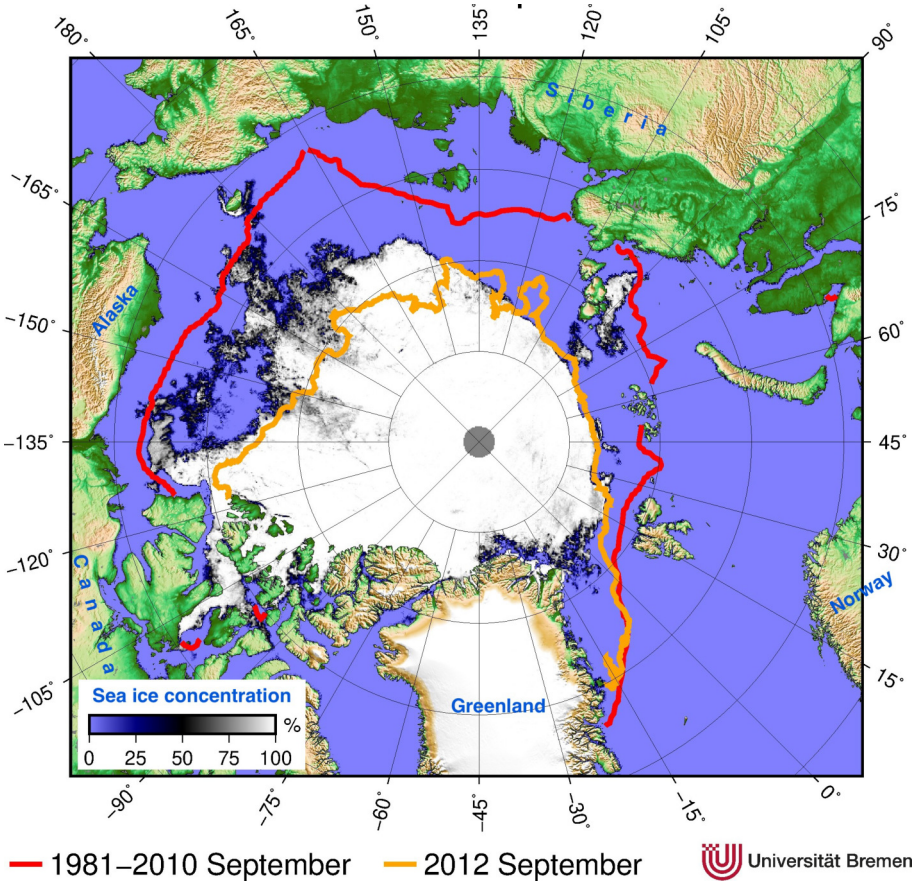

Figure 1.1. Map of the Arctic region (for a reference to the Arctic Ocean bathymetry see Fig 1.2). White-gray colors show an example of the the September sea ice concentration (seasonal minimum) in the recent year 2021. This is compared with the mean ice edge over the period 1981-2010 and the ice edge in 2012 (year of particularly low summer sea ice extent). Modified from the map produced by the Sea Ice section at the University of Bremen (https://seaice.uni-bremen.de/arctic-sea-ice-minima/)

at the Arctic Ocean gates in the 1990s (e.g., Beszczynska-Möller et al., 2011; Tsubouchi et al., 2023) and in few selected regions of the central Arctic after 2000 (e.g., Proshutinsky et al., 2019; Polyakov et al., 2020b), mostly via initiative of single institutions. Satellite observations of the ocean surface in this region encounter no fewer obstacles, with sea ice, persistent cloud cover and low-latitude satellite orbits being the most obvious. One type of satellite technique capable to measure through cloud cover is satellite radar altimetry (Benveniste, 2011). Satellite altimetry observations have been extensively used in the oceans south of 60°N since the mid 1990s to study sea level and surface ocean circulation variability (e.g., Chao and Fu, 1995), and have only in the last decade been adopted to study the Arctic Ocean.

In the wake of the rapid changes happening globally, but especially in the Arctic, in the last decades, the need of new sound techniques to regularly monitor the Arctic Ocean on a basin scales is more than ever compelling. In this thesis I investigate the current quality and resolution of satellite altimetry observations in the Arctic Ocean. Furthermore I explore the possibility to use these data in synergy with model output to understand the variability and forcing of large-scale ocean circulation on seasonal time scales.

1.1 Arctic sea level variability

Sea level is one of the Essential Climate Variables (ECVs) defined by the Global Climate Observing System (GCOS). The GCOS describes it as "the height of the ocean surface relative to a reference geoid (or an agreed

regional datum)." (GCOS, 2022). This variable is an important indicator of global warming (Intergovernmental Panel on Climate Change, 2022). Global mean sea level is rising at an accelerating speed, though not uniformly across the globe, with observational estimates that increase from 1.4 mm yr^{-1} over the period 1901–1990 to 3.6 mm yr^{-1} over the period 2006–2015 (Intergovernmental Panel on Climate Change, 2022) The rise in global mean sea level is linked to rising atmospheric temperatures via two mechanisms (e.g., Horwath et al., 2022), i.e., (1) a net transfer of water mass from land into the oceans and (2) thermal expansion. Ocean mass changes are mainly driven by changes in land ice, which includes ice sheets and glaciers. These release liquid water mass in the form of runoff and solid ice mass by calving at the ice-ocean interface. Furthermore, regional changes in sea level on various spatial scales are driven by regional changes in ocean mass and density integrated throughout the water column. These are driven by wind-related convergence of mass and by non-uniform ocean warming and salinity variations (e.g., Wunsch et al., 2007).

The high latitudes covered by the Arctic Ocean and its geographical characteristics provide a unique setting for the forcing of both mass and steric contributions to sea level variability (Fig. 1.2). First and foremost, the presence of sea ice has a multifaceted influence on the forcing of the ocean. Surface transport of water mass is affected by sea ice, which mediates the momentum transfer from the atmosphere to the ocean all year round. Depending on the roughness and the mobility of the sea ice, different sea ice types can impede or favour the wind forcing of the underlying ocean (e.g., Martin et al., 2014). Thick multi-year ice forms in the Arctic because newly formed sea ice, pushed by winds towards the western Arctic Ocean coastal boundaries, partly piles up there and can survive as a permanent ice cover for several years (e.g., Maslanik et al., 2011; Ricker et al., 2018). Sea ice also regulates the vertical heat fluxes at the ocean surface, by shielding the ocean from solar radiation and insulating it from the atmosphere. Furthermore, it modifies the salinity of the upper ocean when forming and melting. This process is particularly relevant for the forcing of sea level variability in polar regions, as at low temperatures (close to the freezing point) variations in density are dominated by changes in salinity (McPhee, 2008). Finally the Arctic Ocean, surrounded by land, receives yearly 11% of the global river discharge, despite representing only 3% of the global ocean (Dai and Trenberth, 2002). This is an important source of low buoyancy waters relevant for sea level variability.

Up to the early 2000s, most of the knowledge on Arctic sea level and surface circulation was gathered from sparse in-situ observations, interpreted in the context of the large-scale variability by means of model simulations (e.g., Proshutinsky and Johnson, 1997). With the advent of satellite altimetry in the Arctic Ocean, our knowledge on the sea level field in this region has expanded enormously (e.g., Farrell et al., 2012; see Sect. 1.3 for more details). One of the major features of the mean Arctic sea level is a doming of the sea surface in the Canada Basin, associated with an atmospheric high-pressure cell (the Beaufort High) centered above the Canada Basin in the western Arctic (e.g., Proshutinsky et al., 2019). The sea surface then gently slopes towards the eastern Arctic, reaching a minimum in an elongated trough along the Eurasian Basin and the Nordic Seas, driven by a low sea level atmospheric pressure system centered between Greenland and Iceland (the Icelandic Low). Horizontal gradients of sea surface height are related to geostrophic ocean velocity at the sea surface. In the Arctic, geostrophically balanced flow represents a good approximation on spatial scales larger than ten kilometres (Nurser and Bacon, 2014) and timescales longer than a few days. The two sea surface height features described above give rise to two opposing large-scale circulation cells in geostrophic equilibrium, anticyclonic in the western and cyclonic in the eastern Arctic Ocean (Timmermans and Marshall, 2020). The anticyclonic ocean circulation cell in the Canada Basin is referred to as Beaufort Gyre. The cyclonic cell is instead composed of the broad Transpolar Drift stream, crossing the central Arctic, and several narrower currents topographically guided from the North Atlantic into the Arctic, along the Norwegian and Eurasian continental slope.

The Arctic sea level exhibits variability on a range of timescales and spatial scales, depending on the character of the variability. On the one hand, at high latitudes the coherence between sea level variability and barotropic, mass-related variability is very high (e.g., Bingham and Hughes, 2008; Quinn and Ponte, 2012).

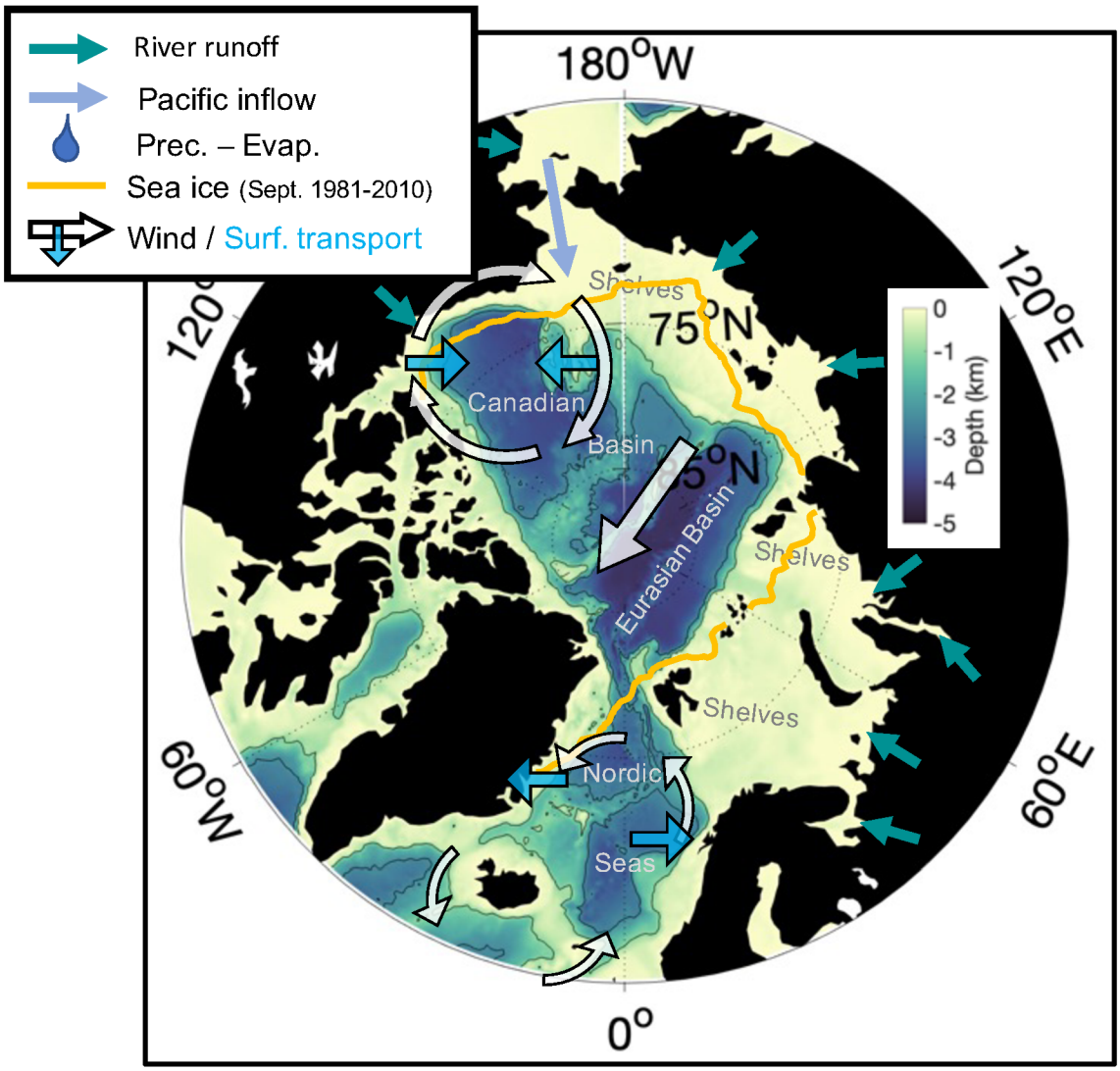

Figure 1.2. Schematics showing the main freshwater sources and wind forcing in the Arctic Ocean. This includes: major river and Pacific inflow (green and light blue arrows), the positive Precipitation minus Evaporation budget and the redistribution of fresh water in a solid form by means of sea ice formation and melting (yellow line indicates the average observed 1981-2010 September sea ice extent); the thick white arrows indicate the main atmospheric patterns forcing the Arctic Ocean (Beaufort High over the Canadian Basin and Icelandic Low over the Nordic Seas) and their effect on water mass transport (convergence and divergence respectively, indicated by the thick turquoise arrows). Depth contours are drawn at 1000 m and 2500 m depth.

At the same time, the Arctic Ocean stores a large reservoir of fresh water (e.g., Rabe et al., 2011; Solomon et al., 2021), both in liquid and solid form, whose variability gives rise to density-related sea level variability (e.g., Giles et al., 2012; Rabe et al., 2014). Mass-related oscillations in the Arctic have been observed on weekly to intra-seasonal timescales. These have been associated with fast barotropic waves (e.g., Peralta-Ferriz et al., 2011; Fukumori et al., 2015; Danielson et al., 2020), transient atmospheric cyclones (e.g., Brown et al., 2023; Kudryavtsev et al., 2023), or variability in large-scale atmospheric patterns like the Arctic Oscillation (e.g., Peralta-Ferriz et al., 2014; Armitage et al., 2016, 2018). Density-related variability happens on decadal and longer timescales, and it is mainly associated with the redistribution of the freshwater reservoir within the Arctic and its export to the subpolar North Atlantic (e.g., Giles et al., 2012; Rabe et al., 2014). Freshwater enters the Arctic Ocean via precipitation, river runoff, ice sheet discharge and relatively fresh Pacific oceanic inflow (Fig 1.2). Annual freshwater variability, mainly forced by the input by river discharge, inflow through Bering Strait net precipitation, is relatively small with respect to the total Arctic storage (e.g., Serreze et al., 2006; Haine et al., 2015) The Arctic freshwater storage shows instead a pronounced decadal memory of atmospheric forcing,

with persistent atmospheric forcing having the biggest effect (Rabe et al., 2014; Johnson et al., 2018). Rabe et al. (2014) showed that Arctic freshwater content correlates better with changes in Arctic regional sea level pressure fields than with the larger-scale atmospheric changes, described for instance by the Arctic Oscillation. This seems to be in agreement with results from a modelling study by Johnson et al. (2018), indicating that Arctic freshwater content change is largest in response to an atmospheric mode of variability that projects more strongly onto the strength of the Beaufort High rather than on the Arctic-Subarctic large-scale atmospheric pattern

A prominent theory of the decadal variability of the Arctic sea surface height and surface ocean circulation was proposed in 1997 by Proshutinsky and Johnson (1997). In this model-based study, two wind-driven regimes were identified, associated with strengthening and weakening of the Beaufort High. While during the "anticyclonic" phase the Beaufort Gyre expands and the origin of the Transpolar Drift shifts towards Europe, in the "cyclonic" phase the Beaufort Gyre shrinks and the Transpolar Drift shifts towards the eastern Siberian shelf. In the last decade, satellite altimetry reached the maturity to allow the study of basin-scale shifts between these two regimes in combination with in-situ data (Morison et al., 2012; Mizobata et al., 2016; Regan et al., 2019; Morison et al., 2021). However, satellite-based studies of sea level and circulation variability at smaller scales are to date lacking due to the limited reliability of altimetry on such scales in the ice-covered ocean (e.g., Armitage et al., 2018). This methodological gap prevents to use this technique to deepen our understanding of the Arctic Ocean circulation system, where the high-latitude ocean dynamics are shaped by a small first baroclinic Rossby radius and high-frequency barotropic fluctuations (Nurser and Bacon, 2014; von Appen et al., 2016; Pnyushkov et al., 2018; Peralta-Ferriz et al., 2011; Quinn and Ponte, 2012; Danielson et al., 2020). Particularly, the study of the Arctic slope current system would benefit from high-resolution satellite altimetry. Slope currents in the Arctic import warm and salty Atlantic Water and export cold and fresh Polar Water to the North Atlantic. Investigating their pathways and variability is therefore highly relevant to understand how the Arctic Ocean is changing and how these changes might impact the global ocean circulation.

1.2 Slope currents in the Arctic Ocean

Boundary currents are ubiquitous features of the global ocean circulation, which can form through various mechanisms connected to the presence of ocean boundaries (e.g., coasts or continental slopes). Wind forcing is responsible for driving boundary currents via two main mechanisms. The formation of western boundary currents in the sub-tropical and sub-polar gyres has been explained in the framework of potential vorticity dynamics, forced by wind (Talley et al., 2011). Western boundary currents are western-intensified jets (Stommel, 1948; Munk, 1950) that develop in response to the wind-driven meridional flow in the gyre interior (Sverdrup transport, Sverdrup, 1947), to return the fluid to its original latitude. They manifest at the shelf break, where the advection of planetary vorticity is balanced by boundary frictional torque (Stommel, 1948; Munk, 1950). Eastern boundary currents originate instead via Ekman dynamics in the coastal strip (Talley et al., 2011). Alongshore wind stress creates either offshore or onshore Ekman transport, slanting the sea surface height and resulting in shallow geostrophic currents along the coastal boundaries. Another mechanism forcing boundary currents, not initiated by wind stress, is known as Joint Effect of Baroclinicity and Relief (JEBAR; see Simpson and Sharples, 2012). The JEBAR effect generates strong persistent flows on the eastern boundary of oceans, for instance along the slope of northwest Europe. Here, meridional density gradients form due to the decrease of temperature with latitude, and run along the meridionally-oriented continental slope (i.e., perpendicular to the bathymetry gradient). The water column contracts towards higher latitudes, at a rate proportional to the ocean depth (faster in the deep ocean). Therefore, the shelf-ocean sea surface height slope increases with latitude, generating a flow parallel to continental slope, the boundary current.

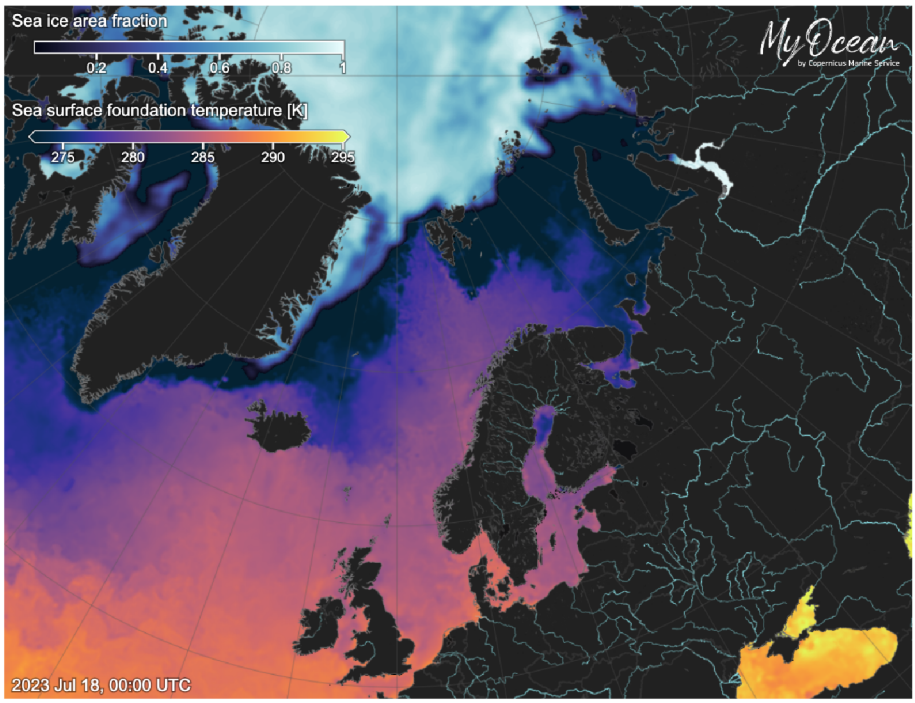

Figure 1.3. Example of daily sea surface temperature in the region of transition between the North Atlantic and the Arctic region from satellite remote sensing. Daily maps of sea surface temperature and ice concentration from the OSTIA global reprocessed product (Good et al., 2020) are provided via the CMEMS portal (https://data.marine.copernicus.eu/products).

Boundary currents flowing along continental slopes are called slope currents. Slope currents act as a conduit for water masses along thousands of kilometers, and control the shelf-basin exchange of properties (e.g., Rudels et al., 2000; Thompson et al., 2018). Several slope currents contribute to advect warm low-latitude waters within the meridional overturning circulation, a system of ocean currents that regulates the Earth's climate by redistributing the radiative heat input at low latitudes via transport of warm water poleward (e.g. Bryden and Imawaki, 2001; Buckley and Marshall, 2016; Frajka-Williams et al., 2019). For instance, in the North Atlantic, warm Atlantic water is carried towards the Arctic and Subarctic first by the Gulf Stream on the western boundary, and then by the Norwegian Atlantic Current and the West Spitsbergen Current on the eastern boundary (e.g., von Appen et al., 2016; Stendardo et al., 2020). Trace of the pathway of Atlantic water towards the Arctic can be observed in the sea surface temperature by remote sensing (Fig. 1.3). Furthermore, slope currents act as a barrier between shelf seas and deep basins, thereby regulating the offshore export of river runoff, nutrients and particles from continents (e.g., Rogge et al., 2023). Cross-slope exchanges of water masses takes place through mechanisms other than geostrophic mean flows, which are though mediated by the swift flow of boundary currents (e.g., Forest et al., 2007; Mathis et al., 2007). In polar oceans, both dense and fresh shelf waters are exported to the basin, carrying along properties from the shelf. Dense waters, formed on the shelf due to water freezing and brine ejection, cascade into the basin following gravity (e.g., Ivanov and Shapiro, 2005; Thompson et al., 2018). Depending on the original depth and density, dense shelf waters can either sink along the slope into the basin or get entrained and be swept along with the slope currents (Rudels et al., 2000). Fresh shelf waters is transported at the surface towards the basin interior by eddies, shedding from the slope current at the shelf break (e.g., Mathis et al., 2007; Spall, 2013; Thompson et al., 2018; Athanase et al., 2021). In the Arctic ocean, besides eddy transport, the mean topographically-guided flow contributes as well to advect shelf water towards the central deep basins. Fresh shelf waters from the Barents Sea and the Kara Sea flows in the northern Kara Sea guided by the St. Anna Through towards the Eurasian Basin, where it continues cyclonically around the Arctic continental slope (Aksenov et al., 2011, see more details below).

Slope currents are present in both polar oceans as a circumpolar feature. The Arctic Boundary Current (Aksenov et al., 2011), has been defined as a continuous flow around the whole periphery of the Arctic Ocean, if all its constituent branches are considered. The vertical hydrographic and velocity structure of this current derives from a transformation of the slope currents coming from the North Atlantic as they interact with Arctic water masses. Before entering the Arctic, a mostly barotropic slope current carries Atlantic Water from the coast of Norway northwards, towards the Fram Strait (Beszczynska-Möller et al., 2012), being partially redirected towards the Barents Sea south of Bear Island (Smedsrud et al., 2013). As the boundary current is steered eastwards, north of Svalbard, warm and salty Atlantic Water is subducted underneath fresh polar waters (Pérez Hernández et al., 2019), from which it is separated by a thick halocline layer. From this point on, different water masses flow within the Arctic Boundary Current, creating a baroclinic structure that evolves along the Arctic continental slope (Pnyushkov et al., 2015).

A horizontal gradient in the halocline depth between the fast slope current and the slow basin interior is generated due to differential diffusive deepening of the halocline these two regimes (Spall, 2013). Furthermore, as the warm and salty Atlantic Water continues to flow along the continental slope, its contrast with the relatively fresh shelf waters generates as well a horizontal density gradient (front) at the continental slope (Bauch et al., 2014; Aksenov et al., 2011). Additional water masses of Atlantic origin from the Barents Sea and Kara Sea flow out of the northern Kara Sea, guided by the St. Anna Trough, and merge with the slope current, providing new momentum input as well (Karcher et al., 2007; Aksenov et al., 2011). Downstream of the St. Anna Trough, the Arctic Boundary Current is therefore formed by relatively dense and warm water offshore, leaning against fresh halocline and shelf waters close to the shelf break. A similar hydrographic structure, with offshore warm water creating a front against fresh shelf water, is present along the Antarctic continental slope (Thompson et al., 2018). There, regions with the strongest horizontal density gradients ("fresh shelf") are associated with downwelling-favorable winds, shoreward Ekman transport and an intensified slope current. This highlights the role of wind in both maintaining and forcing the variability of the cross-slope hydrographic structure. The variability of the Arctic Boundary Current has also been described in terms of barotropic, wind-driven oscillations both via modelling (e.g., Isachsen et al., 2003) and satellite observations (e.g., Armitage et al., 2018).

Eastward of the St. Anna Trough, the Arctic Boundary Current has been described by Aksenov et al. (2011) as a triple core cyclonic current, carrying waters of Atlantic origin at depth and halocline waters from the shelf within a surface branch. This vertical structure has been in part confirmed by later studies, based on mooring data and hydrographic transects along the Nansen Basin continental slope (e.g., Pnyushkov et al., 2015; Pérez Hernández et al., 2019; Ruiz-Castillo et al., 2023). However, several aspects of the Arctic Boundary Current are still not clear. In this thesis I ask whether satellite altimetry can provide a tool to cover some of these knowledge gaps. Firstly, a good description of the Arctic Boundary Current in the surface layer and close to the shelf break, where the current is strongest, is made difficult by the lack of consistent observations due to the very presence of ice. Therefore, I investigate whether the quality and resolution of state-of-the-art satellite altimetry data in the ice-covered Arctic are capable to provide information on the surface geostrophic variability of the Arctic slope currents. Secondly, the large-scale variability of the Arctic Boundary Current and its drivers is difficult to study, due to the challenge of coordinating the deployment of moored instruments over such large distances and for a long period of time. I attempt therefore to answer this question with the aid of satellite data and model simulations, studying the drivers of the large-scale variability on the seasonal time scale. Finally, I separate the mass-related and density-related contributions to the geostrophic currents variability, to determine whether these can shed light on the nature and origin of the water masses that meet in the boundary current encircling the Eurasian Basin.

1.3 Satellite altimetry in the Arctic Ocean [1]

Regionally enhanced atmospheric warming in the Arctic over the past century has been driving rapid changes at the sea surface. The reduction in concentration and age of sea ice resulted in modified vertical momentum fluxes, which intensified ice and water drift, in turn enhancing sea ice drift and export. Evidence of basin-wide positive trends in sea ice drift, particularly strong in the summer season, has largely been found in satellite observations (Hakkinen et al., 2008; Spreen et al., 2011; Kwok et al., 2013; Kaur et al., 2018). Contrary to studies on ice drift, observational studies of ocean currents, including analysis of regional in-situ data (e.g., McPhee, 2012), indirect calculation from wind and ice drift observation (Ma et al., 2017) or, only recently, satellite altimetry data (Armitage et al., 2017; Morison et al., 2021), give a more fragmentary picture of changes and intensification of surface ocean currents. The reason for this is that, in ice-covered regions, long-term observations of near surface currents, both from in-situ and satellite sensors, have been hindered until recent times by the presence of ice.

Before the advent of satellite observations, the large-scale Arctic Ocean surface circulation (see a schematic in Fig. 2.1) was partially reconstructed from in-situ observations and models, albeit with limitations in terms of spatial extent or processes represented. On the one hand, in-situ observations of surface ocean currents are sparse due to the remoteness of the Arctic environment and to the high risk of loosing sensors in ice-covered areas (Haller et al., 2014). On the other hand, while numerical models allow for the study of basin-wide processes, they rely largely on theoretical formulation of physical processes, often constrained by insufficient in-situ observations (Proshutinsky and Johnson, 1997; Jahn et al., 2010). Satellite-derived data then provided novel alternatives to tackle these issues. By accessing remote regions of the Arctic Ocean, satellite data proved to be a key component in constraining and assessing models, as pointed out by recent ocean reanalysis efforts by Nguyen et al. (2021), and can be used to infer ocean circulation below the ice. For instance, based on assumptions of the ice response to wind forcing (i.e., free drift), Kwok et al. (2013) used satellite sea ice drift observations to deduce near-surface ocean circulation. Beyond ice drift observations, satellite altimetry can provide a more direct way to observe near-surface ocean currents by deriving the surface geostrophic velocity field (Armitage et al., 2017).

Satellite altimetry is a revolutionary technique to measure the global sea level, that developed at a fast pace in the second half of the twentieth century (Benveniste, 2011). Radar altimeters operate both at night and day, providing furthermore a practical means to measure sea surface height through clouds. This technique has been defined as "the most successful ocean experiment of all times" (Walter Munk, speech for the US Commission on Ocean Policy, University of California, San Diego, April 2002). This definition is certainly justifiable if we think that nowadays altimetry underpins five ECVs, namely sea level, sea state, sea ice, ice sheets and surface currents. Measurements of sea level from space were originally envisaged as an opportunity for oceanographers to obtain information about the ocean dynamics below the surface layer. This is because the dynamic ocean topography (a component of the sea surface height as measured by altimetry, see Sect. 2.1) provides a measure of changes in density throughout the water column, from which the geostrophic circulation can be derived. Furthermore, used in combination with satellite gravimetry, it provided absolute velocity, a more complete measure of ocean velocity with respect to the velocity anomaly relative to an assumed "level of no motion" retrieved from sparse in-situ temperature and salinity data (e.g., McPhee, 2012). From a climate perspective, altimetry has allowed a truly global estimate of average sea level rise, providing as well a picture of its spatial variability (see for instance multi-mission maps produced by the European Space Agency, ESA, Fig. 1.4). Furthermore, used in combination with space gravimetry, altimetry provides a means to derive steric sea level changes and therefore compute ocean heat content changes.

[1] *The content of this section is adapted from Doglioni et al. (2023).*

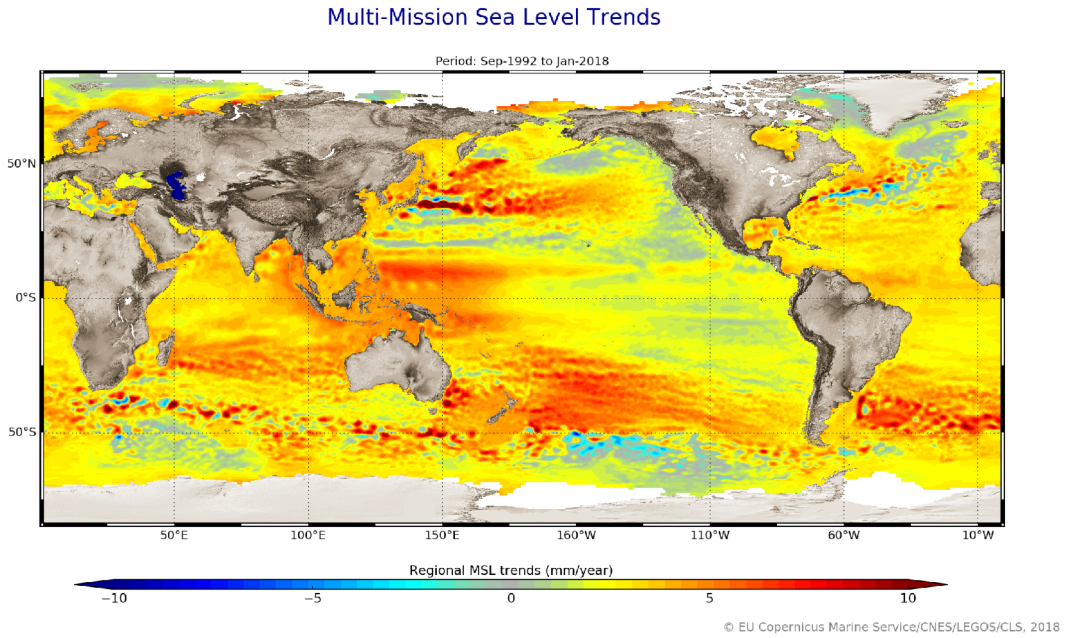

Figure 1.4. Map of sea level trend distribution in the period 1992-2018, derived from integration of multiple satellite altimetry missions (European Space Agency, https://www.esa.int/Applications/Observing_the_Earth/Spotlight_on_sea-level_rise).

Despite the groundbreaking concept behind satellite altimetry, studying ocean dynamics from altimetry data requires many elements to be measured with high precision. Three quantities which must be known with precision to calculate the dynamic ocean topography are the satellite orbit, the satellite range (satellite distance to the ocean surface, measured by the altimeter), and the geoid height (which can only be obtained from an independent approach). While improvements in the knowledge of the satellite orbit contribute to a more accurate representation of the large-scale ocean dynamics, advances in the range measurement and geoid estimate impact most of all the mesoscale and smaller scales. In the 1970s, at the start of the altimetry era, the largest contribution to the error on the dynamic ocean topography was coming from the uncertainty on the satellite orbit. One of the first altimetry missions (GEOS-3, 1975) had an error on the orbit as high as 10 m (Team et al., 2021). One major breakthrough towards high precision altimetry took place with the launch of the joint US-French mission TOPEX/Poseidon in 1992 (Fu, 2001; Benveniste, 2011; Traon, 2013). This altimetry mission was developed during decades of strengthening international cooperation in the oceanographic community, within the framework of the World Ocean Circulation Experiment (WOCE). With TOPEX/Poseidon the error on both the orbit and the range measurements dropped to about one order of magnitude below the world ocean variability, marking the start of high precision altimetry.

The error on state-of-the-art altimetry missions, despite being nominally around a couple of centimeters (Team et al., 2021), varies depending on the satellite and the region. Particularly in ice-covered regions, protocols for processing the satellite signal and corrections to be applied are not standardized yet. Satellite altimetry observation of the Arctic Ocean is particularly affected by this, given its year-round ice coverage, and is also hindered by the lack of high-latitude satellite missions. For instance, the under-representation of the Arctic Ocean in satellite altimetry emerges from maps of global sea level rise (Fig. 1.4), where ice-covered areas north of 60°N are excluded. The sea surface height field beneath the Arctic sea ice can be reconstructed from satellite-based measurements in openings of the sea ice cover, called leads. The first satellite altimetry missions over the Arctic Ocean, launched in the 90s and at the turn of the 21st century, covered it only partially up to 82° N (e.g., ERS 1 and 2, Envisat), or flew over ice regions for limited periods of time (ICEsat-1). CryoSat-2 is currently the mission providing the most complete coverage and longest life span, with observations up to

88° N since 2010 (Wingham et al., 2006). In the years to come, recently launched missions, such as Sentinel-3 and ICEsat-2, will provide an increasing amount of data from the Arctic Ocean.

Despite the availability of data, methodologies for the processing of the signal coming from the ocean in ice-covered regions have taken much longer to develop. The observations were originally aimed at the study of the cryosphere (Laxon, 1994; Alexandrov et al., 2010; Ricker et al., 2014; Armitage and Davidson, 2014), with efforts towards the generation of altimetric datasets for oceanographic purposes being made later (Bouffard et al., 2017). Re-processing of these data from the ocean-altimetry community have finally demonstrated that this is an enormously valuable resource to study the ice-covered oceans as well. However, the quality and density of such observations are low with respect to those from ice-free oceans. This is also due to lower standards in terms of corrections for distortion due to atmospheric and geophysical effects, which would require both more observations and better model performances at these high latitudes.

Finally, in order to be fully exploitable for broader oceanographic and climatic studies, and for operational purposes, along-track data from multiple missions need to be cross calibrated and compiled into homogeneous mean maps. For more than 25 years now, the Data Unification and Altimeter Combination System (DUACS) has integrated a growing number of altimeter missions, covering ice-free oceans, into multi-mission maps or time series (Pujol et al., 2016). However, end-to-end operational solutions are not yet well implemented for the Arctic Ocean, due to the higher uncertainty of data in ice-covered areas (Pujol et al., 2023). For this reason, many available oceanographic datasets are limited either to the open ocean (Volkov and Pujol, 2012; Müller et al., 2019b) or to the ice-covered ocean (Kwok and Morison, 2011, 2016; Mizobata et al., 2016). Long records of re-processed observations, available now for the Arctic (e.g., Baltazar and Malcolm, 2023), require first to be used in case studies to test their robustness (e.g., Mizobata et al., 2016; Armitage et al., 2016; Morison et al., 2021; Prandi et al., 2021; Doglioni et al., 2023), before being integrated into large operational programs. Eventually, multi-mission products (e.g., Prandi et al., 2021) will provide an adequate resolution of the Arctic ocean sea surface variability, characterised by small spatial and short temporal scales (Nurser and Bacon, 2014; Pnyushkov et al., 2015; von Appen et al., 2016; Zhao et al., 2016; Peralta-Ferriz et al., 2011).

Only in the past years have a few basin-wide, multi-annual, gridded datasets of sea surface height been generated at monthly timescales (Armitage et al., 2016; Rose et al., 2019; Prandi et al., 2021). These datasets play an important role in improving our understanding of the Arctic system as a whole, and of its present and future change (Timmermans and Marshall, 2020). However, differences between independent gridded datasets are introduced by the altimeter signal processing (Ricker et al., 2014; Armitage and Davidson, 2014; Passaro et al., 2014), measurements corrections (Carrère et al., 2016; Ricker et al., 2016; Birol et al., 2017) and interpolation of observations onto regular grids. Yet, it is not well known how these products compare to each other, nor to what extent their spatial and temporal resolution is robust in ice-covered regions (e.g., noise to signal ratio). Sea surface height maps have been assessed mostly against tide gauge data at the periphery of the Arctic Ocean, or in ice-covered regions against data from hydrographic profiles, which makes it difficult to evaluate the robustness of monthly estimates (Morison et al., 2012; Mizobata et al., 2016; Armitage et al., 2016; Morison et al., 2018; Rose et al., 2019; Morison et al., 2021; Prandi et al., 2021). Furthermore, so far only one study by Armitage et al. (2017) has provided and evaluated monthly maps of geostrophic velocities.

Satellite altimetry data in the ice-covered and ice-free Arctic are at the base of the work in this thesis. In the following section, I summarize the background information that guided this thesis, and outline the rationale behind the formulation of the research questions of the thesis.

1.4 Research questions and objectives of this thesis

Satellite altimetry has revolutionised the way we observe the global oceans (Traon, 2013). Even so, altimetry provides indirect estimates of sea surface height and surface currents, resulting from a long processing chain which is subject to error propagation from many sources. This is especially true for the Arctic Ocean, due to several environmental and technical constrains that affect the extent and quality of altimetry observations in this region. The spatial extent of satellite sampling is limited by the presence of sea ice and the low northernmost latitude of satellite orbits. The processing of satellite return signal from cracks within the ice requires dedicated processing techniques (Peacock and Laxon, 2004), which are still not well established (Dettmering et al., 2018), introducing discontinuities across the ice edge (e.g. Tilling et al., 2018). Finally, assessment via ground truth is hindered in the Arctic by the sparseness of in-situ data. While global, operational, multi-mission altimetry products have been developed for few decades now (e.g., DUACS products, Pujol et al., 2016), they do not include ice covered regions due to the uncertainties mentioned above. Few experimental products including both ice-free and ice-covered regions exists, which are though generally either very smooth (Armitage et al., 2016) or span short time periods (Prandi et al., 2021), and mostly are not validated in terms of ocean currents (Rose et al., 2019; Prandi et al., 2021).

Scientific applications of satellite altimetry in the Arctic Ocean have addressed in the past primarily large-scale variability (Farrell et al., 2012; Morison et al., 2012; Armitage et al., 2017; Raj et al., 2020), with one focus being for instance the Beaufort Gyre (Giles et al., 2012; Mizobata et al., 2016; Meneghello et al., 2018; Regan et al., 2019), and have often been limited either to southern, ice-free regions (Volkov et al., 2013; Bulczak et al., 2015; Müller et al., 2019a) or to northern, ice-covered regions (Mizobata et al., 2016). In seasonally ice-free regions, multi-mission DUACS products have recently allowed to use altimetry to support in-situ-based results on smaller scales (e.g, Osadchiev et al., 2022). One of the most prominent features of the Arctic Ocean circulation, the slope current system circling the Arctic, has never been studied before using satellite data. On the one hand, this is due to the narrow scale of these currents, while, on the other hand, to their extension across seasonally ice covered regions. Knowing the variability and drivers of this currents is of pivotal importance to know the future evolution of the Arctic ocean. This is because they advect across the Arctic Ocean both warm water masses of Atlantic origin and fresh waters at the surface and within the halocline. Previous works based on mooring data suggest that the seasonal cycle is a major contribution to their total variability (Baumann et al., 2018; Pérez Hernández et al., 2019; Ruiz-Castillo et al., 2023). Given the short time periods covered by in-situ data and their sparseness, strong seasonal biases can prevent their integration and therefore a correct interpretation of the interannual and longer variability. On the other hand, gridded satellite altimetry products in the Arctic Ocean are still in the experimental phase (e.g. Armitage et al., 2016; Rose et al., 2019; Prandi et al., 2021), due to several technical challenges. So the question remains open, whether satellite altimetry can resolve slope currents in the ice-covered ocean and provide a large-scale perspective on the Arctic slope currents seasonality.

I this thesis, I will tackle both the technical and the scientific knowledge gaps pointed above by combining a decade of satellite altimetry data with model simulations. I will address the following three main research questions:

Research question 1: *What is the state of the art of satellite altimetry for the Arctic Ocean, in particular regarding gridded, multi-year datasets in the ice-covered ocean?*

Research question 2: *Is there a large-scale coherence in the sea surface height and slope current seasonality, and is the nature of this variability related to mass or steric changes?*

Research question 3: *Can we infer drivers of the Arctic slope currents seasonality by investigating the mass-related and density-related sea surface height seasonal changes?*

An initial assessment of the existing gridded, multi-year datasets of satellite altimetry for the Arctic, showed that the few available data products are derived using different source data, corrections and gridding methods. Yet, no study has compared these datasets to assess the impact of different approaches on the final product. At the same time, newly reprocessed satellite observations in the ice-covered Arctic Ocean became available, distributed by the Alfred Wegener Institute (AWI). Therefore, **research question 1** was addressed generating a new dataset of pan-Arctic gridded sea surface height and geostrophic velocity including AWI observations in ice-covered areas, evaluating this product by comparison with independent in-situ data, and assessing differences with another gridded altimetry product.

The development of the product and details about the data used for evaluation is described in **Chapter 2**. Observations from the CryoSat-2 satellite mission are used, covering both open ocean and ice-covered (AWI data) areas of the Arctic. Observations are corrected for high-frequency variability and cross-ice-edge biases, and finally gridded at a monthly temporal resolution. In phase of development of the sea surface height fields, I specifically ask what is the impact of improved corrections and refined gridding method on the error of the monthly estimates (results in **Chapter 3**).

In **Chapter 3**, the sea surface height gridded fields are compared over the entire Arctic Ocean to another state-of-the-art altimetry product to assess the impact of different methodologies. Furthermore, the dataset is evaluated in ice-covered and ice-free areas by comparison to in-situ observations from ships, ice tethered profilers and moorings. Specific questions are addressed during the evaluation. The consistency of of the sea surface height fields across the ice edge is evaluated by comparing them to geographically distributed in-situ observations. The temporal evolution of the gridded fields is evaluated locally by comparison to moored observations. Regarding the geostrophic velocity fields, I ask specifically whether boundary currents can be resolved and, if so, over which spatial and temporal scales do they best agree with in-situ observations.

Research question 2 is addressed in **Chapter 4** by focusing the analysis of the seasonal variability. The analysis is performed by means of the developed satellite altimetry product in combination with model simulations (model introduced in **Chapter 2**). The sea surface height seasonality is analysed both at the basin scale and separately in selected shelf seas and deep basins, to identify coherent large-scale patterns. With the aid of model simulations, the mass-related and density-related contributions to the sea surface height variability are separated to study the nature of the large-scale patterns of seasonal sea surface height variability. These are put in relation to patterns in the geostrophic velocity, to explore the pathways of mass-driven and density-driven slope current seasonality.

Research question 3 is addressed in **Chapter 4** by studying the relation between the seasonal variability in the simulated sea surface height and geostrophic velocity, and the model forcing. Specifically, the wind forcing of the mass-related variability is investigated. Mass transport, and the resulting sea surface height variability, is quantified and attributed to specific mechanisms (e.g., Ekman transport). Finally, a detailed analysis of the slope current seasonality, including its vertical velocity and density structure, is performed at the continental slope north of the Laptev Sea. The variability in the local vertical structure is compared to the seasonality in the large-scale mass-related and density-related geostrophic anomalies in order to interpret the geographical origin of changes at the Laptev Sea in the surface, halocline and deep layers (where the Atlantic Water resides).

In **Chapter 5** I provide a synthesis of the results in this thesis, and conclude with possible outlooks on technical and scientific developments that could stem from it.

Chapter 2

Data and Methods[1]

In this thesis I explore the ability of remote sensing, in synergy with model data, to provide a data-based, large-scale picture of the spatial structure, variability and drivers of the ocean circulation in the Arctic. One objective is to investigate the availability, quality and resolution of satellite altimetry data in the Arctic region, in order to provide a quality-controlled, gridded product of sea surface height and geostrophic velocity for this region. In this Chapter, after a brief introduction to the theory of satellite altimetry (Sect. 2.1), in Sections 2.2 to 2.5 I provide details on the altimetry data used, the processing applied to generate gridded fields, and the independent data used for assessment of the product (which is described in mode details later in Chapter 3). This first methodological part is published in Doglioni et al. (2023) and the dataset is publicly available at Doglioni et al. (2021). The main scientific application of this newly published dataset in the context of this thesis is the study the large-scale seasonal variability and drivers of slope currents. In order to provide a dynamically consistent description of the three dimensional flow and its nature (mass- or density-related), I turned to a synergy of the gridded altimetry product and simulation output from a global model. I therefore describe in Sect. 2.6 the model used, in Sections 2.7 the methods applied to isolate the seasonal variability, in Sect. 2.8 the steps required to separate mass-related from density-related variability and in Sect. 2.9 the approach adopted to study the drivers of the mass-related variability.

2.1 Ocean altimetry background

In oceanography, studying sea level variability is relevant to understanding underlying processes linked to steric and mass variations in the water column. These variations can be measured separately by means of in-situ hydrographic profiles (steric) and ocean bottom pressure records (mass), though with limitations in terms of spatial and temporal coverage. An integrated measure of the spatial and temporal variability of these two components, known as dynamic ocean topography (η), can be derived over the global ocean from measurements of sea surface height (h), as obtained from satellite altimetry. In the following, we summarize how η can be derived from altimetry measurements and introduce some notation relevant to satellite altimetry.

h is the ocean height over a reference ellipsoid (e.g., WGS84, TOPEX/Poseidon) and is calculated by subtracting the measurement of the satellite range to the sea surface (R) from the satellite altitude H over the ellipsoid:

$$h = H - (R + C) \tag{2.1}$$

[1] *The content of this chapter is partly adapted from Doglioni et al. (2023)*

where C are corrections to the R measurement. η is then derived from h by removing the geoid height (G), i.e. the static ocean height component given the Earth's gravitational field, as follows:

$$\eta(t) = h(t) - G \tag{2.2}$$

The time varying component of η, the sea surface height anomaly η', is given by h referenced to a long-term mean sea surface height $\langle h \rangle$:

$$\eta'(t) = h'(t) = h(t) - \langle h \rangle \tag{2.3}$$

In order to compute the absolute geostrophic velocity, η is reconstructed by adding the mean dynamic topography $\langle \eta \rangle$, the temporal mean of η. This is derived from $\langle h \rangle$ by removing G, as estimated via a geoid model (e.g., Rio et al., 2011; Farrell et al., 2012; Knudsen et al., 2019; Mulet et al., 2021).

η is used to derive geostrophic velocities at the sea surface. Geostrophic velocities result from the balance of the pressure gradient force and the Coriolis force, valid in the Arctic on spatial scales larger than few kilometres and timescales longer than a few days. The two components can be expressed as:

$$\begin{cases} u_g = -\frac{g}{f R_e} \frac{\partial \eta}{\partial \theta} \\ v_g = \frac{g}{f R_e cos\theta} \frac{\partial \eta}{\partial \phi} \end{cases} \tag{2.4}$$

where θ and ϕ are latitude and longitude converted to radian angles, R_e is the Earth radius, g is the gravitational acceleration and $f = 2\Omega sin(\theta)$ is the Coriolis parameter.

The nomenclature introduced in this section will be used below to describe the datasets used and the ones resulting from the present analysis.

2.2 CryoSat-2 sea surface height in ice-covered and ice-free regions

The monthly gridded dataset generated in this study is based on two sets of η' observations along the satellite ground track (projection of its orbit at the ground), one over ice-covered and a second over ice-free areas. Observations from the European Space Agency's (ESA) CryoSat-2 mission (ESA level L2, Bouzinac, 2012) were selected between 60° N and 88° N over the period 2011-2020. For ice-covered areas, down to ice concentration 15%, we use the Alfred Wegener Institute (AWI) dataset (data version 2.4 Hendricks et al., 2021), available at at ftp://ftp.awi.de/sea_ice/projects/cryoawi_ssh. The AWI data set does not provide estimates below 15% ice concentration, since the retrieval algorithm is optimized for ice-covered areas, while uncertainties increase in areas with low ice concentration (Ricker et al., 2014). The dataset includes year round data (including summer), with along-track resolution of approximately 300 m. In this dataset, radar echoes from the surface (waveforms) are classified into sea ice and open water. Then, sea surface elevations from openings in the sea ice cover (i.e. leads) are retrieved using the retracking algorithm described by Ricker et al. (2014). The processing includes waveforms in the Synthetic Aperture Radar (SAR) and the interferometric SAR (SARIn) modes (ESA level L1b dataset; see the areas covered by each altimeter mode at http://cryosat.mssl.ucl.ac.uk/qa/mode.php). Over the open ocean, up to ice concentration 15%, we use data archived in the Radar Altimetry Database System, with along-track resolution of 7 km (RADS, Scharroo et al., 2013; Scharroo, Remko, 2018), available at http://rads.tudelft.nl/rads/rads.shtml. The merged along-track dataset, as processed in this work (see Sect. 2.5.1), is available in Doglioni et al. (2021).

All η' observations are referenced to the global DTU15MSS mean sea surface (Technical University of Denmark, updated from the DTU13MSS described in Andersen et al., 2015), which uses multimission altimeter data including the satellites Envisat, ICEsat and CryoSat-2. To reconstruct η (Sect. 2.5.2.1), we added our final gridded η' to the mean dynamic topography DTU17MDT (Knudsen et al., 2019), which is the DTU15MSS

minus the OGMOC geoid model both referenced to the T/P ellipsoid (P. Knudsen, personal communication, 8 September 2022).

2.3 Comparative datasets for altimetry evaluation

We use independent satellite and in-situ datasets to evaluate the final monthly fields of altimetry-derived η' and (u_g, v_g). These datasets are described below and the location of moorings is indicated in Fig.2.1.

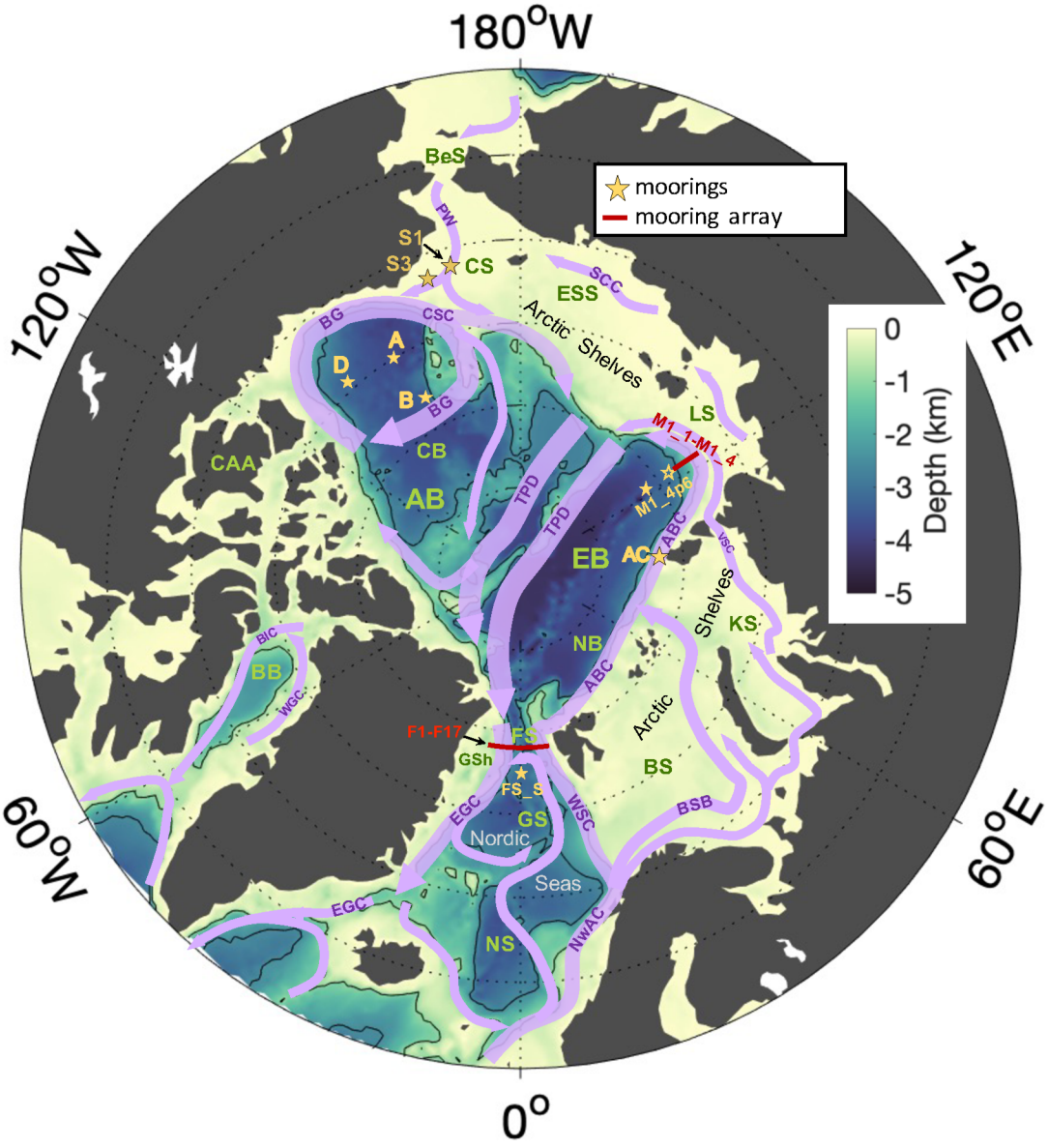

Figure 2.1. Arctic Ocean map and bathymetry (IBCAO, Jakobsson et al., 2012) with the main sub-regions (green acronyms) and the mean surface circulation pathways (purple arrows and acronyms). Location of moorings used for validation are indicated with yellow stars and red dotted lines; at the Laptev Sea continental slope, the empty star indicates where the bottom pressure data are taken. Depth contours are drawn at 1000 m and 2500 m depth. **Regions**: Nordic Seas: Greenland Sea (GS), Norwegian Sea (NS); Arctic Shelves: Barents Sea (BS), Kara Sea (KS), Laptev Sea (LS), East Siberian Sea (ESS), Chukchi Sea (CS), Greenland Shelf (GSh); Arctic Deep Basins: Amerasian Basin (AB), Canada Basin (CB), Eurasian Basin (EB), Nansen Basin (NB); Baffin Bay (BB); Canadian Arctic Archipelago (CAA); Fram Strait (FS); Bering Strait (BeS). **Currents**: West Spitsbergen Current (WSC); Norwegian Atlantic Current (NwAC); Barents Sea Branch (BSB); Vilkitsky Strait Current (VSC); Arctic Boundary Current (ABC); Siberian Coastal Current (SCC); Pacific Water inflow (PW); Chukchi Slope Current (CSC) Beaufort Gyre (BG); TransPolar Drift (TPD); East Greenland Current (EGC); West Greenland Current (WGC); Baffin Island Current (BIC).

2.3.1 Sea surface height

Monthly η' fields were compared to an independent satellite gridded dataset over the entire Arctic. This dataset is described by Armitage et al. (2016) and will be hereafter referred to as CPOM DOT (Centre for Polar Observation and Modelling Dynamic Ocean Topography, available at http://www.cpom.ucl.ac.uk/dynamic_topography). The CPOM DOT is a regional Arctic dataset spanning the years 2003-2014, derived from sea surface height observations (relying on the satellite missions Envisat and CryoSat-2) and a geoid model (GOCO03s). Monthly fields are provided on a 0.75°×0.25° longitude-latitude grid, up to a latitude of 82° N. CPOM DOT was compared to the interpolated η' fields at grid points south of 82º N, for the overlap period between January 2011 and December 2014. Both datasets were referred to their own temporal average over this period.

We further used several sources of in-situ steric height (the height component due to changes in density) plus ocean bottom pressure equivalent height (related to changes in water mass) as ground truth to (i) correct instrumental biases in the along-track η' and (ii) evaluate the spatial and temporal variability of the η' fields.

In a first step we used steric height from hydrographic profiles collected in the Arctic Deep Basins, plus ocean bottom pressure from the Gravity Recovery and Climate Experiment satellite (GRACE), to correct an instrumental offset existing between the along-track AWI and RADS η' observations (Sect. 2.5.1). The hydrographic profiles cover the period 2011-2014 and include data from various platforms, among which ships and autonomous drifting buoys (observations listed in Rabe et al., 2014; extended to 2014 using the sources listed in Solomon et al., 2021; their Table 2). Steric height was computed following Eq. 2.7. Ocean bottom pressure is included in the GRACE release 6 data as provided by the the Jet Propulsion Laboratory (data are available online at https://podaac.jpl.nasa.gov/dataset/TELLUS_GRAC_L3_JPL_RL06_LND_v03).

Then, we assessed whether the offset applied as a correction to the AWI and RADS datasets did not bias the natural sea surface slope induced by geostrophic currents. We evaluated the correction in the Fram Strait, where the Eastern Greenland Current flows in a region of transition from ice-covered to ice-free areas. To this end, we compared zonal cross-sections of the strait from our final η fields to in-situ steric height, based on hydrographic sections in the Fram Strait, plus GRACE data (Sect. 3.2.2.1). The hydrographic sections were taken at 78° 50' N from a ship-based Conductivity-Temperature-Depth (CTD), between late June and early July in 2011 and 2012 (expeditions ARK-XXVI/1 and ARK-XXVII/1 aboard the RV Polarstern; von Appen et al., 2015). As for the hydrographic profiles, steric height was computed following Eq. 2.7 (Sect. 2.5.1).

Finally, we evaluated the temporal variability of the η' fields by comparing them locally to CTD and McLane moored profiler (MMP) data from five seafloor moorings across the central Arctic (Table 2.1). The processing of temperature, salinity and ocean bottom pressure data from moorings is described in Sect. 2.4. Both mooring data and altimetry data from each location were referred to the temporal average over the time span covered by mooring data. The moorings were located in the southern Fram Strait (FS_S), at the shelf break north of Arctic Cape, the headland of Severnaya Zemlya (AC), down the continental slope north of the Laptev Sea (M1_4 and M1_6) and in the Beaufort Sea (A and D). FS_S was part of a meridional mooring array deployed by the AWI in the Fram Strait between 2016 and 2018. Data from the FS_S mooring are available in von Appen et al. (2019). The AC was one of seven moorings deployed between 2015 and 2018 within the context of the German-Russian project Changing Arctic Transpolar System (CATS). Moorings M1_4 and M1_6 were part of a six mooring array deployed in the Laptev Sea continental slope between 2013 and 2015 within the Nansen and Amundsen Basins Observations System II project (NABOS-II). Steric height and bottom pressure equivalent height were calculated from the moorings M1_6 and M1_4 respectively, given that not all measurements were available from a single mooring. Hereafter, the combination of data from the two moorings is indicated as as M1_4p6. Data from the M1_4p6 mooring are available from the Arctic Data Center (Polyakov, 2016, 2019; Polyakov and Rembert, 2019). Data at moorings A and D cover the period 2011-2018 and were collected and

made available by the Beaufort Gyre Exploration Program (BGEP) based at the Woods Hole Oceanographic Institution, in collaboration with researchers from Fisheries and Oceans Canada at the Institute of Ocean Sciences (https://www2.whoi.edu/site/beaufortgyre/). Furthermore, we compared our η monthly fields to monthly averages of the hydrographic profiles from the Arctic Deep Basin described above.

Table 2.1. Names, locations, monthly data availability and temperature/salinity sensors depth for the seafloor moorings used as a comparison dataset to validate altimetry-derived η' (refer to Fig. 3.8).

Name	Longitude	Latitude	No. months (years)	T/S sensors depth (m)
FS_S	0° E	78°10' N	23 (2016-2018)	49 / 231 / 729
AC	94°51' E	82°13' N	34 (2013-2018)	50 / 131 / 196 / 293 / 593 / 1448
M1_4p6	125°42' E	78°28'-81°9' N	24 (2013-2015)	26 / 42 / 53, MMP profiler 70-760
A	150°1' E	75°0' N	57 (2011-2017)	MMP profiler 50-2001
D	139°59' E	74°0' N	88 (2011-2018)	MMP profiler 50-2001

Table 2.2. Name, locations, monthly data availability and averaging depth range for the seafloor moorings used as a comparison dataset to validate altimetry-derived geostrophic velocity; moorings are located across the Fram Strait (first 17 rows), across the Laptev Sea continental slope (following 4 rows) and in the Beaufort Sea (following 3 rows) and in the eastern Chukchi Sea (last 2 rows). Variable locations indicate the relocation of the moorings in some years; in the third column, values in parenthesis indicate the years of data availability. Data from mooring records longer than 24 months (in bold) were used to compute correlation with altimetry.

Name	Longitude	Latitude	No. months (years)	Depth range (m)
Fram Strait				
F1	8°40' E	78°50' N	7 (2015)	75
F2	8°20' E	78°49'–79°00' N	**42** (2011-2012,2015-2018)	75
F3	8°00' E	78°50'–79°00' N	**73** (2011-2018)	75
F4	7°01' E	78°50'–79°00' N	**71** (2011-2018)	75
F5	5°40'–6°01' E	78°50'–79°00' N	**73** (2011-2018)	75
F6	4°20'–5°00' E	78°50'–79°00' N	**34** (2015-2018)	75
F7	4°00'–4°05' E	78°50' N	**38** (2012-2015)	75
F8	2°45'–2°48' E	78°50' N	**25** (2012-2014)	75
F15	1°35'–1°36' E	78°50' N	**42** (2011-2014)	75
F16	0°00'–0°26' E	78°50' N	**70** (2011-2014, 2016-2018)	75
F9	0°49' W	78°50' N	21 (2011-2012, 2014)	75
F10	2°03'–1°59' W	78°50' N	**68** (2011-2016)	75
F11	3°04' W	78°48' N	9 (2011-2012)	75
F12	4°01'–3°59' W	78°48' N	13 (2011-2012)	75
F13	5°00' W	78°50' N	20 (2011-2012)	75
F14	6°30' W	78°49' N	12 (2011-2012)	75
F17	8°7 ' W	78°50' N	13 (2011-2012)	75
Laptev Sea				
M1_1	125°48'–125°50' E	77°04' N	**62** (2013-2018)	20-50
M1_2	125°48' E	77°10' N	**60** (2013-2018)	20-50
M1_3	125°48' E	77°39' N	**61** (2013-2018)	20-50
M1_4	125°54'–125°58' E	78°28' N	**61** (2013-2018)	20-50
Beaufort Sea				
A	150°1' W	75°0' N	**82** (2011-2012, 2013-2018)	20-40
B	150°2' W	77°59' N	**83** (2011-2016, 2018)	20-40
D	139°59' W	74°0' N	**74** (2011-2014, 2015-2018)	20-40
Chukchi Sea				
S1	-167°15' E	71°10' N	**37** (2011-2014)	35
S3	-164°43' E	71°14' N	**37** (2011-2014)	35

2.3.2 Velocity

We used measurements of near-surface velocity from a total of nineteen moorings to evaluate monthly geostrophic velocity n four different regions within the Arctic. The validation points include eastern and western Arctic circulation regimes, the central Arctic Ocean, Arctic shelf seas and the main exchange gateways of the Arctic. Data from two mooring lines in the Fram Strait and down the continental slope of the Laptev Sea were used to assess how well our final geostrophic fields resolve strong and narrow slope currents. Data from three moorings in the Beaufort Sea were used to evaluate our geostrophic fields in an open ocean region characterised by weak and broad currents. Data from the Chukchi Sea served to evaluate how our dataset performs in a shallow shelf sea

In the Fram Strait, we employed ten out of seventeen moorings from the array located along a zonal section at 78°50' N, between the longitudes 9° W and 8° E, maintained since 1997 by the AWI (moorings F1–F10 and F15/F16; Beszczynska-Möller et al., 2012) and the Norwegian Polar Institute (NPI, moorings F11–F14 and F17; de Steur et al., 2009). Velocity measurements were acquired by Acoustic Doppler Current Profilers (ADCP) and Current Meters (CM). We performed the comparison using the time series recorded by the shallower CM (75 m) and by the ADCP bin nominally closest to the CM sensor depth. The mooring data are available through PANGAEA (von Appen et al., 2019; von Appen, 2019).

For the Laptev Sea, data were used from four moorings deployed in a meridional transect along the 126° E meridian within the context of the NABOS-II project (moorings M1_1 to M1_4). All four moorings provide records spanning five years, between 2013 and 2018 (data are available from the Arctic Data Center, in Polyakov, 2016, 2019; Polyakov and Rembert, 2019). In the Beaufort Sea, ADCP data from the BGEP moorings A, B and D were used, covering the period 2011-2018 (available at https://www2.whoi.edu/site/beaufortgyre/). In the Chukchi Sea we used ADCP data from the two moorings S1 and S3 over the period 2011-2014, processed by ASL Environmental Sciences and available from the NOAA National Centers for Environmental Information (?). At the two mooring arrays, we compared the (u_g, v_g) component normal to the mooring line, linearly interpolated to the moorings locations (v_n), to monthly averages of the in-situ measured velocities normal to the transects (v_{ni}). In the Beaufort Sea and the Chukchi Sea, we compared speed and bearing of velocity from altimetry and moorings. The comparison was limited to those mooring locations where more than 24 months of in-situ data were available at the time of manuscript preparation (Table 2.2). ADCP velocity ADCP velocity measurements from the Laptev Sea continental slope and the Beaufort Sea were averaged in the depth range 20-50 m, in order to capture the geostrophic flow at the surface while still excluding the surface Ekman layer (McPhee, 1992; Cole et al., 2014). In the Chukchi Sea currents were processed and archived at three depths, of which only one within in the 20-50 m range (Mudge et al., 2015); however it has been shown that currents at this location are mostly barotropic (Fang et al., 2020).

2.4 Deriving steric height and bottom pressure from mooring data

Time series of in-situ steric height anomaly (η'_S) and bottom pressure equivalent height anomaly (η'_P) were computed from mooring based measurements of water density and ocean bottom pressure. The relation between η' and the time anomaly of *i)* the vertical density profile $(\rho'(z))$ and *ii)* the ocean bottom pressure (P'_b), is derived by integration of the hydrostatic balance from the sea surface down to the bottom depth, D:

$$P'_b = \rho_0 g \eta' + g \int_{-D}^{0} \rho'(z) dz \tag{2.5}$$

where g is the gravitational acceleration and ρ_0 is a reference ocean water density, set to 1028 kg m^{-3}. Based on this relation, we defined η'_S and η'_P at the mooring sites FS_S, AC and M1_4p6 as:

$$\begin{cases} \eta'_S = -\frac{1}{\rho_0}\int_{-D}^{0}\rho'(z)dz \\ \eta'_P = \frac{P'_b}{\rho_0 g} \end{cases} \tag{2.6}$$

Vertical density profiles were obtained from temperature and salinity profiles using the Fofonoff, N.P, and Millard, R.C. (1983) formula for density. In turn, temperature and salinity profiles were obtained from moored-sensor data by linear interpolation on a regular pressure grid (2 dbar) between the shallowest and the deepest measurement (see Table 2.1). Near the surface, data were extrapolated assuming temperature and salinity constant and equal to the uppermost measurement. Below the deepest measurement, we assumed the density anomalies to be zero and did not perform extrapolation to the bottom. In the above procedure we made assumptions on the vertical density profile, necessary to reconstruct the total steric variability from discrete measurements. First, we applied a conservative approach in the deep part of the water column by neglecting the temporal variability there. While this might have resulted in a slight underestimation of η'_S, it avoided propagating anomalies for several hundred meters to the bottom, where we don't expect much variability. Furthermore, linear interpolation of temperature and salinity between the discrete measurement levels might have introduced biases in η_S. Given that we are concerned here with temporal anomalies (η'_S), we tested how well different interpolation methods reconstructed the variability from a selection of more than 400 continuous CTD profiles from the Fram Strait. We found that linear interpolation was the optimal approach. This method, applied to vertically sub-sampled profiles, was able to reproduce a very large fraction of the total variability in the steric height (on average 88%), larger than what obtained with a more complex interpolation scheme like spline.

Ocean bottom pressure records P'_b were de-tided by first performing a tidal analysis on the records using the Matlab function *t_tide* (Pawlowicz et al., 2002), and then removing the resulting tidal time series. Linear trends were removed to account for instrumental drifts. The time series at FS_S exhibited large pressure anomalies, developing on timescales of several months, whose amplitude was at least one order of magnitude too large to be explained by changes in ocean currents. Therefore, we high-pass filtered this time series with a cutoff frequency of 2 months. Despite the fact that this procedure discards part of the low frequency variability, it has been shown that the coherence between satellite data of sea level and ocean bottom pressure is highest at timescales shorter than about 2 months (Quinn and Ponte, 2012). Furthermore, we note that we have also compared the filtered time series at the FS_S mooring with a filtered bottom pressure record from a mooring located 150 km apart, both at depth of about 3000 m, which resulted in high correlation coefficient. No other bottom pressure time series was affected.

2.5 Deriving gridded monthly fields from altimetry

2.5.1 Along-track sea surface height anomaly

We generated an Arctic-wide dataset of along-track η' by merging the AWI and RADS η' datasets. Inconsistencies between the two datasets were reduced by: i) creating a uniform along-track sampling, ii) reducing biases due to different retracking algorithms, and iii) substituting geophysical corrections where two different corrections were used in the two source products. In this section we first give details about these methods and then present an estimate of the along-track η' observational uncertainty.

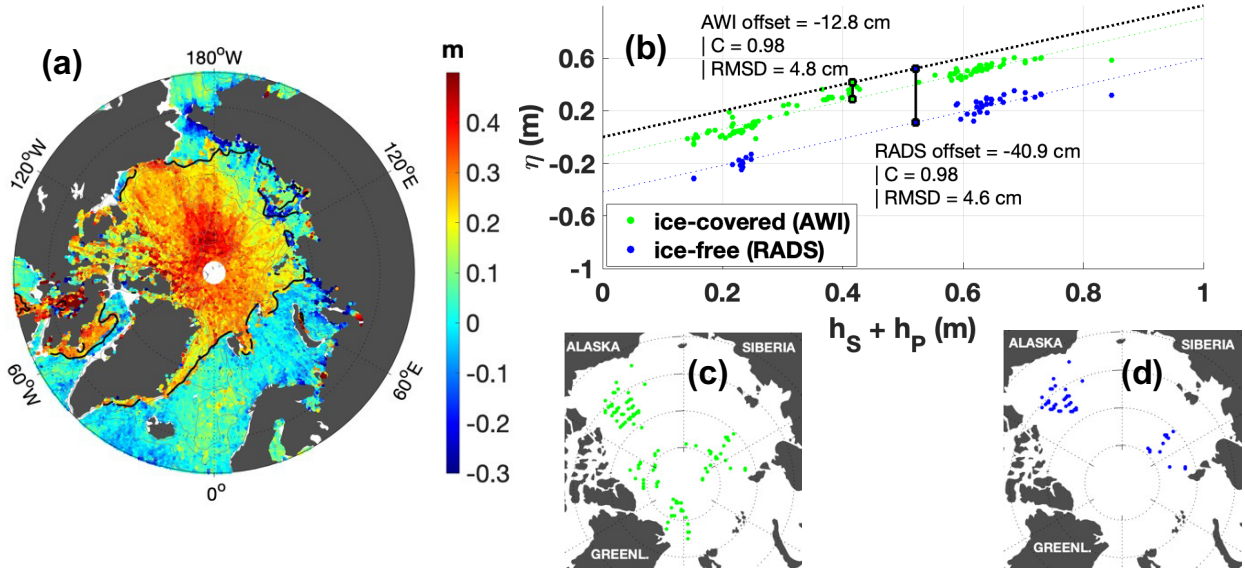

Figure 2.2. Characterisation of the respective η' bias over leads and open ocean. (a) Scatter plot of AWI (ice-covered) and RADS (ice-free) η' observations for July 2015 prior correcting the offset. The black solid line indicates the 15% sea ice concentration as derived from the OSI SAF ice concentration products (archive OSI-401-b, available at ftp://osisaf.met.no/archive/ice/conc/). (b) steric height plus ocean bottom pressure (h_S+h_P) versus η for the ice-covered altimetry data (AWI) and ice-free altimetry data (RADS). Vertical bars indicate the offset between the two altimetry datasets and h_S+h_P. The two upper panels show the grid points where h_S+h_P data points overlap with along track η data points from the AWI (green, panel c) and RADS (blue, panel d).

Merging leads and open ocean data

Prior to merging the AWI and RADS datasets we standardized their along-track sampling rates, which originally were 300 m and 7 km respectively. With this aim, the AWI dataset was first smoothed by averaging over a 7 km along-track moving window, and then linearly interpolated, following time, onto equally spaced locations (7 km) along the satellite tracks. Smoothing the AWI data along the tracks was beneficial to reduce noise, also in view of the computation of geostrophic velocity (see Eq. 2.10), given that the finite difference operator acts as a high-pass filter (e.g, Liu et al., 2012).

A step-like variation in the η' observations at ocean-ice transitions appeared because different models are used to retrack radar signal returns in ice-covered and ice-free regions (Fig. 2.2a). This is commonly referred to as the "lead-open ocean bias" (Giles et al., 2012). Due to the technical nature of this bias, it is difficult to determine the true bias in the post processing phase. This is why differences between leads and open ocean are usually corrected in terms of a simple offset (e.g., Giles et al., 2012; Armitage et al., 2016; Morison et al., 2018). To estimate the offset, we compared altimetry to independent in-situ hydrography data, similarly to the approach taken by Morison et al. (2018). This approach gives the advantage that circulation features derived from spatial η difference at the transition between AWI and RADS data will be consistent with in-situ hydrography.

A good proxy for altimetry-derived η is the sum of hydrography-derived steric height (h_S), and GRACE-derived ocean bottom pressure (h_P, equivalent water thickness). We used hydrographic profiles in the Arctic Deep Basins (Fig. 2.2b) and compared those to the AWI and RADS along-track η (given by $\eta = \eta' + \langle\eta\rangle$, where $\langle\eta\rangle$ is the DTU17MDT described in Knudsen et al., 2019). We computed h_S as the vertical integral of the specific volume anomaly $\delta(p)$ relative to 400 db (Fofonoff, N.P, and Millard, R.C., 1983):

$$h_S = g^{-1} \int_0^{400} \delta(p)\, dp \tag{2.7}$$

where $\delta(p) = v(S,T,p) - v(35,0,p)$, and $v(S,T,p) = 1/\rho(S,T,p)$. The software used is from the seawater library for Matlab (Mathworks), Version 3.1 (Morgan and Pender, 2009). The depth range considered here captures

changes in the Polar Mixed Layer (Korhonen et al., 2013), which resides in the top 200 m across the Arctic, and includes the main component of steric height variability up to sub-decadal timescales.

η and h_S+h_P were compared using all available data in the overlapping period 2011-2014. All η, h_S and h_P data points were bin-averaged on an equal area grid with a resolution of 25-km. At each bin, average η from AWI and RADS datasets were compared separately to h_S+h_P. In Fig. 2.2b we show the result of this comparison. Both AWI and RADS data are linearly related to h_S+h_P, with a correlation coefficient of 0.98. This gave us confidence that the AWI and RADS dataset differed by a simple offset, and that altimetry-derived η patterns are consistent with in-situ hydrography. We computed two separate offset values, for the AWI and RADS datasets, by taking the average difference between binned η and binned h_S+h_P in ice-covered and ice-free regions respectively. The two offsets amount to -12.8 cm and -40.9 cm. We corrected altimetry data by removing each offset from the respective along-track η'. After correcting for the two offsets, η and h_S+h_P had a RMSD of 4-5 cm over a range of 70 cm.

Corrections

As second step, we checked that all corrections applied to the satellite range R (Eq. 2.1) were consistent between ice-covered and ice-free regions (Table 2.3 lists the products used here). Standard corrections (European Space Agency, 2016) were applied to both regions to account for i) the reduction in satellite signal speed caused by the presence of the atmosphere (dry gases, water vapour, ions); ii) the difference in reflection properties of wave troughs and crests at the sea surface (sea state bias correction, applied solely in the open ocean); and iii) solid earth tides.

Table 2.3. Altimetry corrections applied in this study. Acronyms: ECMWF (European Centre for Medium-range Weather Forecast); CNES (Centre National d'Etudes Spatiales); MOG2D (Modèle d'ondes de gravité 2D); FES2014 (Finite Element Solution 2014); GDR-E (Geophysical Data Record, version E).

Correction	Source	Reference
Dry troposphere	from mean surface pressure (based on ECMWF model)	European Space Agency (2016)
Wet troposphere	from mean surface pressure (based onECMWF model)	European Space Agency (2016)
Ionosphere	Global Ionospheric Map (CNES)	Komjathy and Born (1999)
Dynamic Atmosphere	Inverted Barometer + MOG2D barotropic model	Carrère et al. (2016)
Sea State Bias	Hybrid (parametric/non-parametric)	Scharroo and Lillibridge (2005)
Ocean Tide	FES2014	Lyard et al. (2021)
Solid Earth Tide	Cartwright model	Cartwright and Edden (1973)
Geocentric Polar Tide	Instantaneous Polar Location files (CNES)	Wahr (1985)
Orbit	GDR-E	European Space Agency (2016)

Two further corrections are used to remove the high-frequency ocean variability due to ocean tides and the ocean response to atmospheric pressure and wind forcing. These corrections contribute to reduce the aliasing of sub-monthly temporal changes into spatial variability, which emerges in average fields as meridionally

elongated patterns (meridional "trackiness", Stammer et al., 2000). In order to remove the most variability, we tested two products for each correction. First, to correct ocean tides we used the model FES2014 (Lyard et al., 2021), a more recent version of the FES2004 model (provided by ESA as standard correction product; Lyard et al., 2006). FES2014 was previously found to perform better than FES2004 in the Arctic (Cancet et al., 2018), and has been already used to correct most recent satellite altimetry products in this region (e.g., Rose et al., 2019; Prandi et al., 2021). Furthermore, in support of our choice, we found that the noise on the monthly fields, in areas of high tidal amplitude, was reduced by 20% by using FES2014 with respect to FES2004 (see results of analysis in Sect. 3.1.1, Fig. 3.1).

To correct the effect of atmospheric pressure and wind forcing, we used the Dynamic Atmosphere Correction (DAC, Carrère et al., 2016). The DAC is conventionally used today over the global ocean because it better suppresses the high-frequency variability due to non-local forcing (Carrère and Lyard, 2003; Quinn and Ponte, 2012; Carrère et al., 2016). However, for ice-covered regions ESA still suggests using an Inverted Barometer (IB) formula, which only accounts for the ocean response to local pressure forcing. This is because to date there is little knowledge about which of the DAC and IB corrections performs better in ice-covered regions (e.g., Robbins et al., 2016). Studies from the last two decades have shown that the deviation of ocean response from a simple IB response is larger at higher latitudes (e.g., Stammer et al., 2000; Vinogradova et al., 2007; Quinn and Ponte, 2012). In the Arctic, the effect of pressure and wind forcing is not only local, but also travels across the region in the form of mass waves (Fukumori et al., 1998; Peralta-Ferriz et al., 2011; Fukumori et al., 2015; Danielson et al., 2020). This indicates that it would be appropriate to apply the DAC to both, ice-covered and ice-free regions.

To support our choice of using DAC over IB, we looked at which of them reduced the standard deviation of the along-track η' the most with respect to the uncorrected η' (see detailed results in Sect. 3.1.2, Fig. 3.4). Results showed that DAC outperforms the IB in shallow shelf regions (particularly the East Siberian Sea and the Chukchi Sea, in agreement with findings by Piecuch et al. (2022)) and that they perform equally well over the deep basins (Fig. 3.2). For instance, in the East Siberian Sea the DAC reduced the uncorrected η' standard deviation by 50% at periods shorter than 20 days, in contrast to no reduction when applying a simple IB (see Table 3.1). The improvement of DAC with respect to IB over the shelves appears also in the η' monthly grids, where meridionally oriented patterns of η' are evidently reduced (Fig. 3.3).

Merged along-track dataset and uncertainty estimate

The final merged along-track dataset is composed of two sub-datasets, one for the ice-covered region and one for the ice-free region. The consistency between these two sub-datasets is indicated by their comparable Arctic-wide standard deviation over the period 2011-2020, amounting to 11.1 cm and 10.4 cm respectively.

The average monthly standard deviation and data points density, over the period 2011-2020, is shown in Fig. 2.3, both for the merged dataset and separately for AWI and RADS datasets. The two datasets display consistent spatial and temporal variability in the overlap regions, with standard deviation largest in shallow areas throughout the year, and enhanced in winter everywhere. The transition between ice-covered and ice-free regions is generally smooth (Figs. 2.3a and 2.3b) except for increased standard deviation and decreased data density following the marginal ice zone in Fram Strait. The distribution of data density shows that, both during summer and winter, more than about 50 observations per 100 km^2 per month are available everywhere, except for the region north of the Canadian Arctic Archipelago in winter, when the ocean is almost fully covered by pack ice.

Despite the smooth distribution in the average monthly statistics, we note that some residual large-scale sub-monthly variability persists in the data. Figure 2.3g shows, for instance, a decrease of ~20 cm in η' north of Greenland between the first and the fourth week of July 2015. This suggests that, despite correcting

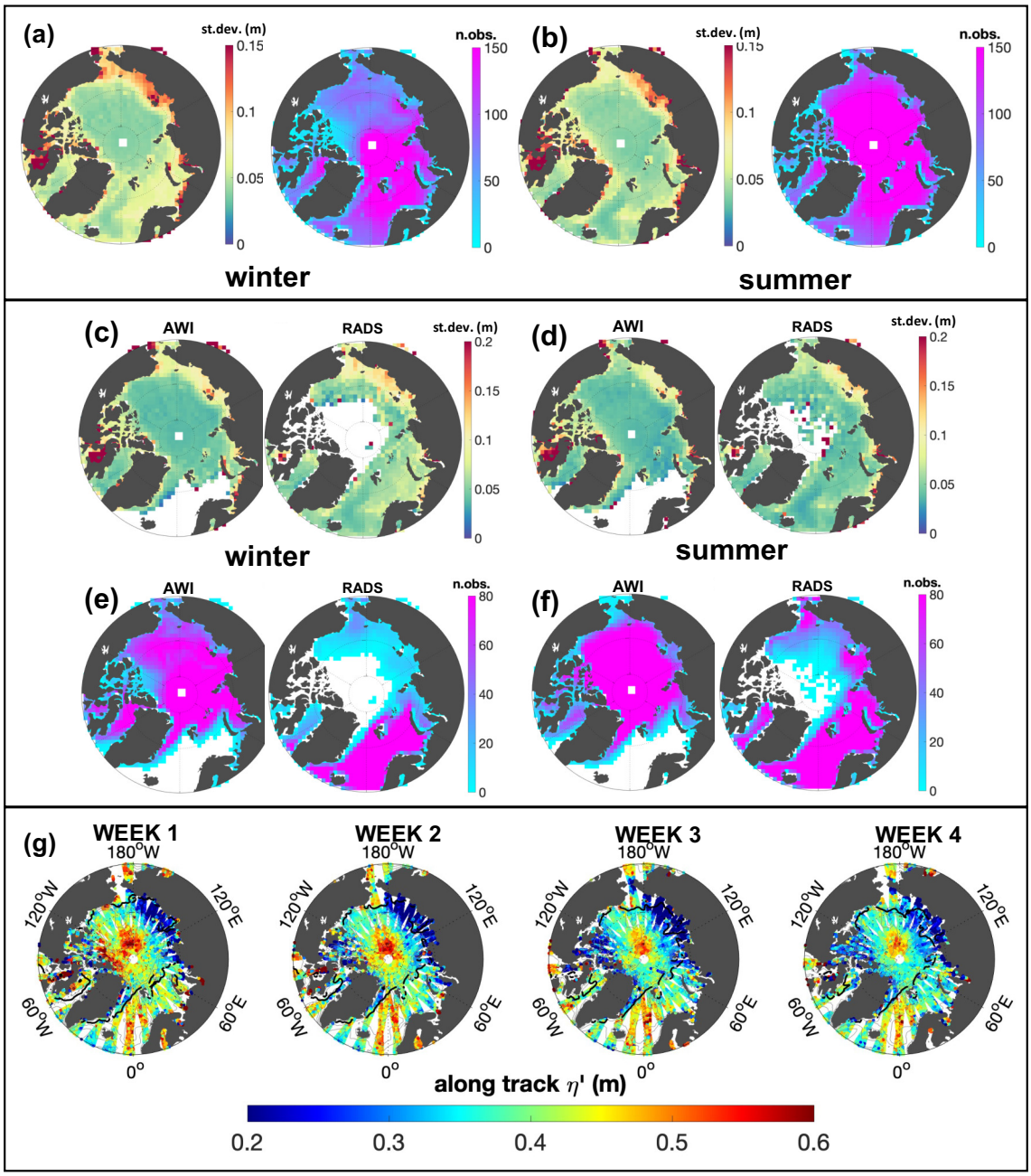

Figure 2.3. Average monthly statistics of the along-track η' dataset over the ice-covered and ice-free Arctic Ocean, in the period 2011-2020. Standard deviation (panels a-left, b-left, c, d) and number of observations per 100 km^2 per month (panels a-right, b-right, e, f) for the merged dataset (a,b), and separately the AWI and RADS datasets (c,d,e,f) are shown for the winter (October to April) and summer (May to September) seasons. (g) Example of weekly along-track data in the month of July 2015; the black solid line indicates the 15% sea ice concentration as derived from the OSI SAF ice concentration products. Note the different color scales of panels a and b with respect to panels c-d-e-f.

high-frequency variability using the DAC and a state-of-the-art ocean tidal correction, η' is subject to residual large-scale variability on timescales shorter than a month. Constructing monthly maps based on sampling this large-scale, high-frequency variability at different times in different locations, will artificially produce short wavelength patterns. A clear example of this pattern is shown in chapter 3, Sect. 3.1.3, highlighting that residual high-frequency variability can result in representativity error on the monthly fields. We address this issue in phase of interpolation (Sect. 2.5.2) and provide in Sect. 2.5.2 an estimate of the contribution of this unresolved variability to the error on the monthly η' fields.

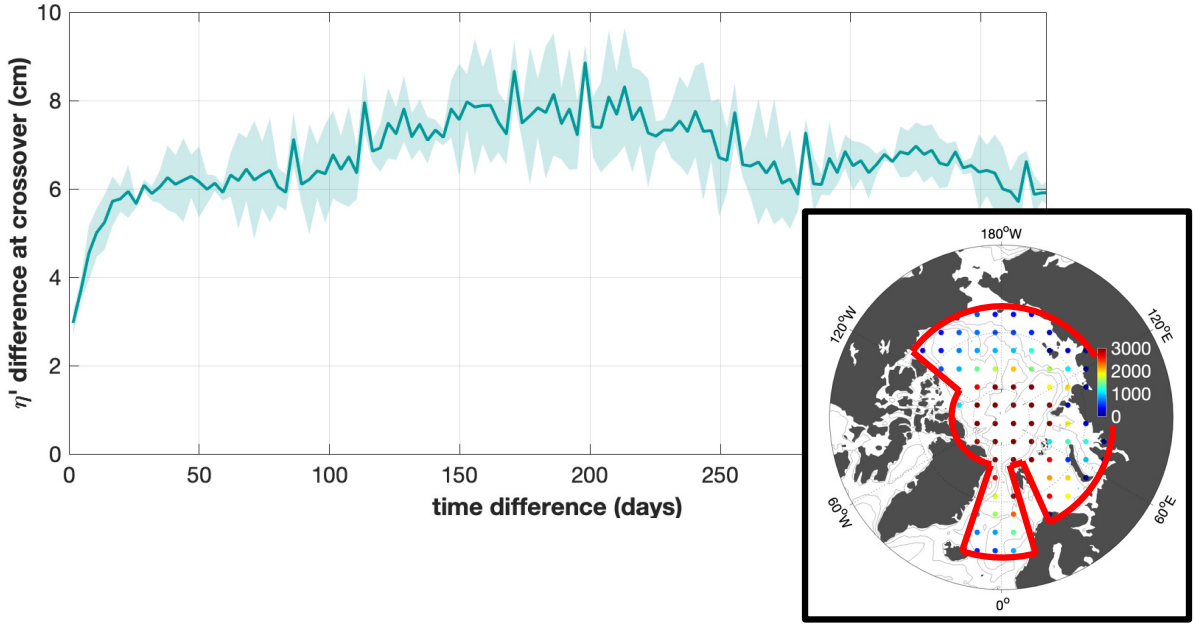

Figure 2.4. Absolute value of η' difference at crossovers between satellite tracks in a period of time up to 1 year, computed using data inside the red line in the inset panel. The solid line in the main panel is the crossover difference averaged every 3 days; the shaded area shows the standard deviation of crossover difference, averaged every half a day. Crossovers differences were computed using data within 100 km around the locations indicated in the inset panel. The color of dots in the inset panel indicates the number of crossovers found around that location.

On top of the representativity error, several sources contribute to the uncertainty on the single along-track η' observations. This uncertainty includes contributions from the altimeter measurement uncertainty, the waveform retracking method, the corrections and orbit uncertainty. Given the difficulty of assessing the contribution of each of these sources, we provide here a comprehensive estimate of the observational uncertainty based on the absolute difference of the along-track η' at satellite tracks crossovers (Fig. 2.4). We first defined crossovers as those pairs of η' observations within a distance of 7 km. We excluded pairs belonging to the same satellite pass by verifying that they are separated by more than one hour. We finally evaluated the absolute value of η' differences at $\sim 7 \cdot 10^7$ crossovers, distributed within 100 km from the locations indicated in Fig 2.4 (inset panel). In Fig. 2.4 we see that the crossover difference is small for short time differences and increases as crossovers are separated by a larger time difference. For crossovers very close in time, we expect the difference to approximate the observational uncertainty, while we expect it to increase with time due to additional variability. Therefore, we estimated the observational uncertainty as the average difference at crossovers separated by no more than 3 days, which is 3 cm.

This analysis provides additional information about the η' de-correlation timescale. The η' crossover difference increases with time above the uncertainty due to local variability. Fig. 2.4 shows that variability increases very rapidly by about 3 cm in the first couple of weeks, then by a further 2 cm after six months, to decrease then again by 2 cm after a full seasonal cycle. This indicates that, at timescales shorter than one year,

η' has a short de-correlation timescale below one month (in agreement with Landy et al., 2021) and a long de-correlation timescale of six months.

2.5.2 Gridded fields

We generated monthly η' fields over the period 2011-2020, by interpolating the along-track data onto a longitude-latitude grid of resolution 0.75°×0.25°, from 60° N to 88° N. In Sect. 2.5.2 we provide a global estimate of the standard error on the monthly η' fields. Finally, based on the analysis of the error given in Sect. 2.5.2, in Sect. 2.5.2.1 we describe the steps taken in phase of interpolation to reduce the noise due to residual sub-monthly variability.

Interpolation using the Data-Interpolating Variational Analysis

Along-track data were interpolated to obtain η' fields on a regular latitude-longitude grid. We used the Data-Interpolating Variational Analysis (DIVA, Troupin et al., 2012; Barth et al., 2014), a tool based on a technique called variational inverse method (VIM, Brasseur and Haus, 1991). DIVA has been successfully applied in the past by several studies (e.g., Tyberghein et al., 2012; Capet et al., 2014; Lenartz et al., 2017; Iona et al., 2018; Belgacem et al., 2021) to a variety of data types (e.g., temperature, salinity, chlorophyll concentration, nutrients, air pollutants), spatial and temporal extents, and regions (global ocean, Mediterranean Sea, Black Sea). We applied this method for the first time to altimetry observations in the Arctic Ocean.

Rixen et al. (2000) showed that the performance of the VIM is comparable to the widely used optimal interpolation technique (in its original formulation, Bretherton et al., 1976). DIVA offers advantages when treating large datasets in regions of complex topography. One advantage is that the VIM maintains low numerical cost when the number of data points is large compared to the grid points (Rixen et al., 2000). This was suitable for our case, with a number of data points in one month ($\sim 10^5$) ten times larger than the number of grid points ($\sim 10^4$). Furthermore, DIVA allows us to naturally decouple basins that are not physically connected by using a regularity constrain based on the gradient and Laplacian of the gridded field (Troupin et al., 2010).

A short description of the working principles of DIVA is given in the following. The optimal field in VIM is found by minimising a cost function (e.g., Brasseur and Haus, 1991; Troupin et al., 2012; Barth et al., 2014, 2021), which satisfies basic requirements for the analysis field φ, such as its closeness to data and its regularity (no abrupt changes). DIVA formalises these principles in a cost function as follows:

$$J(\varphi) = \sum_{i=1}^{N} \mu\,[d_i - \varphi(\mathbf{x}_i)]^2 + \int_\Omega \frac{1}{L^4}\varphi^2 + \frac{2}{L^2}\nabla\varphi\cdot\nabla\varphi + (\nabla^2\varphi)^2\,d\Omega \tag{2.8}$$

In Eq. (2.8), the first term assures the closeness of the analysis field to the data. This is achieved by globally minimizing the difference between φ at the data locations $\mathbf{x}_i$, and the data themselves d_i, which are associated to a weight μ. The second term generates a smooth field over the domain Ω (Troupin et al., 2012), where L defines the length scale over which the data should be propagated spatially. In general, the field φ and the data d_i should be understood as anomalies relative to a background estimate. The data weights μ are directly proportional to the signal-to-noise ratio λ (ratio of the error variance of the background estimate, σ^2, to the error variance of the observations, ϵ^2) and inversely proportional to the square of the length scale L (Brasseur et al., 1996):

$$\mu = 4\pi\frac{\lambda}{L^2} \tag{2.9}$$

As explained further below, the interpretation of weights μ in terms of the signal-to-noise ratio allows DIVA to calculate error maps at low computational cost.

The length scale L is a parameter related to the distance over which ocean state variables decorrelate. In the Arctic Ocean, boundary currents can be as narrow as few tens of kilometres (Beszczynska-Möller et al., 2012; Pnyushkov et al., 2015). Even though satellite altimetry provides a tool to investigate the surface expression of these dynamic features, maps of sea surface height in the Arctic are commonly smoothed over hundreds of kilometres (Kwok and Morison, 2016; Pujol et al., 2016; Armitage et al., 2016; Rose et al., 2019; Prandi et al., 2021). In order to retain the possibility to resolve Arctic boundary currents in our maps of geostrophic currents, we generated monthly maps using a length scale smaller than a hundred kilometers, while relying on a background field derived using a large length scale. Namely, we applied a two-step interpolation as follows. We first computed a background field using all η' observations in the period 2011-2020, interpolated with a large length scale of 300 km. In a second step, we interpolated weekly subsets of the data relative to the background field using a short length scale of 50 km. Finally, as explained in Sect. 2.5.2.1, we obtained monthly maps by averaging four weekly fields. The scale used in the second step (50 km) defines the spatial scale beyond which we expect to resolve the temporal variations, as assessed and discussed in Sects. 3.2.2 and 3.3.3. This length scale assured us to have enough tie points for the interpolation (see Fig. 2.3a and 2.3b), while attempting to resolve scales shorter than previous works. From Fig. 2.3a we can see that the least constrained region is the ice-covered ocean north of the Canadian Arctic Archipelago, where in winter there are on average less than 50 data points per month per 100 km^2.

The signal-to-noise ratio λ is to be interpreted as the ratio between the fraction of data variance that is representative of the final analysis field (σ^2) and the fraction that is to be considered noise (ϵ^2). The latter might in general include the observational error as well as representativity errors (e.g., instantaneous measurements are not a good representation of a long term mean). One possible way to give an estimate of λ is the generalized cross validation technique (Troupin et al., 2010). However, this technique has led in past studies to an overestimation of λ when applied to non-independent data (Troupin et al., 2010), in particular in applications where averaged fields were created (Troupin et al., 2012; Lauvset et al., 2016; Belgacem et al., 2021). We estimated instead ϵ^2 and σ^2 separately from η' observations, based on the approximation that weekly data subsets were not subject to error of representation (see Sects. 2.5.1 and 2.5.2.1). We thus considered the observational uncertainty, calculated in Sect. 2.5.1, as the dominant source of noise over a period of one week, hence took ϵ equal to 3 cm. Under the same assumption, we took σ equal to 8.2 cm, estimated taking the data signal σ^2 equal to the spatial variance of weekly data subsets, averaged in the period 2011-2020. The signal-to-noise ratio λ, defined by the ratio of σ^2 over ϵ^2, was therefore 7.5. This estimate lies in the range of values ($\lambda \sim$ 1-10) used in previous studies applying DIVA to generate averaged fields (Troupin et al., 2010, 2012; Tyberghein et al., 2012; Lauvset et al., 2016; Iona et al., 2018; Watelet et al., 2020; Belgacem et al., 2021). Furthermore, we noted that the standard deviation of our analysed η' fields changed by only a small fraction when varying λ in the range of 1-10.

Along with the gridded fields, DIVA has the capability to provide associated error maps using several different methods, each having different computational costs. A review of methods is provided by Beckers et al. (2014). Among these, we selected the clever poorman's estimate due to its fast calculation (CPME, Beckers et al., 2014). The CPME speeds calculations by circumventing the extraction of the data covariance matrix, which is never explicitly computed in DIVA. The CPME takes advantage of the fact that the absolute interpolation error scaled by the variance of the background field can be derived with good approximation by applying the DIVA analysis to a vector of unit values (Beckers et al., 2014). We thus generated maps of relative error via the CPME, given as fraction of the variance of the background field. These maps allow the user to assess the data coverage given by the distribution of the data in space, scaled by the length scale L and the signal-to-noise ratio λ.

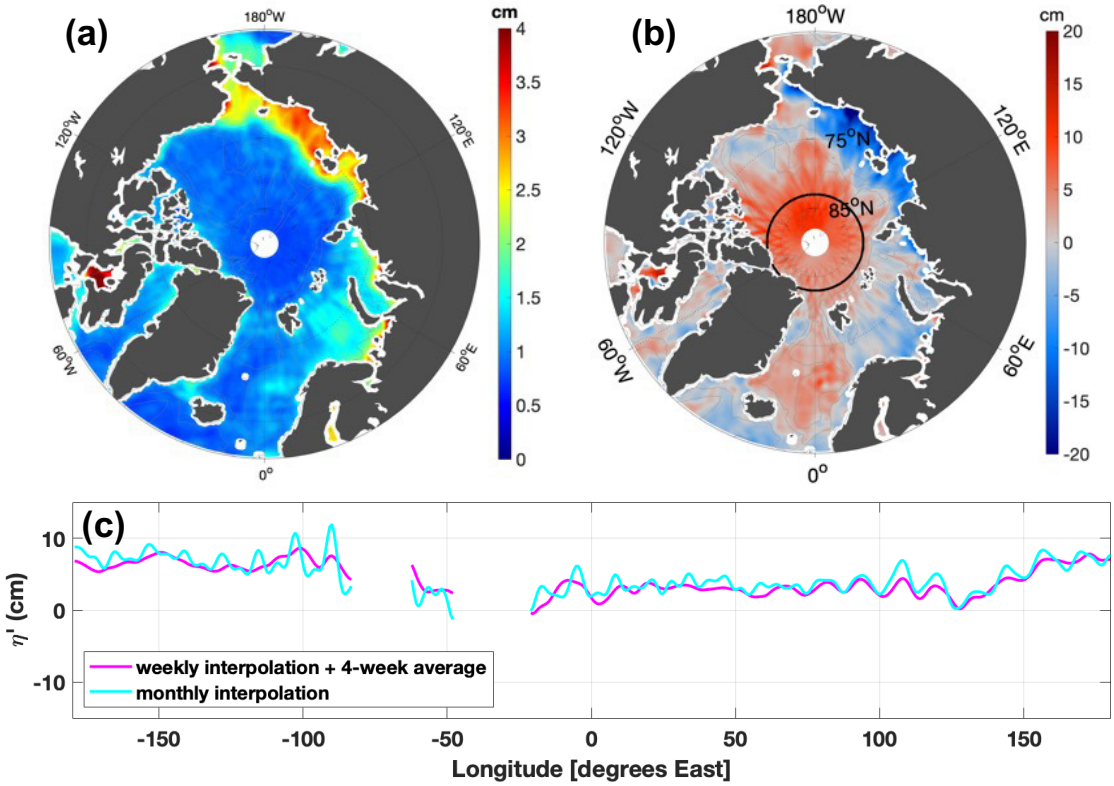

Figure 2.5. Residual sub-monthly variability in the gridded η' fields. (a) The sub-monthly contribution to the standard error on monthly η' maps, computed from weekly maps, averaged over the period 2011-2020. (b) The July 2015 monthly gridded η' field obtained by interpolating monthly data input. (c) η' along a latitude (83° N) circle; η' obtained from weekly interpolation plus averaging (Fig. 3.5a) and from monthly interpolation (panel b) are shown with magenta and cyan lines, respectively. Bathymetry contours are drawn at 100 m, 1000 m and 2500 m depth.

Error on monthly fields

The standard error in the monthly η' fields comprises a component arising from the observational uncertainty and another arising from representativity error due to unresolved sub-monthly variability. We provide here an average estimate of these two contributions was computed over the area shown in the inset panel of Fig. 2.4, as follows.

The component deriving from the observational uncertainty was obtained for each month as the uncertainty estimate of an individual measurement, derived from the crossovers analysis (i.e. 3 cm, Sect. 2.5.1), divided by the square root of the average number of data points per cell per month. This component of the standard error, averaged over the period 2011-2020, amounts to 1.7 cm. The monthly component stemming from the sub-monthly variability was first calculated at each grid point as the standard deviation of the four weekly η' values divided by the square root of four. To verify that weekly interpolated fields were statistically independent, we calculated the integral timescale of η' (Emery and Thomson, 2001) from the time series of weekly values between 2011 and 2020, high-pass filtered with a cutoff of two months to exclude longer decorrelation timescales. Across the whole Arctic we found an integral timescale of about one week, in agreement with results by Landy et al. (2021), supporting the hypothesis of statistically independent weekly fields. The monthly average standard error yielded by this approach is 1.1 cm over the period 2011-2020. The time average distribution of this contribution is displayed in Fig 2.5c, which shows values of 1-4 cm in areas shallower than 100 m, with peak values of more than 3 cm in the East Siberian Sea. We assumed that the observational and sub-monthly contributions to the error are independent, and computed the total error by

adding them in quadrature. This amounts to 2 cm, which is a conservative estimate of the total standard error on monthly averages over the period 2011-2020.

2.5.2.1 Minimisation of sub-monthly variability

As seen in Sect. 2.5.1, the residual sub-monthly variability produces marked meridional trackiness if the interpolation is performed on a monthly set of η' observations (see also results in Sect. 3.1.3). To further reduce the sub-monthly variability, we performed the interpolation on weekly data subsets instead. Monthly η' maps were obtained as the average of four weekly maps. Furthermore, the analysis of the η' decorrelation timescales presented in Sect. 2.5.2 showed that weekly estimates are statistically independent. Therefore, the associated interpolation error was computed by adding in quadrature of four weekly error maps. By comparing Fig. 2.5b with Fig. 3.5a (final monthly gridded product) one can appreciate how trackiness is reduced in a given month over the entire Arctic. In Fig. 2.5c we show in detail the η' profile along a latitude circle, as an example of the trackiness reduction obtained thanks to this approach. The field displayed in Fig. 2.5a shows the contribution of the sub-monthly variability to the error on the monthly η' fields, computed as explained in Sect. 2.5.2.

Gridded geostrophic velocity

Monthly η fields were reconstructed by adding up the $\langle\eta\rangle$ DTU17MDT, the η' background field over the period 2011-2020 and the gridded η' maps resulting from the steps described above. Based on the η fields, geostrophic velocity was computed on the output grid following Eq. 2.4, with partial derivatives approximated by finite differences. The components of velocity on the longitude-latitude grid at indices i, j are given by:

$$\begin{cases} u_{g,ij} = -\frac{g}{fR_e}\frac{\eta_{i+1,j}-\eta_{i-1,j}}{\theta_{i+1,j}-\theta_{i-1,j}} \\ v_{g,ij} = \frac{g}{fR_e}\frac{1}{cos(\theta_{ij})}\frac{\eta_{i+1,j}-\eta_{i-1,j}}{\Phi_{i+1,j}-\Phi_{i-1,j}} \end{cases} \tag{2.10}$$

where variables are defined as for Eq. 2.4.

2.6 The Finite Elements Sea ice-Ocean Model

With the aim of describing the nature and drivers of the large-scale seasonal variability in the Arctic sea surface height and slope currents, I supported remote sensing data with simulations from a global version of the Finite-Element-Sea ice-Ocean-Model (FESOM). FESOM was developed in the Climate Dynamics section of the Alfred Wegener Institute. It consists of a finite element ocean model (Danilov et al., 2004; Wang et al., 2008), coupled to a sea ice model (Timmermann et al., 2009). This model employs a finite element discretization of the governing equations, allowing the use of unstructured meshes which can be locally refined in areas of interest and kept coarse in other parts of the global oceans. In the context of this thesis, I used the FESOM version 1.4, where the resolution is locally increased over the Arctic Ocean to 4.5 km. This fine resolution provides the advantage of resolving well the narrow slope currents in the Arctic Ocean, where the local baroclinic Rossby deformation radius is particularly small (Nurser and Bacon, 2014). The model has been described and validated by Wang et al. (2018b) and Wang et al. (2019). The run used in this work is the historical run used by Wang et al. (2020), forced by the atmospheric reanalysis data JRA55-do v.1.3 (Tsujino et al., 2018). In the following, I provide basic details about the dynamic and thermodynamic equations governing the ocean component of FESOM v1.4. This will be useful to the reader as a reference for the analysis carried out in Chapter 4.

The ocean component solves the standard set of hydrostatic primitive equations with the Boussinesq approximation, where density anomalies are only considered in the buoyancy term of the vertical momentum equation. The system of governing equations includes a dynamical part and a thermodynamical part, which

are solved separately. The dynamical part includes the momentum equations in three dimensions, the vertically integrated continuity equation and the hydrostatic pressure equation which are solved for horizontal velocity, sea surface height and pressure:

$$\partial_t \mathbf{u} + \mathbf{v}\cdot\nabla_3\mathbf{u} + \mathbf{f}\times\mathbf{u} + g\nabla\eta + \frac{1}{\rho_0}\nabla p_0 = \nabla\cdot A_h\nabla\mathbf{u} + \partial_z A_v \partial_z \mathbf{u}, \tag{2.11}$$

$$\partial_t \eta + \nabla\cdot\int_{z=-H}^{z=\eta}\mathbf{u}\,dz = 0, \tag{2.12}$$

$$\partial_z p_0 = -g\,\rho, \tag{2.13}$$

where $\mathbf{v}\equiv(\mathbf{u}, w)\equiv(u, v, w)$ is the velocity vector, $\mathbf{f} = f\mathbf{k}$, with $f = f(\theta)$ the Coriolis parameter dependent on the latitude θ and $\mathbf{k}$ the vertical unit vector, g is the gravitational acceleration, ρ_0 and ρ are the mean sea water density and the deviation from it, respectively, η is the sea surface height, $p_0 = \int_z^0 g\,\rho\,dz$ is the hydrostatic pressure anomaly obtained by integrating the hydrostatic equation in the vertical from $z = 0$, A_h and A_v are the lateral and vertical momentum diffusion coefficients, respectively. The upper limit in the integration in equation 2.12 is set to zero, which implies a linear free-surface approximation. ∇ and ∇_3 stand for the 2-dimensional and 3-dimensional gradient and divergence operators, respectively. In equation 2.12, an explicit formulation for the surface vertical transport of freshwater into the ocean (precipitation, river runoff and sea ice melting) and out of the ocean (evaporation and sea ice freezing) is omitted. This is instead implicitly accounted for by vertical fluxes of temperature (T) and salinity (S), as in Eq. 2.18.

Boundary conditions are set at the ocean surface, bottom and lateral vertical rigid walls. At the ocean surface, vertical momentum diffusion is equal to the wind stress and p_0 is zero, bottom drag has quadratic dependence to the bottom velocity, and no-slip boundary conditions are applied at the lateral boundary. The vertical velocity w is diagnosed from the continuity equation:

$$\partial_z w = -\nabla\cdot\mathbf{u}, \tag{2.14}$$

which has the following kinematic boundary conditions at the surface and at the bottom:

$$w = \partial_t\eta \text{ at the surface }, \tag{2.15}$$

$$w = -\nabla H\cdot\mathbf{u} \text{ at the bottom }. \tag{2.16}$$

In the thermodynamical part of the ocean model we solve the tracer equations for potential temperature T and salinity S:

$$\partial_t C + \mathbf{v}\cdot\nabla_3 C = \nabla\cdot K_h\nabla C + \partial_z K_v\partial_z C, \tag{2.17}$$

with C standing for T or S and K_h and K_v standing for the lateral and vertical diffusivity for the particular tracer, respectively. The following boundary conditions have to be fulfilled for the tracer equations:

$$K_v\partial_z C = -q, \text{ at the surface} \tag{2.18}$$

$$(K_h\nabla C, K_v\partial_z C)\cdot\mathbf{n}_3 = 0 \text{ at the bottom and lateral boundary }, \tag{2.19}$$

where q stands for the surface flux for T and S. The density ρ is diagnosed based on T, S and p_0, via the equation of state according to Jackett and Mcdougall (1995).

2.7 Seasonal cycle from altimetry and model data

A convenient way to describe the spatial characteristics of the η' seasonal cycle is by identifying few parameters to describe it. Previous studies showed that a simple harmonic with annual period is a good approximation for the η' seasonal cycle over most of the Arctic Ocean (Volkov et al., 2013; Armitage et al., 2016; Müller et al., 2019b). This can be expressed, following Volkov et al. (2013), as:

$$\eta'_{\text{seas}} = A \cos\left[2\pi\left(\frac{t-\alpha}{P}\right)\right] \tag{2.20}$$

where A is the seasonal amplitude, α the phase (month of annual maximum), t is time (here the month number), and P is the period (here equal to 12 months). I therefore applied a harmonic least-square fit to monthly values of η' from both the SAGA and FESOM data (2011-2020) to estimate the seasonal amplitude and phase as in equation (2.20). Based on these two parameters, I identified and discussed spatial patterns in the seasonality of η', thereby validating the seasonal variability as simulated by FESOM (chapters 3 and 4). I furthermore evaluated the fraction E of the total variance explained by η'_{seas} at each grid point following:

$$E = 100\,(1 - \frac{\text{var}(x - x_F)}{\text{var}(x)}) \tag{2.21}$$

with η' as x and η'_{seas} as x_F.

2.8 Steric and mass-related variability from FESOM output

2.8.1 Sea surface height

With the aim of attributing the η' variability to either buoyancy or wind forcing, I used FESOM output fields to separate sea surface height variability into its steric and mass-related contributions. I used temperature and salinity to calculate steric sea level anomaly in time (η'_S) at each FESOM grid point as follows:

$$\eta'_S = -\frac{1}{\rho_0}\int_{-H}^{0} \rho'(z)\,dz \tag{2.22}$$

where H is the model bathymetry, $\rho'(z)$ is the density anomaly relative to the mean density in the period 2011-2018, and ρ_0 is the reference density equal to 1028 kg m^{-3}. Mass-related sea level anomaly (η'_M) was then computed by subtracting η'_S from η':

$$\eta'_M = \eta' - \eta'_S \tag{2.23}$$

2.8.2 Ocean mass data from the Gravity Recovery and Climate Experiment

In order to validate ocean mass changes diagnosed from the FESOM output fields, I compared these to ocean mass fields based on the Gravity Recovery and Climate Experiment satellite data (GRACE). I used the Jet Propulsion Laboratory Release-06 GRACE mascons solution (based on Watkins et al., 2015), derived by solving for mass variations using local spherical cap mass concentration elements (mascons). These solutions provide advantages over commonly used harmonic solutions in that they suffer less from land leakage errors and north-south striping (Wiese et al., 2016).

2.8.3 Geostrophic speed anomaly from steric and mass-related variations

As described by equation (2.4), the meridional and zonal components of geostrophic currents $\mathbf{u_g}$ are linearly related to spatial gradients in η. The temporal variability of $\mathbf{u_g}$ derives therefore from spatially non-uniform changes in η over time, caused in turn by both steric and mass-related variability. The relation between the geostrophic variability of ocean currents and steric and mass-related changes in the water column provides a method to infer drivers of geostrophic circulation by investigating the nature of the sea surface height variability. Density-driven currents will result from local changes in the steric height, which could be due for instance to the coastal spread of river runoff or to advection of meltwater. Mass-related currents are the result of gradients in the mass-related height, generated either by local wind-driven mass convergence or by the propagation of mass waves. This method would be of particular interest for the Arctic should it prove capable of explain drivers of changes in the Arctic slope currents. These are narrow topographically-guided currents which act as pathways of warm and salty Atlantic waters into Arctic (Schauer et al., 2004; Smedsrud et al., 2010) which contributes to ocean-driven changes in sea ice, in turn adding to the exceptional Arctic sea-ice retreat observed over the past decades (Polyakov et al., 2017).

In order to evaluate the steric and mass-related contributions to the seasonal modulation of Arctic currents, I therefore decomposed the total variability of $\mathbf{u_g}$ into density-related and mass-related variability. The decomposition was obtained by taking the mean sea surface height field $\overline{\eta}$ and calculating geostrophic anomalies induced by changes in the $\overline{\eta}$ spatial gradient due to steric and mass-related anomalies (η'_S and η'_M respectively). The calculation consisted therefore in applying equation (2.4) to monthly maps of $\eta_S = \overline{\eta} + \eta'_S$ and $\eta_M = \overline{\eta} + \eta'_M$ respectively.

2.9 Forcing of mass-related variability

In this thesis, the analysis of seas surface height drivers on the seasonal time scale focused on the wind forcing of the mass-related component. By using ocean surface stress fields and 3-D ocean velocity fields from the FESOM model, I investigated the mechanisms by which wind drives exceptionally large seasonal oscillations in the shelf seas of the Eurasian Arctic.

2.9.1 Surface wind stress

Wind stress at the ocean surface ($\tau_\mathbf{o}$) is computed in the FESOM model using winds from the JRA55-do reanalysis and the FESOM output of ocean and ice velocity. Taking into account the simulated sea ice distribution, surface stress at the ice-ocean and atmosphere-ocean interfaces ($\tau_\mathbf{io}$ and $\tau_\mathbf{ao}$) is computed using bulk formulas as described by Timmermann et al. (2009) (their equations (24) and (25)). The total ocean surface stress is then given by the area-weighted average:

$$\tau_\mathbf{o} = A \cdot \tau_\mathbf{io} + (1 - A)\tau_\mathbf{ao} \tag{2.24}$$

where A is the ice concentration over the model grid cells.

To understand the qualitative relation between the surface wind forcing and the seasonal mass-related height variability, I computed seasonal composites of $\tau_\mathbf{o}$ fields. The composites were derived as the average of monthly $\tau_\mathbf{o}$ fields over different phases of the η'_M seasonal cycle, determined through Empirical Orthogonal Function (EOF) analysis as described in the following section.

2.9.2 EOF analysis of mass-related variability

EOF analysis is a statistical technique which allows to identify the key spatio-temporal patterns of variability of a field. This analysis partitions the variance of a spatially distributed, time-varying field $F(x, y, t)$ into statistical modes of variability (functions) which are independent from each other (orthogonal). Each mode consists of a spatial distribution $m_i(x, y)$ and a temporal evolution $PC_i(t)$, called Principal Component (Emery and Thomson, 2001). The total variability of the time time-varying field is given by the linear superposition of an infinite series of EOF modes, with most of the variability generally represented by the first three modes: $F(x, y, t) = \sum_{i=1}^{\infty} PC_i(t) \cdot m_i(x, y)$. I performed an EOF analysis of the η'_M fields north of 60°N by applying the dedicated script from the Climate Data Toolbox for MATLAB by Greene et al. (2019).

2.9.3 Ekman transport

In order to provide a quantitative estimate of mass-related changes in the Eurasian shelf due to wind forcing, I firstly investigated in which measure the seasonal patterns of η'_M on the western shelf seas (Barents and Kara Seas) can be attributed to cross-slope Ekman transport at the ocean surface (Ekman, 1905, here indicated as $\mathbf{U^{ek}}$). Surface Ekman velocities are the direct result of the balance between the wind friction on the ocean and the Coriolis force. Mass-related height changes result from net Ekman transport of water volume into a certain area. By calculating the height changes implied by Ekman transport, referred to as "equivalent height" changes, one can therefore directly compare wind-forced transport to observed changes in η'_M.

I first derived the zonal and meridional components of $\mathbf{U^{ek}}$ from the $\tau_\mathbf{o}$ fields as:

$$\begin{cases} U^{ek} = \frac{1}{\rho_0 f} \tau_o^y \\ V^{ek} = -\frac{1}{\rho_0 f} \tau_o^x \end{cases} \tag{2.25}$$

I then computed the net volume transported via Ekman transport into the Barents and Kara Seas across at transect enclosing these two seas (Fig. 2.6). To this end, I first took the transport normal to the transect at each transect point (U_N^{ek}), and then integrated this along the transect and over time. The transect was composed by segments about 2 km long, to avoid under-sampling the FESOM fields (output on a grid with 4.5 km resolution). The Ekman transport equivalent height is finally given by the transported volume divided by the shelf area A:

$$\Delta\eta_{Mek} = \frac{1}{A} \Delta t \int_T U_N^{ek} \, ds \tag{2.26}$$

where T indicates the transect and Δt denotes the time change over a month.

2.9.4 Deep ocean transport

An analysis of full onshore ocean transport is supplementary to the calculation of Ekman transport to better understand the dynamics of cross-slope transport. Full transport is calculated directly from horizontal ocean velocity and provides an overview on the intensity and spatial distribution of the cross-slope transport. I therefore used FESOM ocean velocity to calculate the net onshore full transport across the transect enclosing the Barents and Kara Seas (Fig. 2.6). With the aim of investigating the deep ocean response to exceptionally high (low) onshore Ekman transport, I computed composite sections of cross-slope full transport by averaging monthly velocity sections when onshore Ekman transport was higher (lower) than one standard deviation above (below) the mean.

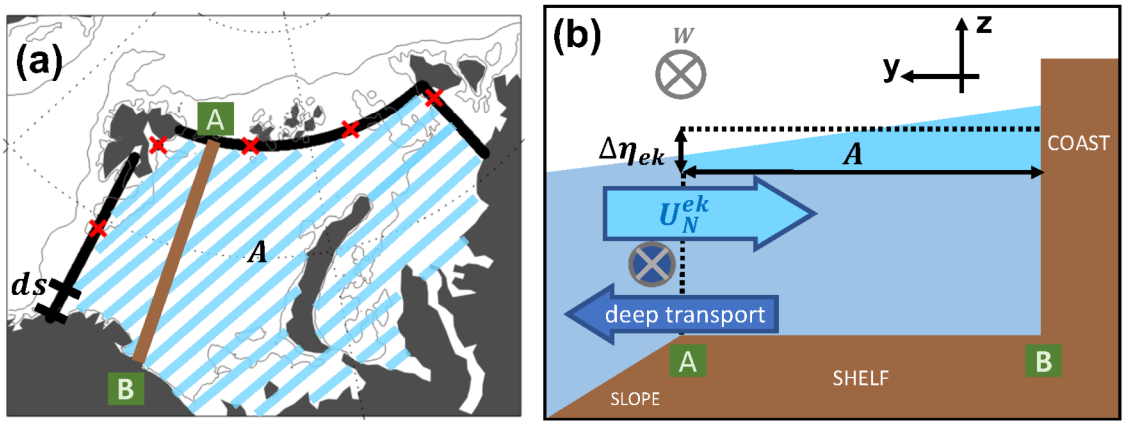

Figure 2.6. Ekman transport and associated equivalent height. (a) The map displays the transect over which the Ekman transport was computed (black line, red crosses each 500 km); the brown line indicates a possible coast-shelf-basin reference for panel (b). (b) Schematic showing illustrating the calculation of the Ekman transport equivalent height: light blue water represent the water volume transported via Ekman dynamics, A is the shelf area and $\Delta\eta_{Mek}$ is the equivalent height; the light blue arrow pointing towards the shelf represent the Ekman transport, the dark blue arrow going into the page below the Ekman layer is the slope current and the dark blue arrow directed towards the basin represents deep ocean transport.

2.9.5 Equation for the barotropic vorticity

In an effort to provide a process-oriented interpretation of the shelf mass budget in the Eurasian Arctic, I present here a description of ocean mass variability via the barotropic vorticity equation. With respect to the sole wind forcing, this equation represents a more complete description of the balance driving barotropic flows. This includes, in addition to wind stress, the effect of bottom topography, the Coriolis force and dissipation. Past research has used the principle of conservation of the barotropic vorticity to study drivers of the variability in a barotropic ocean (e.g., Nøst and Isachsen, 2003; Isachsen et al., 2003; Volkov et al., 2013). Isachsen et al. (2003) demonstrated that a simplified linear barotropic model (including surface wind forcing and linear bottom drag) is able to reproduce the observed variability of depth-averaged transport in the Arctic region on time scales between 3-4 months and a few years. Volkov et al. (2013) (hereafter V13) used the vorticity equation to analyse the drivers of mass-related sea level variability in the Barents Sea. Here, I attempt to supplement the diagnostic analysis of the shelf mass budget provided in Sect 4.2.2, based on ocean velocity, by analysing the terms of the vorticity equation as formulated by V13 in their Eq. (7).

The form of the barotropic (depth-averaged) vorticity balance used by V13 is written as follows:

$$\frac{\partial\zeta}{\partial t}+\overline{\mathbf{u}}\cdot\nabla\zeta+\beta v-\frac{\zeta+f}{H}\left(-\nabla\cdot\mathbf{U}+\overline{\mathbf{u}}\cdot\nabla H\right)=\nabla\times\frac{\tau_o}{\rho H}-D \tag{2.27}$$

where $\overline{\mathbf{u}}=\frac{1}{H}\int_{-H}^{0}\mathbf{u}\,dz$ is the depth-averaged ocean velocity, $\zeta=(\nabla\times\overline{\mathbf{u}})\cdot\hat{\mathbf{k}}$ is the vertical component of the relative vorticity, $\beta=\partial f/\partial y$, f is the planetary vorticity, H is the bottom depth, $\mathbf{U}=H\overline{\mathbf{u}}$ is the depth-integrated velocity and D is the dissipation. D represents all non-linear dissipative processes which cannot be resolved by time mean values, therefore it is derived as the residual of all other terms. In order to investigate the temporal mass-related variability in sea surface height, the divergence of the depth-integrated velocity can be used as a proxy for changes in η_M following:

$$\frac{\partial\eta_M}{\partial t}+\nabla\cdot(H\overline{\mathbf{u}}) \quad = \quad \frac{\partial\eta_M}{\partial t}+\nabla\cdot\mathbf{U} \quad = \quad 0 \tag{2.28}$$

With respect to the complete form of the vertically integrated continuity equation in FESOM's primitive equations (Eq. 2.12), Eq. 2.28 neglects the influence of vertical freshwater fluxes and focus on investigating mass-related variability rather than the full seas surface height variability. By analysing the single terms in 2.27

I therefore aim at investigating changes in η_M due to: (1) local variations in the relative flow vorticity (first term on the left hand side (lhs)); (2) advection of relative vorticity (second term on the lhs); (3) advection of planetary vorticity (third term on the lhs); (4) a non-zero flow component perpendicular to the bathymetry gradient (called the "flow over bathymetry" term, fifth term on the lhs); (5) surface wind forcing (first term on the right hand side (rhs)); (6) any dissipation process, for instance due to lateral diffusion or to bottom friction (second term on the rhs). Spatially averaged values of the above terms are analysed in the central Barents Sea, between longitudes 30°E and 50°E and latitudes 72°N and 75°N. The temporal evolution of the spatial average and the correlation between terms is presented and discussed in Sect. 4.2.3 and 4.4.5.

Chapter 3

Monthly fields of Arctic sea level and geostrophic velocity from satellite altimetry[1]

In the previous Chapter 2, I described the processing of altimetry data to generate gridded fields of sea surface height and geostrophic velocity, published in PANGAEA as Doglioni et al. (2021). In this Chapter, I first evaluate this product against independent in-situ and satellite data, assessing its temporal and spatial resolution and its robustness with respect to the methodology. Finally I provide a first insight into emerging large-scale variability patterns.

3.1 Sub-monthly variability of Arctic sea level

When generating monthly average maps of sea surface height, sub-monthly ocean variability must be corrected for in order to reduce the aliasing of sub-monthly temporal changes into spatial variability. In the following, I compare the performance of various correction products for the ocean tides (tidal correction) and the ocean response to local and remote forcing by wind and atmospheric pressure (DAC). Besides giving practical indications on which correction product removes the most variability, this analysis provides insight into the sub-monthly sea surface height variability in the Arctic Ocean. For instance, I specify two regions where an improved tidal correction reduces the variability greatly, indicating that these regions are subjected to strong tidal variability. Furthermore, I show that a correction product including the effect of remote forcing by wind and atmospheric pressure performs better that a classical inverted barometer, demonstrating that the propagation of wave-like signal is also relevant in ice-covered regions. Finally, I show that residual sub-monthly variability is present after applying the tidal and DAC corrections. This points to additional high-frequency variability related to processes that are not captured by these two corrections.

3.1.1 Ocean Tides Correction

Following the European Space Agency indications (European Space Agency, 2016; Lyard et al., 2006), tidal variability has in the past been corrected using the standard tidal model FES2004 or equally performing models (e.g., Pujol et al., 2016; Mizobata et al., 2016; Armitage et al., 2016; Müller et al., 2019b). Recent works (e.g., Rose et al., 2019; Prandi et al., 2021) have instead used new model versions with improved performance (Cancet

[1] *The content of this chapter is mostly adapted from Doglioni et al. (2023)*

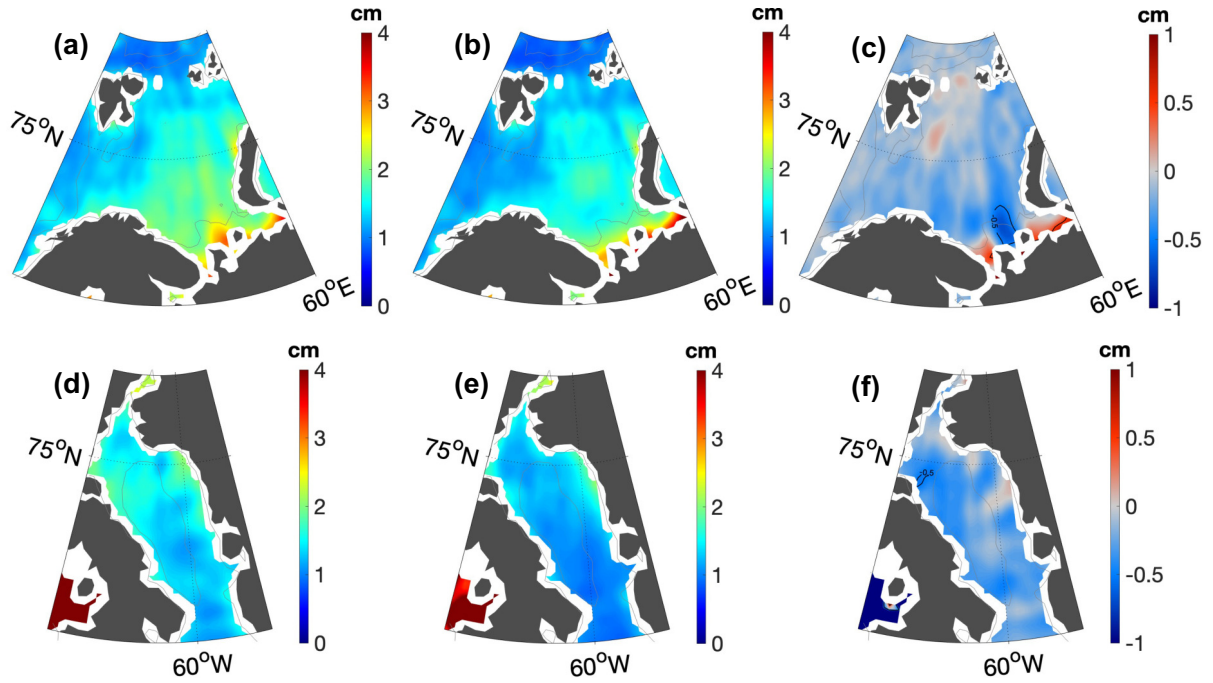

Figure 3.1. Comparison of performance of FES2004 and FES2014-based tidal corrections. Sub-monthly contribution to the standard error on monthly η' maps in the Barents Sea (a, b, c) and Baffin Bay (d, e, f) when using the tidal correction FES2004 (a, d) and FES2014 (b, e). In panels (c) and (f) is shown the reduction in the error obtained with FES2014 with respect to FES2004.

et al., 2018) such as the FES2014 model (Lyard et al., 2021). In order to support our choice to use FES2014 over FES2004, we compared their performance by evaluating the difference in residual noise on the monthly maps due to unresolved sub-monthly variability (computed as in Sect. 2.5.2).

We display here in Fig. 3.1 the sub-monthly contribution to the standard error in two areas of high tidal amplitude, namely the Barents Sea and the Baffin Bay. We note that, in both regions, FES2014 reduces the standard error of values up to 0.3-0.5 cm with respect to FES2004 (Fig. 3.1c and 3.1f), which is about 20% of its local value and 30%-50% of the average value over the whole Arctic. In agreement with these results, findings from Cancet et al. (2018), who compared the performances of several tidal models in the Arctic, show that differences in tidal amplitude and phase with respect to tide gauge data are much lower for FES2014 than for FES2004.

3.1.2 Dynamic Atmospheric Correction

The DAC corrects the local and the dynamic ocean response (waves) to pressure and wind changes and is derived from the sea surface height output of a barotropic model (Carrère and Lyard, 2003; Carrère et al., 2016). Up until the early 2000s, the effect of atmospheric pressure and winds on sea surface height had instead been corrected using an Inverse Barometer formula (IB, e.g., Ponte and Gaspar (1999); Carrère and Lyard (2003)). In the IB assumption, the sea surface height responds locally to changes in pressure, decreasing of approximately 1 cm for each increase in pressure of 1 mbar

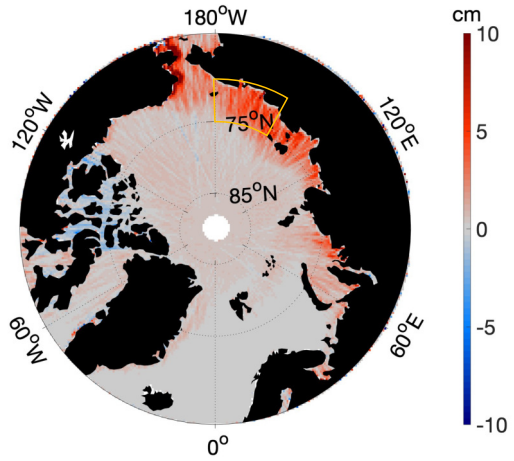

Figure 3.2. The along-track improvement of DAC correction, with respect to IB, in removing η' high-frequency variability. Colours indicate the difference between the standard deviation of along-track η' corrected IB and corrected with DAC. The yellow square indicate the region of the East Siberian Sea where the frequency analysis was performed.

(atmospheric loading). Even though it has been shown that the IB is not always a good approximation of the ocean response, especially on timescales shorter than 20 days (Carrère and Lyard, 2003), little is known of what is the response in ice-covered regions (Robbins et al., 2016). Furthermore, recent results by Piecuch et al. (2022) suggest that deviations of the ocean response from a simple IB are particularly enhanced in the Arctic shelf regions with respect to the global average.

To establish whether DAC should be used also in ice-covered regions, we compared the reduction in altimetry standard deviation obtained by applying DAC with respect to IB in ice-covered regions of the Arctic Ocean. Figure 3.2a shows the binned difference in standard deviation applying the two corrections, where positive values indicate better performance of DAC over IB. The DAC outperforms the IB in shallow shelf regions, and the two corrections perform equally well over the deep basins.

Table 3.1. Standard deviations of the three time series of along-track η', averaged over the East Siberian Sea box (Fig. 3.2), using uncorrected η', η' corrected by IB and η' corrected by DAC. For each year only ice-covered data are used, in the months November-July. Standard deviations are presented for the time series filtered in three different frequency bands.

standard deviation (cm) [uncorrected / IB / DAC]	T > 20 days	20 days > T > 5 days	T < 5 days
2011-2012	16.2 / 14.3 / 13.3	9.3 / 9.2 / 5.8	3.1 / 3.4 / 2.2
2012-2013	14.7 / 10.8 / 9.7	8.9 / 9.7 / 4.8	3.2 / 3.7 / 2.2
2013-2014	12.0 / 12.5 / 9.9	8.5 / 9.1 / 4.0	3.2 / 3.6 / 2.4
2014-2015	7.3 / 8.0 / 7.7	9.3 / 9.9 / 4.5	2.4 / 2.9 / 1.9
2015-2016	19.3 / 15.7 / 15.7	7.3 / 7.8 / 3.6	3.0 / 3.6 / 2.2
2016-2017	15.3 / 13.5 / 13.1	8.8 / 9.7 / 4.4	3.2 / 4.0 / 2.3
2017-2018	10.0 / 7.4 / 6.8	9.2 / 11.0 / 4.8	3.4 / 3.8 / 2.5

To understand which frequency bands have mostly contributed to this improvement, we took as an example the East Siberian Sea (yellow square indicated in Fig. 3.2a). We generated three time series of uncorrected η', η' corrected by IB and η' corrected by DAC, averaged with timestep of 1 day over the indicated region. For each year we analysed periods between November and July, which are the only months when data from leads are available. For each time series, we computed the standard deviation in frequency bands with periods T > 20 days, 5 days < T < 20 days, T < 5 days (Table 3.1). Results show that DAC reduced the uncorrected η' standard deviation by 50% at periods shorter than 20 days, in contrast to no reduction when applying a simple IB.

Furthermore, standard deviation at periods between 20 days and 5 days is larger than 60% the standard deviation at periods longer than 20 days, confirming that high-frequency variability represent a high portion of the total variability in the Arctic Ocean. The improvement of DAC with respect to IB over the shelves appears also in the η' monthly grids, where meridionally oriented patterns of η' are evidently reduced (two examples are given for the months of November 2014 and November 2017 in Fig. 3.3).

3.1.3 Aliasing of residual sub-monthly variability

As stated in the main text, we performed the interpolation on weekly data subsets of observations of η'. Monthly maps were then obtained as the average of four weekly maps. The reasoning behind our approach is based on the fact that sea surface height in the Arctic exhibit large-scale, high-frequency (sub-monthly) variability, associated in part to the fast propagation of large-scale barotropic waves across the Arctic (Peralta-Ferriz et al., 2011; Fukumori et al., 2015; Danielson et al., 2020). This means that the variability is spatially coherent over hundreds of kilometers, yet it decorrelates quickly over time (e.g. weeks). Thus, measurements taken along

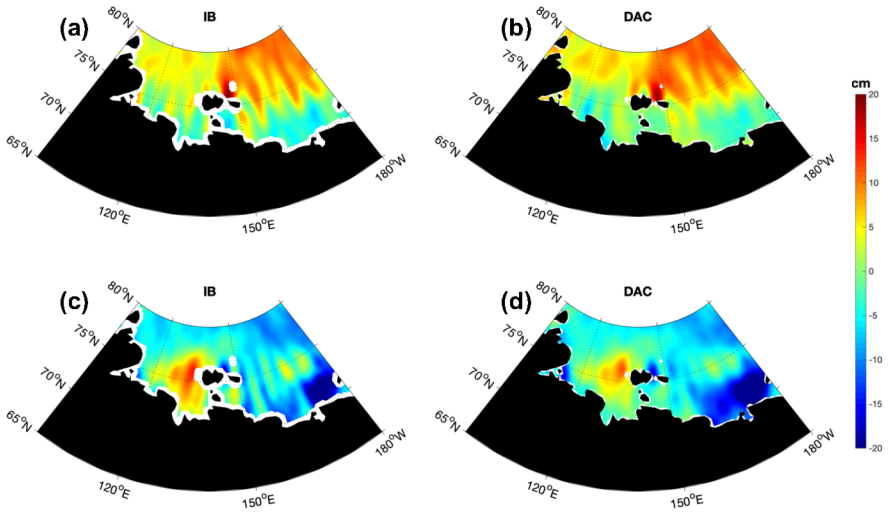

Figure 3.3. Effect of using correction DAC (panels (b) and (d)) instead of IB (panels (a) and (c)) on the monthly gridded η' fields (see Sect. 2.5.2). Two examples are shown for the months of November 2014 (panels (a) and (b)) and November 2017 (panels (c) and (d)).

tracks that are far away from each other, yet within a few days from each other, may still be able to resolve to some extent the spatial-temporal characteristics of the ocean variability. Instead, measurements taken along tracks that are close to each other, yet taken two weeks apart from each other, will create stripes (strong spatial sea surface height gradients) by not resolving the temporal variability. Since CryoSat-2 samples close-by regions at times separated by a large gap over the course of a month, trackiness will occur.

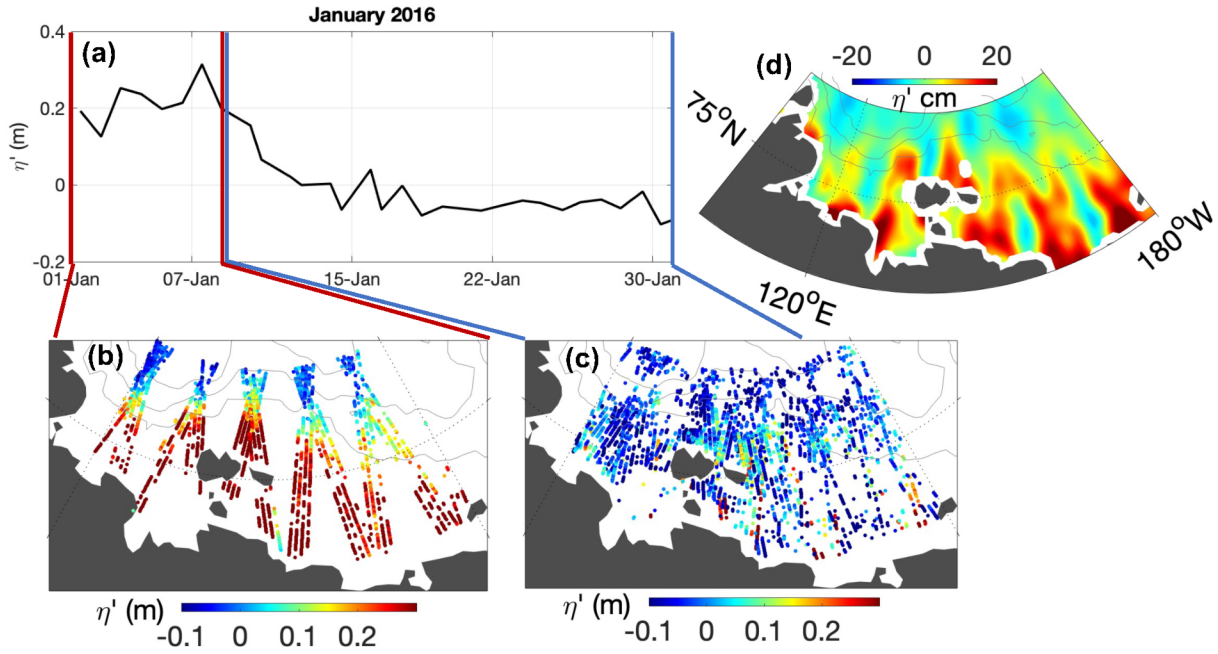

Figure 3.4. Trackiness introduced by sub-monthly variability. (a) Time series of average along- track η' in the East Siberian and Laptev Sea for the month of January 2016. Bottom panels: scattered along-track η' in the periods of (b) 1-8 January and (c) 9-31 January. (d) η' field for the month of January 2016 if interpolation is performed on a monthly set of observations.

Therefore, constructing monthly maps based on sampling this large-scale, high-frequency variability at different times in different locations, will artificially produce short wavelength patterns. We demonstrate this

effect exemplarily in Fig. 3.4. One can clearly see how the sudden change in the large-scale sea surface height between the first and the following weeks produces artificial stripes in the map when the monthly subset of data is interpolated.

3.2 Characteristics and evaluation of monthly fields

Here we first describe the characteristics of the monthly maps of η' and geostrophic velocity (u_g, v_g), then present the results of their comparison with independent datasets, and lastly display the most prominent aspects of the η' and (u_g, v_g) seasonal cycle.

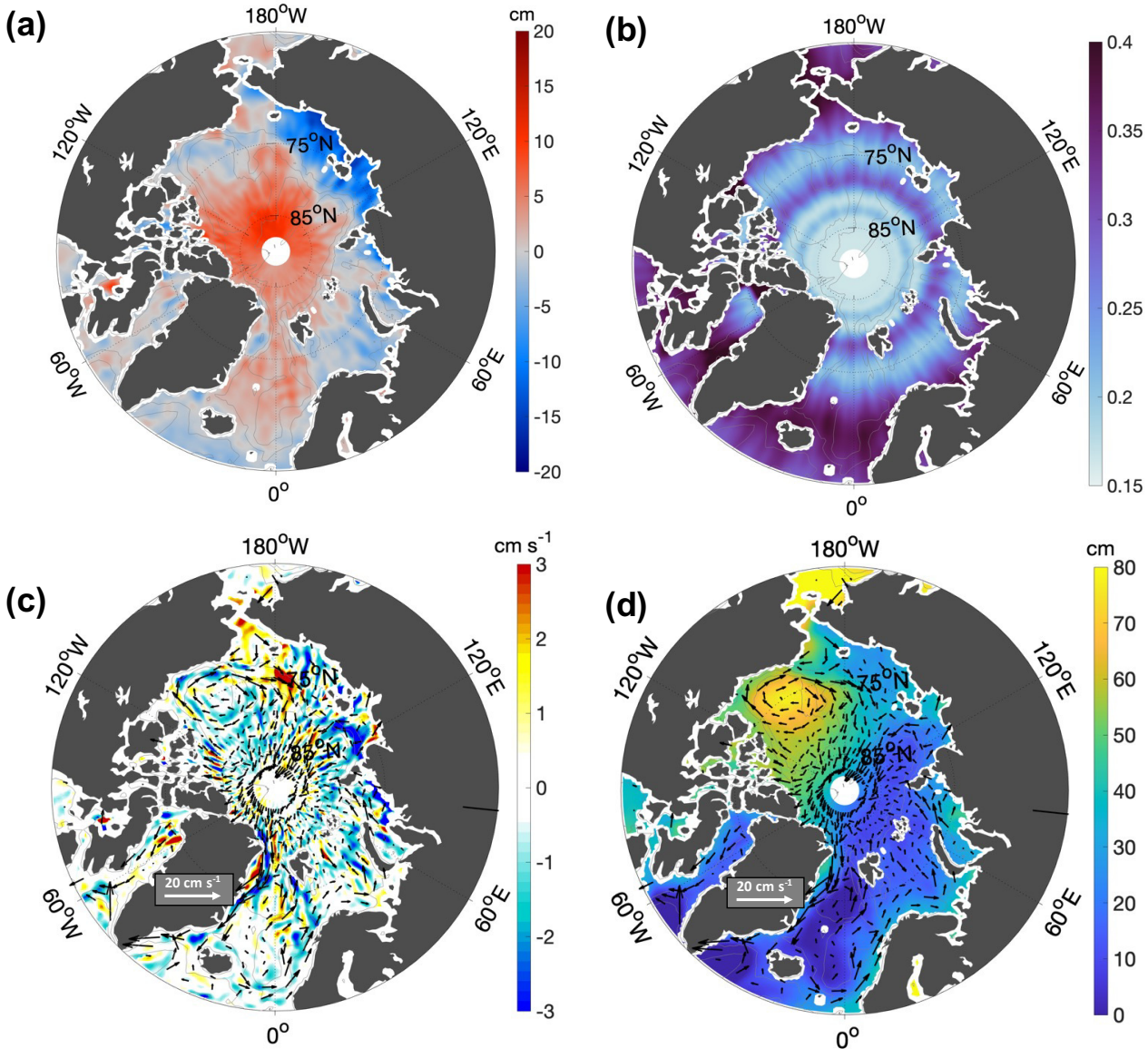

Figure 3.5. Example of monthly gridded fields included in the final data product, for the month of July 2015. (a) η' field above the 2011-2020 background field. (b) Relative error field on the interpolated η', given as fraction of the variance of the background field. (c) (u_g, v_g) field. Arrows in panel c represent the absolute (u_g, v_g) field for the month of July 2015, whereas colour highlights the anomaly of the monthly geostrophic speed ($V_g = \sqrt{u_g^2 + v_g^2}$) with respect to the the mean geostrophic speed over the period 2011-2020. (d) Dynamic ocean topography (η, background color) and the associated geostrophic velocity field (as in panel c). Bathymetry contours are drawn at 100 m, 1000 m and 2500 m depth.

3.2.1 Monthly fields of sea surface height anomaly and geostrophic velocity

As an example to describe general characteristics of a given monthly map over the 2011-2020 period, here we present results from the month of July 2015. Figure 3.5 shows fields of η', relative error (associated with the interpolation) and (u_g, v_g) for July 2015. The description below makes reference to the Arctic Ocean sub-regions and surface circulation pathways presented in Fig. 2.1.

In the η' monthly fields we generally find that there are extended regions of either positive or negative values. In Fig. 3.5a, for instance, η' is positive in deep regions, i.e. in the Nordic Seas and across the Arctic Deep Basins, and negative over the shelf seas. η' also varies within these regions, being for instance maximum (~10 cm) north of 85º N, and minimum in the East Siberian Sea. Superimposed on these large-scale patterns, residual meridional trackiness appears south of 80° N, especially in shallow areas, where the error related to the residual sub-monthly variability is highest (Fig. 2.5a).

The relative error for the month of July 2015 is on average 0.23, with a minimum below 0.2 around the North Pole and a maximum above 0.3 south of 70° N (Fig. 3.5b). The largest relative error values are found in regions with data gaps (see weekly data distribution in Fig. 2.3g): i) south of 75° N, where the distance between the satellite tracks increases considerably; ii) in a zonal band around 80° N, where the weekly data distribution is not uniform due to the satellite orbit geometry; and iii) in regions covered by multiyear ice during winter months (Fig. 2.3a, right)

In Fig. 3.5c we present the geostrophic velocity field (u_g, v_g), with background colors highlighting monthly speed anomalies relative to the 2011-2020 mean speed. The distribution of anomalies aligns well with known circulation pathways, such as slope currents, found along steep bottom topography gradients, or large-scale current patterns like the Beaufort Gyre and the Transpolar Drift. For instance, speed anomalies displayed in Fig. 3.5c show that in July 2015 currents were weak around the Nordic Seas (East Greenland Current, West Spitsbergen Current and the Norwegian Atlantic Current) and at the Laptev Sea continental slope (Arctic Boundary Current), while they were intensified in the westernmost branch of the Beaufort Gyre and in the Pacific Water inflow across the Bering Strait. This indicates that our data set yields realistic variability over a large span of the Arctic Ocean. Still, there are confined areas where speed anomalies do not follow circulation pathways but rather appear along meridionally elongated stripes. These patterns result from gradients between residual η' sub-monthly variability and do not correspond to real monthly velocity anomaly.

3.2.2 Comparison to independent datasets

We evaluated both η' and (u_g, v_g) fields against independent data in order to: i) test the robustness of the monthly η' fields, both in ice-free and ice-covered regions, by comparison to the satellite-derived, gridded CPOM dataset; ii) verify the spatial consistency of our η' fields in the Fram Strait, a region of transition between ice-covered and ice-free ocean; iii) assess the agreement in time and space between our gridded η' and (u_g, v_g) fields and mooring-based data in seasonally ice-covered regions over a time span of few years.

3.2.2.1 Sea surface height

We first compared our gridded η' fields with the CPOM DOT. In this instance we aimed at testing the robustness of the temporal variability of our monthly η' fields over the entire Arctic. A comparison of Arctic regional products to independent altimetry products was previously either not done (Armitage et al., 2016; Kwok and Morison, 2016; Rose et al., 2019), or only using products that were not tailored for ice-covered regions (Prandi et al., 2021). Results show good agreement of our gridded η' fields with the CPOM DOT over most of the Arctic domain, with a correlation between datasets above 0.7 for 85% of the grid points (Fig. 3.6a). The comparison yields lower correlation values (0.3 to 0.7) along the Canadian and Greenland coasts (where the multi-year ice

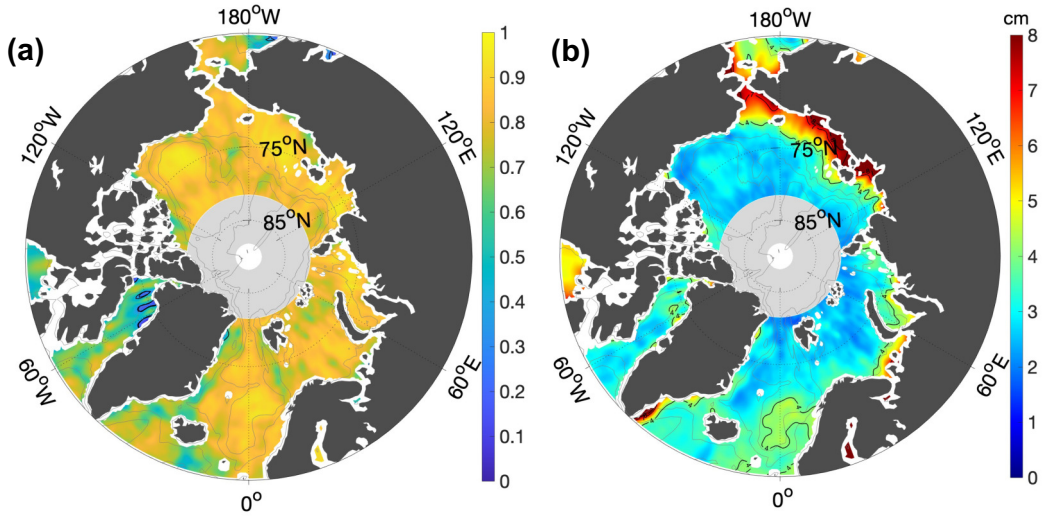

Figure 3.6. (a) Pearson's correlation coefficient and (b) RMSD between the gridded η' fields as derived in this work and the CPOM DOT published by Armitage et al. (2016). Each dataset was referred to its own average over the period 2011-2014 before comparison. In panel (a), correlation is <0.3 and p-value >0.05 in the small area in the Baffin Bay encircled by a thick black line. In panel (b), thick black lines are contours of 4 cm, 7 cm and 8 cm. The region shaded in gray north of 82° N is not included in the comparison because not covered by the CPOM DOT. Bathymetry contours (dotted lines) are drawn at 100 m, 1000 m and 2500 m depth.

persists for most of the year) and in sparse areas of the central Arctic and in the Barents Sea. Only in less than 1% of the domain the correlation is below 0.3 (Baffin Bay). The root-mean-square-deviation (RMSD, Fig. 3.6b) exhibits low values (2 cm to 4 cm) over more than 80% of the domain, including most of the regions with water depth greater than 100 m. The RMSD is high (7-8 cm) over the East Siberian Sea and Chukchi Sea, where the error due to sub-monthly variability is also highest. These results seem to indicate that altimetry-derived month to month variability is generally robust in relation to the methodology applied, also in ice-covered regions, with few exceptions that we will discuss in Sect. 3.3.

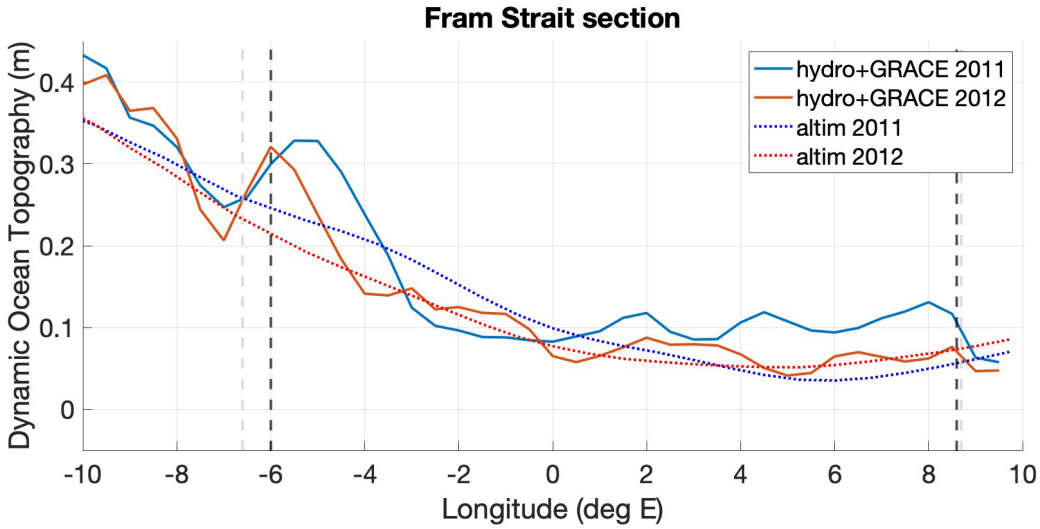

Figure 3.7. Cross sections of η across the Fram Strait at 79° 50' N in June 2011 and June 2012. Altimetry-derived η is displayed against steric height h_S from in-situ hydrographic sections plus ocean bottom pressure h_P from GRACE. Light gray and dark grey vertical dashed lines indicate the 300 m and 400 m isobaths respectively.

Secondly, we wanted to demonstrate that in Fram Strait, a transition zone between ice-covered areas in the west and ice-free areas in the east, the spatial sea surface slope associated with the local ocean circulation is retained in our η fields (computed as described in Sect. 2.5.2.1). In order to do this, we carried out a comparison with independent hydrography data, not used for the offset correction displayed in Fig. 2.2. In Fig. 3.7 we

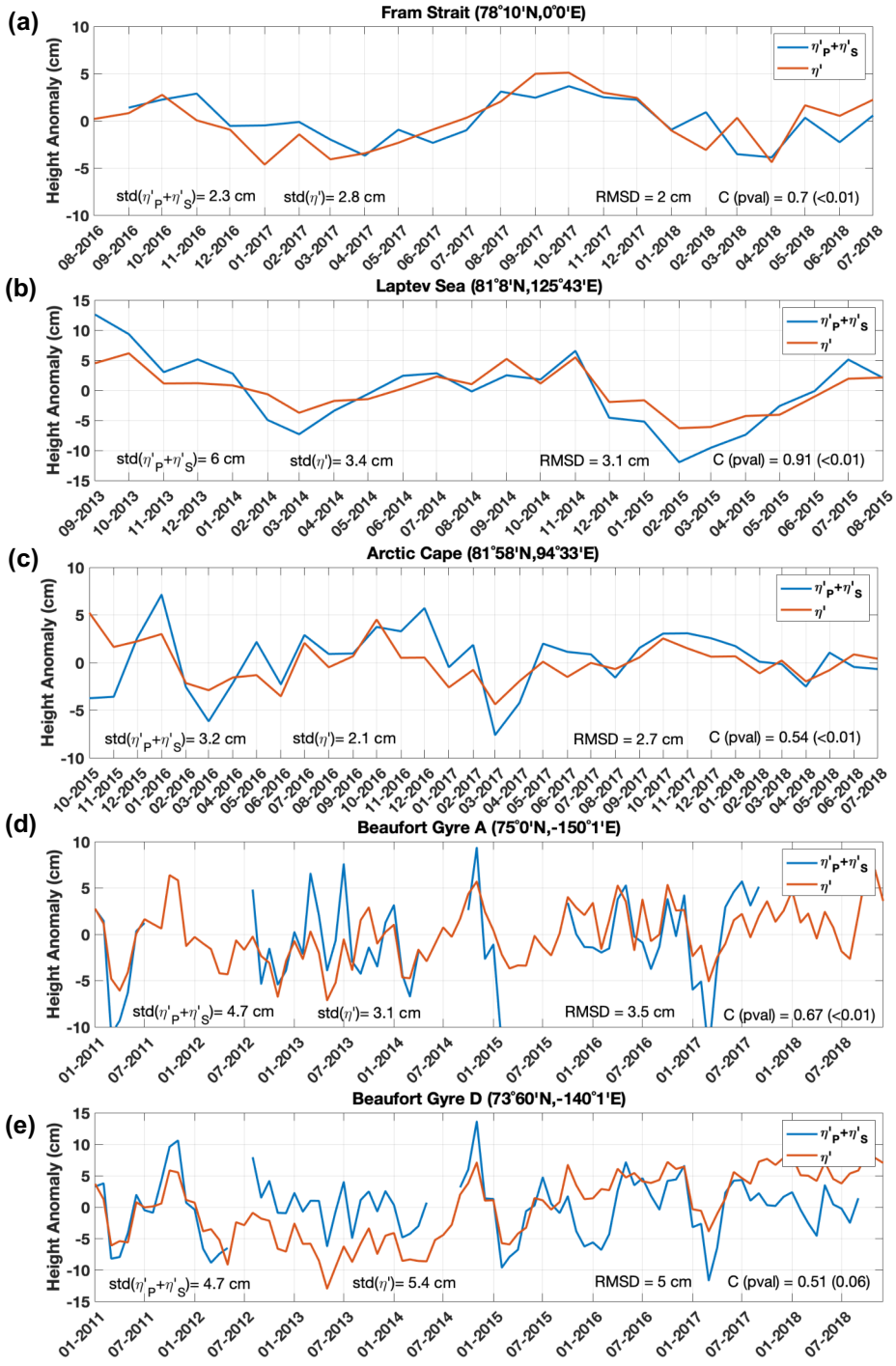

Figure 3.8. The sea level anomaly $(\eta'_P + \eta'_S)$ derived from data at moorings (a) FS_S, (b) AC, (c) M1_4p6, (d) A, (e) D (blue line) is displayed against the η' interpolated at the mooring location (red line). Standard deviations of η' and $\eta'_P + \eta'_S$ are displayed in the bottom left corner, while RMSD and correlation coefficient in the bottom right corner (Pearson's correlation coefficient, where p-value was computed using the effective number of degrees of freedom, Emery and Thomson, 2001).

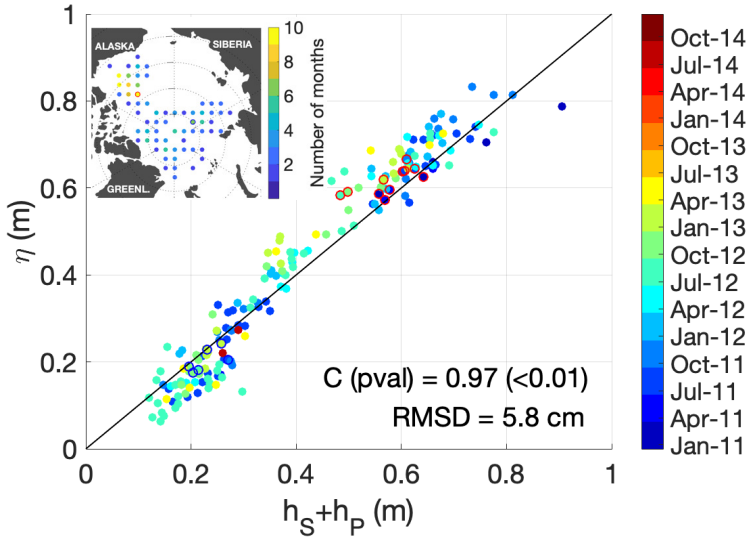

Figure 3.9. The steric height plus ocean bottom pressure ($h_S + h_p$) derived from hydrographic profiles in the Arctic Deep Basins and GRACE data is displayed against the gridded altimetry-derived η, each averaged in equal area grid cells with resolution of 200 km. The red and blue circles indicate data points from the most populated grid cells in the Amerasian and Eurasian basins respectively.

display two cross sections of altimetry-derived η across the Fram Strait, in the months of June 2011 and June 2012, against dynamic height from ship-based CTD sections plus ocean bottom pressure from GRACE data. In the East Greenland Current (7° W to 2° W), at the transition between ice-covered and ice-free regions in the western Fram Strait, the broad cross shelf variation in η is comparable to in-situ data. We note though that the strong local gradients between 7°W and 4°W, each spanning a distance of about 30-40 km, are not captured. This is likely due, on the one hand, to the 50 length scale used to smooth altimetry data, and on the other hand, to the fact that profiles from the altimetry fields represent monthly averages while those from in-situ data represent a snapshot of hydrography over the course of a few days. Despite the above mentioned differences, this comparison seems to indicate that the differential offset correction applied to altimetry data between ice-free and ice-covered areas (shown in Fig. 2.2) have preserved the broad spatial sea surface slope associated with the East Greenland Current.

After having demonstrated the spatial consistency of our data set, we now turn to the question to which degree the time variability in the gridded η' fields is representative of independently observed variability. With this purpose, we compared in-situ time series from five moorings at different locations in the Arctic Ocean to time series extracted locally from our η' fields. Time series of η' from altimetry, and $\eta'_P + \eta'_S$ from mooring data (computed as described in Sect. 2.4), are shown in Fig. 3.8. The correlation between the altimetry and mooring time series is higher than 0.5 with p-value lower or equal to 0.06 at all five sites. The correlation is highest at the M1_4p6 mooring, where in-situ hydrography is measured up to 26 m below the sea surface. Sea surface height from altimetry and mooring follow roughly similar patterns, varying within a range of ±10 cm over the comparison period at all sites. The sea level at the moorings in the Eurasian Arctic (FS_S, AC and M1_4p6) is characterised by seasonal oscillations, with the signal amplitude decreasing during winter, starting in October, and increasing during summer, starting in March. In the Beaufort Sea, seasonality has a similar phase, though strong intra-seasonal and interannual variability is also present. At moorings A and D, altimetry and in-situ data show agreement at interannual timescales. This is visible for instance in alternating years of non detectable seasonal cycle (2012, 2013, 2015, 2016) and peaked seasonal cycle (2011, 2014). On the other hand, a trend between 2013 and 2018 is evident in the altimetry time series at mooring D, while not present in the in-situ time series. At all sites, particularly in the Beaufort Sea, short term variability appears in phase

most of the time, though month to month variations are larger in mooring data than altimetry, as reflected in the relatively high RMSD between them.

Finally, we compared our gridded η estimates to data from the Arctic Deep Basins, presented in Sect. 2.5.1, on a monthly basis. Each data source was spatially averaged for each month on the same equal area grid with resolution of 200 km (Fig. 3.9).There is good agreement between the dynamic ocean topography estimated from the two methods, with correlation a coefficient of 0.97 and an RMSD of 5.8 cm over a range of about 70 cm. This indicates that the basin-scale gradients in sea surface height between the western and the eastern Arctic Ocean are preserved in our η maps. The spread accounts for different temporal and spatial coverage of in-situ and satellite data within each cell. Despite this spread, when we isolate data points from the most populated grid cells in the Amerasian and Eurasian basins we see that the temporal variability of in-situ data is still reasonably represented by altimetry estimates.

Table 3.2. Comparison of velocity from altimetry and mooring data. Moorings from the two mooring lines are listed, from top to bottom, respectively as the westernmost to easternmost in the Fram strait and southernmost to northernmost in the Laptev Sea continental slope. At these two arrays, the component normal to the array is compared (northward and eastward respectively). In the Beaufort Sea, current speed and bearing are compared. The first two columns display the Pearson's correlation coefficient and the RMSD; correlations with p-value<0.05 are highlighted in bold (p-values were computed using the effective number of degrees of freedom, Emery and Thomson, 2001). The next four columns show the mean and standard deviation of the altimetry-derived and mooring velocity.

	Correlation	RMSD (cm s^{-1})	mean altim. (cm s^{-1})	mean moor. (cm s^{-1})	std altim. (cm s^{-1})	std moor. (cm s^{-1})
Fram Strait						
F10	0.01	5.3	-7.3	-7.9	1.8	5.0
F16	**0.22**	6.8	-4.3	1.1	1.5	7.1
F15	0.17	6.7	-2.9	-0.8	1.3	6.9
F8	-0.28	5.8	-1.8	6.1	1.2	5.5
F7	-0.18	7.2	-0.3	-2.5	1.3	6.9
F6	0.16	6.8	0.9	-2.6	1.3	7.0
F5	**0.33**	6.3	2.8	5.3	1.7	6.7
F4	**0.38**	6.7	4.0	6.0	1.8	6.2
F3	**0.54**	6.8	4.5	17.0	1.7	7.6
F2	0.30	7.2	4.5	18.1	1.8	7.6
Laptev Sea						
M1_1	**0.77**	5.7	4.7	12.1	2.3	7.4
M1_2	0.06	4.6	4.6	3.5	2.2	4.2
M1_3	0.17	2.0	4.1	3.4	1.3	1.8
M1_4	**0.45**	1.1	2.9	1.6	0.8	1.2
Beaufort Sea						
A speed (cm s^{-1})	0.03	2.0	1.5	2.1	1.1	1.7
A bearing (°)	0.12	144	310	255	73	103
B speed (cm s^{-1})	**0.53**	2.3	3.5	3.6	0.9	2.6
B bearing (°)	**0.26**	76	83	100	24	68
D speed (cm s^{-1})	0.18	1.7	3.1	2.5	1.1	1.4
D bearing (°)	0.24	51	166	151	26	50
Chukchi Sea						
S1 speed (cm s^{-1})	**0.59**	2.2	4.4	4.7	1.6	2.7
S1 bearing (°)	0.21	125	69	31	36	41
S3 speed (cm s^{-1})	**0.69**	3.7	5	7.1	1.9	3.8
S3 bearing (°)	**0.50**	61	100	106	44	64

3.2.2.2 Velocity

Satellite-derived maps of surface geostrophic velocity offer the advantage of a quasi-synoptic view of ocean surface currents and their variability. We evaluated this variability locally by comparison to mooring near-surface velocity. Given that the variability represented by the two data sources differ to some extent due to the different nature of the measurements and spatio-temporal resolution, in our comparison we further assessed what are the spatial and temporal scales over which these two data sources provide consistent information on the underlying variability.

a. Correlation and RMSD at mooring locations

The agreement of altimetry-derived and in-situ velocities at mooring locations is summarized in Table 3.2. Hovmoeller diagrams of velocity normal to the Fram Strait and Laptev Sea mooring lines are displayed in Fig. 3.10 and 3.11, while the comparison of the speed and bearing at moorings in the Beaufort Sea and Chukchi Sea is shown in Fig. 3.12. In the Fram Strait, the correlation is significant (p-value < 0.05) and higher than 0.3 at moorings F3 to F5, across the continental slope in the eastern part of the strait. At these 3 moorings, both the mean v_n and v_{ni} are consistently positive and higher or comparable to the corresponding standard deviation. The correlation is highest at mooring F3, the mooring with the longest continuous time series. Over the Laptev Sea continental slope the correlation is highest at the M1_1 mooring, in the uppermost part of the slope. At this mooring, v_{ni} is on average four time larger than further down the slope. At the moorings located down the slope, the correlation is lower, being still significant at mooring M1_4, but non-significant at moorings M1_2 and M1_3. In the Beaufort Sea, the mean current's speed and their standard deviation is muche lower than along the continental slopes and the variability is dominated by month to month variations. The agreement is best at mooring B, located in the northern branch of the Beaufort Gyre. As already noted by Armitage et al. (2016), the current bearing ADCP measurements at this mooring in the years 2011 to 2013 are offset around late summer, which might indicate a data bias related to different deployments; the in-situ and altimetry bearing estimates agree more closely after late summer 2014. At mooring A, closest to the Centre of the Beaufort Gyre, low correlation is associated with very weak mean currents (< 2 cm s^{-1}) and large oscillations in the currents' direction. Despite the low correlation coefficient, both data sources clearly identify a period, between 2013 and 2016, when the current bearing is consistently more stable and slowly rotating clockwise. Currents at the Chukchi Sea moorings S1 and S3 are faster than in the basin, and correlation values higher. While at mooring S3 both currents speed and bearing are well captured by altimetry, at mooring S1 altimetry shows an offset of about 40° clockwise.

b. Spatial and temporal resolution

By examining the mean and standard deviation of velocity along the mooring lines, we note differences between gridded altimetry and in-situ data in terms of spatial and temporal resolution. The mean v_n shows low spatial variability and smooth transitions between nearby sites. Note that this variability is governed by the averaging scales underlying the DTU17MDT product. The scales captured by the DTU17MDT are defined by the resolution of the geoid model used to compute it. Previous studies, mentioning also the geoid model used by DTU17MDT, indicate that these scales are not smaller than 100 km (Gruber and Willberg, 2019; Bruinsma et al., 2014; Farrell et al., 2012). These large scales contrast with the high spatial variability of the v_{ni} mean flow, which is derived by pointwise measurements. This is shown for instance by abrupt changes between moorings F15 and F8 (27 km apart) and F8 and F7 (25 km apart) or between M1_1 and M1_2 (11 km apart). The high spatial variability observed by the mooring data is ascribable to the small Arctic first baroclinic Rossby radius, which is below 10 km in the two study regions (Nurser and Bacon, 2014; von Appen et al., 2016; Pnyushkov et al., 2015). Despite the different spatial resolution of source data, in our comparison at the two mooring lines

we observe that altimetry-derived geostrophic velocity capture transitions in the moored velocity from strong to weak mean flow occurring over distances of about 50-70 km. For instance, both altimetry and mooring data in the Fram Strait show a change from a strong mean flow at moorings F2-F3 to a weak mean flow at moorings F5-F6, within a distance of 50-60 km. At the Laptev Sea continental slope, where the in-situ-measured currents intensity significantly decreases from mooring M1_1 to mooring M1_2, altimetry-derived currents only weaken significantly over a distance of about 70 km, at the position of mooring M1_3.

Furthermore, in the altimetry dataset the time variability associated to mesoscale processes is smoothed out due to the 50 km decorrelation scale applied through the interpolation. This is reflected in the standard deviation of v_n, which is about four to five times smaller than that of v_{ni} at most moorings.

To establish the spatial scales over which altimetry-derived currents approximate best the temporal variability of in-situ measured currents, we compared spatially averaged v_n and v_{ni} at the two mooring lines. We performed five tests, averaging data over sets of at least two moorings chosen among those closest to the shelf break (tests 1 to 5 in Table 3.3). In order to take into account the fact that time series of moorings closer to each other are less independent, we performed a weighted average of the v_n and v_{ni} time series. Each mooring was assigned a weight proportional to its distance to the two neighbouring moorings (e.g., for mooring j the weight is: $w_j = \frac{d_{j,j-1}+d_{j,j+1}}{2}$, where d is the distance) or to the one neighbouring mooring (e.g., if j is the first mooring in a set, its weight will be $w_j = d_{j,j+1}$).

In the Fram Strait, averaging over moorings F3 to F5 (test 2, spanning a distance of 45 km) yielded a correlation higher than that using data only from the F3 mooring (where the pointwise comparison was highest; compare Tables 3.2 and 3.3). Results from tests 1 and 3 yielded correlations comparable to that at F3. All three tests reduced the RMSD by about 2-3 cm with respect to that at F3. At the Laptev Sea continental slope, neither test 4 nor test 5 improved the correlation with respect to the comparison at the M1_1 mooring. This appears plausible, as visual inspection of the in-situ observations reveals the slope current to be restricted to site M1_1 and not to extend out to M1_2 and beyond (Fig. 3.11b). This indicates that the spacing of moorings is likely too wide to adequately resolve the scales of the slope current. Nevertheless, both tests 4 and 5 reduced the RMSD with respect to the value at M1_1 (2-4 cm lower).

Table 3.3. Comparison of spatially averaged altimetry and mooring velocity at the mooring lines. Each test (described in Sect. 3.2.2.2b) corresponds to the averaging of data from two or more moorings (names of moorings used in each test and cross-flow distance covered by them are indicated in the header). The first two rows show the Pearson's correlation coefficient and RMSD between horizontally averaged v_n and v_{ni}. The last two rows show correlations at frequencies lower and higher than 4 months. All correlations in this table have a p-value <0.01, computed using the effective number of degrees of freedom (Emery and Thomson, 2001).

	test 1 20 km F3, F4	**test 2** 45 km F3 to F5	**test 3** 85 km F3 to F7	**test 4** 11 km M1_1, M1_2	**test 5** 61 km M1_1 to M1_3
Correlation	0.55	0.62	0.49	0.61	0.36
RMSD (cm s^{-1})	4.9	3.1	2.6	4.0	2.3
Correlation 4 months low-pass	0.63	0.68	0.61	0.62	0.37
Correlation 4 months high-pass	0.37	0.33	0.11	0.58	0.27

Finally, we looked at the correlation between the spatially averaged v_n and v_{ni} in two frequency bands (Table 3.3), namely seasonal to interannual (lower than 4 months) and the intra-annual (higher than 4 months). In the seasonal to interannual frequency band, v_n and in v_{ni} correlate better or equally than without filtering (Table 3.3), whereas in the intra-seasonal frequency band the correlation worsens. The percentage of variance explained by each frequency band in each dataset was evaluated as in eq. 2.21, where x is the horizontally averaged v_n or v_{ni} time series (tests 1 to 5), and x_F is the correspondent filtered time series. We find that seasonal to interannual frequencies explain most of the variability of the spatially-averaged v_n and in v_{ni}. They

constitute about 80% of the total variability in the Fram Strait, and about 90% at the Laptev Sea continental slope.

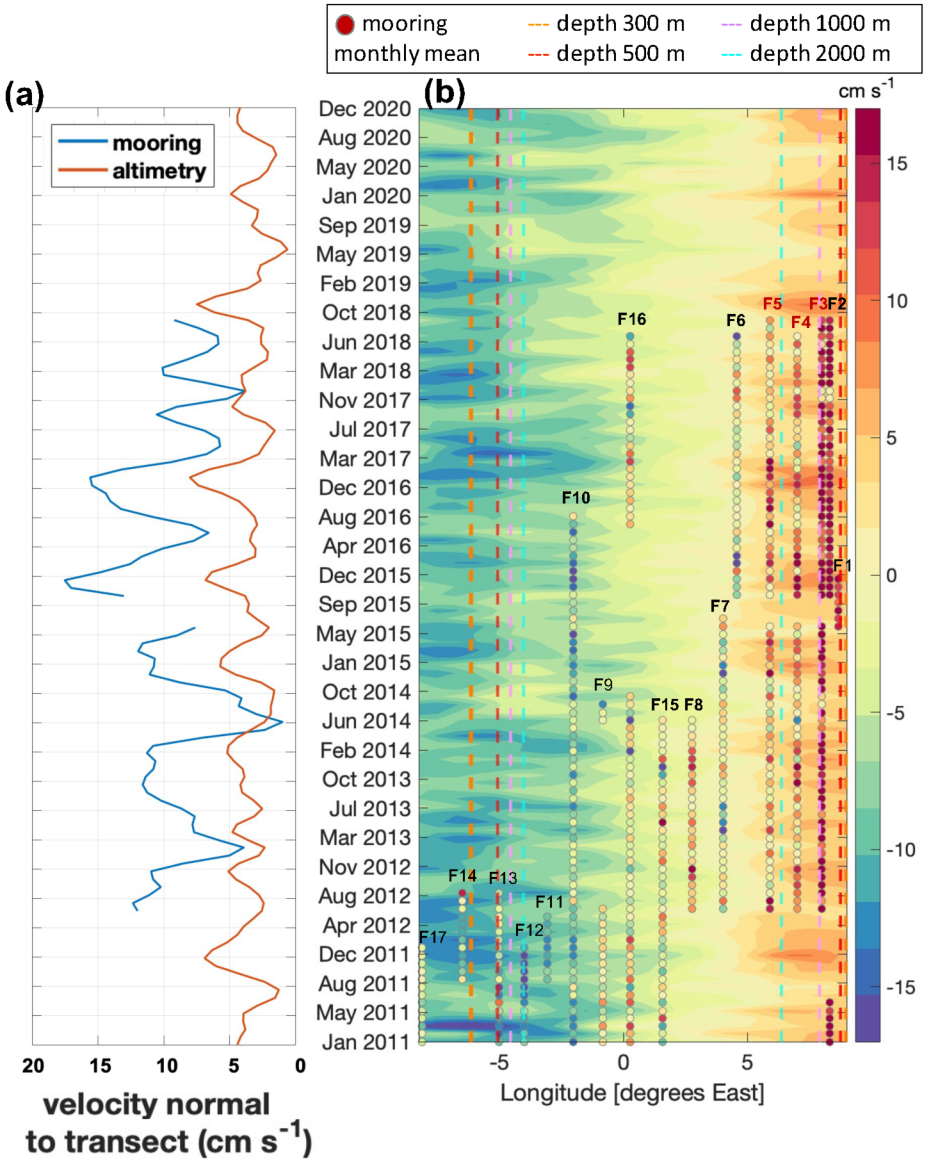

Figure 3.10. The altimetry-derived geostrophic velocity is shown against the in-situ surface velocity at the moorings transects in the Fram Strait, along latitude 78° 50' N (see Fig. 2.1). The component of the velocity normal to the transect is evaluated, and positive values represent northward velocity. (a) Longitudinal average of altimetry and in-situ velocity across moorings indicated with red letters in panel (b) (corresponding to test 2, see Sect. 3.2.2.2); both time series have been filtered with a 4-months low pass filter. (b) Hovmöller diagram representing the monthly temporal evolution of the altimetry-derived cross-transect geostrophic velocity. The circles represent monthly mean values of in-situ cross-transect velocity. Mooring's names are displayed on top of each mooring's series; at moorings with bold letters, data covered a period longer than 24 months.

In Fig. 3.10a and 3.11a we can see that, both in the Fram Strait and at the Laptev Sea continental slope, the currents variability at timescales larger than 4 months is dominated by seasonal oscillations, which have similar characteristics in the altimetry and mooring data. The seasonal cycles of v_n and v_{ni} are in phase there, with peaks occurring in winter, and troughs in early summer. Furthermore, v_n and v_{ni} show similarities in the interannual variability. For instance, in the Fram Strait both datasets feature a double peaked seasonal oscillation in some years (e.g. winters 2013-2014, 2017-2018). At the Laptev Sea continental slope the seasonal cycle amplitude decreases in both datasets between 2016 and 2018. In the western Arctic (Fig. 3.12), seasonal oscillations are observed at the moorings in the Chukchi Sea, where altimetry and in-situ data consistently

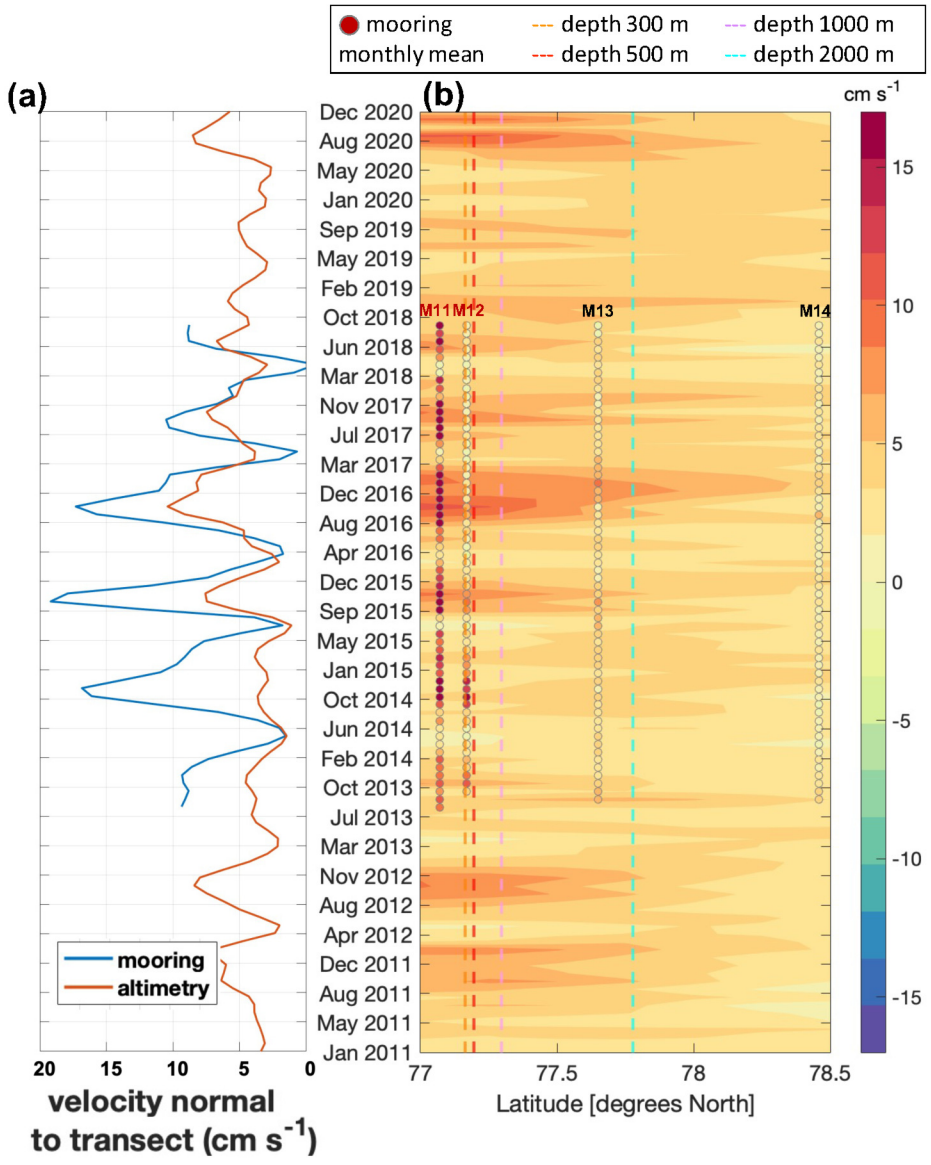

Figure 3.11. As in Fig. 3.10, for velocities at the Laptev Sea continental slope, along longitude 126° 50' E (see Fig. 2.1). The component of the velocity normal to the transect is positive eastward. The time series in panel (a) correspond to test 4 (see text).

show maximum speed in mid-summer and minimum in mid-winter. In contrast, a seasonal cycle is not clearly recognisable in the Beaufort Gyre currents at the location of the A, B and D moorings.

In summary, the comparisons with moored observations suggest that the satellite-derived velocities can provide reliable information both on time mean properties and seasonal changes of the flow field on spatial scales exceeding 50-70 km.

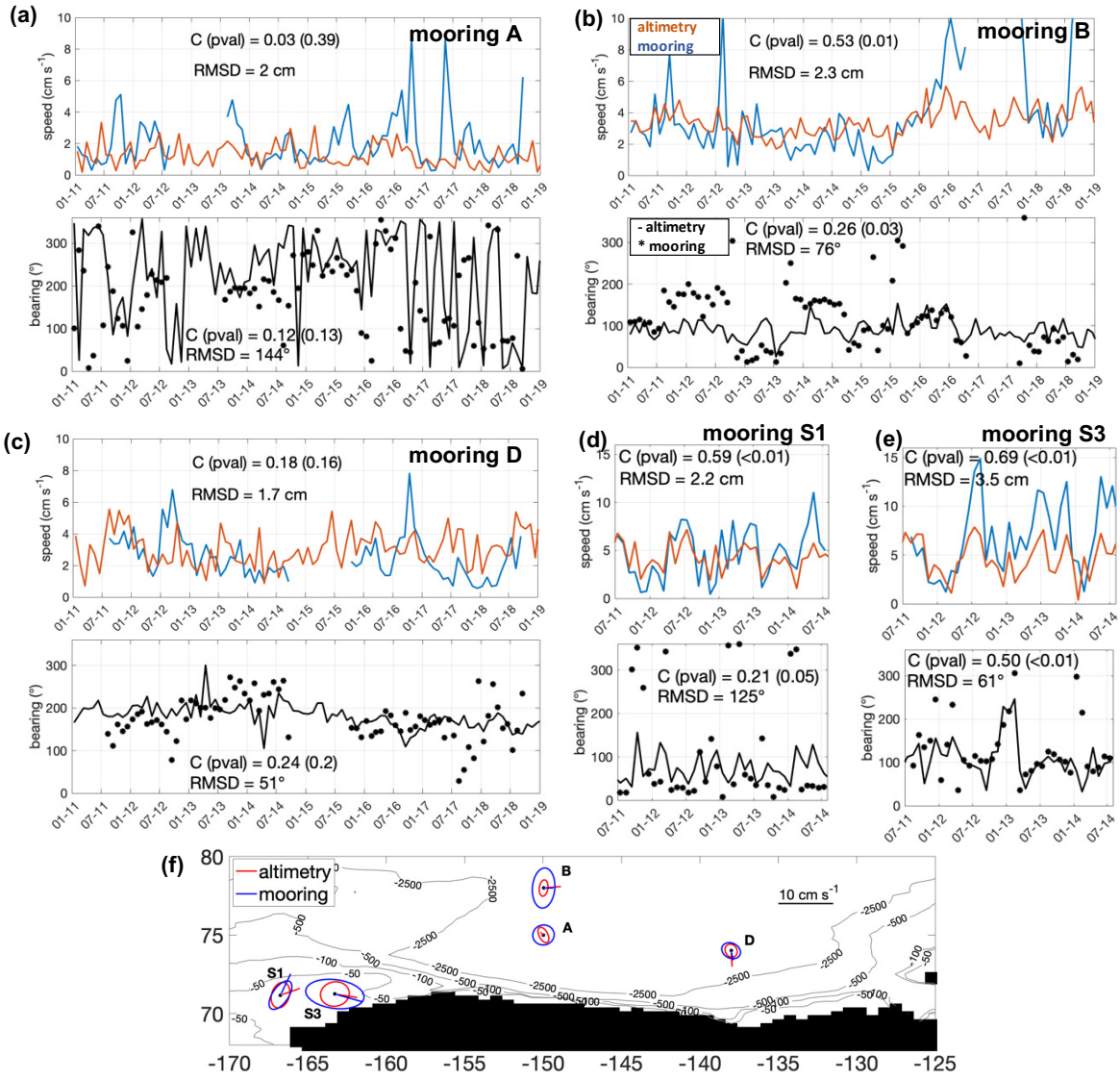

Figure 3.12. The altimetry-derived currents speed and bearing are shown against the in-situ measured ones at moorings A (panel a), B (panel b) and D (panel c) in the Beaufort Sea, and moorings S1 (panel d) and S3 (panel e) in the Chukchi Sea (see Fig. 2.1 for map of locations). (f) Mean currents and variance ellipses at each location.

3.2.3 Seasonal cycle

The seasonality of the Arctic sea level and surface currents has been studied in several previous works (e.g., Volkov et al., 2013; Armitage et al., 2016; Beszczynska-Möller et al., 2012; Baumann et al., 2018), giving us the opportunity to assess our dataset based on this literature. In the following subsection I provide an overview of the amplitude and phase of the η' seasonal cycle, estimated from my product as described in Sect. 2.7, putting emphasis on the regions where the seasonal variability explains a fraction of the total variability higher than 20%. The values and spatial distributions resulting from this analysis are then put into context of the available literature in Sect. 3.3.

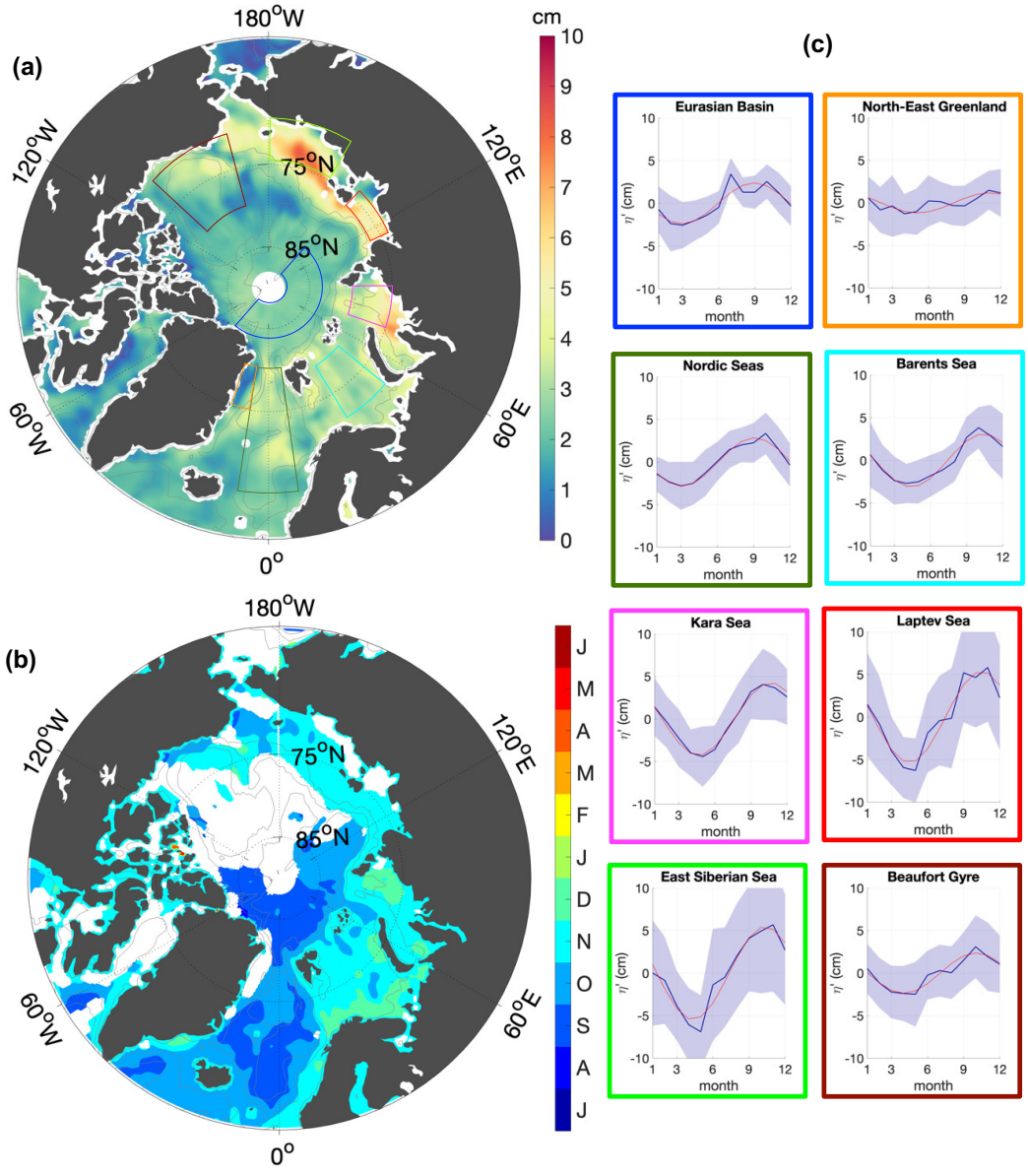

Figure 3.13. (a) Amplitude and (b) phase of the η' annual harmonic oscillation between 2011 an 2018. Blanked areas in (b) are those areas where the seasonal cycle explains less than 20% of the total variance. (c) Panels representing the η' monthly climatology (blue line, with standard deviation as shading) and the η'_{seas} (red line) averaged over the areas marked in the map with the corresponding color. Bathymetry contours are drawn at 100 m, 1000 m and 2500 m depth.

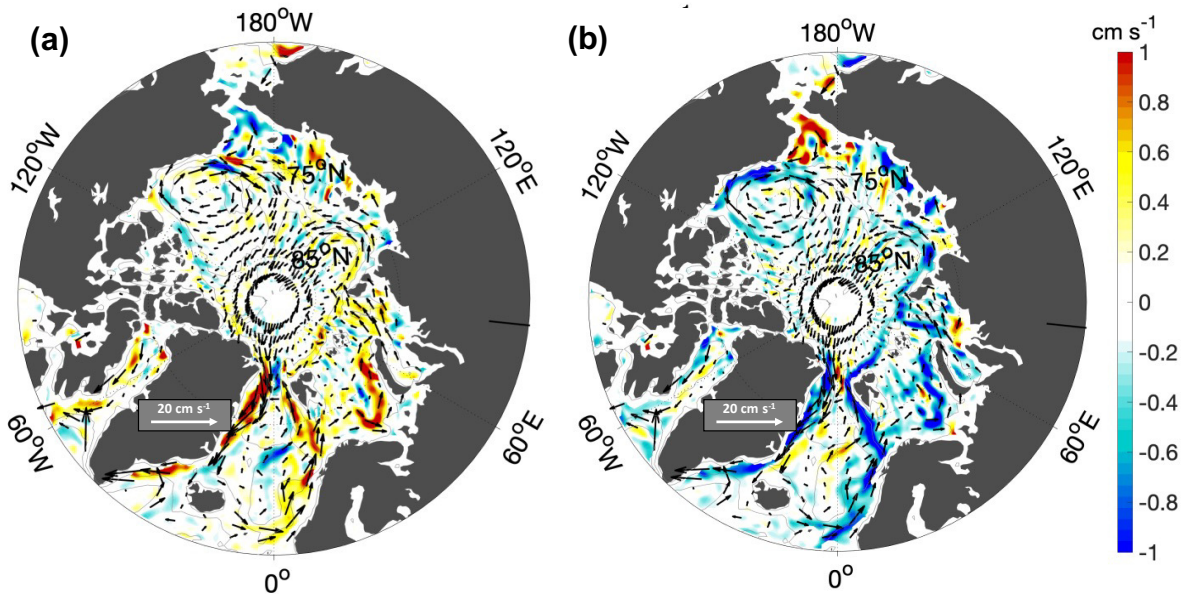

Figure 3.14. Average (u_g, v_g) fields over the (a) winter months January-February-March and the (b) summer months June-July-August. Bathymetry contours are drawn at 100 m, 1000 m and 2500 m depth. Arrows and colours are to be interpreted as described for Fig. 3.5c.

3.2.3.1 Sea surface height

The amplitude A and the phase α of the η' seasonal cycle are displayed in Fig. 3.13. The amplitude ranges between 1 and 8 cm, with values above 3 cm in shallow shelf regions, in the southwestern Canada Basin and in the Nordic Seas (Fig. 3.13a). In these regions and in the Eurasian Basin, the seasonal cycle explains more than 20% of the total variability. η'_{seas} is maximum in early winter across the Arctic Ocean, even though not uniformly (Fig. 3.13b). On the Eurasian side, we see a clear divide between deep and shallow regions, with η'_{seas} peaking earliest (September-October) in the Nordic Seas and the Eurasian Basin, and later (November-December) all along the Eurasian shelves, from the Barents Sea to the East Siberian Sea. On the Amerasian side, η'_{seas} peaks earliest in the southwestern Canada Basin and later in the Chukchi Shelf.

In Fig. 3.13c we also display the monthly climatology of η' observed in selected regions, computed as the January to December monthly averages over the years 2011-2020. We see that the harmonic fit is a good approximation of the climatology in most of these regions. One exception is the secondary peak in June-July exhibited by the climatology in the Canada Basin, the Eurasian Basin, the Laptev and East Siberian Sea, and the northeastern Greenland Shelf.

3.2.3.2 Geostrophic velocity

Fig. 3.14 shows the winter (January to March) and summer (June to August) average fields of (u_g, v_g) over the period 2011-2020. Seasonal speed anomalies are most pronounced south of 80°N, namely along the shelf edges, in some coastal regions, in the southern Canada Basin and in the Barents Sea. The strongest variation in current speed between summer and winter is about 3 cm s^{-1}. The time of seasonal maximum of some of the main Arctic currents is shown in Table 3.4. From the comparison between summer and winter we observe a basin-wide, coherent seasonal acceleration of the Arctic slope currents in winter and a deceleration in summer. The speed of these slope currents peaks between September and April. Namely, currents along the Nansen Basin shelf break, between the Fram Strait and the Lomonosov Ridge, peak in early winter (September to December); currents along the eastern shelf break of the Nordic Seas, in the Barents Sea and in the Baffin Bay peak in mid winter (November to February); the East Greenland Current peaks in late winter (February to

April). Seasonality is also recognisable in some currents not along the continental slopes. For instance, currents in the Kara Sea (peak between November and January), in the southern and western branches of the Beaufort Gyre (peak in November-January and March-May respectively) and in the Chukchi Sea (peak in June-August).

3.3 Discussion

The dataset presented in this paper provides monthly maps of sea surface height anomaly η' up to 88° N, derived from CryoSat-2 altimetry observations, over the time span of 10 years. In addition, we also provide the associated geostrophic velocity (u_g, v_g), which was not available before north of 82° N. Both sea surface height and geostrophic velocity were validated against independent data, including one satellite product and in-situ data in both ice-covered and ice-free regions. The extensive validation, covering a large portion of the Arctic, provided a robust assessment of the capability of our satellite product to reveal realistic spatio-temporal variability in agreement with in-situ observations. Furthermore, the comparison to an independent altimetry product allowed us to assess the consistency of the variability at monthly to interannual timescales between independently derived products.

In the following, we use results from the validation to discuss the following points. First, our multi-year, Arctic-wide comparison of monthly η' fields against an independent altimetry product revealed isolated sites with low correlation across data sets, despite the general agreement. Thus, we discuss whether this is related to the methods used. Then, we discuss our results from the comparison to in-situ data in terms of the spatial and temporal resolution of our altimetry dataset and the underlying dynamic regimes. Finally we put our findings on the seasonal cycle of sea surface height and geostrophic flow in the context of previous literature.

3.3.1 Impact of methodology

The comparison of our dataset with the CPOM DOT (Sect. 3.2.2.1) yielded a correlation higher than 0.7 over 85% of the domain. This indicates that month to month variability is generally robust in relation to the methodology applied, an encouraging result not yet emerged from previous studies. However, correlation coefficients are lower in some regions, with non-negligible differences between the datasets there. Many data sources and processing steps, thus just as many sources of uncertainty, are taken to generate monthly gridded sea surface height. As a starting point to support future product development, in the following we discuss what are the methodological steps that may generate the largest differences between these two data sets.

In the first place, source data used for the two products in ice-covered areas (ellipsoidal heights from CryoSat-2) have been derived applying different algorithms for the processing of satellite waveforms. Regional differences in the monthly fields might thus have occurred due to different data density. For instance, in our comparison the correlation is low in some areas of the ice-covered Arctic, where leads are detected based on surface classification techniques. These differ substantially between studies, depending on the parameters considered or statistical techniques applied, and are to date a source of uncertainty (Dettmering et al., 2018). More conservative techniques might be used to discard observations and reduce uncertainty. This results however in low data density in the central and western Arctic, where the most compact multi-year ice is located and leads are sparse (Willmes and Heinemann, 2016). Furthermore, generating data over the marginal ice zone still represents a challenge to overcome. This is because neither ocean-type retrackers nor ice-type retrackers are well suited to process altimetry waveforms there, resulting in noisy or unusable data (Quartly et al., 2019). It is perhaps not surprising then, that our comparison shows correlation values lower than 0.7 in open ocean areas of the central Arctic and the Baffin Bay, where large patches of low ice concentration form at the end of summer.

Secondly, different approaches were used in this study and in Armitage et al. (2016) to reduce unresolved sub-monthly variability in along-track data. On the one hand, we analysed the sea level variability at sub-monthly timescales, finding that in the Arctic this variability can yield substantial noise in the monthly gridded fields, especially in the shelf regions (Sect. 2.5.2). To reduce this noise we took two steps. First, we aimed at removing the highest possible fraction of high-frequency variability (due to ocean tides and the ocean response to pressure plus wind) by using up- to-date corrections (FES2014 and DAC respectively). Second, we applied the DIVA analysis on weekly rather than monthly data input (Sect. 2.5.2.1). On the other hand, no dedicated analysis of this source of noise was made in Armitage et al. (2016), where relatively old corrections for tide- and wind-related high-frequency variability were used (FES2004 and IB respectively). In their study, a generic approach is used to reduce spatial noise, which consists in bin-averaging the along-track data over longitude-latitude grid cells with resolution of 2°X0.5°. These different approaches are most likely responsible of differences between the two datasets in regions where the sub-monthly variability is strongest (Fig. 2.5c). For example, the two datasets have the highest RMSD in the East Siberian Sea and the Chukchi Sea regions, where we found that the DAC yielded the most improvements over the IB (Sect. 3.1.2). Furthermore, relatively low correlation values are shown in the Barents Sea and the Baffin Bay, two regions of strong tidal variability where the tidal model FES2014 performs better than the previous version FES2004 (Sect. 3.1.1) and in general better than most of the models available for the Arctic Ocean (Cancet et al., 2018).

Finally, this study and the study by Armitage et al. (2016) applied different methods to grid the data into monthly estimates. In this work, we used a two-step gridding method which, in a first step, provides a background field as a backup field and, in a second step, grids the data into monthly fields using a decorrelation radius of 50 km. The gridding method applied in Armitage et al. (2016) instead does not rely on a background field, but rather smooths the previously binned data with a Gaussian convolution filter of radius 100 km. In the first place, these two different approaches provide different results where the interpolation is not well constrained by data, for instance, as mentioned above, in regions of very compact ice or in the marginal ice zone. Furthermore, in the two cases data are gridded using different decorrelation radius, that sets the actual dataset resolution. This introduces therefore a difference in the resolution between the two datasets, regardless of the chosen grid.

3.3.2 Pointwise comparison between satellite altimetry retrievals and in-situ data

Pointwise comparison with independent in-situ mooring-based time series of sea surface height were used to assess the time variability of our altimetry product in three separate regions of the central Arctic, i.e., the Fram Strait, the Nansen Basin and the Beaufort Sea (Fig. 3.8). Results showed that altimetry and in-situ data yield roughly consistent temporal patterns, exhibiting variability on similar timescales. For instance, a seasonal signal is visible at all sites with a common peak in autumn, more clearly defined in the Eurasian Arctic and more variable in intensity in Beaufort Sea, and month to month variability is enhanced in the Beaufort Sea. Correlation is significant at all sites, with coefficients ranging between 0.5 and 0.9. The RMSD between altimetry and open ocean mooring observations (2-5 cm) was consistent with other studies comparing altimetry to in-situ observations. For instance, studies comparing altimetry data with tide gauges found RMSD values in the range of 2 to 12 cm across the Arctic (Volkov and Pujol, 2012; Armitage et al., 2016; Rose et al., 2019). A similar result was obtained via comparison of altimetry with steric height from hydrographic profiles in the Arctic Deep Basins (Kwok and Morison, 2011).

Despite the broad agreement between altimetry- and mooring-derived sea surface height observations from the open ocean (Fig. 3.8), correlations were lower or comparable to previous studies which compared altimetry to near-shore tide gauge measurements (Volkov and Pujol, 2012; Armitage et al., 2016; Rose et al., 2019). This can be expected for a few reasons. First, while tide gauges measure sea surface height, directly

comparable to altimetry, estimates of sea surface height from mooring data include uncertainty resulting from limited vertical resolution. This agrees with our results, showing that altimetry correlates best with mooring data at the site with the most continuous and extended vertical sampling (M_4p6). Secondly, we expect tide gauge measurements to correlate better with altimetry given that sea surface height variability near the coast shows larger amplitudes than in the open ocean (see Fig. 3.13).

Altimetry-derived geostrophic velocity were compared to moored velocity at nineteen moorings, including moorings located at important exchange gateways of the Arctic, i.e. in the Fram Strait and the Chukchi Seas. Results showed that the correlation is significant where variability on timescales of seasonal or longer is present. In contrast, large differences emerge at intra-seasonal timescales, especially in regions of weak mean currents (central Fram Strait, interior of the Eurasian Basin, Beaufort Sea). Another study by Armitage et al. (2017) compared altimetry-derived currents with moored currents velocity from the interior of the Beaufort Sea. Correlation values in Armitage et al. (2017) were lower or equal to 0.54, in line with our findings at most mooring sites, except for moorings M1_1, S1 and S3 which show correlation values larger than 0.6. The RMSD values of 1-2 cm s^{-1} over weak mean currents of 2-4 cm s^{-1} found in Armitage et al. (2017) also agree well with what we find in the same region.

3.3.3 Temporal and spatial resolution of altimetry-derived monthly estimates

The comparison between our altimetry-derived dataset and in-situ data showed that agreement between these two data sources can be expected at scales of about 50-70 km and larger, both for sea surface height and surface circulation.

Large-scale patterns of altimetry-derived dynamic ocean topography are consistent with hydrography-based sea surface height in the central Arctic (Fig. 3.9). For instance, both data sources consistently show a decrease in sea surface height of about 70-80 cm from the Amerasian to the Eurasian basin, which was also found in the comparisons carried out in Armitage et al. (2016) and Kwok and Morison (2016). Additionally, comparing monthly profiles to snapshots from hydrographic sections in the Fram Strait (Fig. 3.7), we saw that the cyclonic shape in sea surface height characteristic of the Nordic Seas is well reproduced, with a minimum in the centre of the strait. Furthermore, this comparison shows the continuity of the altimetry field across the ice edge, in the western part of the strait. On the other hand, we note that altimetry is unable to resolve gradients in sea surface height on short scales of about 30-40 km, which are captured by in-situ profiles in the western part of the Fram Strait. This is consistent with the smoothing applied to the altimeter data in the gridding process, where a 50 km decorrelation radius was used.

The large spatial extent covered by the two mooring arrays allowed us to examine the agreement of altimetry and in-situ velocity over different dynamic regimes and spatio-temporal scales. We found that correlation is highest in regions where the flow variability is dominated by steady currents (e.g. boundary currents) and lowest where it is dominated by nonstationary eddy activity. The change in correlation with dynamic regime can be explained considering the different sampling of mesoscale activity by moorings and by altimetry. Mesoscale features are not resolved in our monthly altimetry fields because of the 50 km smoothing scale used in the interpolation. This is equivalent to about ten times the local first mode baroclinic Rossby radius (Nurser and Bacon, 2014; von Appen et al., 2016; Pnyushkov et al., 2015), which roughly sets the horizontal scale of mesoscale eddies. For this reason we see also that the correlation coefficient improves when time series are low-pass filtered to retain only the seasonal and longer timescales, thereby suppressing the effect of mesoscale eddies (test results in Table 3.3).

We find evidence of different correlation in connection with dynamic regime at both mooring lines and in the western Arctic. In the Fram Strait, altimetry and in-situ data show the highest correlation on the shore and continental slope east of 5°E, within the West Spitsbergen Current, with maximum correlation in the

core, non-eddying part of the current (mooring F3, Beszczynska-Möller et al., 2012). In the Laptev Sea the correlation is highest at mooring M1_1, close to the shelf break, where the Arctic Boundary Current is strongest (Aksenov et al., 2011; Baumann et al., 2018). On the contrary, in both regions the correlation breaks down where mean currents are slow and the mesoscale activity is enhanced. Namely, the correlation is low and non-significant at moorings in the central Fram Strait, where the surface circulation is dominated by westward eddies propagation (von Appen et al., 2016; Hattermann et al., 2016). The comparison of temporally filtered time series in this region (test 3 in Table 3.3) clearly shows that the strongest decrease in correlation happens at intra-seasonal timescales, while the correlation on longer timescales remains stable. Similarly, correlation was low in the offshore part of the Laptev Sea continental slope, where current speed is low and eddy activity increases (Pnyushkov et al., 2015, 2018; Baumann et al., 2018). Our comparison with data from the moorings in the Beaufort Sea and the Chukchi Sea also support the above results. While there is significant correlation of altimetry with data from within the relatively strong Pacific Water inflow in the Chukchi Sea (Woodgate et al., 2005; Fang et al., 2020), low and generally non-significant correlation is shown with data from the weak flow of the central Beaufort Gyre. In particular, the correlation is lowest at the two moorings located in southern portion of the Beaufort Gyre, where the highest concentration of eddies is found (Zhao et al., 2016).

We thus used in-situ surface velocities to evaluate the effective spatial and temporal resolution of altimetry-derived monthly currents. Looking at the mean spatial variability, we found that altimetry captures transitions from strong to weak currents occurring over distances of 50-70 km. Accordingly, spatially averaged velocity have generally higher temporal correlation than velocity at a single mooring. For instance, in the region of the West Spitsbergen Current, the correlation is higher when averaging over about 50 km relative to about 20 km (compare test 1 and 2 in Table 3.3). This indicates that the boundary current variability as observed by our altimetry-derived velocity agree most closely with the in-situ observed variability when both are averaged across at least 50 km. On the other hand, slightly lower correlation values are obtained when averaging data further into the central Fram Strait (about 80 km, see test 3 in Table 3.3), due to the different dynamic regime. There, eddies are a source of variability at intra-seasonal timescales, which is not resolved by our altimetry maps and biases the large-scale average velocity from moorings. By low-pass filtering velocities with a cutoff of 4 months, we found, indeed, that the correlation between altimetry and in-situ data is increased both in the Fram Strait and at the Laptev Sea continental slope.

The considerations above suggest that our maps of monthly geostrophic velocities for the Arctic Ocean can resolve seasonal to interannual variability of boundary currents wider than about 50 km. The current that we analysed more in detail in this respect is the West Spitzbergen Current, which had not been shown to be resolved using altimetry before this study (Armitage et al., 2017). We suggest however that this result is relevant also for studies who wish to investigate other relatively narrow slope currents systems of the Arctic Ocean, for instance the Arctic Boundary current (Baumann et al., 2018; Pérez Hernández et al., 2019) or the Chukchi Slope Current (Min et al., 2019). We do not resolve, however, mesoscale variability at intra-seasonal timescales. Past studies have shown that multi-altimeter integration is necessary over large part of the global oceaan to resolve mesoscale activity (e.g., Pujol et al., 2010). In a recent study, Prandi et al. (2021) combined altimeter data from three satellites flying over the Arctic Ocean, covering a time span of three years. Using tide gauge data as reference signal, they estimate that the improvement in resolution of the mapped sea surface height from a single altimeter product to a combined one is on average from 3 to 1.5 months. This indicates that future efforts to increase the temporal resolution of gridded altimetry products should be directed towards the integration of data from more than one satellite. This comes however at the expense of the duration of the time series, which is limited in the Arctic region by relatively short overlap periods of satellites' activity.

Table 3.4. Time of seasonal maximum occurrence in the currents of the Arctic Ocean in the results of this study. The acronym of currents correspond to those indicated in Fig. 2.1 and slope currents are marked in bold. The third column indicate previous studies that find seasonality in agreement with our results.

Current	Time of seasonal maximum	Other studies
WSC (and NwASC)	November to February	Beszczynska-Möller et al. (2012); von Appen et al. (2016)
BSB	November to February	Schauer et al. (2002)
VSC	November to December	Janout et al. (2015)
ABC	October to January (western Nansen Basin) September to December (Laptev Sea cont. slope)	Pérez Hernández et al. (2019) Baumann et al. (2018)
BG	October to January (southern branch)	Proshutinsky et al. (2009); Armitage et al. (2017)
CSC	August to October	Min et al. (2019)
PW	June to August (central-eastern Chukchi Sea)	Woodgate et al. (2005)
EGC	February to April	Bacon et al. (2014); Le Bras et al. (2018); de Steur et al. (2018)

3.3.4 Seasonality

The sea surface height seasonal cycle is driven by changes in the steric component (due to vertical buoyancy fluxes and advection) and the mass component (due to water accumulation or release, precipitation, evaporation, river runoff). Previous studies identified the seasonal cycle as the dominant component of the sea surface height variability in the Arctic (e.g., Volkov et al., 2013; Armitage et al., 2016; Müller et al., 2019b). Our results confirm these findings, showing that this variability explains a fraction higher than 20% of the total variability in large areas of the Arctic, including the Arctic Shelves, the Nordic Seas, the Eurasian Basin and part of the Canada Basin. Additionally, from monthly time series of altimetry-derived and in-situ geostrophic velocity we found that the variability of boundary currents at seasonal to interannual timescales dominates over intra-seasonal variability.

Large-scale features emerge in the seasonal cycle of η' and (u_g, v_g). First, η' has seasonal maximum in winter, between September and December, over most of the Arctic. Furthermore, we found that the amplitude of the seasonal cycle of η', as well as the fraction of variability explained, are higher over the shelf regions than in open ocean regions of the Arctic interior. Lastly, we found that geostrophic currents consistently strengthen along the continental slopes in winter and weaken in summer. These features find support in the literature. The wintertime occurrence of the η' seasonal maximum is in agreement with previous studies of steric height seasonality from in-situ data. For instance, from hydrographic profiles, the steric height was found to peak between September and November in the Greenland and Norwegian Seas (Siegismund et al., 2007), in the central Barents Sea (Volkov et al., 2013) and in the Canada Basin (Proshutinsky et al., 2009). Besides, the secondary peak appearing from the η' climatology in most of the Arctic interior (Fig. 3.13c) is in agreement with the late summer peak of ocean mass found by Peralta-Ferriz and Morison (2010) from GRACE data. Overall, both the Arctic-wide occurrence of the winter maximum and the decoupling of shallow and deep regions agree well with the two first Empirical Orthogonal Functions of sea surface height derived by Bulczak et al.

(2015) and Armitage et al. (2016): a basin-wide oscillation with a wintertime maximum and an anti-phase oscillation between shelf regions and deep basins. Finally, the strengthening of boundary currents in winter was documented for several regions by previous studies based on in-situ data, satellite data and model output (Table 3.4). Exceptions to the wintertime peak are though also observed, for instance in the Pacific Water inflow. Both our dataset and past literature reveal that currents there are weaker in winter, when stronger winds oppose the flow driven by the Pacific pressure head into the Arctic (Woodgate et al., 2005; Peralta-Ferriz and Woodgate, 2017). Our dataset is thus able to describe the seasonality of sea surface height and geostrophic currents across the Arctic, consistent with previous studies.

3.4 Conclusions

With this work we aim to contribute to basin scale observational studies of the Arctic Ocean circulation by providing a new Arctic-wide gridded product of satellite-derived sea surface height anomaly (η') and geostrophic velocity (u_g, v_g). We present monthly maps of η' and (u_g, v_g), spanning the years 2011 to 2020, covering both the ice-free and ice-covered parts of the ocean. We believe that this dataset can be used to study variability with spatial scales above 50 km, at seasonal to interannual timescales. Furthermore, both the gridded and the along track data provided with this dataset offer a valuable tool for constraining and evaluating new ocean reanalysis products for the Arctic (e.g., Nguyen et al., 2021; Fukumori et al., 2021).

We find that sub-monthly variability in the Arctic Ocean, due to tides and the response to wind and pressure, is a source of noise in the η' monthly fields. We reduced this noise by i) applying up-to-date altimetry corrections; and ii) averaging four weekly interpolated maps. The comparison of our dataset with the independent altimetry dataset CPOM DOT at monthly timescales yields a correlation coefficient higher than 0.7 over most of the Arctic, indicating that altimetry-derived sea surface height variability is relatively robust with respect to the methodology applied. Isolated areas of lower agreement are attributable to differences in the data coverage in ice-covered regions, in the approach used to correct sub-monthly variability and in the interpolation method, including different spatial decorrelation scale.

The comparison of altimetry-derived monthly fields with in-situ data shows that agreement between these two data sources can be expected at scales exceeding roughly 50 km, both for sea surface height and surface circulation patterns. Altimetry-derived temporal variability in sea surface height shows agreement with mooring data at seasonal and longer timescales, while differences persist at monthly timescales. The agreement between velocities varies depending on the underlying nature and scale of the variability, showing the highest correlation in regions where a stable flow (e.g. boundary currents) dominates the mesoscale eddy activity. For instance, within boundary currents the pointwise correlation coefficient between altimetry and moored velocity is highest close to the shelf break, both in the Fram Strait (0.54) and at the Laptev Sea continental slope (0.77). Furthermore, our results show that seasonal flow variability is also resolved in the ocean interior, away from boundary currents. In the western Arctic, correlation is relatively high both within the strong Pacific Water inflow in the Chukchi Sea (0.69) and at the moorings in the Beaufort Sea (0.53), although lower in the eddy rich part of the basin.

Lastly, large-scale patterns emerge from a preliminary analysis of the seasonality: η' exhibits a basin-wide coherent seasonal cycle, with a maximum between September and December and higher amplitude on the shelves; the (u_g, v_g) features an intensification of the Arctic slope currents in winter and a weakening in summer. The agreement of these features with previous in-situ based studies points to the important role that altimetry has in the Arctic Ocean, integrating individual mooring-inferred results into a basin-wide perspective.

Chapter 4

Large scale forcing of the Arctic sea level seasonality and implications for slope currents

In Chapter 3, I presented an evaluation of the Sea level Anomaly and Geostrophic velocity of the Arctic ocean (SAGA) gridded altimetry dataset by comparing it to in-situ data. The results from this chapter contributed to assessing the extent and limitations of the observational capabilities of satellite altimetry in the Arctic, which had previously only been evaluated in coastal areas and to a very limited extent in the central Arctic (e.g., Morison et al., 2012; Armitage et al., 2016; Rose et al., 2019). My results complemented existing studies by evaluating the temporal variability of sea surface height and associated geostrophic velocities in the central Arctic, using long-term open-ocean mooring observations for comparison. An important result that emerged from the comparison of geostrophic velocity to moored near-surface velocity, is that the SAGA altimetry product is able to accurately capture seasonal and longer-term variability in slope currents across the Arctic (Fig. 3.10, 3.11 and 3.12, Table 3.4).

In particular, the comparison of currents in the Fram Strait and at the Laptev Sea continental slope revealed a common seasonality there, with wintertime strengthening close to the shelf break. Seasonal composites from SAGA's velocity fields confirmed that this wintertime acceleration pertains to the entire system of topographically steered slope currents enclosing the Arctic Eurasian shelf seas. The satellite-based results presented here therefore provide a large-scale perspective to previous mooring-based results on the seasonal evolution of Arctic slope currents, pointing to a coherent seasonality in the current intensity both at the outer rim of the shelf seas (Beszczynska-Möller et al., 2012; Pérez Hernández et al., 2019; Ruiz-Castillo et al., 2023; Baumann et al., 2018) and across the Barents and Kara Seas (Schauer et al., 2002).

Furthermore, results from Chapter 3 showed that the seasonal acceleration in slope currents occurs in phase with a seasonal rise in the shelf sea level, which opens the question how these two processes are connected. Previous studies have investigated sea surface height variability and its drivers in order to explain the variability in Arctic surface currents (e.g., Armitage et al., 2018; Proshutinsky et al., 2015). These show that Arctic sea surface height variability can be related, depending on the time scales considered, either to wind-driven barotropic variability or to the availability and distribution of fresh water. It is however not clear so far what is the relative contribution of the mass- and density-related forcing of sea surface height on the seasonal timescale, and how this in turn influences the current variability at the Arctic continental slopes. Furthermore, there is a lack of studies specifically estimating how the action of such drivers leads to the observed amplitude of the sea surface height response.

In this chapter I therefore apply the SAGA dataset to investigate the nature and drivers of the Arctic-wide seasonal sea surface height variability, with the aim of understanding the mechanisms behind the observed large-scale wintertime slope current acceleration. Alongside the SAGA data, I use output from the FESOM model to have a dynamically consistent, three dimensional representation of currents, sea surface height and driving processes. I firstly describe the temporal and spatial patterns of the Arctic sea surface height seasonality, specifying where these are related to changes in density and mass (Sect. 4.1). Then, I analyse possible drivers of sea surface height variability (Sect. 4.2). Finally, I analyse the Arctic-wide seasonal modulations in geostrophic currents, focusing specifically on the Eurasian part of the slope currents (Sect. 4.3).

4.1 Large scale characteristics of the sea surface height seasonal cycle

In this section I characterise the seasonality of the Arctic sea surface height using the altimetry dataset SAGA (Ch. 3) and output fields from the FESOM model (run described in Sect 2.6). I first identify common large scale patterns between the altimetry data and model output, thereby validating the seasonal cycle as simulated by the model. Then, I use model data to attribute the observed spatial distribution of the seasonal cycle to either steric or mass-related effects.

4.1.1 Seasonality in sea surface height from altimetry and model data

As a first step to describe the large-scale characteristics of the η' seasonal cycle, I computed the average climatology of η' for selected areas (Fig. 4.1). The climatology from the SAGA dataset and the FESOM simulations agree well in terms of temporal evolution and spatial variability. In all areas, the climatology presents one dominant peak and one trough, with the sea surface being lowest in late winter to early summer, and highest in late summer. This seasonal evolution suggests that over most of the Arctic Ocean the sea surface height seasonal cycle can be modelled by an annual harmonic oscillation, as previously found for instance by Volkov et al. (2013) for the Barents Sea. Deviations from a single peaked harmonic behaviour emerge in a few regions (e.g. in the Laptev Sea, the East Siberian Sea, the Beaufort Gyre and the Baffin Bay), where both altimetry and model data show a secondary peak in June-July. This aspect of the seasonality will become clearer once the steric and mass-related contributions are analysed in Sect. 4.1.2. Spatial heterogeneity in the amplitude of the seasonal variability emerges from comparison between different regions. Both data sources indicate η' to exhibit stronger seasonal oscillations on the shelf seas than in the deeper basins. The peak to trough difference in η' is largest in the East Siberian Sea (12.9 cm from SAGA and 17.8 cm from FESOM) and smallest in the Eurasian Basin (5.1 cm from SAGA and 5.2 cm from FESOM). Furthermore, the spread around the climatological mean values is highest on the eastern shelf seas (Laptev Sea and East Siberian Sea), suggesting that the η' seasonality is subject to stronger interannual variability there than in other regions. While the analysis of the seasonal climatology provides an insight on the area-averaged temporal evolution of the seasonal cycle, I applied an annual harmonic analysis (Sect. 2.7) to both altimetry and model data in order to observe in more detail the spatial characteristics of the seasonal cycle, keeping in mind the above mentioned deviations from it.

From the harmonic analysis (Fig. 4.2), it emerges that the seasonal cycle explains a fraction of the total variability larger than 20% over most of the Arctic Ocean, including all seas shallower than 500 m, the Nordic Seas, the Eurasian Basin and the southwestern Beaufort Sea (Fig. 4.2c and 4.2c). I will consider below only these regions to describe the most relevant characteristics of the η' seasonal cycle. Over these regions, the spatial distribution of the η' seasonal amplitude and phase simulated by the model closely resemble altimetry observations (Fig. 4.2). The seasonal phase is mostly uniform over large regions (e.g. shelf seas and basins) in the model as well as in the altimetry data, with the seasonal peak occurring between September and December.

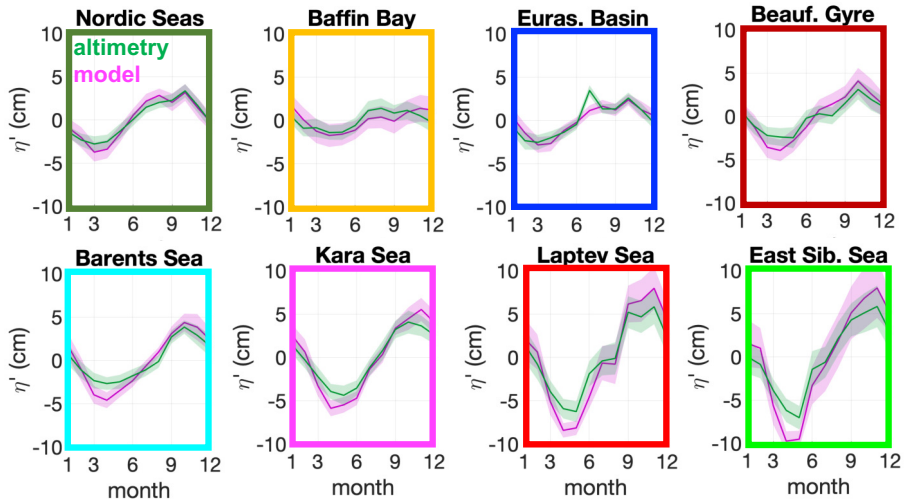

Figure 4.1. Climatology of η' (period 2011-2020) from altimetry (SAGA) and model (FESOM) data, over selected regions; the color code used for each region refers to the boxes indicated in Fig. 4.2. Solid lines indicate the average climatology and shading the climatological standard error in each region in the period 2011-2020.

The latest phase, between November and December, is observed in the shallow shelf seas, while an earlier phase is observed in the basins (September to October). Likewise, shelf seas and basins are characterized by distinct η' seasonal amplitude. This is typically lower and higher than 3 cm in areas deeper and shallower than 500 m, respectively. The SAGA dataset and the FESOM output display similar spatial variability also on scales smaller than single basins or seas. For instance, within the Barents and Kara seas both sources show the latest phase to be along the coasts of Norway, Siberia and Novaya Zemlya (December), and the earliest phase over the Central Basin of the Barents Sea (October). Furthermore, relatively small areas of enhanced seasonal amplitude are displayed in the altimetry and model data in the same regions: these are, on the shelves, the southern Kara Sea and the central Est Siberian Sea, while in the basins, the Lofoten Basin, Greenland Sea and southwestern Canada Basin. Despite the widespread consistency between model and altimetry observations, modelled and observed seasonal amplitudes diverge in the coastal regions. While the largest values from altimetry are 8-9 cm, the model reaches values above 10 cm. In Sect. 4.4 I will discuss this discrepancy in relation to the processing and smoothing of altimetry data to derive the SAGA product. The above results from the harmonic analysis highlight the good spatial agreement between the SAGA dataset and the FESOM simulation. Both datasets highlight the dominance of the seasonal variability over the total variability, and its uniform characteristics over wide regions, with pronounced differences in phase and amplitude between shallow and deep regions.

Specifically, on the Eurasian side of the Arctic both the SAGA and the FESOM data identify a decoupling between areas shallower and deeper than about 500 m (Fig. 4.2e and 4.2f). The 500 m isobath approximately indicates the position of a steep topographic slope separating the shallow Eurasian shelf seas from the deep basins of the Nordic Seas and the Eurasian Basin. In the shallow and deep domains, the seasonality of η' develops with distinct amplitude and phase. From average values of the SAGA dataset (Fig. 4.2e), I found that the amplitude in shallow regions is one and a half times larger than in deep regions, and the maximum occurs 1.5 months later (mid November rather than beginning of October). The same analysis applied to the FESOM output also yields double amplitude and 1.5 months lag in shallow areas with respect to deep areas (Fig. 4.2f). Thus, both altimetry and model data indicate a spatial transition between an early and less pronounced peak in the deep basins and a late and intensified maximum in the shelf seas. Furthermore, the seasonal phase transition between deep and shallow regions is closely aligned with the steep slope separating the two regions (Fig. 4.2c and 4.2d), along which slope currents flow from the North Atlantic into the central Arctic. Given that geostrophic current variability is related to spatial differences in sea surface height variability, the decoupling of

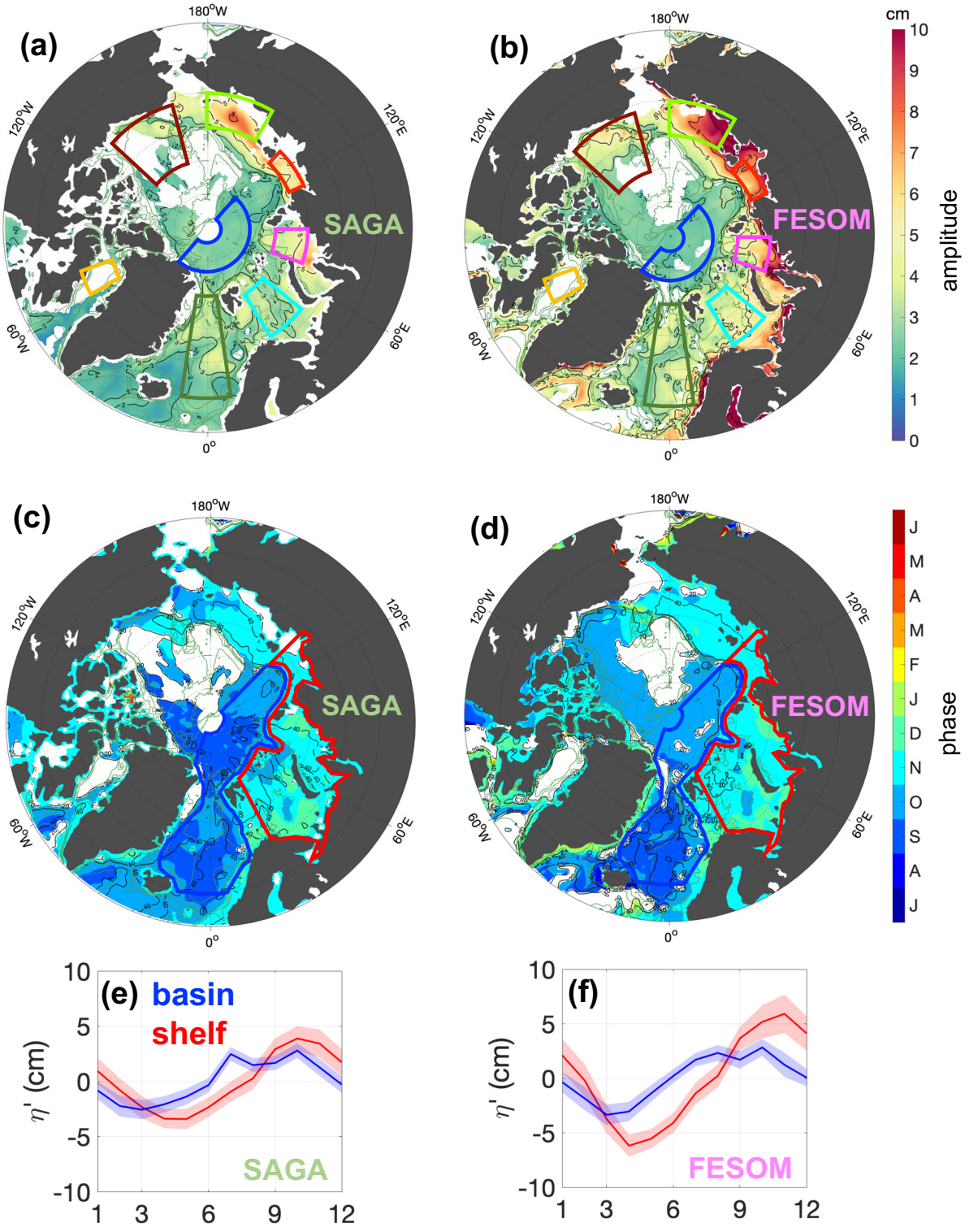

Figure 4.2. Amplitude (a and b) and phase (i.e., month of seasonal maximum, c and d) of the annual harmonic fit to the η' seasonal cycle. Left panels show results from the altimetry dataset (SAGA) and right panels from the model output (FESOM). Boxes in panels (a) and (b) indicate the regions selected to compute the climatologies displayed in Fig. 4.1. In panels (a) to (d), regions where the harmonic seasonal cycle explains less than 20% of the total variability have been blanked. Panels (e) and (f), derived from SAGA and FESOM data respectively, show in solid lines the 2011-2020 average climatology over areas deeper (blue) and shallower (red) than 500 m in the Eurasian Arctic (see blue and red regions encircled in panels (c) and (d)); shading indicates the climatological standard error in 2011-2020. Bottom depth (green contours) is drawn at 300 m, 500 m, 1000 m, 2500 m.

the η' variability at the continental slope suggests that there might be an impact of the above mentioned pattern on the seasonality of the slope currents (e.g., Armitage et al., 2018). In the following I try to understand whether the differential changes between these two regions can be associated with steric or mass-related variability.

4.1.2 Steric and mass-related contributions to sea surface height seasonality

Results from Sect. 4.1.1 provides confidence in the ability of FESOM to realistically simulate the Arctic sea surface height seasonal cycle. The comparison with altimetry data highlights agreement both in the area-averaged characteristics of the seasonal cycle, as well as in its spatial patterns. Most notably, both the model and the altimetry data identify a spatial decoupling in the η' seasonality across the continental slope, which is relevant to understand geostrophic anomalies in the slope currents. In the following, as a first step to identify the drivers of the Arctic η' seasonality, I use the FESOM model data to examine the nature of this variability. I attribute the spatial patterns identified in Sect 4.1.1 to either steric or mass-related variability (hereafter η'_S and η'_M respectively, computed as in section 2.8), with special focus on the shelf-basin decoupling.

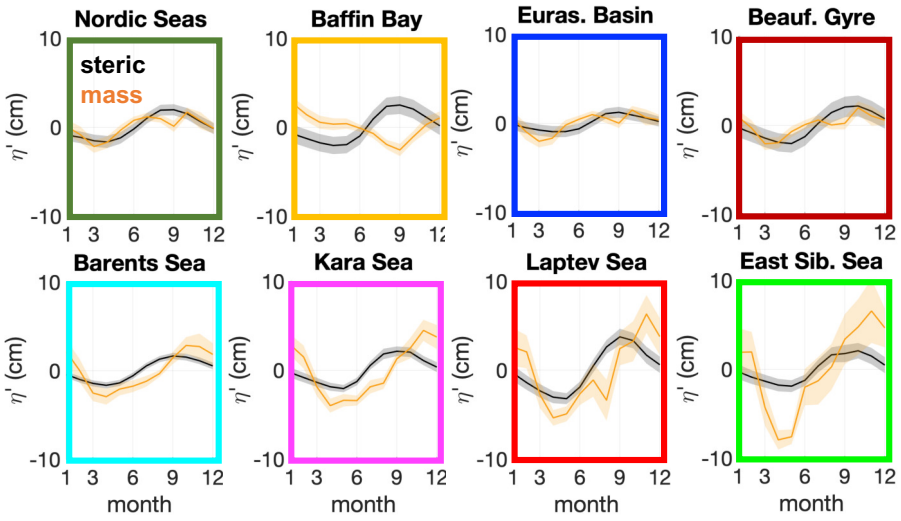

Figure 4.3. Climatology of η'_M (orange) and η'_S (black) from model data (FESOM, period 2011-2020), over selected regions; the color code for the regions is referred to the boxed indicated in Fig. 4.2. Solid lines indicate the average climatology and shading the climatological standard error in each region in the period 2011-2020.

A comparison between the average climatologies of steric and mass-related height variability in selected areas (shown in Fig. 4.3) allowed to outline the area-averaged characteristics of their seasonal cycle and establish their relative contribution to the total seasonal variability in different regions. In deep regions the two components contribute equally to the seasonal signal, whereas in the shelf seas the mass-related contribution exceeds the steric one. While η'_S peaks at 1-3 cm independently of ocean depth, η'_M has larger peak values in shallow regions, progressively intensified from the Barents Sea eastward, up to a peak of 7 cm in the East Siberian Sea. The evolution of the η'_S seasonal cycle is smooth and characterised by a single peak, with uniform phase across all regions (September). The η'_M climatology instead displays a main seasonal peak with about one month delay in shallow regions (November) with respect to deep ones (October). A secondary peak in η'_M occurs in many regions in July, whose genesis will be discussed later in Sect. 4.4. The area-averaged climatologies therefore seem to indicate that, while the steric variability makes the sea surface pulse at seasonal timescales over the entire Arctic, the mass-related variability introduces a lag and an amplification of the η' seasonal peak in the shelf seas with respect to their neighbouring deep basins.

From the above analysis I hypothesise that the shelf-basin decoupling observed in the η' seasonal cycle can be attributed to η'_M. I therefore applied the annual harmonic fit to η'_S and η'_M (Fig. 4.4) to observe in

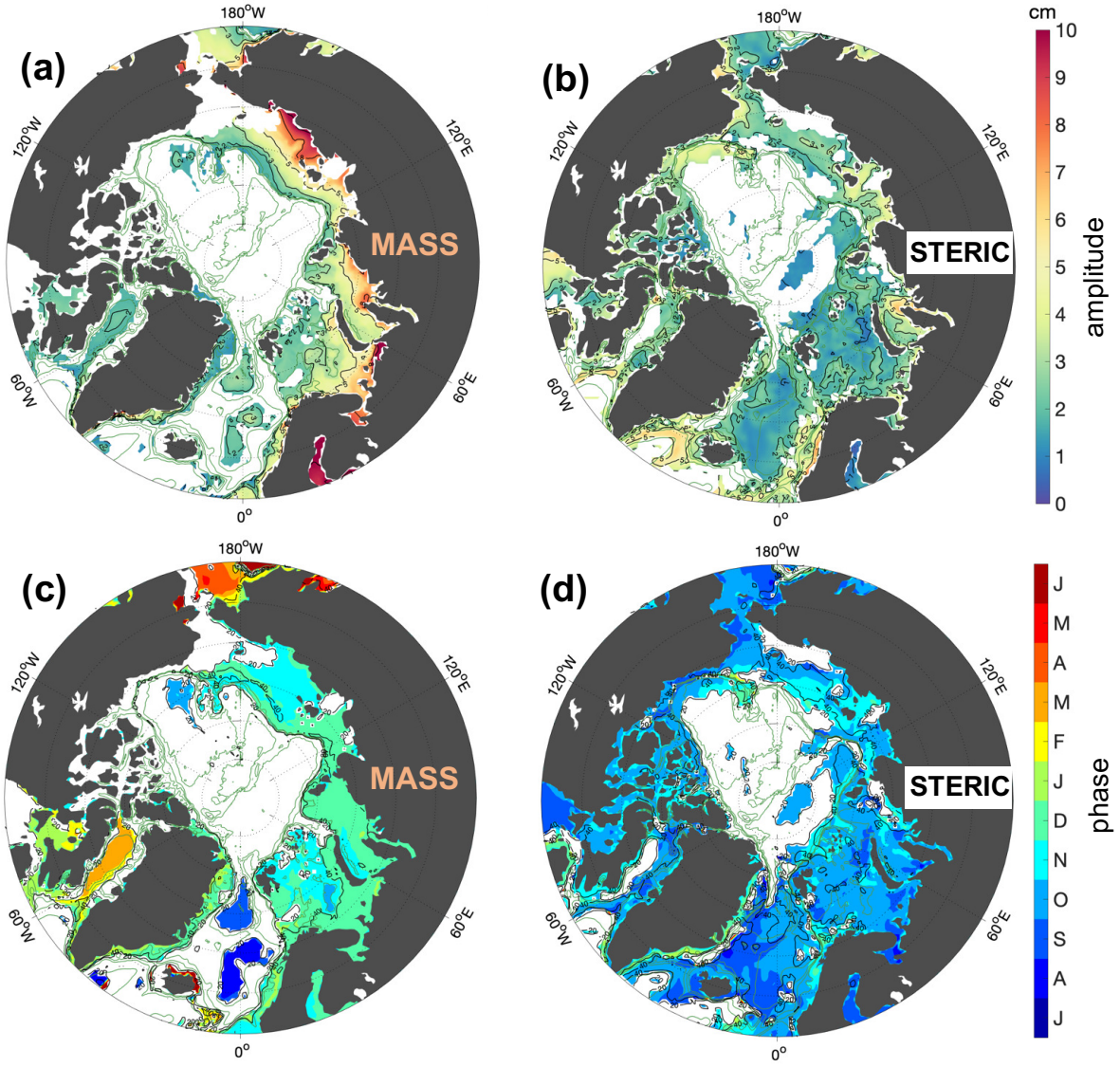

Figure 4.4. Amplitude (a and b) and phase (i.e., month of maximum, c and d) of the annual harmonic fit to the η'_S (left panels) and η'_M (right panels) seasonal cycle. All panels show results of the analysis of model output (FESOM). In each panel, regions where the harmonic seasonal cycle explains less than 20% of the total variability of η'_M (a, c) or η'_S (b, d) have been blanked. Bottom depth (green contours) is drawn at 300 m, 500 m, 1000 m, 2500 m.

detail the spatial distribution of their seasonal cycle. Areas where η'_M and η'_S explain a fraction higher than 20% of the total variability correspond to the Eurasian Arctic shallower than the 300 m isobath in the first case, and to year-round or seasonally ice-free regions in the second case (Fig. 4.4c and 4.4d). While the amplitude of the seasonal cycle for η'_M increases as the water column gets shallower, ranging from 2 cm up to 10 cm, η'_S amplitude peaks at 5 cm within narrow elongated bands not everywhere aligned with bottom topography. Furthermore, while the seasonal phase of η'_S is uniform around the Arctic and centred around October, the phase of η'_M has a lag of about 2-3 months in the shelf seas (December) with respect to the deep Nordic Seas and southwestern Canada Basin (September-October). Therefore, the harmonic analysis validates our hypothesis that a bathymetry-related amplification and delay of the η' seasonal cycle is to be attributed to mass variability.

In order to better understand the extent of the shelf-basin decoupling, I considered the two periods when the average difference in η' between areas of the Eurasian Arctic shallower and deeper than 500 m (refer to regions in Fig. 4.2) is maximum (November to January) and minimum (May to July). Maps of seasonal

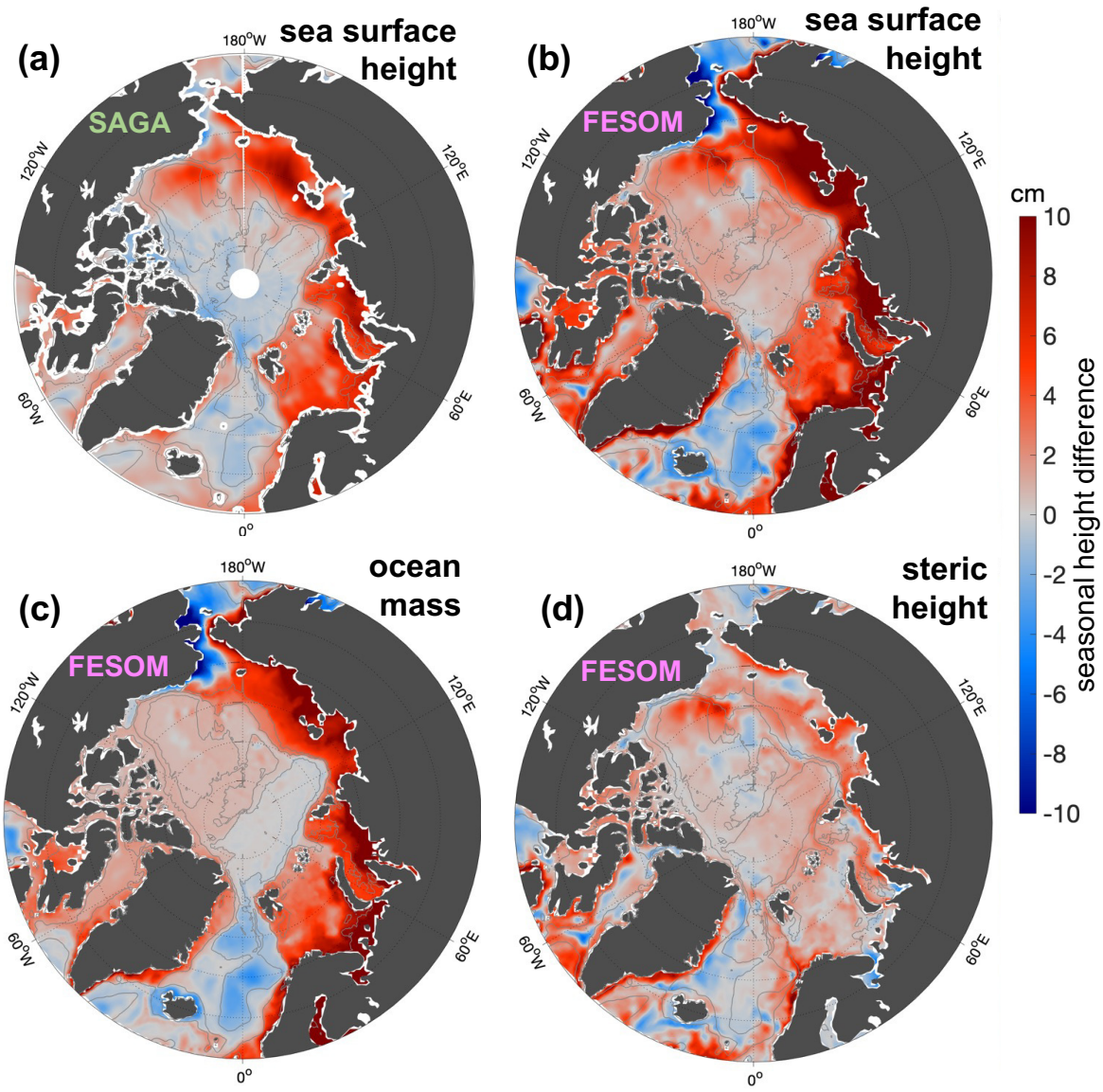

Figure 4.5. Seasonal differences in sea surface height between the winter period November-December-January and the summer period May-June-July. The upper panels represent the differences in η' computed from altimetry (SAGA, panel (a)) and model (FESOM, panel (b)) data. the lower panels represent the differences in η'_M (panel (c)) and η'_S (panel d()) computed from model (FESOM) data. Bottom depth (green contours) is drawn at 100 m, 500 m, 2500 m.

differences in η', η'_M and η'_S between these two time periods are displayed in Fig. 4.5. Differences in η' from both SAGA and FESOM data are larger in shallow than in deep regions over the entire Arctic, defining a clear shelf-basin decoupling in the Eurasian Arctic. A sharp transition between positive differences larger than 5 cm and weak differences (less than 1 cm) is aligned to the entire continental slope from the Norwegian coasts to the East Siberian Sea. Both SAGA and FESOM exhibit negative differences in the Nordic Seas basins and minor seasonal changes in the deep basins north of 80°N (although differing in the sign there). Furthermore, shelf-intensified positive differences are also observed on the eastern Greenland shelf and in the Baffin Bay. In the western Arctic, the sign of seasonal differences is reversed between deep and shallow regions. Positive differences are confined to the southwestern Canada basin and negative differences to the shallow eastern Chukchi Sea. Which of these seasonal patterns can be observed in the maps of η'_M and η'_S differences?

According to the FESOM simulations, a large-scale shelf-basin decoupling in the Eurasian Arctic exists also in seasonal mass-related height differences (Fig. 4.5c). The largest seasonal changes in η'_M (8-10 cm)

occur in regions shallower than 100 m, for instance in the shallow Kara, Laptev and East Siberian Seas. Deep regions exhibit either negative values (Nordic Seas) or very small values (less than 1 cm in the Eurasian Basin). To validate these results, based on independent measurements of ocean mass changes, I compared the FESOM-derived seasonal changes to seasonal differences in the ocean mass fields as derived from GRACE data (Fig. 4.6). FESOM and GRACE data present a consistent picture of the mass-related seasonal differences. Firstly, they agree in amplitude, showing peaks of more than 10 cm on the Eurasian shelves. Although this is in apparent disagreement with low seasonal mass variations found by Armitage et al. (2016), it should be mention that, while the JPL Release-06 GRACE data are used here, the JPL Release-05 is used by Armitage et al. (2016), which has been shown to attenuate the annual cycle of ocean mass (Volkov et al., 2013). Secondly, GRACE data confirm the presence of a seasonal shelf-basin decoupling in mass-related variability on the Eurasian side of the Arctic. GRACE seasonal differences in this part of the Arctic are largest and positive close to the coast, decrease following bathymetry gradients and become weak or negative across the continental slope in the Nordic Seas and central Arctic basins. In the eastern Chukchi Sea and eastern Greenland shelf, shelf-intensified seasonal differences are also attributable to mass-related changes. Contrary to that, mass-related seasonal differences are rather uniform in the Amerasian basin, Canadian Arctic Archipelago and Baffin Bay (even though the sign in the observations and the model do not agree). In Sect. 4.2 I will carry out an in-depth analysis of the forcing of mass-related variability.

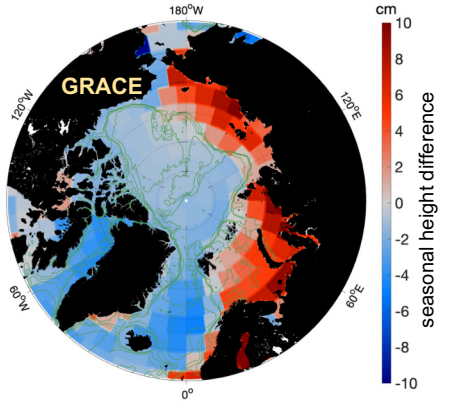

Figure 4.6. Seasonal differences in ocean mass equivalent height from GRACE between the winter period November-December-January and the summer period May-June-July. Bottom depth (gray contours) is drawn at 300 m, 500 m, 1000 m, 2500 m.

In contrast to the shelf-basin decoupling emerging from mass-related seasonal changes, FESOM simulations indicate that η'_S has everywhere higher values in November-December-January than in May-June-July (Fig. 4.5d). This visualisation of steric seasonal changes complements the results from the climatology and the harmonic analysis, which showed, as well, that η'_S peaks over most of the Arctic in October, being still relatively high in the following months. Superimposed to this basin-scale mode, we note that η'_S seasonal differences are enhanced in confined regions across the Arctic. For instance, the shelf-intensified seasonal differences in the Baffin Bay, and partly on the eastern Greenland shelf, previously identified from η' fields, seem to be attributable to steric changes. The same holds true for changes in the southwestern Canada Basin. Furthermore, the FESOM simulations suggest that part of the seasonality on the Eurasian shelf seas is also of steric nature. For example an enhanced steric signal is visible along the Norwegian coast, in the western Barents Sea, and downstream of the Ob, Yenisei and Lena rivers in the Kara, Laptev and East Siberian Seas. In these confined regions, higher η'_S in November to January than during May to July can be explained by seasonal variability in the local hydrography. On the Greenland shelves, steric height changes follows the glaciers' runoff season in the period from June to August (e.g., Solgaard et al., 2022). In the Canada Basin, a combination of higher availability of fresh water after the summer and peak in the wind momentum transfer to the ocean, result in a peak freshwater content in the Beaufort Gyre around November (Proshutinsky et al., 2009). Along the Atlantic Water pathways, following the coasts of Norway and northwards towards Spitsbergen, a warming of the Atlantic Water in summer contribute to a strong decrease in the density of the upper ocean throughout this season, therefore an increase in steric height, with the strongest density decrease close to the shelf break (von Appen et al., 2016). Finally, freshwater plumes of the siberian rivers, with runoff peaking in June, spread

eastward along the shore as a buoyancy-driven boundary current (Osadchiev et al., 2020), being transported to neighbouring shelf seas (Janout et al., 2015).

4.2 Forcing of mass-related variability by wind

In Section 4.1 I identified a delay and amplification of the η' seasonal peak on the Eurasian shelf with respect to the neighbouring basins, attributable to the η'_M seasonality. This suggests that the shelf-basin decoupling could be attributed to a lagged seasonal accumulation and retreat of water mass from the shelves. Large-scale variability in the Arctic sea surface height and surface currents has in the past been attributed to both mass and fresh water redistribution by large-scale patterns of wind variability. On sub-seasonal timescales, wind forcing has been shown to drive basin-scale coherent sea surface height and bottom pressure variability, particularly enhanced in shallow waters (e.g., Peralta-Ferriz et al., 2011; Armitage et al., 2018). On interannual and longer timescales, wind-related sea surface height variability is attributed to changes in the freshwater pathways and distribution, relevant in determining the anticyclonic or cyclonic character of the surface circulation in the central Arctic (e.g., Proshutinsky and Johnson, 1997; Morison et al., 2012, 2021). Results from previous studies suggest therefore that wind forcing is relevant to drive the sea surface height variability over a range of timescales, with basin-scale oscillations of ocean mass being predominant on shorter timescales. This agrees well with the mass-related character of the seasonal oscillations on the Eurasian shelf observed in Sect. 4.1, indicating that wind stress at the ocean surface ($\tau_{\mathbf{o}}$) might drive a seasonally anomalous transport of ocean mass on the shelf.

One major contributor to the ocean mass budget is the wind-driven Ekman transport (Eq. 2.25). Ekman dynamics are often proposed to intuitively explain variability in sea surface height, based on large scale wind patterns. For instance, previous studies have identified modes of sea surface height decoupling between the Arctic shelves and deep basins at monthly and interannual time scales (Peralta-Ferriz et al., 2014; Armitage et al., 2016, 2018). Those studies attributed the decoupling to a shoreward Ekman transport implied by a cyclonic anomaly in the Arctic winds associated to a negative Arctic Oscillation index. However, in the Arctic Ocean the Ekman layer is relatively shallow, extending approximately down to a depth of 20 m (Hunkins, 1966; McPhee, 1992; Cole et al., 2014; Peterson et al., 2017), and little has been said about how the flow below the Ekman layer actually closes the mass budget.

In the following, I use FESOM output fields to investigate the mechanisms by which wind drives the large-scale seasonal variability in the mass-related component of the Arctic sea level. In particular, I focus on understanding the forcing mechanisms behind the decoupling of shelf seas and deep basins, which modulates the sea surface height slope at the shelf break, in turn accelerating and decelerating the geostrophic component of the slope currents.

4.2.1 Ocean mass variability and surface stress field

The harmonic analysis of η' highlighted that the seasonal cycle explains a major fraction of the Arctic sea surface height variability. On the large scale, the η' seasonality manifests in the form of a decoupling between shallow and deep regions, dominated by the mass-related variability. This is reflected in the temporal and spatial characteristics of the first EOF mode of the η'_M fields north of 60° N (44% of the total variability, Fig. 4.7a). Firstly, this mode oscillates seasonally between a positive phase, with a maximum in winter, and a negative phase, with a minimum in summer (Fig. 4.7b). Secondly, the spatial distribution of this mode features a decoupling of shallow and deep regions over the whole Arctic Ocean. In the positive phase, the surface height anomaly is positive everywhere in the shelf seas, reaching values up to 10 cm std^{-1}, while it is not consistently positive nor negative over the deep basin, where it reaches at most values of ± 1 cm std^{-1}. The

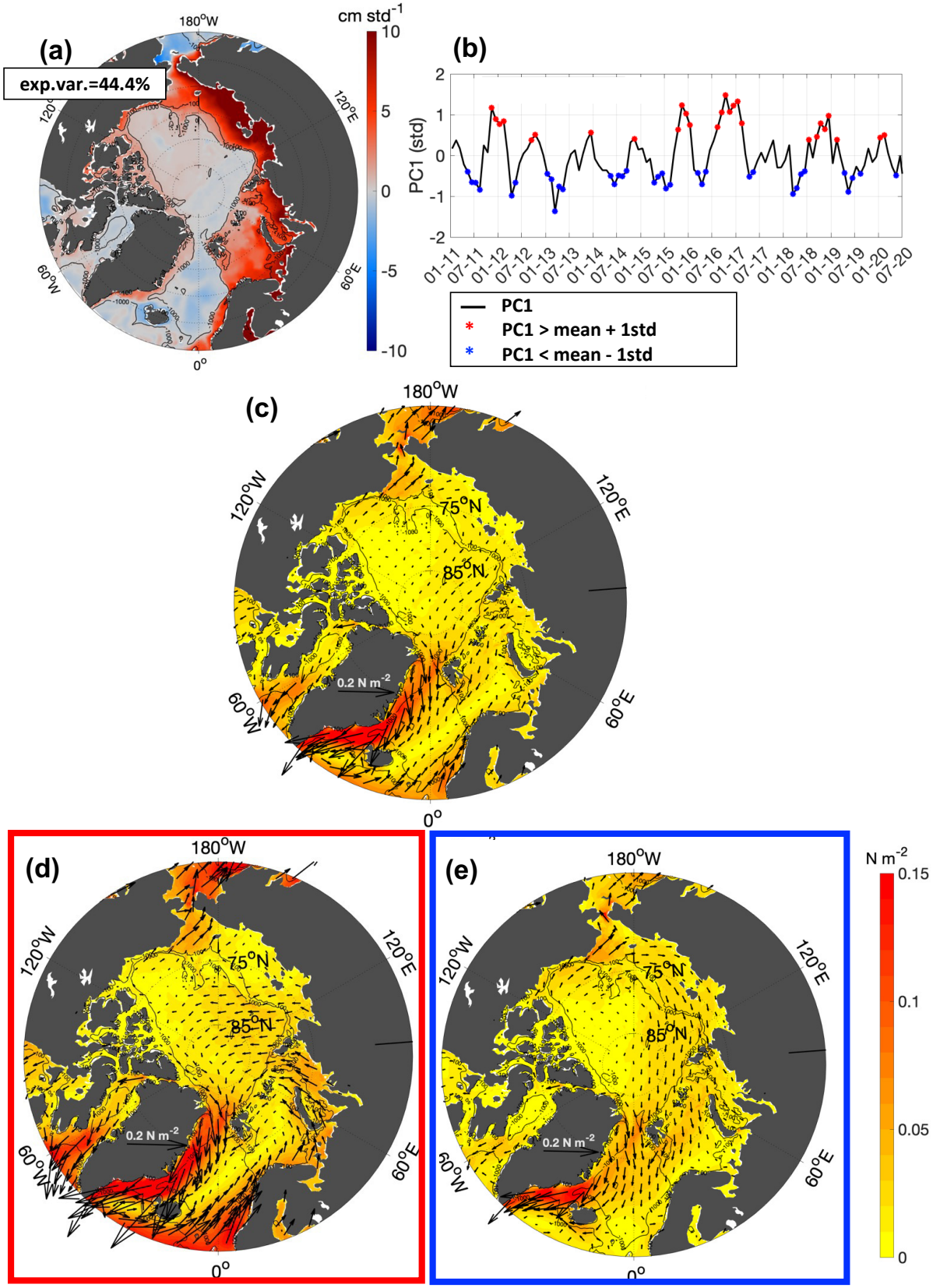

Figure 4.7. Relation between seasonal η'_M variability and wind stress field. (a) First EOF and (b) first principal component of the η'_M fields north of 60° N. Lower panels show the mean wind stress field in 2011-2020 in panel (c), and averages of wind stress over months when the shelf η'_M is higher (panel (d)) and lower (panel panel (e)) than one standard deviation, as indicated in panel (b) by red and blue dots, respectively.

spatial pattern of the first EOF mode seems to indicate that the shelf region behaves as a highly connected region on a seasonal time scale. A possible mechanism driving this connected behaviour might be large-scale wind forcing, if a sizable seasonal change in the cross-slope Ekman transport can be demonstrated. As a first step to investigate the action of the wind on shelf mass variability, I looked at seasonal $\tau_{\mathbf{o}}$ fields (Sect. 2.9.1). These were constructed as composite maps for phases of high and low shelf ocean mass, based on the temporal evolution of the first EOF mode of η'_M.

The Arctic mean wind field features two major patterns, the Beaufort High, centered over the Canada Basin, and the Icelandic Low, stretching between the North Atlantic and the Barents Sea (Timmermans and Marshall, 2020; Smedsrud et al., 2013). I find these patterns in the mean $\tau_{\mathbf{o}}$ field (Fig. 4.7c): while a strong cyclonic forcing covers the Nordic Seas and the Barents sea, closing across the Kara Sea, a broad and relatively weak anticyclonic forcing extends along the borders of the central Arctic deep basins. These two patterns are alternately dominating the $\tau_{\mathbf{o}}$ composites for winter (when the shelf mass is maximum, Fig. 4.7d) and summer (when the shelf mass is minimum, Fig. 4.7e). In winter, the composite maps of $\tau_{\mathbf{o}}$ are dominated by the cyclonic forcing, which is intensified and reaches the eastern shelf seas beyond Vilkitsky Strait. In summer, $\tau_{\mathbf{o}}$ is instead anticyclonic over most of the Arctic, with westward stress acting all along the Eurasian continental slope. The seasonally alternating predominance of these two wind patterns results in generally east-/northeastward forcing along the Eurasian continental slope during winter, and westward forcing during summer. Furthermore, year-round southwestward stress in the Chukchi Sea and Bering Strait is strongest in wintertime and weakest in summertime. The joint action of these wind stress patterns is consistent with a shelf-wide shoreward Ekman transport in winter and offshore Ekman transport in summer, suggesting that the seasonal sea surface variability on the shelf might be linked to wind forcing via Ekman dynamics. In the following section, I therefore investigate the actual role of Ekman dynamics in driving cross-slope transport, and ask whether other processes contribute significantly to drive cross-slope transport.

4.2.2 Cross-slope transport

To gain insight into the driving processes of mass-related variability on the shelves, I analysed the contributions to changes in the shelf ocean mass by cross-slope transport at different depths and across various parts of the slope. Firstly, I compared the average observed η'_M variability on the shelf to the equivalent height change on the shelf produced by surface Ekman transport across the shelf edge (see Eq. 2.26 and Fig. 2.6). Additionally, I examined horizontal ocean velocities from FESOM to determine where and at what depth other first order contributions to onshore transport originate. I specifically focused on the western portion of the Eurasian shelf (Barents Sea and Kara Sea). In this region, the η'_M interannual variability is lower than in the eastern shelves (Sect. 4.1, see also Calafat et al. (2013)), therefore allowing a more robust analysis of the processes acting on the seasonal timescale. In Sect. 4.4, I discuss whether the results below can be extended to the entire Eurasian shelf.

In Fig. 4.8a I compare the climatology of the average η'_M over the Barents Sea and Kara Sea (area shown in Fig. 4.8b) and the climatology of the Ekman transport equivalent height ($\Delta\eta_{Mek}$, Eq. 2.26) due to Ekman transport across the encompassing shelf break. The climatologies of η'_M and $\Delta\eta_{Mek}$ oscillate seasonally with the same phase, decreasing in late winter and increasing in late summer. This suggests that Ekman transport could indeed be the driver of the observed seasonal η'_M changes, with enhanced cyclonic winds over the shelf driving onshore Ekman transport in winter. This hypothesis is supported by the analysis of the composite averages of wind stress fields over months of anomalously high or low onshore Ekman transport (exceeding one standard deviation from the mean, Fig. 4.8d and 4.8e), which resemble the average winter and summer wind stress fields, respectively (Fig. 4.7d and 4.7e). In the high Ekman transport case, a northward shift in the North Atlantic storm track brings prevailing southwesterly winds over the Barents and Kara Seas and generally

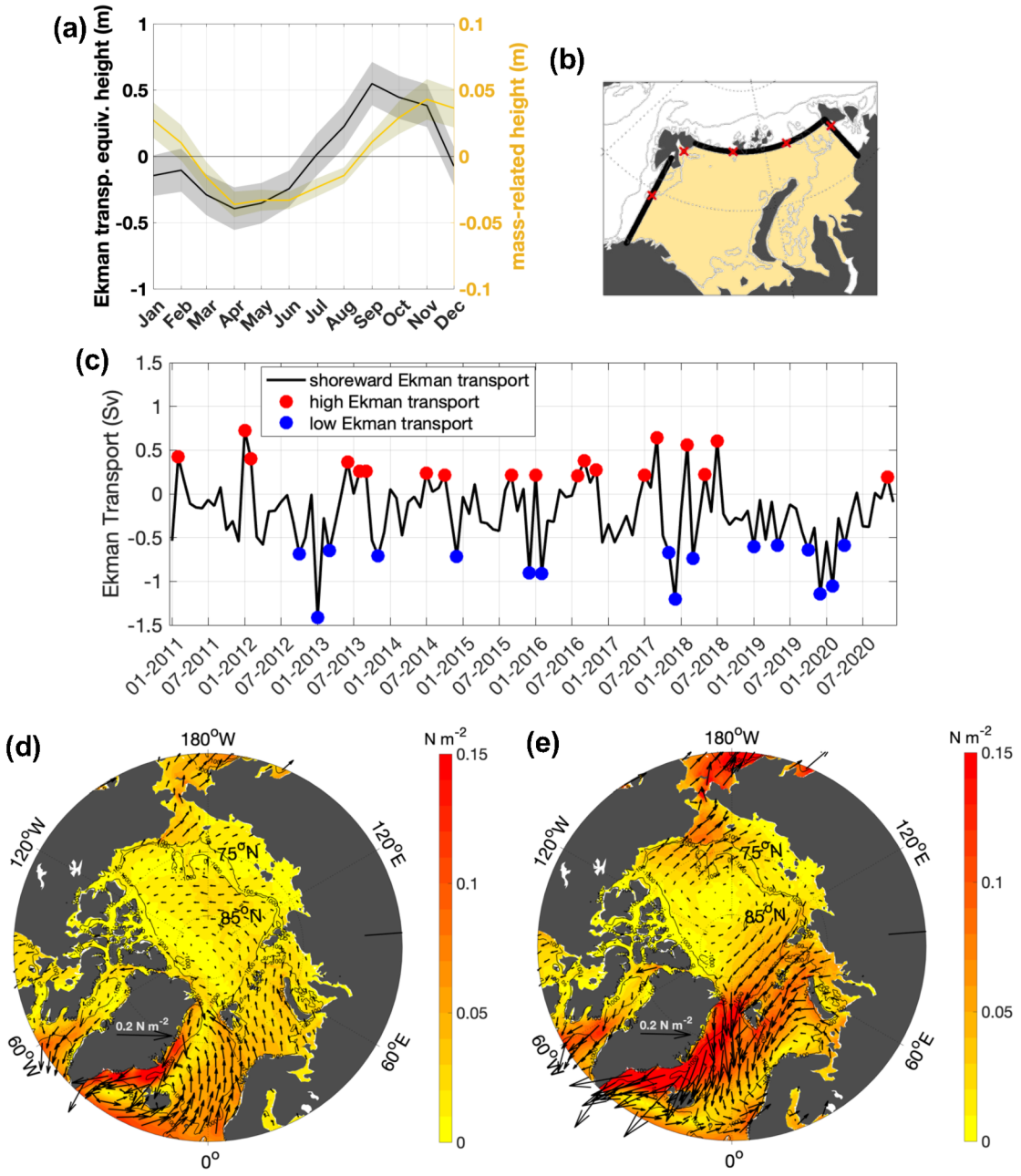

Figure 4.8. Cross-shelf Ekman transport in the western Eurasian shelf and associated wind stress field. (a) Comparison between the climatology (2011-2020) of onshore Ekman transport equivalent height (black line, left axis, see definition in Eq. 2.26) and average shelf mass-related height (yellow line, right axis); shading indicates the climatological standard error in the period 2011-2020. (b) The map displays (*i*) the transect across which the Ekman transport was computed (black line, red crosses each 500 km) and (*ii*) the shelf area over which the mass-related height was averaged (yellow area); bottom depth (gray contours) is drawn at 100 m, 500 m, 2500 m. (c) Time series of shoreward Ekman cross-slope transport anomaly; dots identify the months when the Ekman transport anomaly was higher than one standard deviation above the mean (red) or lower than one standard deviation below the mean (blue). Panels (d) and (e) represent composites of the wind stress field in periods of high and low shoreward Ekman transport anomaly, respectively.

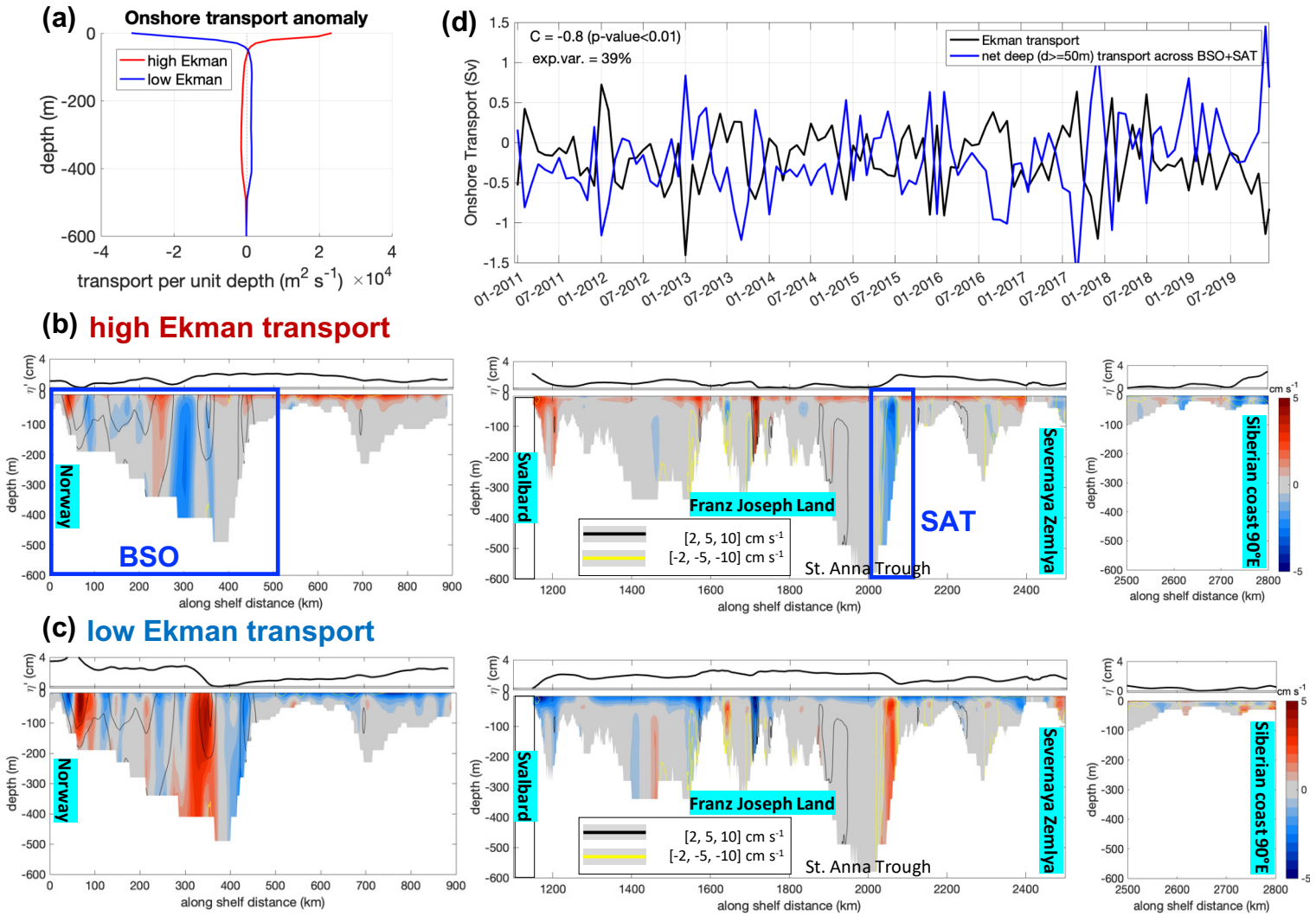

Figure 4.9. Shoreward ocean transport anomalies from FESOM horizontal velocity fields. (a) Shelf-integrated shoreward ocean transport anomaly (across the transect outlined in Fig. 4.8a) in months of high and low onshore net Ekman transport anomaly (refer to red and blue dots in Fig. 4.8c). Panels (b) and (c) display vertical sections of shoreward ocean velocity anomaly at the shelf edge (transect indicated in Fig 4.8b), averaged over months of high and low shoreward Ekman transport, respectively; contours of the mean onshore velocity are shown with black lines (2,5,10 cm s^{-1}), and yellow lines (-2,-5,-10 cm s^{-1}) respectively; the regions of Barents Sea Opening (BSO) and St. Anna Trough (SAT) are marked by blue squares in panel (b). The upper insets in panels (b) and (c) show the η' profile along the transect. (d) The time series of shoreward Ekman transport (black line, same as in Fig. 4.8c) is shown against the time series of shoreward ocean transport across the BSO plus SAT (blue line).

cyclonic circulation over the entire Arctic. In the low Ekman transport case, a southward shift in the storm track carries prevailing east-/northeasterly winds over the Barents and Kara Seas. Despite the resemblance between the seasonal wind stress fields and the Ekman composites, Fig. 4.8a also reveals that the seasonal oscillations observed in the η'_M climatology are one order of magnitude smaller than those exhibited by $\Delta\eta_{Mek}$. This implies that surface Ekman transport is too large to directly explain the seasonal variability of η'_M. Furthermore, the climatological spread of $\Delta\eta_{Mek}$ is much larger than that of η'_M, indicating a much stronger interannual variability in the Ekman-related variability (visible also in the Ekman transport time series, Fig. 4.8c). Large parts of both the seasonal and non-seasonal variability of $\Delta\eta_{Mek}$ must therefore be compensated by an opposing transport at depth, bringing the shelf mass budget in agreement with the observed seasonal η'_M variability.

To identify additional contributions to the cross-slope exchange, taking place in response to anomalous Ekman transport, I computed composite averages of horizontal cross-slope ocean velocity in periods of anomalously high and low shoreward Ekman transport. From along-slope-integrated vertical profiles (Fig. 4.9a), the signature of the Ekman velocities in the surface layer can be clearly recognized as a surface intensified transport anomaly, extending down to a depth of about 15-20 m. In the case of a positive (negative) shoreward Ekman transport anomaly, I observe that negative (positive) transport anomalies are found below the Ekman layer, which tend to compensate the surface transport. It is of interest to understand whether or not the surface Ekman transport and the compensating transports are locally aligned with each other. To this end, I analysed along-slope sections of the cross-slope velocity anomalies (Fig. 4.9b and 4.9c, along the transect indicated in Fig. 4.8b). The sections show that, while the surface Ekman transport takes place throughout the entire shelf edge, the deep response does not take place uniformly. It instead manifests itself as localised barotropic velocity anomalies in regions of sloping bottom topography, where known circulation pathways are present. Namely, the strongest anomalies occur in the St. Anna Through (SAT, northern Kara Sea) and in the Barents Sea Opening (BSO, southwestern Barents Sea). These two troughs are the major gateways for inflow (BSO) and outflow (SAT) of Atlantic Water in the western Eurasian shelf (Schauer et al., 2002; Dmitrenko et al., 2015). With a positive anomaly in the shoreward Ekman transport I observe a strengthening of both the outflow through the SAT and the deep outflow in the central BSO (located between two surface Atlantic Water inflow branches). The opposite happens in the case of a negative anomaly in the shoreward Ekman transport. In this case I observe a weakening of the outflow through the SAT and a strengthening of the Atlantic Water inflow branches in the central BSO. The predominance of the velocity anomalies at the BSO and the SAT raises the question whether a major fraction of the variability in the cross-slope surface Ekman transport can actually be explained by the variability in the deep transport along these two major circulation pathways. To find this out, I compare the time series of Ekman transport with the time series of depth-integrated (below 50 m) net shoreward transport across the BSO (along shelf distance 0-500 km) plus the SAT (along shelf distance 2000-2100 km). The net deep transport explains 41% of the variability in the surface Ekman transport, and the two have a high correlation coefficient of -0.8 (Fig. 4.9d). This result suggests that, in the western Eurasian shelf, a large part of the cross-slope surface Ekman transport is compensated by the net imbalance between deep shelf inflow at the BSO and outflow at the SAT.

An additional wind-driven cross-slope transport pattern can be identified from the velocity sections, which does not represent a compensation of the surface cross-slope Ekman transport (Fig. 4.9b and 4.9c). Barotropic flow anomalies develop in coastal areas, positive (negative) shoreward during months of positive (negative) shoreward Ekman anomalies. These are visible for instance at the Norwegian coast, at the eastern coast of Svalbard (around 1100 km along shelf distance) and west of Franz Joseph Land (around 1700 km along shelf distance). These anomalies are consistent with geostrophic adjustment of the flow to changes in the coastal sea level, following water transport towards the coast via along-shore wind anomalies. It has been shown, for instance, that North Atlantic storms passing by the Norwegian coast drive local daily variability in the

Norwegian Atlantic Current, which then integrates over time to shape its monthly variability (Calafat et al., 2013; Brown et al., 2023). The wind stress composite in Fig. 4.8d illustrates how a shift of the North Atlantic storm track towards Greenland brings at the same time northward winds along the Barents Sea Opening, consistent with high cross-slope Ekman transport, and along-shore winds at the Norwegian coast, which lead to a rise in sea level and the strengthening of the Norwegian Atlantic Current. Therefore, this suggests that the wind forcing affects the cross-slope transport also by generating near-coastal pressure gradients driving anomalies in the geostrophic transport.

Figure 4.10. Time series of shoreward transports across the transect outlined in Fig. 4.8b. (a) Ekman transport computed from wind stress fields is shown against the full shelf- and depth-integrated transport computed from ocean velocities. (b) Shelf-integrated ocean transport computed from ocean velocities in the top 40 meters and below 40 m.

The analysis of the velocity sections indicates that, while Ekman transport constitutes a relatively large fraction of the transport above 50 m, it does not account for the full variability of the surface flow. By comparing the time series of Ekman transport and surface transport (above 50 m) between 2011 and 2020 (Fig. 4.10), I find that Ekman transport explains 84% of the total variability, which drops to 53% if only the months with weak Ekman transport are considered. Furthermore, the compensation of the surface shoreward transport via deep transport is not only observed during events of anomalous cross-slope Ekman transport, but occurs on all time scales. The along-slope-integrated surface and deep transports (Fig. 4.10b) are highly anticorrelated throughout the period under study (Pearson's correlation coefficient C=-0.97 with p-value<0.01), remaining highly anticorrelated even when only seasonal and longer time scales are considered (C=-0.98 with p-value<0.01). In particular, I observe that the surface transport anomaly is generally positive in the summer months and negative in the winter ones, while the opposite is true for the deep transport. This indicates that the observed seasonality of mass-related height on the shelves is resulting from a tiny residual of a near-perfect balance between surface and deep transport, rather than being solely controlled by the Ekman transport.

From a shelf-integrated perspective, the transport in the upper 50 m is compensated by the flow below this depth, with the residual transport being one order of magnitude smaller than the Ekman transport. The shelf-integrated vertical profile of shoreward velocity anomaly in periods of enhanced Ekman transport (Fig.

4.9a) shows that large but localised velocity anomalies in the top few tens of meters ($\sim 3 \cdot 10^{-2}$ Sv per unit depth) are balanced by weak but vertically extended velocity anomalies of opposite sign over a few hundred meters to the ocean floor (less than $3 \cdot 10^{-3}$ Sv per unit meter). The vertically-integrated velocity anomalies result in a surface (above 50 m) and a deep (below 50 m) shoreward transport anomalies of 0.42 Sv and -0.45 Sv for the case of positive Ekman transport anomaly, and -0.48 Sv and 0.54 Sv for the case of negative Ekman transport anomaly. These estimates amount to a residual full-depth transport of O(10^{-2} Sv) in periods of anomalous cross-slope Ekman transport. Furthermore, the 2011-2020 time series of full-depth ocean transport shows that the compensation occurs consistently throughout this period (Fig. 4.10a). This residual transport, considering a seasonal integration time and a shelf area of $\sim 2 \cdot 10^{12} \mathrm{m}^2$, is in agreement with the observed seasonal shelf ocean mass changes of about 10-20 cm.

From the above analysis I conclude that seasonal cross-slope transport originates to a large extent from wind driven Ekman dynamics. However, other dynamics must be taken into account to fully explain the seasonal mass-related sea surface height variability. Firstly, about 16% of the surface transport variability is not explained directly by Ekman transport. From horizontal velocity sections I find that this variability can be attributed mostly to geostrophic adjustments of the flow at coastal boundaries. Additionally, time series of depth-integrated transports indicate that the surface transport is almost perfectly compensated by deep transport. The horizontal velocity sections show that this compensation takes place at major cross-slope circulation pathways, which strengthen or weaken in response to anomalous surface transport. In conclusion, I find that the seasonal mass-related sea surface height variability of about 10-20 cm is set by a tiny transport residual resulting from the compensation of surface transport by deep transport.

4.2.3 The barotropic vorticity equation

In the previous analysis I explained the observed mass-related height variability using a descriptive approach focused on Ekman dynamics and the deep ocean response to it. In the following, I attempt to introduce a process-oriented interpretation of the area-averaged variability over the central Barents Sea based on the equation for barotropic vorticity. In Sect. 2.9.5 I introduced a form of the barotropic vorticity equation used by Volkov et al. (2013) (hereafter V13). This form of the equation allows a direct attribution of the η_M variability to different kinds of forcing (wind stress, bottom topography, the Coriolis force and dissipation), as the divergence of the depth-integrated flow ($-\nabla \cdot \mathbf{U}$) is used as a proxy of the tendency of η_M ($\partial \eta_M / \partial t$). In the following I reproduce their results, making reference to the terms indicated in Eq. 2.27. My objectives in this section are to (i) show where my results support the understanding by V13, and (ii) highlight inaccuracies in their methods which might lead to mistaken interpretation of their results.

The approach taken here was, following V13, to first find the terms in Eq. 2.27 that constitute the first order balance, and then verify whether the residual of these terms is able to diagnose changes in mass-related height (for the meaning of each term in the equation, make reference to explanation in Sect. 2.9.5). I first looked at the role of wind stress and dissipation in the balance (terms on the rhs of Eq. 2.27). In agreement with V13 (their Fig. 14), Fig. 4.11a seems to indicate that wind stress curl is almost in full balance with the terms on the lhs of Eq. 2.27. In particular, V13 state that, among the terms on the left side of Eq. 2.27, the flow over bathymetry is the one largely balancing the wind stress. In Fig. 4.11a, the comparison between the time series of wind stress and flow over bathymetry verify this statement, showing how these two terms have the same sign and evolve consistently over time, with very similar magnitude. Finally, the dissipation term appears to be also significant in the balance, having a standard deviation approximately half that of the wind stress term. I ask then, whether the three large terms analysed above (wind stress, dissipation and flow over bathymetry) are sufficient to establish a first order balance that explains the variability in η_M. Following V13, I investigate this aspect by evaluating the correlation between each term in Eq. 2.27 and $-\nabla \cdot \mathbf{U}$, used by V13 as a proxy for the

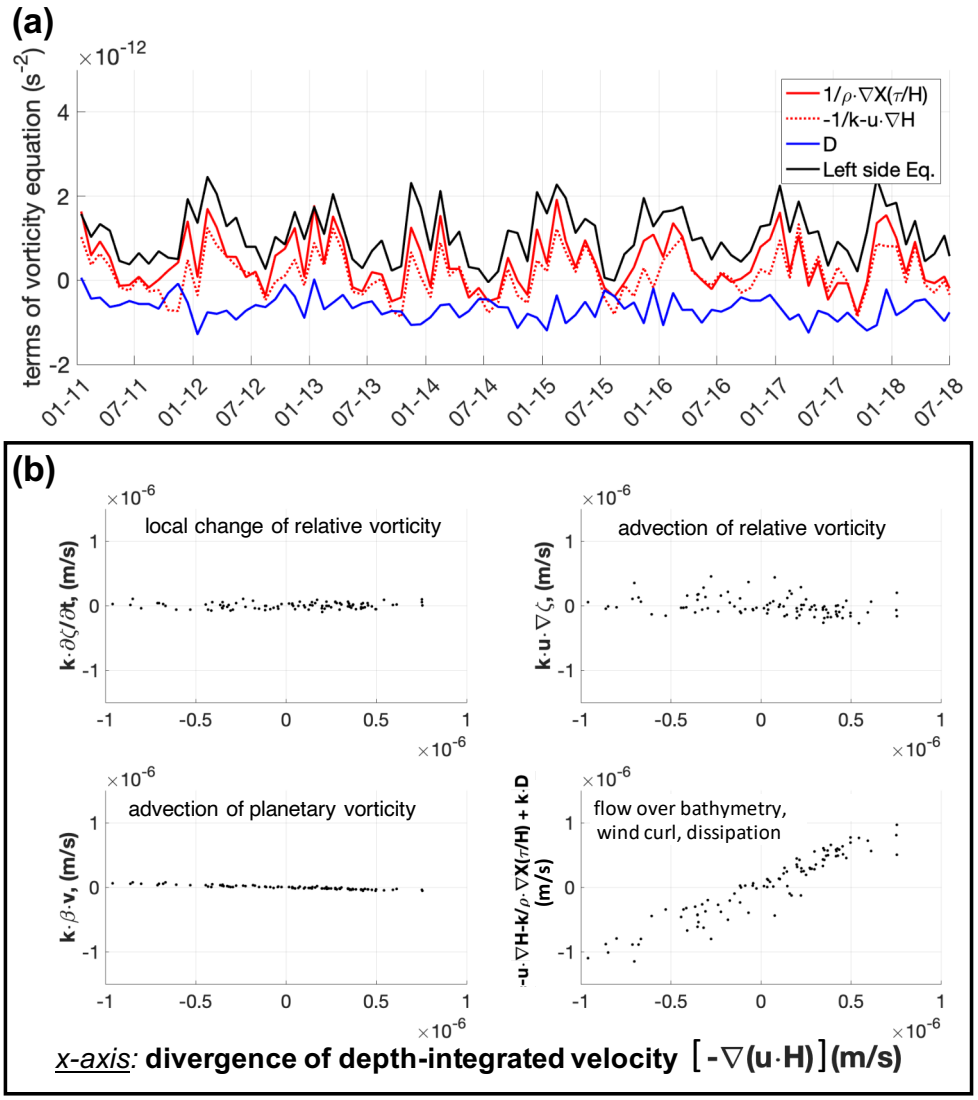

Figure 4.11. Components of the barotropic vorticity budget following the method of Volkov et al. (2013) (Eq. 2.27). FESOM outputs are averaged over the region of longitude between 30°E and 50°E and latitude between 72°N and 75°N. (a) Time series of: the sum of the terms on the left side of Eq. 2.27 (black), the wind stress curl term (red solid), the flow over bathymetry term (red, dashed), and the dissipation term (blue). (b) Scatter plot of terms in Eq. 2.27: the divergence of the depth-integrated velocity (x-axis) is show against the vorticity tendency (top,left), the advection of relative vorticity (top,right), the advection of planetary vorticity (bottom,left) and the sum of flow over bathymetry, wind stress and dissipation (bottom,right).

tendency of η_M based on Eq. 2.28. In Fig. 4.11b, equivalent to Fig. 15 of V13, one can appreciate that most of the variability in the divergence of the depth-integrated velocity is indeed explained by the variability in these three terms, whereas the vorticity tendency and the advection of relative and planetary vorticity vary over a much smaller range. This analysis therefore suggests that sea surface height variability is determined by the balance between the vorticity input to the system via wind stress, vorticity dissipation and changes due to flow across topographic slopes.

Some limitations emerge in the above analysis. Results from V13's analysis indicate that dissipation plays a sizable role in the balance, contributing to offset the mean input of vorticity and reducing its month to month variability. However, we note that the dissipation term is computed by V13 as the residual between all other terms in their Equation (7) (Eq. 2.27 in this thesis), thereby assuming that all terms not explicitly represented in thi equation represent dissipative processes. Given that the derivation of Equation (7) in V13 is not explicit,

some terms might have been discarded which do not belong to the dissipative processes. In particular, the balance as written above has the pitfall to neglect a term, denominated Joint Effect of BAroclinicity and Relief (JEBAR), which is a correction required when using the depth-averaged velocity rather than the bottom velocity to calculate vortex stretching over topography (Isachsen et al., 2003). In my discussion in Sect. 4.4, I provide an alternative treatment of the vorticity equation to possibly provide a more explicit meaning to the dissipation term, or residual term, and to verify whether the JEBAR term has a relevance in our analysis.

4.3 Implications for surface circulation and slope currents

Results in Sect. 4.2 suggest that wind-driven cross-slope mass transport is responsible for large sea surface height variability confined to the shelf seas of the Eurasian Arctic. This locally-enhanced variability modulates horizontal sea surface height gradients, potentially having an effect on the geostrophic component of the surface circulation. Specifically, the sea surface height seasonality sharply changes across the shelf edge in the Eurasian Arctic, along the pathway of the Arctic slope currents. Therefore in this section I focus on investigating the impact of the sea surface height seasonality on the slope currents.

4.3.1 Seasonality in geostrophic velocity from altimetry and model data

Maps of mass-related seasonal differences between winter and summer examined in Sect. 4.1.2 (Fig. 4.5) reveal that the spatial distribution of mass increase in winter is tightly linked to the bottom topography. Wind-driven wintertime rise in mass-related height is not only more pronounced on shelves than in basins, but is especially prominent in coastal regions when compared to the outer shelf. Cross-topography sea surface height gradients are, therefore, modulated seasonally by wind forcing, thereby affecting the geostrophic component of the topographically-steered flow. This is reflected in a large scale wintertime strengthening and summertime weakening of geostrophic currents along the continental slopes of the Arctic (Fig. 4.12). Both SAGA and FESOM show that currents are strongest in the season from November to January, when η'_M in the shelf seas is highest, and are weakest from May to July. In the Eurasian Arctic, currents speed up in winter on both sides of the Nordic Seas, across the Barents and Kara Seas and surrounding the Nansen Basin. In the Amerasian Arctic, speeds increase in winter along the northern to the Alaskan shelf break (in the southern Beaufort Gyre) and close to the coasts in Baffin Bay.

Notably, these seasonal changes in current speed occur almost simultaneously along the entire slope currents system extending from Norway to the Laptev Sea and across the Barents Sea (Fig. 4.13a-d). Model and altimetry data depict a consistent picture of the seasonal evolution of the current system (Fig. 4.13e). At selected locations along the slope, I observe low current speeds throughout late winter and summer (March to July) and peak current speeds in winter (October to January). Furthermore, current speed peaks slightly earlier along the outer slope of the Barents Sea (panels e3, e5, e6) than within the Barents Sea (panels e7, e8, e9). Despite the agreement in the spatial patterns of seasonal variability in the SAGA and FESOM data, the summer to winter speed increase observed from altimetry data (2-3 cm s^{-1}) is smaller than what is simulated by the model (4-5 cm s^{-1}). A pronounced discrepancy is observed at transect (1), along the Norwegian Atlantic Current, where SAGA shows a seasonal speed increase of about 4 cm s^{-1}, against about 15 cm s^{-1} from the FESOM output. One likely reason for this is the proximity of the current to the coast of Norway. Firstly, satellite data too close to the coast are masked in the altimetry dataset to avoid land contamination in the radar data (see discussion in Sect. 4.4). Furthermore, the difference between satellite and model fields is accentuated by the contrast between the smoothing applied to the altimetry data (tens of kilometers) and the high resolution of the model (4.5 km).

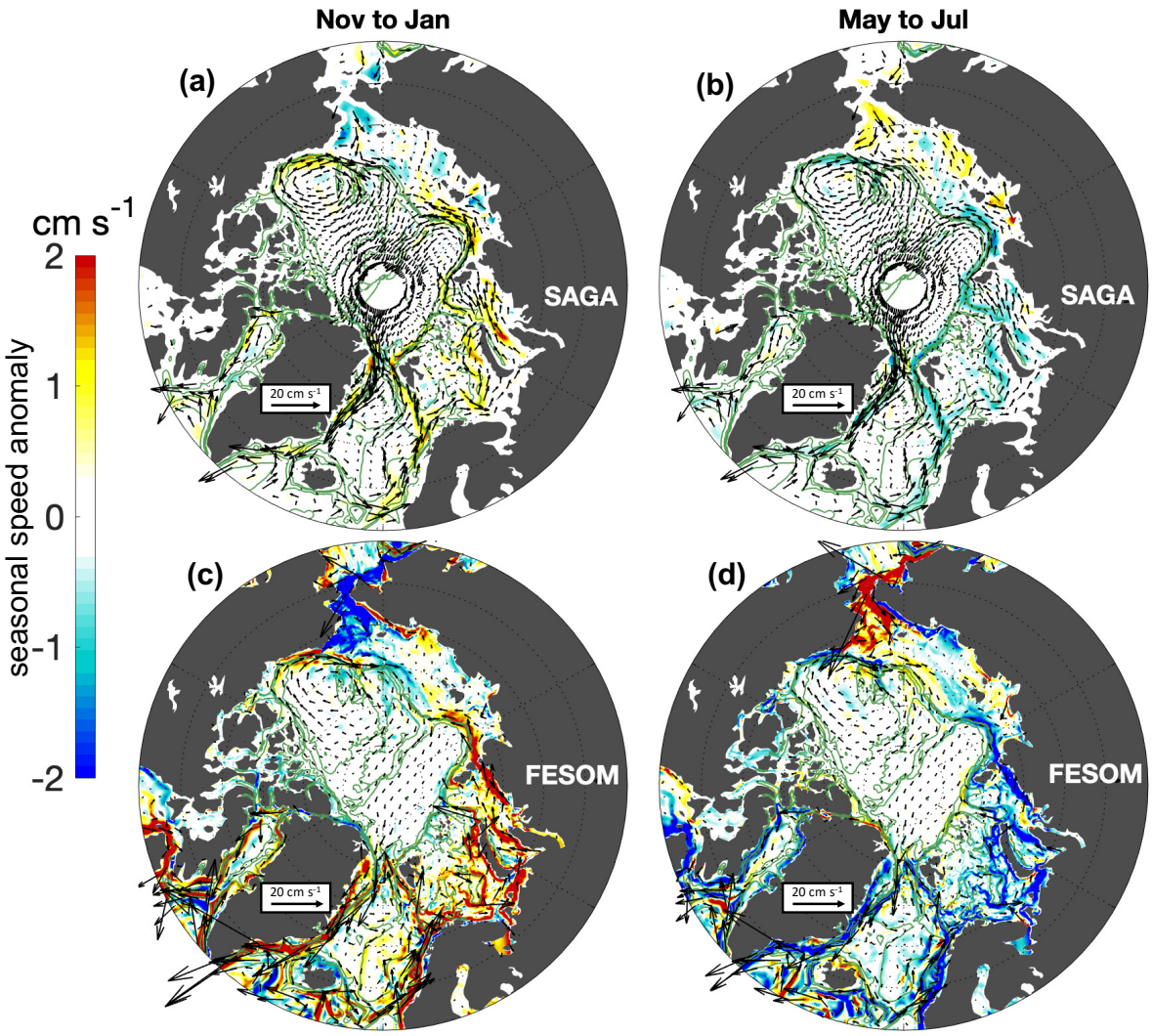

Figure 4.12. Arctic-wide, seasonally averaged geostrophic currents from SAGA (upper panels) and FESOM (lower panels) in winter (November to January, left panels) and summer (May to July, right panels). Vectors indicate the absolute geostrophic velocity averaged over those periods, while colours indicate the seasonal speed anomaly with respect to the 2011-2020 mean speed. Bottom depth (green contours) is drawn at 300 m, 500 m, 1000 m, 2500 m.

How does the seasonal evolution of surface geostrophic currents reflect on the variability at lower depths? To answer this question, I analyse seasonal geostrophic current anomalies together with vertical sections of horizontal cross-slope velocity anomalies at the shelf margins (Fig. 4.14a-b). The vertical sections feature a bottom-reaching strengthening (weakening) of currents along major current pathways during winter (summer), particularly enhanced in the BSO inflow and SAT outflow. This indicates that the coherent large-scale seasonal acceleration of slope currents, observed from satellite data, is not limited to the near-surface ocean, but has a strong barotropic component. Superimposed to this, a closer analysis of the vertical structure of the seasonal velocity anomalies reveals the presence of a baroclinic component in the BSO and SAT. While current anomalies in the BSO are maximum at the surface, in the SAT they are maximum below the surface, between 50 m and 100 m. This spatial variability is consistent with a cooling and densification of the Atlantic Water in its transit through the Barents Sea (Smedsrud et al., 2013). The unified description of surface and deep seasonal evolution of slope currents suggests therefore that large-scale barotropic anomalies are superimposed to local baroclinic variability.

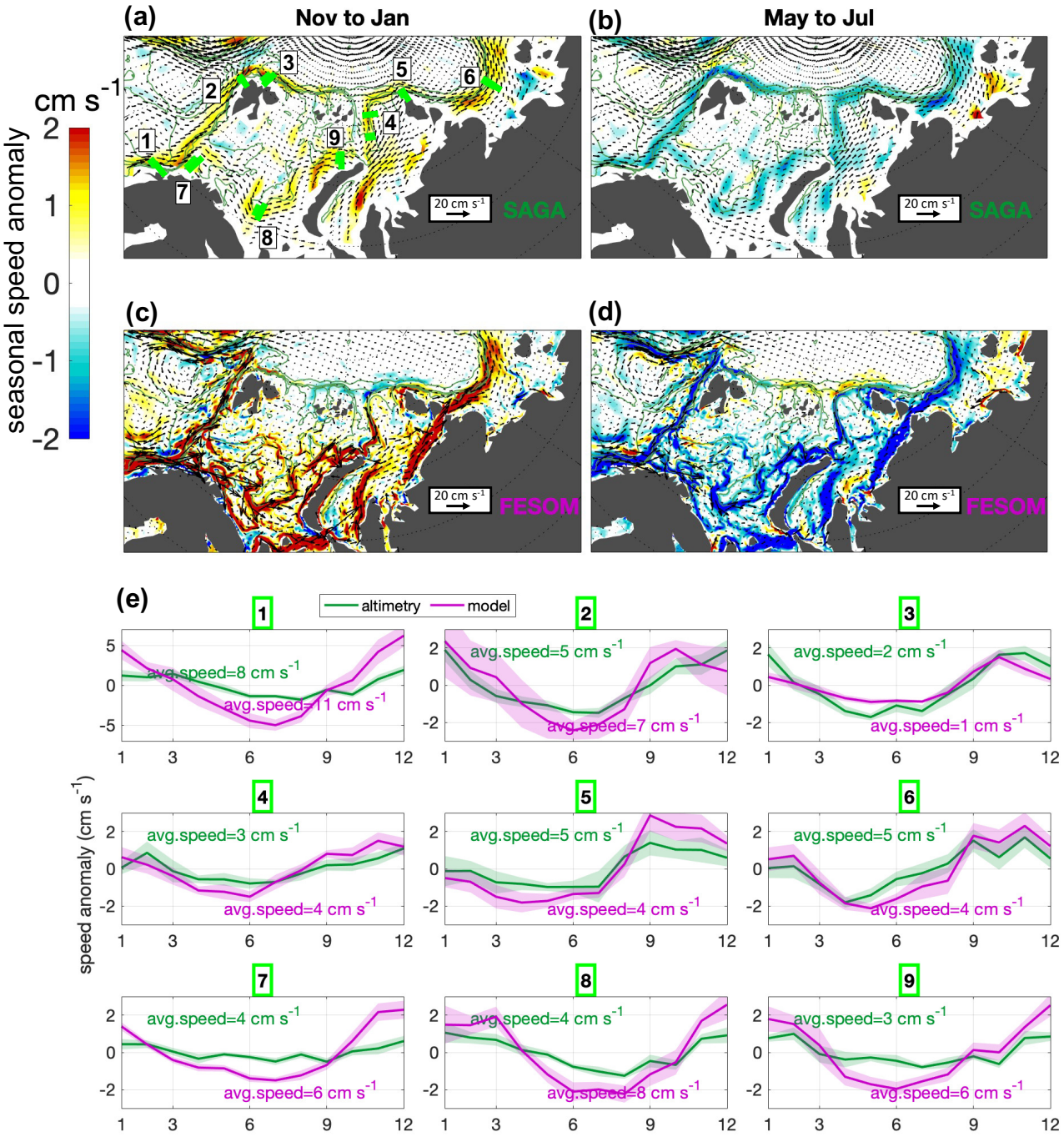

Figure 4.13. Zoom of Fig. 4.12 in the Eurasian Arctic, showing seasonally averaged geostrophic currents from SAGA (panels a and b) and FESOM (panels c and d) in winter (November to January, panels a and c) and summer (May to July, panels b and d). See Fig. 4.12 for explanation of vectors and colors. (e) Climatological mean speed anomaly (lines) and standard error (shading) in 2011-2020 at the transects indicated in panel (a) for SAGA (green line) and FESOM (violet line); long term average speed is written on each panel both for SAGA (green) and FESOM (violet). Bottom depth (green contours) is drawn at 300 m, 500 m, 1000 m, 2500 m.

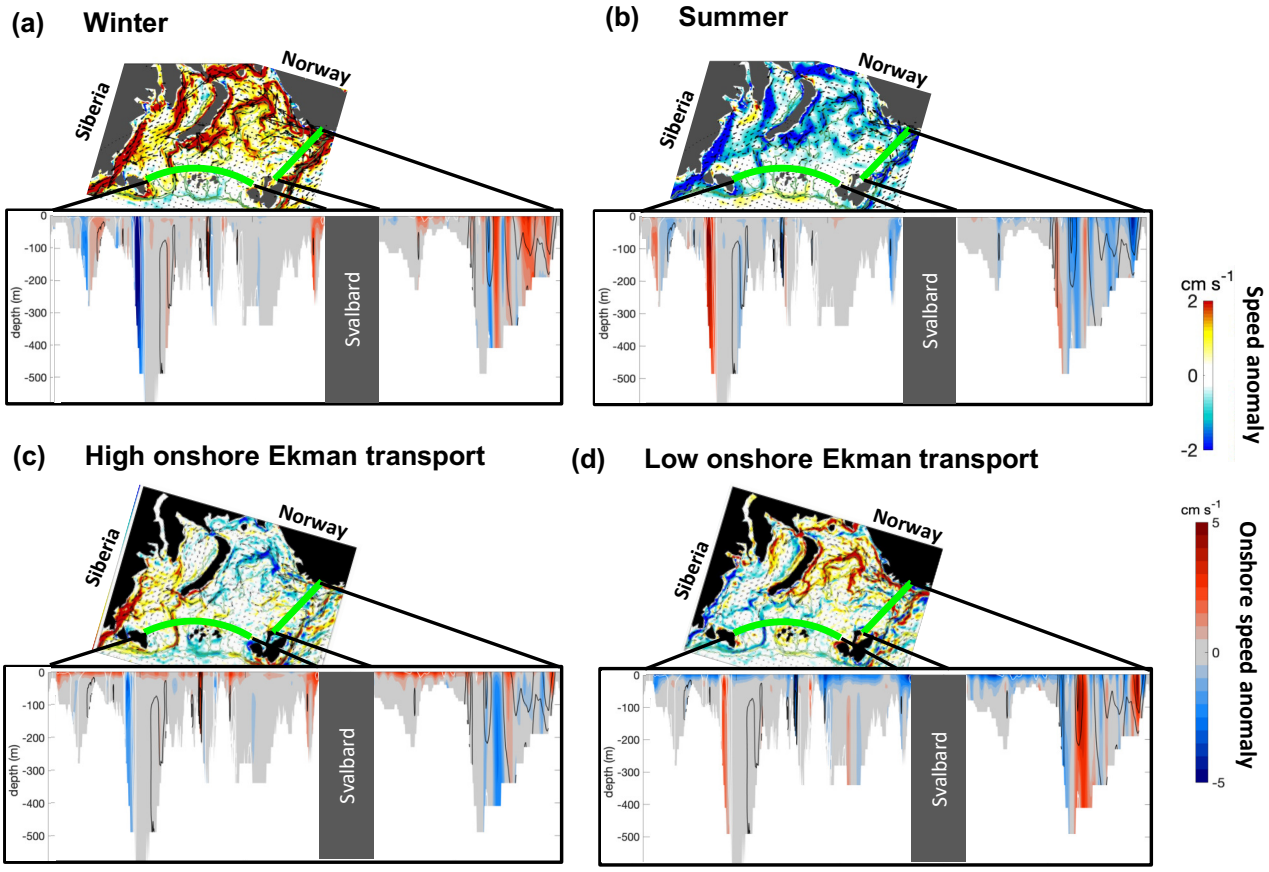

Figure 4.14. Overview on the surface and deep currents anomalies in the western Eurasian shelf from FESOM output. Panels (a) and (b) show seasonal anomalies whereas panels (c) and (d) anomalies averaged over months of high and low shoreward Ekman transport, respectively. Within each panel, the map represents the geostrophic field, whereas the vertical sections represent full ocean velocity. In panels (a) and (b) the geostrophic velocities are the same shown in Fig. 4.13a-b, while in panels (c) and (d) the vertical sections are the same shown in Fig. 4.9b-c

I similarly used a combined analysis of geostrophic current anomalies and sections of cross-slope velocity anomalies in periods of high and low shoreward Ekman transport (Fig. 4.14c-d) to try and reconcile the seasonal evolution of slope currents with Ekman-related cross-slope transport (identified in Sect. 4.2). I find that geostrophic anomalies, developed during periods of net onshore (offshore) Ekman transport (lower panels in Fig. 4.14c-d), tend to weaken (strengthen) the inflow through the BSO and a strengthen (weaken) the outflow through the SAT (upper panels in Fig. 4.14c-d). These anomalies agree well with the barotropic cross-slope velocity anomalies observed in Sect. 4.2, compensating at depth the surface Ekman transport. The residual ocean mass anomalies on the shelf, resulting from the net full-depth transport, arrange along isobaths. The adjustment of geostrophic currents to these mass anomalies finally generates coherent large-scale speed anomalies in the slope current system both at the rim of the shelf seas and across the Barents and Kara seas (Fig. 4.14a-b). One unresolved question is what is the mechanism by which shelf ocean mass anomalies organise following the bottom topography across the entire Eurasian shelf. This aspect is further discussed in Sect. 4.4.

4.3.2 Mass- and density-related seasonal speed anomalies

Seasonal velocity sections analysed in the previous section (Fig. 4.14a-b) show that the seasonal speed anomalies at the BSO and SAT, despite being consistent in sign, are surface-intensified in the first region and deep-intensified in the second one. This suggests that, on a seasonal time scale, density-related speed anomalies locally superimpose to large-scale mass-related anomalies. In this Section I use FESOM output to

analyse the spatial distribution of mass- and density-related seasonal geostrophic anomalies (computed from mass-related and steric sea surface height as explained in Sect. 2.8).

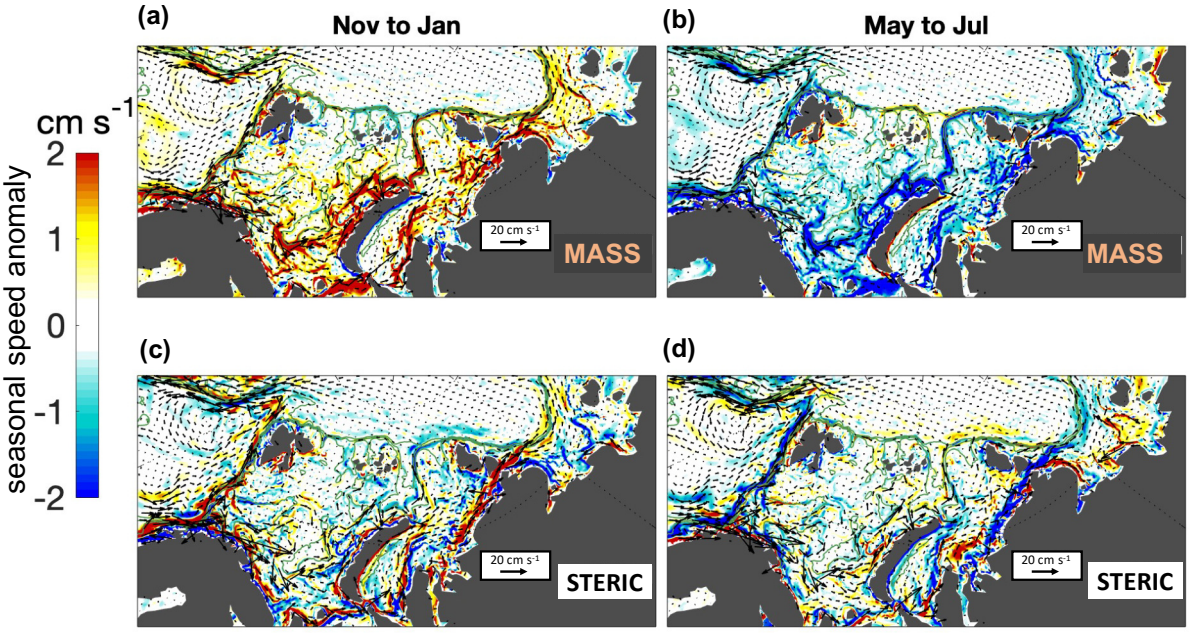

Figure 4.15. Zoom in the Eurasian Arctic showing seasonally averaged geostrophic currents associated to mass-related changes in sea surface height (upper panels) and steric changes (lower panels). All results are obtained from FESOM output. Results are displayed for winter (November to January, panels (a) and (c)) and summer (May to July, panels (b) and (d)).See Fig 4.12 for explanation of vectors and colors. Bottom depth (green contours) is drawn at 300 m, 500 m, 1000 m, 2500 m.

While mass-driven geostrophic speed anomalies are consistently positive in winter (negative in summer) over the entire Eurasian Arctic (Fig. 4.15a-b), density-driven geostrophic speed anomalies are less consistent both in terms of sign and of continuity along the slope current pathways (Fig. 4.15b-c). The spatial coherence of mass-related speed anomalies is in agreement with results in Sect. 4.2, where I found that mass-related changes in sea surface height dominate the large-scale pattern of seasonal variability. Accordingly, mass-related speed anomalies have a sign that is almost everywhere in agreement with the large-scale total seasonal speed anomalies (Fig. 4.13a-b). Specifically, they contribute the most to accelerate currents crossing the Barents and Kara Seas, in agreement with satellite-based results derived from ocean bottom pressure fields by Peralta-Ferriz and Morison (2010). On the contrary, density-driven speed anomalies only affect currents within confined regions, e.g. along the western Barents Sea continental slope and at the eastern Kara Sea coast (east of the Ob and Yenisei rivers). In these two regions, the density of waters transported by the boundary current decreases throughout the summer, thereby intensifying the baroclinic component of the current. The intensification of the baroclinic component throughout the summer season leads then to a peak in current speed in early winter. For instance, at the continental slope between the Nordic Seas and the Barents Sea, a decrease in density close to the shelf break throughout the summer is due to a warming of the Atlantic Water core relative to winter (von Appen et al., 2016). In the Kara Sea, the proportion of fresh river runoff transported within the boundary current increases in the months following the seasonal river discharge (May-July), resulting in a peak in current speed between November and January (Janout et al., 2015).

The above analysis indicates that, while mass-related geostrophic speed anomalies dominate the large-scale character of the slope current system seasonality, density-related anomalies are appreciable only within confined regions. The continental slope north of the Laptev Sea is one of the few regions where mass- and density-related variability seem to contribute equally to the total variability. This region is relatively

complex both from a hydrological and a dynamical point of view. Here, water masses of Atlantic origin encounter fresh shelf water (Janout et al., 2015; Ruiz-Castillo et al., 2023). Furthermore, the horizontal structure of the flow is tightly linked to the bathymetry and the variability of its vertical structure has also been related to winds (Baumann et al., 2018). Warm and salty Atlantic water and fresh shelf waters are redirected from here either to cross the central Arctic or to circulate cyclonically along the continental slope towards the western Arctic (Proshutinsky et al., 2015; Bertosio et al., 2022). It is therefore of interest to deepen our understanding of the currents' structure in this region and the processes that drive their variability. In the next section I therefore use FESOM model fields to describe more in detail the vertical and horizontal structure of the velocity field at the Laptev Sea continental slope. This structure is then put in relation with the density field and the cross-slope profile of mass-related and density-related geostrophic anomalies.

4.3.3 Vertical structure of along slope currents at the Laptev Sea shelf break

In the last twenty years the Laptev Sea continental slope has been relatively well-observed, with a considerable pool of in-situ observations provided in the framework of the NABOS program (Pnyushkov and Polyakov, 2022). Previous results based on these observations allow for the assessment of FESOM simulated currents and hydrography across the Laptev Sea continental slope. In the following I describe results based on FESOM simulations, whose plausibility will be discussed later in Sect. 4.4.4.

FESOM cross-slope sections of density resemble the well know stratified vertical structure present across the Arctic (introduced in chapter 1), with a fresh surface layer separated from a dense deep layer of Atlantic-origin waters by a steep pycnocline (Fig. 4.16). Surface water is generally fresher on the shelf side, with a horizontal gradient towards the basin, suggesting that part of the fresh surface layer is formed by shelf waters spreading seasonally towards the basin. Currents are directed eastward over most of the slope, with the strongest velocities close to the shelf break, between 77°N and 77.5°N. Fig 4.16 shows two velocity cores below about 50 m, centered around 77.3°N (close to the shelfbreak) and 77.7°N (offshore, above the lower slope). The offshore core is deeper and weaker than the one close to the shelfbreak, and they both reach down to about 1000-1500 m (not shown). In the top 30 m, an additional core located within the surface mixed layer is visible in the FESOM output (hereafter referred to as the surface core). This has a maximum above the shelf break core, but laterally extends far onto the shelf and into the deep basin. A velocity minimum separating the surface core from the deeper cores can be partly attributed to horizontal density gradients through the thermal wind relation. For instance, the deep current cores are weakened up until 50 m by downward sloping isopycnals below that depth (isolines deepen going offshore, to level out north of 78°N). Instead, in the upper part of the water column isopycnals are shoaling going offshore (isolines originate at the shelf bottom and outcrop offshore). The upward sloping isopycnals cause a strengthening of the currents from 50 m towards the surface, with a maximum in the surface core.

All the above described cores are visible both in winter and summer. The seasonality of the surface core seems to be partially independent from the deeper ones, with the deep ones maintaining high velocities throughout the winter and the surface one weakening after early winter. Velocities reach values above 10 cm s^{-1} in winter, while maximum velocities in summer are around 5 cm s^{-1}. The strong seasonal variability of velocity and density fields are in part related. The weakest currents occur in summer due to a strong stratification and a consequent flattening of the isopycnals at all depths. In the winter period instead, the mixed layer deepens, tilting the surface isopycnals to an almost horizontal density gradient between the fresh shelf waters and the denser basin waters. In the same period, dense Atlantic Water above the lower slope tend to get deeper, steepening the deep isopycnals towards the basin. This results in relatively high velocities both in the surface and the deep cores throughout winter. In addition to the density-related seasonal variability, a mass-related contribution might be present which can not be diagnosed through the density field. For instance, surface

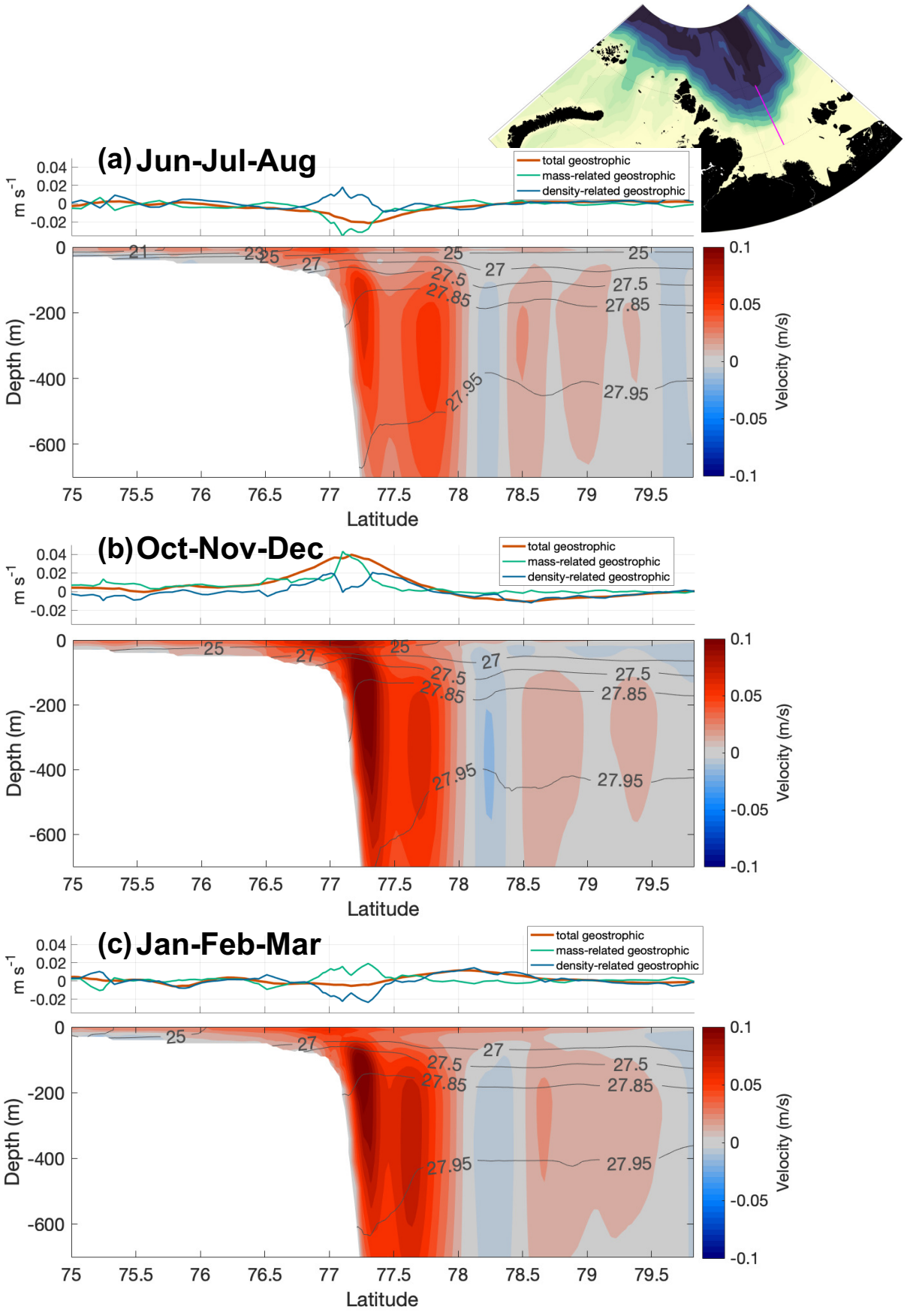

Figure 4.16. Along slope current and density structure at the Laptev Sea continental slope along the 126°E meridian. The lower panels in (a), (b) and (c) show vertical sections of full ocean velocity (colours) and density (black contours) for the periods Jun-July-August (panel (a)), October-November-December (panel (b)) and January-February-March (panel (c)). The upper graphs in panels (a), (b) and (c) show the along-section profile of geostrophic velocity anomaly in the three periods; full geostrophic anomaly (orange line), mass-related anomaly (green line) and density-related anomalies (blue line) are displayed. The reference map and transect for the sections and profiles is shown in the right top corner of the figure.

velocities are weaker in late winter with respect to early winter, despite the horizontal density gradients being still strong. To investigate the presence of a mass-related contribution, in the following I evaluate the relative contribution of mass-related and density-related geostrophic velocity anomaly along the meridional section.

I compare in Fig. 4.16 the cross-slope profiles of surface geostrophic currents and their components to the velocity sections. The strengthening of the total geostrophic velocity in early winter and weakening in late winter to summer corresponds well to the seasonality of the surface velocity core observed in the vertical sections. This suggests that, due to the steep sub-surface pycnocline, the geostrophic current variability at this geographical location is likely representative of changes happening in the upper 50-100 m. The mass-related contribution seems to dominate the peak of the geostrophic variability in early winter and in summer, driving a speed up of currents in first period and a slow down in the second. Consistently, currents are strengthened or weakened throughout the water column in these two periods. In the later winter period instead, the mass-related strengthening of the current at the shelf break is compensated by the density-related contribution at the shelf break. At the same time, a positive anomaly in the density-related anomaly appears at the offshore side of the slope. This distribution of the geostrophic anomaly well describe the variability of the surface velocity branch, showing a weaker core but being broader in late winter than in early winter. Overall, the geostrophic variability seems to be in agreement with changes in the surface velocity, and the analysis of the mass-related and density-related geostrophic anomalies allows to reveal the nature of these changes.

4.4 Discussion

The results in this chapter are based on altimetry and model data, which I have used to study the spatial consistency of the large-scale seasonal variability. Despite the advantage of providing a basin-scale view on the variability, these data sources either provide indirect remote measurements (altimetry), requiring long processing and correction, or do not necessarily represent the true field (model). In this section I therefore firstly discuss the limits of the approach and data used, and evaluate whether I find support from literature based on in-situ observations to the results herein (Sect. 4.4.1, 4.4.3 and 4.4.4). Furthermore, some results presented are limited either in terms of the spatial extent (Sect. 4.2.2) of the depth of analysis (Sect. 4.2.3). In the following I therefore also discuss how the results in this chapter apply to a broader spatial extent (Sect. 4.4.2) and whether they fit within a theoretical framework (Sect. 4.4.5).

4.4.1 Agreement and discrepancies between altimetry and model fields

The results presented in this chapter reveal a general agreement between the altimetry and the model data in terms of spatial patterns and seasonal evolution. This is visible for instance in the comparison of the area-averaged sea surface height climatology from SAGA and FESOM in Sect. 4.1.1 (Fig. 4.1). Past studies, assessing the robustness of model results by means of altimetry over various areas in the Arctic, have also found agreement despite differences in the amplitude of the variability (e.g., Müller et al., 2019b; Xiao et al., 2020; Athanase et al., 2021). Discrepancies in the amplitude of the sea surface height and current speed variability are found in the results of this chapter too. The surface height seasonal variability described in Sect. 4.1, although displaying consistent large scale patterns between SAGA and FESOM, has in some regions larger amplitude in FESOM than in SAGA, particularly in shallow shelf regions like the Laptev Sea and the East Siberian Sea. This is visible in the maps of seasonal cycle amplitude (Fig. 4.2a and b) and seasonal differences (Fig. 4.5a and b). How do these different amplitudes compare to in-situ measurements? In coastal areas, where SAGA displays sea surface height seasonal variations of about 5-7 cm, FESOM simulations exhibit variations of about 12-14 cm. From tide gauge data, Volkov and Pujol (2012) show that sea surface height standard deviation along the coast of Norway is about 6-7 cm, mostly associated with seasonal variability.

This translates into peak-to-peak seasonal variations of around 12-14 cm. While this amplitude is closer to the FESOM results, tide gauges are usually positioned very close to the coast and, therefore, not necessarily representative of the open ocean sea surface height variability. The discrepancy between the SAGA sea surface height variability and in-situ estimates is therefore maximum at tide gauges. The standard deviation of the SAGA sea surface height is instead closer to what observed by offshore moorings, presented in chapter 3.

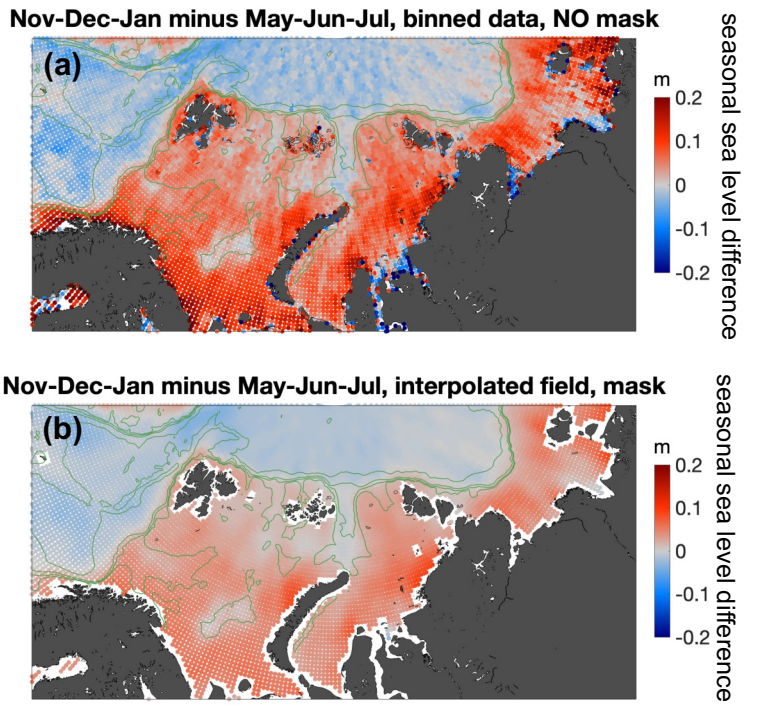

Figure 4.17. Comparison in spatial extent and amplitude of along-track satellite data versus interpolated satellite data. Average (a) interpolated sea level anomaly fields and (b) binned values of along-track sea level anomaly, in the months of November to January 2011-2020. Bottom depth (green contours) is drawn at 300 m, 500 m, 1000 m, 2500 m.

A partial suppression of sea surface height variability by SAGA can be attributed to the smoothing scale applied to the altimetry data in the gridded product (~50 km), which is large compared to the high resolution of the model (~4.5 km). Furthermore, along-track altimetry data within 10 km from the coast, where the variability is highest, have been masked in the SAGA dataset prior to interpolation (compare panels a and b in Fig. 4.17). This is necessary as the reflection of the satellite signal from land is high compared to the one from ocean and corrupts the sea surface height measurements there (e.g., Passaro et al., 2014). An assessment of how seasonal changes are underestimated due to the interpolation process can be obtained by comparing the interpolated fields (Fig. 4.17b) with along-track measurements binned over grid cells (Fig. 4.17a). Along most of the coastal and slope boundaries, the binned difference is generally 3-5 cm larger than the interpolated difference, getting up to 7-8 cm in the southeastern Barents Sea. Smoother sea surface height fields due to interpolation can also explain the low geostrophic current speed in SAGA compared to in-situ measured values (e.g., Fig. 3.10). For instance, west of Svalbard the cross-slope sea surface height difference increases from summer to winter 5 cm more in the binned fields than in the interpolated fields (Fig. 4.17). The suppression of sea surface height seasonal signal in the interpolated fields, when considered over the West Spitsbergen Current width of ~80 km (Beszczynska-Möller et al., 2012), results in a current slower by about 4-5 cm s^{-1}. This is consistent with the RMSD between SAGA and mooring velocity at this location (see Table 3.2 in chapter 3). However, the comparison in Fig. 4.17 also highlights the importance of the interpolation process. Patterns related to the geometry of the satellite tracks emerge in the binned field, suggesting that changes shown there could be biased by sub-monthly variability (see results in chapter 3, Sect. 3.1.3). Finally, discrepancies with the FESOM fields could also emerge due to uncertainty in the model output. For instance, the FESOM model is forced by reanalysis fields, which contain uncertainties that then propagates to the model output.

4.4.2 Shelf seas: coherent variability versus sub-regional patterns

Despite the difference in amplitude, both altimetry and model show a shelf-wide seasonal mode of variability in sea surface height and geostrophic currents. In Sect. 4.2.2 I've studied the possible link between this variability and wind forcing, specifically focusing on the western part of the Eurasian shelf (Barents and Kara Seas). The question remains open though whether wind patterns that force the variability in the western part of the shelf are the same that determine the shelf-wide variability. This will be discussed below based on previous literature.

In Sect 4.2.1, I associated the mass-related sea surface height seasonality in the western Eurasian shelves to the alternating influence of two large-scale wind patterns, the Beaufort High and the Icelandic Low, on the Arctic wind field (Fig. 4.7). These same atmospheric patterns are likely to directly force the eastern shelf as well, causing coherent variability across the entire shelf. The analysis in Sect. 4.2 of this thesis suggests that the mechanism by which these large-scale wind patterns generate a coherent sea surface height variability on the Eurasian shelves is by locally forcing cross-slope transport via Ekman dynamics. Results from previous studies also associate local transport variability in the BSO to large-scale wind patterns in the sub-polar North Atlantic and the Arctic. For instance, Ingvaldsen et al. (2004) found that persistent wide inflows through the BSO, detected via mooring data, are a manifestation of the northward extension of the Icelandic low. A model study by Heukamp et al. (2023) also found that the inflow and outflow variability through the BSO is affected both by the North Atlantic wind variability (reflecting the North Atlantic Oscillation) and by the Arctic wind field variability. Coherent shelf sea surface height variability on seasonal time scales is therefore in part determined by the large-scale character of the seasonal forcing. In addition to that, mass anomalies originated on the western part of the shelf propagate along the shelf guided by strong topographic gradients at the shelf break. The eastward propagation of wind-forced waves along the Arctic Eurasian shelf on short time scales has been demonstrated by Danielson et al. (2020) using in-situ data and modelling. While the waves analysed in Danielson et al. (2020) are short-lived events, associated to strong peaks in wind forcing, the period of waves and the resulting sea surface height fluctuation is dictated by the time-scale of their forcing. Therefore seasonal shelf mass anomalies persist as long as the anomalous wind is present, and sea surface height gradually adjusts over the entire shelf through eastward propagation.

Previous work suggests also that the variability in the western and eastern shelf seas might be partially decoupled. This has been particularly observed on time scales longer than one year. For instance, from tide gauge data Calafat et al. (2013) observed that the interannual sea surface height variability is highly coherent within areas either to the west or to the east of the Vilkitsky Strait, and less coherent across it. They attribute the variability on the western side to the integrated along-shore wind forcing at the Norwegian coast, and the one on the eastern side to changes in the vorticity of the wind field in the central Arctic. The partial decoupling of the eastern shelf variability from the rest of the shelf on interannual time scales has also been found using GRACE data. Peralta-Ferriz and Woodgate (2017) showed that positive sea level pressure anomalies in the central Arctic correlate well with negative mass anomalies in the East Siberian Sea, with the strongest correlation in summer. Additionally, Peralta-Ferriz et al. (2014) showed that a minor mode of variability in ocean mass (9% of variance) reveals a dipole of mass change with two centers of action on the shelf, east and west of the Vilkitsky Strait. More than one study suggest that the decoupling across the Vilkitsky Strait could be related to the occurrence of a low sea level pressure centered over the Laptev Sea. For instance, results by Peralta-Ferriz et al. (2014) indicated that a low pressure centre in this region would act to drive water mass from the Laptev Sea towards the deep basins and the Barents Sea. In agreement with that, Janout et al. (2015) acknowledged the role of a low sea level pressure centre over the Laptev Sea in blocking transport of river discharge from the Kara Sea to the Laptev Sea.

This also points to the fact that the availability and distribution of river runoff might contribute differently to the seasonal variability of sea surface height in the eastern and western Eurasian shelf. Fresh river water can affect both the mass-related and the density-related sea surface height seasonality. For instance, the annual cycle of river discharge has been proposed to explain a summertime peak in Arctic-average sea surface height and ocean mass (Peralta-Ferriz and Morison, 2010; Armitage et al., 2016). In my analysis of the regional mass-related climatologies (Fig. 4.3), I find in addition that this peak is present in the Laptev and Eastern Siberian Seas, but absent in the Barents Sea and Kara Sea. Furthermore, the analysis in Sect. 4.1.2 showed an influence of the fresh Ob-Yensey and Lena rivers runoff also on the seasonal steric height changes in the eastern shelf (Fig. 4.5d). This is visible across the Vilkitsky Strait and in the eastern shelf, where high steric height in winter with respect to early summer indicate the path of spreading of the freshwater plume in this direction. The distribution of the river fresh water is however subject to strong wind-driven interannual variability, as mentioned earlier. The control of the local wind variability over the redistribution of the Ob-Yensey and Lena River plume over different years has been documented by several studies through observations of the salinity field and from satellite imagery (Dmitrenko et al., 2008; Janout et al., 2015; Osadchiev et al., 2020).

In conclusion, while basin-scale wind patterns cause shelf wide coherent variability in the Eurasian sector, local mass- and density-related processes generate differences between the different shelf seas. In the following, I discuss whether the deep ocean response to onshore Ekman transport, found from the FESOM analysis, can be considered realistic.

4.4.3 Deep ocean response to Ekman onshore transport: observations

Observational evidence supports my FESOM-based findings (Sect. 4.2.2) on the relation between surface Ekman transport and flow response at depth. FESOM simulations indicate that anomalous net onshore Ekman transport triggers flow anomalies below the Ekman layer, which tend to compensate the surface transport (and are in in geostrophic balance; see Fig. 4.9b-c). Local geostrophic adjustment of the flow field to wind-driven Ekman transport was also deduced from mooring data in the BSO and in the SAT. Based on the analysis of 4-year-long current meter time series across the BSO, Ingvaldsen et al. (2004) found that geostrophic flow anomalies caused by the regional wind field in the BSO can persist for several weeks. Furthermore, based on a unique one-year-long time series of velocity (2009-2010) from a mooring deployed at the eastern slope of the SAT, Kirillov et al. (2012) found a correlation between the largely barotropic current velocities and the near-surface wind, with highest coefficients when southwesterly winds were considered. Further investigations on the SAT outflow by Dmitrenko et al. (2015) show that the barotropic response is dominant on time scales of days to weeks and the baroclinic response on time scales of months to years.

These mooring-based results, despite being in broad agreement with the finding in this work, describe the effect of local wind forcing on the deep flow. Here, I argue that a shelf-wide net onshore Ekman transport can shape the large-scale flow field. On a monthly basis, I found that a net positive onshore Ekman transport implies a weakening of the BSO inflow and strengthening of the SAT outflow (Fig. 4.14). On a seasonal time scale, however, the integrated increase in sea surface height on the shelf, and the large-scale adjustment of mass anomalies, results in a general strengthening of the geostrophic flow across the Barents and Kara Seas (Sect. 4.3.1). In support of this finding, model-based results by Lien et al. (2013) suggest that the wind-forced variability in the SAT is part of a large-scale wind-forced variability in the flow through the Barents Sea. An interesting outlook of the present work would be therefore to investigate the correlation between the shelf-wide net onshore Ekman transport and mooring-based measurements of flow at depth through the BSO and SAT.

4.4.4 Vertical flow structure at the Laptev Sea: observations

The ocean response discussed in the previous section represents barotropic, mass-related variability in the slope currents. This variability can be relatively easily interpreted based on the large scale wind field. In Sect. 4.3.2 I found though, by separating the mass-driven and density-driven geostrophic flow anomalies, that in some regions slope currents are rather modulated by density-related variability. The investigation of density-related variability requires a more in-depth knowledge of the local hydrography, which can be gained only via in-situ data. A region with a very complex hydrography whose variability contributes to seasonally modulate the slope current is the Laptev Sea continental slope. In Sect. 4.3.3 I used FESOM fields to interpret the seasonal changes of along-slope currents in this region, based on the vertical density structure and how it correlates with density-related and mass-related geostrophic anomalies. How do the results in Sect. 4.3.3 though compare to observation-based results?

Some insight into the vertical structure of the density field and current variability can be gained through a synthesis of observation-based studies. The vertical density structure at the Laptev Sea continental slope is characterised by a cold and fresh surface mixed layer, covering the upper 20-50 m, separated from water of Atlantic origin (below ~100-200 m) by a thick halocline layer (e.g. Baumann et al., 2018; Polyakov et al., 2020a; Pnyushkov et al., 2021). The FESOM density sections analysed in Sect. 4.3.3 (Fig. 4.16) agree quite well with this structure, with densities going from 24-26 kg m^{-3} in the surface layer to about 28 kg m^{-3} below 200 m. FESOM fields furthermore suggests that fresh water coming from the shelf is creating a density front (horizontal density gradient) in the surface layer, shifts further towards the basin in summer. This is in agreement with observations by Bauch et al. (2014), who found a frontal system between the Laptev Sea shelf and the Eurasian Basin in the upper water column (100 m).

The description of the along-slope velocity structure from observations is less clear. Currents are generally strongest close to the shelf break and weakest towards the interior of the basin (Polyakov et al., 2020b; Pnyushkov et al., 2021). Following Polyakov et al. (2020b), a 70 km-wide slope segment is occupied by the topographically steered boundary current, with maximum velocity larger than 10 cm s^{-1} at the shelf break. FESOM fields also display strong velocities at the shelf break, declining towards the basin. Observations suggest also that the current is composed by multiple cores. In a study combining modelling and NABOS in-situ data, Aksenov et al. (2011) describes three cores: a surface intensified core in the upper 200 m, very close to the shelf break (Arctic Shelf Break Branch); a weak and relatively deep core (750-1000 m), close to the intermediate slope (Barents Sea Branch); one core at intermediate depth (250-750 m) further offshore, above the lower continental slope (Fram Strait Branch). These three cores advect, respectively, halocline water formed in the Barents Sea northern shelf, Barents Sea deep water and Atlantic Water coming from the Fram Strait. While the Arctic Shelf Break Branch described by Aksenov et al. (2011) is surface intensified, the offshore Fram Strait Branch is sub-surface intensified, giving the current a baroclinic character documented by Pnyushkov et al. (2015). FESOM velocity sections also feature two cores below the halocline layer. The strongest, further onshore, can be identified with the Arctic Shelf Break Branch and the weakest and deepest, further offshore, correspond well with the Fram Strait Branch. In the surface layer, FESOM identifies a further velocity core. A vertical structure with a surface-intensified and a sub-surface intensified branch in this region has also been diagnosed using the NEMO model by Janout et al. (2015). Upstream of the Laptev Sea continental slope, their analysis tracked the surface-intensified branch back to the fresh near-surface Vilkitsky Strait Current, and the dense subsurface branch to the slope further west. Bauch et al. (2014)'s analysis further supports the existence of an eastward-directed surface velocity core at the shelf break, revealed by the distribution of fresh riverine waters and meltwater along the Laptev Sea continental slope.

A mooring-based analysis of the currents seasonality by Baumann et al. (2018) indicate that current speed close to the shelf break (south of 77.5°N) is generally higher in winter than in summer throughout the water

column, while it is not seasonally consistent in the lower part of the slope. They also suggest that the amplitude of seasonal changes is largest above 100 m and below 200 m, close to the shelf break. The seasonal evolution of the along-slope flow simulated by FESOM is also intensified in the surface layer and below the lower part of the halocline, with a layer of lower seasonal variability between 50 m and 100 m. Fig. 4.16 indicates that the variability below 50 m, within the halocline layer and the Atlantic Water layer, is coherent and partially decoupled from the variability in the surface layer. Pnyushkov et al. (2021) also found that mean currents in the halocline layer and Atlantic Water layer at the Laptev Sea continental slope are strongly coherent and generally aligned to isobaths, concluding that at annual temporal scales the flow is essentially barotropic. This description is supported by mooring-based results from the lower slope domain by Baumann et al. (2018), who identified barotropic pressure changes from the bottom up to about 60 m depth. Instead, less coherence of the variability below the halocline layer has been found with the surface flow variability (Pnyushkov et al., 2021) and with the wind speed variability at 10 m (Pnyushkov et al., 2015). Comparisons between FESOM sections of full ocean velocity and geostrophic velocity in Sect. 4.3.3, also suggested that geostrophic variability is most representative of the variability in the surface branch (upper 50 m). This could for instance explain why a comparison of altimetry- and mooring-based barotropic volume transports by Pnyushkov et al. (2021) showed that altimetry consistently overestimates mooring estimates for 30 months between 2008-2011. This mismatch could be related to a difference between depth-integrated velocities and altimetry-derived transport, due to the baroclinicity of the velocity field.

The variability of the surface and the deep branches is therefore likely driven by different mechanisms, related to the different origin of these branches upstream of the Laptev Sea (Janout et al., 2015). The separate origin of these branches, merging at the Laptev Sea continental slope, is also visible in the analysis of geostrophic currents from SAGA and FESOM in Sect. 4.3.2. Specifically, I show there that density-driven variability at the Laptev Sea continental slope is following from a branch coming from the shelf, through the Vilkitsky Strait (Fig. 4.15c-d), while mass-variability can be tracked to the continental slope west of the Laptev Sea (Fig. 4.15a-b). These different branches converge different water masses to the Laptev Sea continental slope. Indeed, baroclinic variability there is driven by lateral shifts of the front between shelf waters, slope waters and Atlantic Water from the basin Bauch et al. (2014); Baumann et al. (2018). For instance, lateral shifts in the Atlantic Water at seasonal and longer time scales have been suggested to derive from shelf convection accompanied by cascading (Pnyushkov et al., 2015). In their analysis of the Arctic Boundary current, Aksenov et al. (2011) conclude that the variability of the cyclonic boundary current in the Eurasian Arctic is primary following the variability of the flow through the St Anna Trough, in turn driven in the Barents Sea both through buoyancy loss and zonal pressure gradient induced via Ekman dynamics. They however also acknowledge the presence of cold surface waters from the Kara Sea continuing eastward through Vilkitsky Strait and then along the shelf break as the uppermost part of the shelfbreak branch.

The density and velocity structure described in Sect 4.3.3 is therefore plausible and supported both by observations and previous modelling studies. The presence of multiple velocity cores in the FESOM sections finds explanation from the literature in their different geographical origin and density. This furthermore justifies the apparent decoupling of the surface variability from the mid-depth and deep variability. This analysis also highlights how the study of mass- and density-related geostrophic velocity anomalies is a viable method to trace back the origin of local variability to the large-scale variability. A study of the nature of Arctic surface circulation solely based on satellite altimetry and gravimetry would be a compelling outlook of this work, provided increased satellite resolution is achieved in the Arctic (especially in terms of ocean mass equivalent height).

4.4.5 Depth-integrated vorticity balance

In Sect. 4.2.3 I introduced the depth-averaged vorticity equation (Eq. 2.27) in an effort to interpret the seasonality of sea surface height in the Eurasian shelves from a theoretical point of view. The analysis performed in Sect. 4.2.3 showed that the results in this thesis agree with a previous study by Volkov et al. (2013), used as a reference, but also highlighted that this approach is incomplete as it does not provide clear indication on what the sinks of vorticity are. Here, I propose an alternative form of the vorticity equation, the depth-integrated form, to treat more explicitly all terms contributing to the vorticity budget. I furthermore discuss whether the vorticity equation can serve as a reliable diagnostic to determine the spatial distribution of seasonal sea level change.

I start the derivation of the depth-integrated vorticity equation from the horizontal Navier-Stokes equation in the form:

$$\partial_t \mathbf{u} + \mathbf{v} \cdot \nabla_{\mathbf{3}} \mathbf{u} + \frac{\nabla p}{\rho_0} + \mathbf{f} \times \mathbf{u} = \partial_z \tau + \mathbf{a} \tag{4.1}$$

where $\mathbf{u} = (u, v)$ is the horizontal velocity, $\mathbf{v} = (\mathbf{u}, w)$ is the three-dimensional velocity, p the pressure, $\mathbf{f} = \mathbf{k} \cdot f$ the planetary vorticity, $\partial_z \tau$ is the vertical viscosity (parameterized as the vertical stress gradient) and $\mathbf{a}$ is the horizontal viscosity (both viscosities are already divided by ρ_0). By integrating vertically from the bottom (z = -H) to the surface (z = 0), with $\mathbf{U} = \int_{-H}^{0} \mathbf{u}\, dz$, we have:

$$\partial_t \mathbf{U} + \mathbf{B} + \frac{1}{\rho_0} \int_{-H}^{0} \nabla p\, dz + \mathbf{f} \times \mathbf{U} = \tau_{\mathbf{S}} - \tau_{\mathbf{B}} + \mathbf{A} \tag{4.2}$$

where $\mathbf{B} = \int_{-H}^{0} \mathbf{v} \cdot \nabla \mathbf{u}\, dz$ is the integrated non-linear term, $\mathbf{A} = \int_{-H}^{0} \mathbf{a}\, dz$ is the integrated horizontal viscosity, and $\tau_{\mathbf{S}}$ and $\tau_{\mathbf{B}}$ are respectively the stress at the ocean surface (wind stress) and at the ocean bottom. In order to be able to treat the pressure term at a later stage, we re-write it as:

$$\int_{-H}^{0} \nabla p\, dz = \nabla \int_{-H}^{0} p\, dz - p_B \cdot \nabla H \tag{4.3}$$

and substitute this in Eq. 4.2. We derive the z-component of the depth-integrated vorticity equation by taking the curl of Eq. 4.2:

$$\partial_t Z + \nabla \times \mathbf{B} - \frac{1}{\rho_0} \nabla \times (p_B \nabla H) + f \nabla \cdot \mathbf{U} + \mathbf{U} \cdot \nabla f = \nabla \times (\tau_{\mathbf{S}} - \tau_{\mathbf{B}}) + \nabla \times \mathbf{A} \tag{4.4}$$

where $Z = \partial_x V - \partial_y U$ is the depth-integrated relative vorticity. The terms in the above equation represent, from left to right, (1) changes in the depth-integrated relative vorticity, (2) the curl of non-linear stresses, (3) the bottom pressure torque (arising from changes in pressure along isobaths), (4) the divergence of the depth-integrated velocity, (5) the advection of planetary vorticity, (6) the difference between the wind stress curl and the bottom stress curl, (7) the curl of horizontal viscous stresses.

We can apply Eq. 4.4 to the Arctic Eurasian shelves by considering some approximations. For the Arctic domain, one can neglect: (i) changes in the depth-integrated relative vorticity, which will be small when averaged over a large area including the shelf and slopes; (ii) the curl of non-linear stresses, considering a linear approximation; (iii) the advection of planetary vorticity, as the gradient of the Coriolis parameter f is small at high latitudes. In order to introduce sea level changes into Eq. 4.4, based on Eq. 2.12 I can substitute $\nabla \cdot \mathbf{U} = -\partial_t \eta$, relating a divergent flow to sea level decrease. I am finally left with the following equation:

$$-f \partial_t \eta = \frac{1}{\rho_0} \nabla \times (p_B \nabla H) + \nabla \times (\tau_{\mathbf{S}} - \tau_{\mathbf{B}}) + \nabla \times \mathbf{A} \tag{4.5}$$

Eq. 4.5 is a form of the vorticity equation that explicitly expresses sea level changes in terms of possible sources and sinks of vorticity. While this similar to the method used by Volkov et al. (2013) (see Eq. 2.27), the above derivation differs from their approach under few aspects. Firstly, I provide theoretical arguments to neglect changes in sea surface height due to variation in relative vorticity and to the meridional advection of planetary vorticity (in addition to having previously proved that these terms are indeed negligible, see Fig. 4.11). Secondly, deriving the equation in a depth-integrated rather than depth-averaged form simplifies the treatment of the pressure gradient term, allowing the inclusion of the bottom pressure torque in the final equation. Finally, I provide explicit meaning to four terms that were instead collectively represented by a single dissipation term in Volkov et al. (2013). These are: (1) the torque due to non-linear processes, (2) the bottom pressure torque, (3) bottom stress torque and (4) the torque due to horizontal viscous stresses.

Provided that the wind stress curl represents the vorticity input term, and that the sea surface height variations are the object of investigation in this thesis, it is worth discussing here the role of the remaining three terms in Eq. 4.5. A form of the vorticity equation similar to Eq. 4.5 was derived and analysed by Hughes and de Cuevas (2001) and by Isachsen et al. (2003). In the first study, Hughes and de Cuevas (2001) evaluate 4-year average spatial distribution of each term for the global ocean (between 80°S and 80°N) using the Ocean Circulation and Climate Advanced Modelling project model (OCCAM). Isachsen et al. (2003) instead analysed area-averaged time series of the vorticity equation terms in the Norwegian Basin. Both of these studies identify the wind stress curl as largest positive term, source of vorticity. From the average spatial distribution, Hughes and de Cuevas (2001) shows that bottom stress curl is a first order vorticity sink most in shallow areas, where the surface and bottom stress directly compensate given the proximity of the ocean surface to the bottom (with the bottom stress curl being equal to the wind stress curl at the coastal limit). Results by by Hughes and de Cuevas (2001) show large residuals between wind and bottom stress curl in the global ocean largest basins, away from the coasts, but also closer to coastal boundaries in regional seas, including the Arctic Ocean. In the subtropical regions, these residuals appear to be compensated in large part via the advection of planetary vorticity. This vorticity sink becomes instead negligible north of 60°N, where the relatively large residuals close to coastal boundaries are compensated via the bottom pressure torque. The analysis by Isachsen et al. (2003), who looked at temporal variations of the vorticity equation terms averaged over the Norwegian Basin, presents a slightly different picture. Wind stress input appears to be mainly balanced by horizontal viscous stress torque, with the bottom stress torque playing a minor role and the bottom pressure torque being negligible. These findings can though be reconciled with those by Hughes and de Cuevas (2001) by considering the specific geography of the Norwegian Basin and the area-averaged analysis carried out by Isachsen et al. (2003). Firstly, the bottom stress torque plays a minor role in deep basins than in shallow areas. Secondly, the bottom pressure torque becomes small when integrated around a closed depth contour. Therefore it appears that the largest compensation of wind stress curl in the Norwegian Basin happens via the torque generated by the strong horizontal velocity shear between the basin interior and the slopes and, to a less extent, via the bottom stress.

Based on the results from previous studies presented above, I discuss below (i) whether it is possible to use the vorticity equation to diagnose the spatial distribution of seasonal sea level change, and furthermore (ii) if this equation can provide insight into the mechanisms that regulate this variability. In the western Eurasian shelf, I can assume that the main balance in areas of flat bottom topography is between the surface and the bottom stress curl, as shown in the second panel of Fig. 4 in Hughes and de Cuevas (2001). The same figure though also shows that the residual between these two terms is not negligible along the Norwegian coast and north of Novaya Zemlya, close to the St. Anna Trough. These residuals are compensated by the bottom pressure torque, as shown in the fourth panel of their Fig. 4. Having identified the dominant contributions to the vorticity balance in the surface and bottom stress curl and the bottom pressure torque, one can use these to interpret ocean response to wind forcing identified in Sect. 4.2.2. The wind stress torque seasonally accumulates mass over the shelves. A non-homogeneous anomaly in the distribution of the water mass sets

up a geostrophic flow anomaly, i.e. a flow perpendicular to the pressure gradient. Therefore bottom friction is required to export the mass via bottom stress torque. This discussion points to the fact that the divergence of the depth-integrated velocity (i.e., the sea surface height variability) is generally found to be a minor term in the barotropic vorticity balance. I also showed in Sect. 4.2.2 that sea surface height variability results from a tiny residual between wind forcing and a compensating process. This indicates that, to estimate the sea level variability via the vorticity balance, all terms in Eq. 4.5 must be known with precision. It therefore remains an open question whether this equation can be used to provide a reliable diagnostic of sea level variability.

4.5 Summary

The research laid out in this chapter provided a description of the seasonal slope current variability in the Arctic by mean of altimetry and model data, connecting that to the shelf sea surface height variability. SAGA and FESOM presented a consistent large-scale variability of the slope currents on the seasonal time scale, which was attributed to wind-forced mass variability. The central finding of this chapter is that cross-slope ocean mass transport via Ekman dynamics, almost perfectly compensated via a return flow at depth, when integrated on the seasonal time scale to generate net positive ocean mass anomalies on the shelves in winter. These anomalies are therefore a tiny residual of the large seasonal exchange flows between the shelf and the open ocean. Positive mass-related sea surface height anomalies on the shelf strengthen in turn the large-scale slope current system. The results presented here are in agreement with previous research based on in-situ data. In an attempt to provide a theoretical framework to the processes involved in the shelf-basin exchange flow, I examined the shelf sea surface height budget based on the vorticity equation following the method by Volkov et al. (2013). I find though that the approach used by Volkov et al. (2013) is not completely explicit in terms of inclusion of sea surface height changes in the equation and in diagnosing the vorticity dissipation terms. Therefore I propose an alternative treatment of the vorticity equation, and discuss whether the vorticity equation is at all reliable as diagnostic to determine the spatial distribution of the seasonal sea level change.

Chapter 5

Conclusions and outlook

In this thesis I explored the current capability of satellite altimetry to observe the sea level and slope current variability in the Arctic Ocean. I furthermore used satellite data in combination with model simulations to understand the dynamics underlying this variability on the seasonal time scale. The first phase of the project was dedicated to the technical development of a pan-Arctic gridded data product of sea surface height and geostrophic currents, and its validation across the Arctic. Besides publishing a quality-controlled dataset, this part of the work revealed information on the sea level and ocean circulation variability in different areas of the Arctic, furthermore indicating how remote sensing estimates compare to in-situ ones. In the second phase of this thesis, I applied the developed satellite dataset to study the large-scale patterns of seasonal sea level variability in the Arctic, and how these are related to the slope current seasonality. I specifically focused on the Eurasian part of the Arctic, where I investigated the large-scale, coherent seasonal patterns in slope currents, the associated sea surface height patterns and the factors that influence this variability.

In the following I synthesize results from Chapters 2, 3 and 4, to answer step by step the three main research questions guiding this thesis.

Research question 1: ***What is the state of the art of satellite altimetry for the Arctic Ocean, in particular regarding gridded, multi-year datasets in the ice-covered ocean?***

A major effort in the first phase of my project involved generating a new dataset of Arctic-wide gridded sea surface height and geostrophic velocity at monthly resolution (**Chapter 2**), referred to as Sea level Anomaly and Geostrophic velocity of the Arctic ocean (SAGA). This dataset covers the entire Arctic over a time span of 10 years (2011-2020), and is based on data from the CryoSat-2 mission, the satellite altimetry mission that has to date flown over the Arctic Ocean for the longest period (since late 2010) and to the northernmost latitude (88°N). CryoSat-2 based estimates of sea surface height from ice-free areas (Scharroo et al., 2013) and ice-covered areas (Hendricks et al., 2021) have been quality-controlled and homogenised in terms of cross-ice-edge biases and corrections for high-frequency variability (ocean tides, effect of atmospheric pressure and wind forcing). Along-track data have finally been gridded on a latitude-longitude grid, yielding monthly mean sea surface height in the period 2011-2020. Geostrophic velocities have been calculated from sea surface height. Both sea surface height and geostrophic velocities have been evaluated in the ice-covered Arctic by comparison with in-situ data. Sea surface height is compared to in-situ based estimates of steric plus mass variability (from temperature, salinity and ocean bottom pressure observations), whereas geostrophic velocity fields are compared to near-surface mooring velocity (**Chapter 3**). The open-access publication of the SAGA dataset (Doglioni et al., 2021, 2023) represents a significant achievement in the PhD work, as it provides the

international scientific community with a novel, quality-controlled gridded dataset to study basin-wide Arctic sea level and surface circulation changes over the time span of a decade (2011-2020).

The analysis and processing of along-track data prior to gridding (**Chapter 2**) provided information on the high frequency variability of sea surface height in the Arctic Ocean, and how this affects the monthly gridded product. I found that high-frequency processes, like ocean tides and the response of the ocean to atmospheric pressure and wind changes on these time scales, contribute to up to 50% of the standard deviation of sea surface height, particularly in some regions like the East Siberian Sea (Sect. 3.1). This variability is however under-sampled by the satellite tracks, and therefore not fully resolved. Even after correcting for these processes, residual large-scale (several hundred km, see Fig. 3.4) short-term (1-2 weeks, Fig. 2.4) oscillations introduce noise in the monthly satellite estimates. Therefore, an additional approach to reduce the residual variability was used in phase of gridding (Sect. 2.5.2.1). First weekly subsets of data were gridded, and then monthly estimates were computed at each grid point as the average of four following weekly values. This approach, as any other attempting to reduce the noise due to high-frequency variability, resulted in a trade off between resolving spatial and temporal variability and providing an accurate estimate of those. Comparisons with mooring data showed that, while correlation coefficients between remote and in-situ monthly averages is relatively good, the amplitude of the signal is under estimated in the former with respect to the latter.

The evaluation of the SAGA datset is found in **Chapter 3**. The dataset was firstly tested in terms of robustness of the methodology by evaluating the correlation with the independently-derived satellite dataset from the Centre of Polar Observation and Modelling (CPOM) over the entire Arctic. The SAGA and CPOM sea surface height fields exhibits high correlation on a monthly basis. The correlation between datasets is higher than 0.7 over 85% of the domain, including most ice-covered regions. This result shows that the variability observed by two independently-derived satellite products is consistent despite differences in the data processing (e.g., treatment of ice-ocean biases, corrections, gridding). Still, local differences between the SAGA and the CPOM datasets helped identify weaknesses in the altimetry techniques for oceanography in the Arctic. One relevant issue is the correction of unresolved sub-monthly variability, which is to date not well established for the Arctic (e.g. tides, response to remote forcing by wind and atmospheric pressure, commonly known as dynamic atmosphere correction). The results of the comparison between the SAGA and CPOM datasets show that using different approaches to correct for this variability can lead to mismatching amplitudes and locally reduced correlation between datasets.

Secondly, few aspects of the SAGA dataset were evaluated by comparison to in-situ data. The large-scale, mean spatial distribution of the SAGA sea surface height was compared to hydrographic profiles in the ice-covered deep basins (Fig. 3.9). While the mean field underlying the SAGA sea surface height was reconstructed starting from an independent auxiliary product (the DTU Mean Dynamic Topography, see Sect. 2.2), this was then integrated with 10 years of additional sea level anomaly data, processed furthermore following different approaches in ice-covered and ice-free regions. A comparison with in-situ data was therefore necessary to demonstrate that the SAGA dataset is still based on a reasonable mean spatial distribution. Remote and in-situ measurements have correlation coefficient of C = 0.97, a value consistent with previous studies (e.g., Kwok and Morison, 2011; Mizobata et al., 2016). This result mainly reflects a good representation, in the SAGA dataset, of the large-scale gradient in sea surface height across the central Arctic between the dome in the Canada Basin and the minimum in the Eurasian Basin. The robustness of the spatial variability was additionally evaluated on smaller scales in the Fram Strait, a year-round transition zone between ice-covered areas in the west and ice-free areas in the east. The comparison there is relevant to evaluate the accuracy and continuity of the satellite fields across the ice edge, which represents a particularly strong challenge. The SAGA sea surface height fields for two summer months are evaluated against hydrographic sections across the Fram Strait (Fig. 3.8). There, I showed that in the Fram Strait the processing applied to homogenise the datasets in ice-covered and ice-free areas preserves the sea surface height gradient associated

with the East Greenland Current. Additionally, I found that the agreement between the SAGA sea surface height monthly fields and in-situ data holds down to spatial scales of about 50 km.

In order to provide an evaluation of the robustness of the monthly estimates, I assessed the temporal variability of both sea surface height and geostrophic velocity via comparison to mooring-based time series in the Eurasian Arctic, in the Canada Basin and in the eastern Chukchi Sea. Sea surface height shows reasonable agreement with in-situ steric height plus bottom pressure equivalent height at all comparison locations, with correlation coefficients larger than 0.5 (p-value lower than 0.06). The RMSD between 2 cm and 5 cm, mostly associated to differences on monthly time scales, indicates that short-term mesoscale variability, strongly affecting the in-situ measurements, is not resolved by the SAGA dataset. This is inherent to the different nature of in-situ and remote measurements, which leads to a trade off between accurate representation of the spatial and temporal variability in the satellite dataset in phase of interpolation. On time scales longer than one month, I found that altimetry and in-situ sea surface height time series provide a consistent picture of the variations in the temporal variability across different geographical locations. Both in-situ and altimetry data suggest that the sea surface height variability is dominated by the seasonal cycle in the Eurasian Arctic, while it contains stronger month-to-month and interannual variability in the Canada Basin.

Finally, the comparison of geostrophic velocity against near-surface velocity from moorings aimed at evaluating the geostrophic fields and establishing whether slope currents can be resolved and, if so, over which spatial and temporal scales. Results from the comparison in different regions showed that the agreement varies depending on the underlying dynamical regime. Namely, the pointwise correlation coefficients between time series at monthly resolution are larger than 0.3 and are significant in regions where in-situ mean currents are stronger than about 4 cm s^{-1} and dominate the mesoscale variability. These conditions are generally met in the core, non-eddying part of slope currents. The temporal and spatial scales at which the SAGA datasets resolves slope currents were evaluated by comparison with data at at two mooring arrays along the continental slope of the Eurasian Arctic Correlation coefficients are higher when data are averaged over 50-60 km across the slope current and intra-seasonal frequencies are removed (Table 3.3). The comparison also highlights systematic underestimation of the current speed in the SAGA altimetry product. The discussion in Sect. 4.4.1 showed that slower current speed can be attributed to smoothing of the sea surface height gradients in the gridding phase. In synthesis, results from the first part of this work therefore indicate that the SAGA dataset is able to resolve seasonal and longer temporal variability in the Arctic sea surface height and geostrophic velocity.

The assessment of the SAGA dataset against in-situ data contributed to evaluate the potentiality of single-mission satellite altimetry datasets for the study of sea level and surface circulation in the Arctic Ocean. From the evaluation against in-situ measurements, it emerges that the correlation varies depending on the spatial and temporal scales considered, due to the different nature of these two data sources. In particular, the SAGA dataset proved to be suitable to gain a deeper understanding of the dominant Arctic seasonal signal. Results from Chapter 3 highlighted that the seasonal cycle is a major contribution to the variability of the sea surface height and surface geostrophic circulation over large parts of the Arctic Ocean. This is visible both from the pointwise evaluation of the SAGA dataset (e.g., Figures 3.8, 3.10 and 3.11) and from the assessment of seasonal spatial patterns based on the SAGA fields (e.g., Fig. 3.13). An increase in the resolution of altimetry in the Arctic Ocean is to be expected in the near future, as more satellite missions become available for polar latitudes (ICEsat-2, SWOT, CRISTAL), and the development of new techniques to detect the sea surface within leads, or even across the ice edge, are developed (e.g., Ricker et al., 2014; Passaro et al., 2018; Poisson et al., 2018). Altimetry products are therefore likely to become more accessible for the investigation of the Arctic Ocean circulation, and serve science where gaps in in-situ data limit our understanding (Witze, 2022).

A deeper understanding of the seasonality of Arctic slope currents is essential to study interannual and long-term changes in the Arctic-Subarctic exchange of heat and fresh water and in the transport of different

water masses across the Arctic Ocean, happening via these oceanic routes. While traditionally the seasonality of slope currents has been studied at separate locations by mean of mooring data (e.g., Beszczynska-Möller et al., 2012; Pnyushkov et al., 2015; Pérez Hernández et al., 2019; Ruiz-Castillo et al., 2023), the strong seasonal signal often masks variability on longer time scales, especially in short and pointwise in-situ time series. Strong seasonal biases can prevent the integration of in-situ data, and therefore the correct interpretation of the interannual and longer variability. Recent studies of the Arctic surface circulation and its drivers based on satellite altimetry suggest that satellite data could be used also to study the slope currents variability (e.g., Armitage et al., 2018; Morison et al., 2021). It was shown in Chapter 3 that the SAGA dataset is able to resolve the large-scale seasonal patterns of the relatively narrow Arctic slope current system. In **Chapter 4**, I utilized the SAGA dataset to describe the large-scale seasonal patterns of the geostrophic surface currents and their associated sea surface height patterns. I then used a synergy of altimetry data and model simulations to study the contributions to this variability (mass- or density-driven) in different parts of the Arctic, thereby assigning its possible drivers.

Research question 2: ***Is there a large-scale coherence in the sea surface height and slope current seasonality, and is the nature of this variability related to mass or steric changes?***

The seasonal cycle of the Arctic surface geostrophic circulation features large-scale, coherent patterns, identifiable both from the altimetry and model fields. Current speeds strengthen in winter and weaken in summer along the Arctic continental slopes. This indicates a large-scale coherent strengthening and weakening of the slope currents on a seasonal basis. The existence of a large-scale coherence in the slope current seasonality is furthermore supported by the comparison with mooring data from the Fram Strait and the Laptev Sea continental slope in Chapter 3. The associated sea surface height in winter is characterised by positive anomalies shoreward of the continental slopes (on the shelf seas) and negative anomaly offshore (basins in the central Arctic and in the Nordic Seas). Area-averaged climatologies of the sea surface height fields, as well as annual harmonic analysis applied to each grid point, delineate a seasonal cycle with a relatively smooth harmonic evolution, and a delay and amplification of the seasonal peak on the Eurasian shelf with respect to the neighbouring basins. This decoupling in the seasonality across the continental slope modifies the cross-slope sea surface height gradient, thereby modulating the geostrophic currents along the slope current system.

The separation of the simulated sea surface height fields into their mass-driven and density-driven contributions allowed to disentangle the patterns related to wind-driven ocean mass transport from those related to buoyancy changes in the water column. I found that, on the seasonal time scale, the mass-related contribution determines the large-scale patterns, whereas the density-related contribution mostly affects confined spatial patterns. The pattern generated by the mass-related variability consists of out-of-phase sea surface height anomalies between the Eurasian shelf and the neighbouring basins. These anomalies are ultimately responsible for the coherent strengthening and weakening of the geostrophic currents, on a seasonal basis, along the entire Eurasian continental slope. The seasonality of the slope current system in the Eurasian Arctic is therefore correlated across extensive distances, driven by oscillations resulting from the exchange of water mass between the peripheral shelf seas and the central basins.

Research question 3: ***Can we infer drivers of the Arctic slope currents seasonality by investigating the mass-related and density-related sea surface height seasonal changes?***

Results from previous studies suggest that accumulation and retreat of water mass from the shelves could be driven by winds on intra-seasonal time scales (e.g., Volkov and Landerer, 2013; Peralta-Ferriz et al., 2014; Armitage et al., 2016). In the second part of **Chapter 4** I therefore investigated whether the shelf-basin decoupling pattern observed in the seasonal mass-related sea surface height changes can be explained by the regional wind field variability.

A qualitative assessment of the wind stress seasonal composites shows that the large-scale wind forcing is compatible with onshore Ekman transport in winter and offshore transport in summer. However, a quantitative evaluation reveals that the average shelf sea surface height change due to water mass transported onto the shelf seas via Ekman transport is one order of magnitude larger than the observed mass-related sea surface height seasonal changes. This result indicates that Ekman transport at the surface might drive a compensatory response at depth. From the analysis of simulated ocean velocities close to the shelf break, I demonstrated that a counter flow develops below the surface Ekman layer, achieving a nearly perfect compensation of the surface cross-slope transport. The counter flow does not take place uniformly along the shelf margins, but rather manifests itself as localised barotropic velocity anomalies in regions of sloping bathymentry. In the western Eurasian shelf, net onshore Ekman transport causes negative anomalies in the Atlantic Water inflow through the Barents Sea Opening and positive anomalies in the outflow through the St. Anna Trough. These anomalies are in geostrophic balance, and are visible from composites of the simulated geostrophic currents. Finally, tiny residuals between surface Ekman transport and geostrophic return flow (transport of $O(10^{-2}$ Sv)) result in seasonal sea surface height changes of 10-20 cm over the Eurasian shelf.

A further effort was made to interpret the shelf sea surface height budget within a theoretical framework, based on the depth-averaged vorticity equation following the approach by Volkov et al. (2013). In this approach, changes in the sea surface height are directly expressed in terms of vorticity inputs and sinks. Following the method by Volkov et al. (2013), the analysis in this thesis seems to indicate that the first order vorticity balance is achieved via wind stress curl, changes in sea surface height, flow across topographic slopes and dissipation. However, the treatment of the vorticity equation as in Volkov et al. (2013) presents two major problems. Firstly, it is not explicit in terms of inclusion of sea surface height changes in the equation, which is instead represented via the divergence of the depth-integrated flow. Furthermore, the dissipation term is calculated as residual of the equation, without attributing an explicit analytical form to it. This will by definition lead to a correlation with the rest of terms in the equation. Therefore, in my discussion I propose an alternative treatment of the vorticity equation, based on the depth-integrated rather than depth-averaged velocities, which allows to provide explicit meaning to four vorticity sink terms (Eq. 4.5). I discuss the derived equation based on previous works (Hughes and de Cuevas, 2001; Isachsen et al., 2003), coming to the conclusion that changes in the sea surface height variability are very small and result from a residual between wind forcing and vorticity sink terms, mainly bottom stress curl and the bottom pressure torque. I suggest therefore that it would be a worthwhile future application to explore whether Eq. 4.5 can serve as a reliable diagnostic to determine the spatial distribution of the seasonal sea level change.

Although most of the analysis of drivers was focused on the mechanisms driving the mass-related sea surface height seasonality, in some regions density-related changes were as prominent. Results from the geostrophic velocity decomposition indicate that at Laptev Sea continental slope both mass-related and density-related seasonal changes occur. In the last section of **Chapter 4**, I used model simulations to analyse how the changes observed in the geostrophic field are related to changes in the vertical structure of the ocean velocity and density fields. The simulations depict a multiple-core current system in agreement with previous studies based on in-situ data. Previous literature has established that each of the current cores, or branches, has both a different geographical origin and a different density, that determine its depth and distance from the slope. A poorly documented shallow and broad surface branch was identified in Chapter 4 from the simulated ocean velocity fields. This branch has been identified in previous modelling studies (Aksenov et al., 2011;

Janout et al., 2015), that tracked its origin back to the fresh Vilkitsky Strait Current, a density driven coastal current originating from the Kara Sea by Ob-Yenisei riverine outflow. The pathway followed by this water mass, from the river mouths to the Laptev Sea continental slope, was also identified in the maps of density-driven geostrophic velocity anomalies. Furthermore, the mass-related geostrophic current anomalies show that part of the geostrophic variability at the Laptev Sea continental slope originates from the continental slope further west. Indeed, both observation-based and modelling studies clearly describe two further sub-surface branches, exhibiting mostly barotropic variability, that converge at this location from the St. Anna Trough and from the Fram Strait. Therefore, this region provides a case example of how a study of the density-related and mass-related geostrophic current anomalies can provide information on the composition and formation of a shelf break current.

Outlook

The analysis conducted in this thesis points out that altimetry is becoming mature to study the Arctic sea surface height variability and the ocean circulation in ice-covered regions. I demonstrated in particular the ability of the SAGA dataset to describe the seasonal variability and resolve Arctic slope currents. The comparison and combination of the SAGA dataset with in-situ data and model outputs have provided information both on the strengths and limitations of this dataset. Informed by the results outlined in this study, in the following I formulate suggestions for future research both in terms of technical advances and in terms of potential analysis of the Arctic Ocean variability.

A major source of uncertainty in gridded sea surface height fields is the high frequency variability that characterises the Arctic sea surface height, which is not properly resolved by single-altimeter-mission products. To improve the representation of mean gridded fields, future research should cover two aspects. On the one hand, a deeper knowledge of the processes determining the variability on time scales from a day to few weeks must be acquired. These are for instance ocean tides and effects of atmospheric pressure and wind forcing. The latter includes not only effects of local forcing, but also remote forcing due to the fast propagation of sea surface height anomalies in the form of barotropic waves, particularly in the shallow shelf regions. All these processes must be understood and better represented in the models used to generate geophysical corrections for altimetry data. The second aspect that should be improved is the data coverage. An increasing number of overlapping satellite missions sampling the northern Arctic latitudes (CryoSat-2, SARAL, Sentinel-3, ICEsat-2, SWOT, CRISTAL) will allow in the near future to resolve both the high frequency and the small-scale variability that characterises the Arctic sea surface height field and ocean circulation. In order for this process to be successful, the international altimetry community must coordinate efforts to cover the wide range of expertise required to process data from different satellites and to unify the treatment of auxiliary products such as corrections. One further critical aspects is the coordination of data processing in the ice-covered and ice-free regions to create uniform fields across the ice edge. In this respect, efforts to design processing methods that adapt to satellite signal from the open ocean to the pack ice is an approach worth exploring to obtain unbiased fields (e.g., Passaro et al., 2018).

One notable improvement in the SAGA dataset relative to previous data products is the increased northward extension, up to 88°N. This extension covers almost the entire Arctic, and in particular includes a large part of the central Arctic basins, where the Transpolar Drift flows, a major current system of the Arctic Ocean. The Transpolar Drift is a broad surface flow crossing the Arctic from the Eurasian shelf towards the Canadian Archipelago and the Fram Strait, exporting relatively fresh water coming from the Arctic shelf seas and the Pacific Ocean. The SAGA dataset therefore provides the opportunity to study interannual variability in the Transpolar Drift pathway and intensity over the last decade. This knowledge is relevant to interpret changes

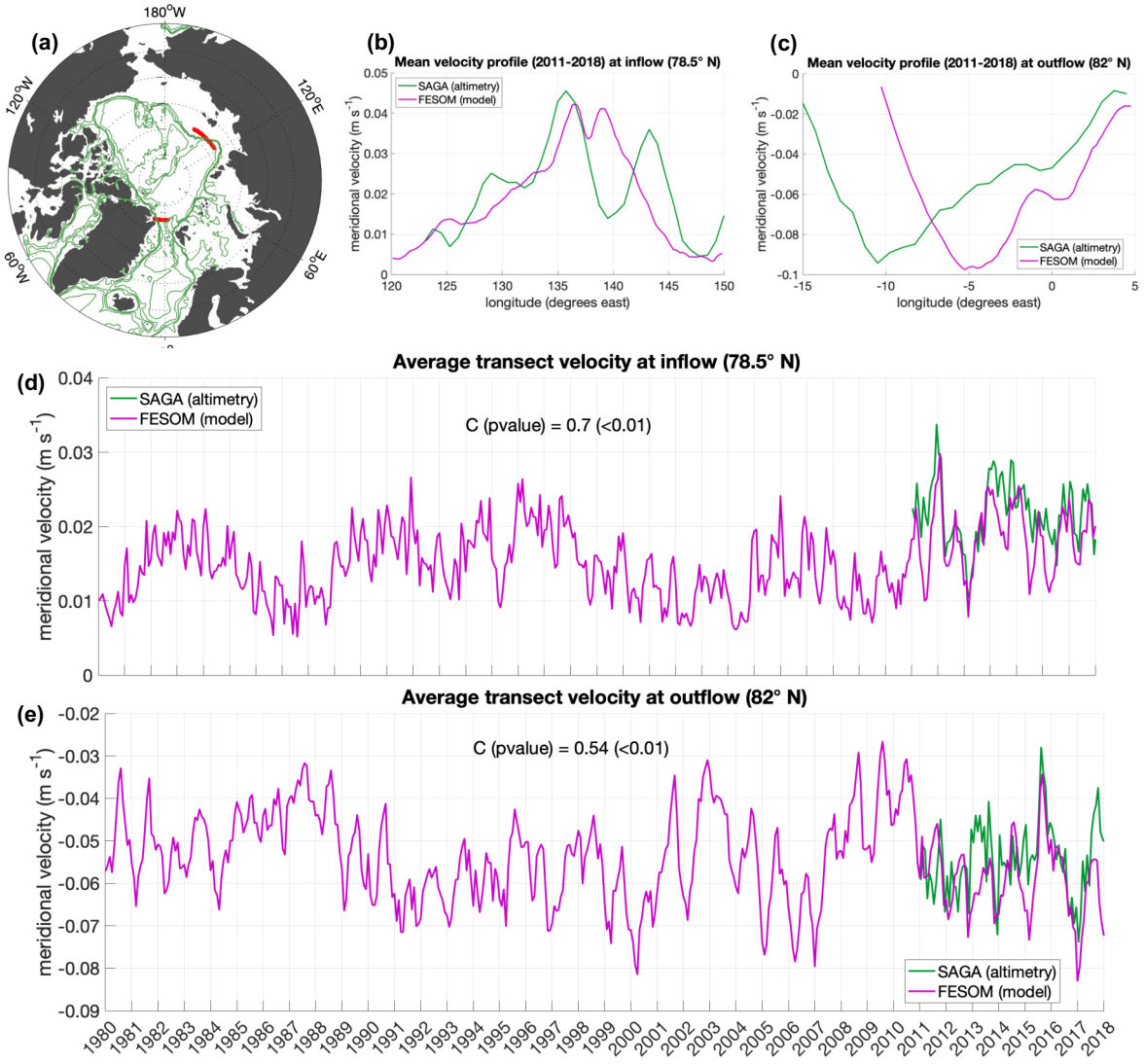

Figure 5.1. Comparison of the mean state and temporal variability of the Transpolar Drift from SAGA and FESOM data. (a) The transects corresponding to the Transpolar Drift inflow and outflow are marked in red on the map; bottom depth (green contours) is drawn at 300 m, 500 m, 1000 m, 2500 m. Mean 2011-2018 geostrophic velocity profile along the (b) inflow and (c) outflow transects from SAGA and FESOM. The two lower panels represent the time series of average geostrophic velocity across the (d) inflow and (b) outflow transects (correlation coefficients and p-values between SAGA and FESOM are indicated).

in the fresh water export from the Arctic, which ultimately influence the deep waters formation in the Nordic Seas and therefore the global conveyor belt. Furthermore, by using a combination of the SAGA dataset and model simulations it would be possible to put observations of the recent Transpolar Drift variability into the context of its long-term variability. An example of a similar comparison is shown in Fig. 5.1, using the model simulations starting as far back as the year 1980. Altimetry data and model simulations show a consistent mean spatial distribution of Transpolar Drift both in the upstream region across the eastern Laptev Sea and in the downstream region north of the Fram Strait (Fig.5.1a-b-c). The time series of observed and simulated average velocities across the transects are well correlated in the period 2011-2018 (Fig.5.1d-e), and thus provide confidence in the model performance. This simple analysis shows an example of how the recent Transpolar Drift variability could be studied based on a combination of altimetry and model data, and further interpreted in the context of quasi-decadal oscillations revealed by the simulation.

Figure 5.1 also shows that some discrepancy in the downstream transect of the Transpolar Drift is present between altimetry and model data. This region, between the north-east Greenland coast and the northern

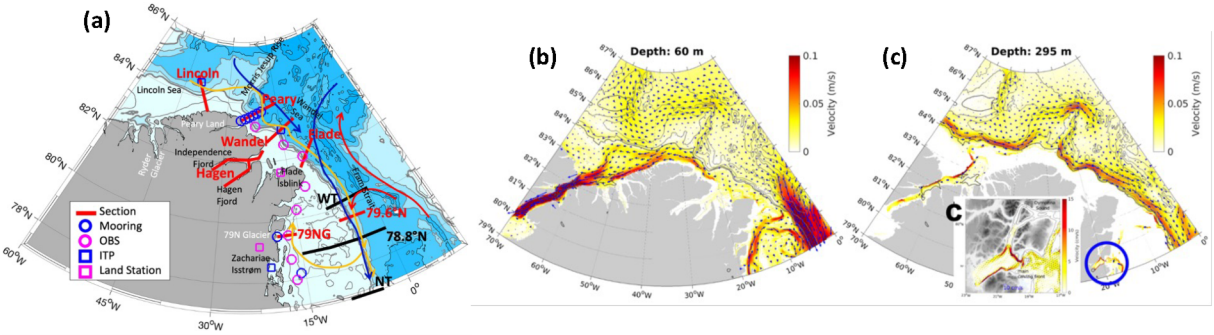

Figure 5.2. Plan of the "ECG sources" expedition (proposed for summer 2025) and model simulation of the ocean circulation in the area. (a) Cruise plan indicating the sections to be performed and the locations of the moorings, OBSs, ITPs, and Land Stations. The two right panels show the ocean circulation in the area north of Greenland at depth of (b) 60 m and (c) 295 m.

coasts of the Canadian Archipelago, is indeed hard to study due to the year-long presence of pack ice. In Chapter 2, for instance, I show that the lowest density of altimetry data is found here. For this reason, future efforts should also address the assessment of altimetry data via in-situ data from this region. One unique opportunity to do this might be provided by two research cruises planned in this region for the 2025-2026 period (Fig. 5.2). The scientific question addressed by these expeditions relates to the origin and variability of the fresh water transported within the East Greenland Current. In this context, satellite altimetry could be used in turn to support in-situ data and provide a longer-term, larger-scale perspective on this question.

Finally, the model-based analysis of density-related and mass-related circulation changes in this thesis suggests several directions to further develop the work in the future. Firstly, a similar model-based analysis could be repeated to study changes on time scales from interannual to decadal. the coherence of ocean mass oscillations and sea surface height variability in the global ocean decreases drastically at periods between 2 and 6 months (Quinn and Ponte, 2012), with results in this thesis indicating that strong seasonal wind changes in the Arctic still drive the large-scale seasonality there. On the contrary, freshwater redistribution has been demonstrated to have a decadal memory of wind forcing (Rabe et al., 2014; Johnson et al., 2018) and other wind-driven processes might have influence on the heat inflow to the Arctic on the decadal time scale (**?**). Therefore, I expect the analysis of variability on interannual to decadal time scales to be increasingly influenced by density-driven changes. Furthermore, a combination of satellite altimetry and gravimetry data could be used for satellite-based studies of the large-scale Arctic sea surface height and freshwater variability, possibly complemented by long-term collections of hydrographic observations. Beyond improvements to satellite altimetry, parallel advances in the resolution of satellite gravimetry would also enable observation-based studies of the patterns, character and drivers of ocean circulation changes, as demonstrated in chapter 4.

Satellite altimetry is becoming a reliable source of data for the Arctic Ocean. The work in this thesis has shown that a data product developed from only one satellite mission can provide a reliable basis to observe sea level and circulation variability on seasonal time scales. I have also show how altimetry can provide insights on the dynamics governing the Arctic Ocean circulation, when used in combination with model simulations. The results and advances achieved in this thesis prompt many opportunities for future research, as further technical improvements and an improved tackling of several scientific questions appears possible.

Acknowledgements

I am happy to dedicate these last page of my dissertation to recognise that many people have accompanied me and supported me during this journey towards my PhD degree. First and foremost, I am very grateful to my supervisor Torsten Kanzow, who trusted me all the way and supported me with insightful scientific discussions from week number one to week number so-many. I thank you for transmitting me your enthusiasm for all topics and your critical way of thinking. At the same time, I am thankful for your kind and constructive attitude, your trust, that helped me to keep up the good work even in moment when I could not see the end of it. Many other colleagues provided me guidance during these years. In particular I thank Ben Rabe for the long and nice discussions on science and for supporting me through the difficult review process of my first paper. A special thank goes as well to Robert Ricker ans Stefan Hendricks for being always available to answer my many questions about the satellite data that were at the base of my work, and for helping out with competent technical support at any time needed. I also thank all the other members of my Thesis Advisory committee, Robert Ricker, Hiroshi Sumata, Klaus Grosfeld, Claudia Wekerle. Many thanks again to Torsten Kanzow and Maren Walter for reviewing my thesis.

I thank the whole OZE section (Physical Oceanography section of the Alfred Wegener Institute) for being such a diverse and stimulating group, providing a welcoming environment where to develop my scientific and personal skills (which is not to be underestimated!). I have met there friendly colleagues who helped me working with and interpreting in-situ data, I mention here Wilken Jon von Appen, Markus Janout, Olaf Boebel. Other colleagues were always available to stop by for a chat and to offer mental relief: Janin Schaffer, Mario Hoppema, Sandra Tippenhauer, Hauke Becker, Elena Schall, Hartmut Hellmer, Jens Hölemann and many other. I am grateful as well to have been able to discuss with you not only about pure science but also about science communication: thanks to all supporters of the OZE knowledge transfer group!

I thank the Helmholtz Graduate School POLMAR for offering a various program of disciplinary and soft-skill courses, from which I have benefited very much. I've had the pleasure to meet many fellow PhD and early career scientists along my path, who helped me to stay mentally healthy, see a variety of different (difficult) situations and, of course, provided lovely company; among them Lukrecia, Nicolas, Janin, Luisa, Stelios, Yangyang, Laura, Vasilis, Krissy, Myriel, Mathias, Pedro, Eugenio, Finn, Alejandra, Moritz, Simon, Ramona, Zerlina, Ole. Thank you all! I also would like to mention and thank here APECS and the organiser of the MOSAiC school Josefine Lenz to provide the unique opportunity to be on a ship during such an exciting interdisciplinary expedition! In this context, I would like to thank in particular two fellows PhD students from the MOSAiC school, which offered during the cruise and in the years afterwards inspiration and insightful discussion, Marylou Athanase and Sam Cornish.

Thanks to all those who helped me with tricky programming problems and who gave me feedback on my writing, one of the most difficult and suffered tasks of a scientist! I mention here Krissy Reeve, Ben Rabe, Robert Ricker, Finn Heukamp, Marylou Athanase, Moritz Zeising, Mathias von Caspel, Sinhué Torres Valdés, Lorenzo Doglioni.

Thanks to all those who in these years of PhD have always offered time for a chat, another perspective, a warm hug, a nice word. Special thanks go to Yangyang, Laura, Janin, Luisa, Andrea, Imke, Fang, Marylou, Mathias, Finn. And last but definitely not least: thanks to my family, for being so warm, open and supportive. Thanks to Claudia, Fabrizio and Lorenzo, my "come-from" family, and to my partner Sinhué, whose unconditional love felt like home and whose alternative perspectives challenged me to always go out of my comfort zone.

Acronyms

Acronym	Description
AC	Arctic Cape
ADCP	Acoustic Doppler Current Profiler
AWI	Alfred Wegener Institute
BGEP	Beufort Gyre Exploration Program
BSO	Barents Sea Opening
CATS	Changing Arctic Transpolar System
CM	Current Meter
CMEMS	Copernicus Marine Environment Monitoring Service
CNES	Centre National d'Études Spatiales
CPME	Cever Poorman's Estimate
CPOM	Centre for Polar Observation and Modelling
CRISTAL	Copernicus Polar Ice and Snow Topography Altimeter
CTD	Conductivity-Temperature-Depth
DAC	Dynamic Atmosphere Correction
DIVA	Data-Interpolating Variational Analysis
DOT	Dynamic Ocean Topography
DUACS	Data Unification and Altimeter Combination System
ECMWF	European Centre for Medium-range Weather Forecast
EOF	Empirical Orthogonal Function
ERS	European Remote Sensing satellite
ESA	European Space Agency
FESOM	Finite Element Sea ice - Ocean Model
FS	Fram Strait
GCOS	Global Climate Observing System
GDR	Geophysical Data Record
GEOS-3	Geodynamics Experimental Ocean Satellite 3
GRACE	Gravity Recovery and Climate Experiment
IB	Invered Barometer
ICEsat	Ice, Cloud, and land Elevation Satellite
IPCC	Intergovernmental Panel on Climate Change
JEBAR	Joint Effect of Baroclinicity and Relief
JPL	Jet Propulsion Laboratory
MMP	McLane Moored Profiler
NABOS-II	Nansen and Amundsen Basins Observations System II
NEMO	Nucleus for European Modelling of the Ocean
NOAA	National Ocean and Atmosphere Administration
NPI	Norwegian Polar Institute
OCCAM	Ocean Circulation and Climate Advanced Modelling
OSISAF	Ocean and Sea Ice Satellite Application Facility
OSTIA	Operational Sea Surface Temperature and Sea Ice Analysis
RADS	Radar Altimeter Database System

Acronym	Description
RMSD	Root Mean Square Difference
RV	Research Vessel
SAGA	Sea level Anomaly and Geostrophic velocity of the Arctic ocean
SAR	Synthetic-aperture radar
SARAL	Satellite for ARgos and ALtiKa
SAT	St. Anna Trough
Sentinel-3	European Earth Observation satellite mission
SWOT	Surface Water and Ocean Topography
TOPEX/Poseidon	joint satellite altimeter mission between NASA and CNES
V13	Volkov et al. (2013)
VIM	Variational Inverse Method
WGS84	World Geodetic System standard 1984
WOCE	World Ocean Circulation Experiment

List of Figures

List of Tables

Bibliography

Aksenov, Y., Ivanov, V. V., Nurser, A. J. G., Bacon, S., Polyakov, I. V., Coward, A. C., Naveira-Garabato, A. C., and Beszczynska-Moeller, A.: The Arctic Circumpolar Boundary Current, Journal of Geophysical Research, 116, 11, https://doi.org/10.1029/2010JC006637, 2011.

Alexandrov, V., Sandven, S., Wahlin, J., and Johannessen, O. M.: The relation between sea ice thickness and freeboard in the Arctic, The Cryosphere, 4, 373–380, https://doi.org/10.5194/tc-4-373-2010, 2010.

Andersen, O., Knudsen, P., and Stenseng, L.: The DTU13 MSS (Mean Sea Surface) and MDT (Mean Dynamic Topography) from 20 Years of Satellite Altimetry, in: IGFS 2014, pp. 111–121, Springer, Cham, Cham, https://doi.org/10.1007/1345_2015_182, 2015.

Armitage, T. W. K. and Davidson, M. W. J.: Using the Interferometric Capabilities of the ESA CryoSat-2 Mission to Improve the Accuracy of Sea Ice Freeboard Retrievals. , IEEE Transactions on Geoscience and Remote Sensing, 52, 529–536, https://doi.org/10.1109/TGRS.2013.2242082, 2014.

Armitage, T. W. K., Bacon, S., Ridout, A. L., Thomas, S. F., Aksenov, Y., and Wingham, D. J.: Arctic sea surface height variability and change from satellite radar altimetry and GRACE, 2003-2014, Journal of Geophysical Research: Oceans, 121, 4303–4322, https://doi.org/10.1002/2015JC011579, 2016.

Armitage, T. W. K., Bacon, S., Ridout, A. L., Petty, A. A., Wolbach, S., and Tsamados, M.: Arctic Ocean surface geostrophic circulation 2003–2014, The Cryosphere, 11, 1767–1780, https://doi.org/10.5194/tc-11-1767-2017, 2017.

Armitage, T. W. K., Bacon, S., and Kwok, R.: Arctic Sea Level and Surface Circulation Response to the Arctic Oscillation, Geophysical Research Letters, 45, 6576 – 6584, https://doi.org/10.1029/2018gl078386, 2018.

Armitage, T. W. K., Manucharyan, G. E., Petty, A. A., Kwok, R., and Thompson, A. F.: Enhanced eddy activity in the Beaufort Gyre in response to sea ice loss, Nature Communications, 11, 1–8, https://doi.org/10.1038/s41467-020-14449-z, 2020.

Athanase, M., Provost, C., Artana, C., Hernández, M. D. P., Sennéchael, N., Bertosio, C., Garric, G., Lellouche, J.-M., and Prandi, P.: Changes in Atlantic Water Circulation Patterns and Volume Transports North of Svalbard Over the Last 12 Years (2008–2020), Journal of Geophysical Research: Oceans, 126, e2020JC016 825, https://doi.org/10.1029/2020jc016825, 2021.

Bacon, S., Marshall, A., Holliday, N. P., Aksenov, Y., and Dye, S. R.: Seasonal variability of the East Greenland Coastal Current, Journal of Geophysical Research: Oceans, 119, 3967–3987, https://doi.org/10.1002/2013JC009279, 2014.

Baltazar, A. O. and Malcolm, M.: Cryo-TEMPO Product Handbook, Tech. rep., ESA Earth Online, URL http://www.cpom.ucl.ac.uk/cryotempo/pdf_viewer.php?theme=polaroceans, 2023.

Barth, A., Beckers, J. M., Troupin, C., Alvera-Azcárate, A., and Vandenbulcke, L.: divand-1.0: n-dimensional variational data analysis for ocean observations, Geoscientific Model Development, 7, 225 – 241, https://doi.org/10.5194/gmd-7-225-2014, 2014.

Barth, A., Troupin, C., Reyes, E., Alvera-Azcárate, A., Beckers, J.-M., and Tintoré, J.: Variational interpolation of high-frequency radar surface currents using DIVAnd, Ocean Dynamics, 71, 293–308, https://doi.org/10.1007/s10236-020-01432-x, 2021.

Bauch, D., Torres-Valdes, S., Polyakov, I., Novikhin, A., Dmitrenko, I., McKay, J., and Mix, A.: Halocline water modification and along-slope advection at the Laptev Sea continental margin, Ocean Science, 10, 141–154, https://doi.org/10.5194/os-10-141-2014, 2014.

Baumann, T. M., Polyakov, I. V., Pnyushkov, A. V., Rember, R., Ivanov, V. V., Alkire, M. B., Goszczko, I., and Carmack, E. C.: On the Seasonal Cycles Observed at the Continental Slope of the Eastern Eurasian Basin of the Arctic Ocean, Journal of Physical Oceanography, 48, 1451–1470, https://doi.org/10.1175/JPO-D-17-0163.1, 2018.

Beckers, J.-M., Barth, A., Troupin, C., and Alvera-Azcárate, A.: Approximate and Efficient Methods to Assess Error Fields in Spatial Gridding with Data Interpolating Variational Analysis (DIVA), Journal of Atmospheric and Oceanic Technology, 31, 515 – 530, https://doi.org/10.1175/jtech-d-13-00130.1, 2014.

Belgacem, M., Schroeder, K., Barth, A., Troupin, C., Pavoni, B., Raimbault, P., Garcia, N., Borghini, M., and Chiggiato, J.: Climatological distribution of dissolved inorganic nutrients in the western Mediterranean Sea (1981–2017), Earth System Science Data, 13, 5915–5949, https://doi.org/10.5194/essd-13-5915-2021, 2021.

Benveniste, J.: Radar Altimetry: Past, Present and Future, in: Coastal Altimetry, edited by Vignudelli, S., Kostianoy, A., Cipollini, P., and Benveniste, J., Springer, URL http://dx.doi.org/10.1007/978-3-642-12796-0, 2011.

Bertosio, C., Provost, C., Athanase, M., Sennéchael, N., Garric, G., Lellouche, J., Kim, J., Cho, K., and Park, T.: Changes in Arctic Halocline Waters Along the East Siberian Slope and in the Makarov Basin From 2007 to 2020, Journal of Geophysical Research: Oceans, 127, e2021JC018 082, https://doi.org/10.1029/2021jc018082, 2022.

Beszczynska-Möller, A., Fahrbach, E., Schauer, U., and Hansen, E.: Variability in Atlantic water temperature and transport at the entrance to the Arctic Ocean, 1997–2010, ICES Journal of Marine Science, 69, 852–863, https://doi.org/10.1093/icesjms/fss056, 2012.

Beszczynska-Möller, A., Woodgate, R., Lee, C., Melling, H., and Karcher, M.: A Synthesis of Exchanges Through the Main Oceanic Gateways to the Arctic Ocean, Oceanography, 24, 82–99, https://doi.org/10.5670/oceanog.2011.59, 2011.

Bingham, R. J. and Hughes, C. W.: The relationship between sea-level and bottom pressure variability in an eddy permitting ocean model, Geophysical Research Letters, 35, L08 607, https://doi.org/10.1029/2007gl032662, 2008.

Birol, F., Fuller, N., Lyard, F., Cancet, M., Niño, F., Delebecque, C., Fleury, S., Toublanc, F., Melet, A., Saraceno, M., and Léger, F.: Coastal applications from nadir altimetry: Example of the X-TRACK regional products, Advances in Space Research, 59, 936–953, https://doi.org/10.1016/j.asr.2016.11.005, 2017.

Bouffard, J., Naeije, M., Banks, C. J., Calafat, F. M., Cipollini, P., Snaith, H. M., Webb, E., Hall, A., Mannan, R., Féménias, P., and Parrinello, T.: CryoSat ocean product quality status and future evolution, Advances in Space Research, 62, 1549–1563, https://doi.org/10.1016/j.asr.2017.11.043, 2017.

Bouzinac, C.: CryoSat Product Handbook, Tech. rep., European Space Agency, URL https://earth.esa.int/documents/10174/125272/CryoSat_Product_Handbook, 2012.

Brakstad, A., Gebbie, G., Våge, K., Jeansson, E., and Ólafsdóttir, S. R.: Formation and pathways of dense water in the Nordic Seas based on a regional inversion, Progress in Oceanography, 212, 102 981, https://doi.org/10.1016/j.pocean.2023.102981, 2023.

Brasseur, P., Beckers, J., Brankart, J., and Schoenauen, R.: Seasonal temperature and salinity fields in the Mediterranean Sea: Climatological analyses of a historical data set, Deep Sea Research Part I: Oceanographic Research Papers, 43, 159–192, https://doi.org/10.1016/0967-0637(96)00012-x, 1996.

Brasseur, P. P. and Haus, J. A.: Application of a 3-D variational inverse model to the analysis of ecohydrodynamic data in the Northern Bering and Southern Chukchi Seas, Journal of Marine Systems, 1, 383–401, https://doi.org/10.1016/0924-7963(91)90006-g, 1991.

Bretherton, F. P., Davis, R. E., and Fandry, C. B.: A technique for objective analysis and design of oceanographic experiments applied to MODE-73, Deep Sea Research, 23, 559–582, https://doi.org/10.1016/0011-7471(76)90001-2, 1976.

Brown, N. J., Mauritzen, C., Li, C., Madonna, E., Isachsen, P. E., and LaCasce, J. H.: Rapid response of the Norwegian Atlantic Slope Current to wind forcing, Journal of Physical Oceanography, 53, 389–408, https://doi.org/https://doi.org/10.1175/JPO-D-22-0014.1, 2023.

Bruinsma, S. L., Förste, C., Abrikosov, O., Lemoine, J.-M., Marty, J.-C., Mulet, S., Rio, M. H., and Bonvalot, S.: ESA's satellite-only gravity field model via the direct approach based on all GOCE data, Geophysical Research Letters, 41, 7508–7514, https://doi.org/10.1002/2014GL062045, 2014.

Bryden, H. L. and Imawaki, S.: Chapter 6.1 Ocean heat transport, International Geophysics, 77, 455–474, https://doi.org/10.1016/s0074-6142(01)80134-0, 2001.

Buckley, M. W. and Marshall, J.: Observations, inferences, and mechanisms of the Atlantic Meridional Overturning Circulation: A review, Reviews of Geophysics, 54, 5–63, https://doi.org/10.1002/2015rg000493, 2016.

Bulczak, A. I., Bacon, S., Garabato, A. C. N., Ridout, A., Sonnewald, M. J. P., and Laxon, S. W.: Seasonal variability of sea surface height in the coastal waters and deep basins of the Nordic Seas, Geophysical Research Letters, 42, 113–120, https://doi.org/10.1002/(ISSN)1944-8007, 2015.

Böning, C. W., Behrens, E., Biastoch, A., Getzlaff, K., and Bamber, J. L.: Emerging impact of Greenland meltwater on deepwater formation in the North Atlantic Ocean, Nature Geoscience, 9, 523–527, https://doi.org/10.1038/ngeo2740, 2016.

Calafat, F. M., Chambers, D. P., and Tsimplis, M. N.: Inter-annual to decadal sea-level variability in the coastal zones of the Norwegian and Siberian Seas: The role of atmospheric forcing, Journal of Geophysical Research: Oceans, 118, 1287 – 1301, https://doi.org/10.1002/jgrc.20106, 2013.

Cancet, M., Andersen, O. B., Lyard, F., Cotton, D., and Benveniste, J.: Arctide2017, a high-resolution regional tidal model in the Arctic Ocean, Advances in Space Research, 62, 1324 – 1343, https://doi.org/10.1016/j.asr.2018.01.007, 2018.

Capet, A., Troupin, C., Carstensen, J., Grégoire, M., and Beckers, J.-M.: Untangling spatial and temporal trends in the variability of the Black Sea Cold Intermediate Layer and mixed Layer Depth using the DIVA detrending procedure, Ocean Dynamics, 64, 315–324, https://doi.org/10.1007/s10236-013-0683-4, 2014.

Carrère, L. and Lyard, F.: Modeling the barotropic response of the global ocean to atmospheric wind and pressure forcing - comparisons with observations, Geophysical Research Letters, 30, 405, https://doi.org/10.1029/2002GL016473, 2003.

Carrère, L., Faugère, Y., and Ablain, M.: Major improvement of altimetry sea level estimations using pressure-derived corrections based on ERA-Interim atmospheric reanalysis, Ocean Science, 12, 825–842, https://doi.org/10.5194/os-12-825-2016, 2016.

Cartwright, D. E. and Edden, A. C.: Corrected Tables of Tidal Harmonics, Geophysical Journal International, 33, 253–264., https://doi.org/https://doi.org/10.1111/j.1365-246X.1973.tb03420.x, 1973.

Chao, Y. and Fu, L.: A comparison between the TOPEX/POSEIDON data and a global ocean general circulation model during 1992–1993, Journal of Geophysical Research: Oceans, 100, 24 965–24 976, https://doi.org/10.1029/95jc02260, 1995.

Cole, S. T., Timmermans, M.-L., Toole, J. M., Krishfield, R. A., and Thwaites, F. T.: Ekman Veering, Internal Waves, and Turbulence Observed under Arctic Sea Ice, Journal of Physical Oceanography, 44, 1306–1328, https://doi.org/10.1175/jpo-d-12-0191.1, 2014.

Dai, A. and Trenberth, K. E.: Estimates of Freshwater Discharge from Continents: Latitudinal and Seasonal Variations, Journal of Hydrometeorology, 3, 660–687, https://doi.org/10.1175/1525-7541(2002)003<0660:eofdfc>2.0.co;2, 2002.

Danielson, S. L., Hennon, T. D., Hedstrom, K. S., Pnyushkov, A. V., Polyakov, I. V., Carmack, E. C., Filchuk, K., Janout, M., Makhotin, M., Williams, W. J., and Padman, L.: Oceanic Routing of Wind-Sourced Energy Along the Arctic Continental Shelves, Frontiers in Marine Science, 7, 815, https://doi.org/10.3389/fmars.2020.00509, 2020.

Danilov, S., Kivman, G., and Schröter, J.: A finite-element ocean model: principles and evaluation, Ocean Modelling, 6, 125–150, https://doi.org/10.1016/s1463-5003(02)00063-x, 2004.

de Steur, L., Hansen, E., Gerdes, R., Karcher, M., Fahrbach, E., and Holfort, J.: Freshwater fluxes in the East Greenland Current: A decade of observations, Geophysical Research Letters, 36, 14 485, https://doi.org/10.1029/2009GL041278, 2009.

de Steur, L., Peralta-Ferriz, C., and Pavlova, O.: Freshwater Export in the East Greenland Current Freshens the North Atlantic, Geophysical Research Letters, 45, 13,359–13,366, https://doi.org/10.1029/2018GL080207, 2018.

Dettmering, D., Wynne, A., Müller, F. L., Passaro, M., and Seitz, F.: Lead Detection in Polar Oceans—A Comparison of Different Classification Methods for Cryosat-2 SAR Data, Remote Sensing, 10, 1190, https://doi.org/10.3390/rs10081190, 2018.

Dickson, R. R. and Brown, J.: The production of North Atlantic Deep Water: Sources, rates, and pathways, Journal of Geophysical Research: Oceans, 99, 12 319 – 12 341, https://doi.org/10.1029/94jc00530, 1994.

Dmitrenko, I. A., Kirillov, S. A., and Tremblay, L. B.: The long-term and interannual variability of summer fresh water storage over the eastern Siberian shelf: Implication for climatic change, Journal of Geophysical Research: Oceans, 113, https://doi.org/10.1029/2007jc004304, 2008.

Dmitrenko, I. A., Rudels, B., Kirillov, S. A., Aksenov, Y. O., Lien, V. S., Ivanov, V. V., Schauer, U., Polyakov, I. V., Coward, A., and Barber, D. G.: Atlantic water flow into the Arctic Ocean through the St. Anna Trough in

the northern Kara Sea, Journal of Geophysical Research: Oceans, 120, 5158 – 5178, https://doi.org/10.1002/2015jc010804, 2015.

Doglioni, F., Ricker, R., Rabe, B., and Kanzow, T.: Pan-Arctic monthly maps of sea surface height anomaly and geostrophic velocity from the satellite altimetry Cryosat-2 mission, 2011-2020, URL https://doi.pangaea.de/10.1594/PANGAEA.931869, 2021.

Doglioni, F., Ricker, R., Rabe, B., Barth, A., Troupin, C., and Kanzow, T.: Sea surface height anomaly and geostrophic current velocity from altimetry measurements over the Arctic Ocean (2011–2020), Earth System Science Data, 15, 225–263, https://doi.org/10.5194/essd-15-225-2023, 2023.

Ekman, V. W.: On the influence of the Earth's rotation on ocean-currents., Ark. Mat. Astron. Fys., 2, 1–53, 1905.

Emery, W. J. and Thomson, R. E.: Chapter 3 - Statistical Methods and Error Handling, in: Data Analysis Methods in Physical Oceanography, edited by Emery, W. J. and Thomson, R. E., pp. 193–304, Elsevier Science, Amsterdam, https://doi.org/10.1016/B978-044450756-3/50004-6, 2001.

European Space Agency: Geophysical Corrections in Level 2 CryoSat Data Products, Tech. Rep. IDEAS-VEG-IPF-MEM-1288, European Space Agency, 2016.

Fang, Y. C., Weingartner, T. J., Dobbins, E. L., Winsor, P., Statscewich, H., Potter, R. A., Mudge, T. D., Stoudt, C. A., and Borg, K.: Circulation and Thermohaline Variability of the Hanna Shoal Region on the Northeastern Chukchi Sea Shelf, Journal of Geophysical Research: Oceans, 125, 195, https://doi.org/10.1029/2019jc015639, 2020.

Farrell, S. L., McAdoo, D. C., Laxon, S. W., Zwally, H. J., Yi, D., Ridout, A., and Giles, K. A.: Mean dynamic topography of the Arctic Ocean, Geophysical Research Letters, 39, 1–5, https://doi.org/10.1029/2011GL050052, 2012.

Fofonoff, N.P, and Millard, R.C.: Algorithms for computation of fundamental properties of seawater, Tech. rep., UNESCO, URL https://repository.oceanbestpractices.org/handle/11329/109, 1983.

Forest, A., Sampei, M., Hattori, H., Makabe, R., Sasaki, H., Fukuchi, M., Wassmann, P., and Fortier, L.: Particulate organic carbon fluxes on the slope of the Mackenzie Shelf (Beaufort Sea): Physical and biological forcing of shelf-basin exchanges, Journal of Marine Systems, 68, 39–54, https://doi.org/10.1016/j.jmarsys.2006.10.008, 2007.

Frajka-Williams, E., Ansorge, I. J., Baehr, J., Bryden, H. L., Chidichimo, M. P., Cunningham, S. A., Danabasoglu, G., Dong, S., Donohue, K. A., Elipot, S., Heimbach, P., Holliday, N. P., Hummels, R., Jackson, L. C., Karstensen, J., Lankhorst, M., Bras, I. A. L., Lozier, M. S., McDonagh, E. L., Meinen, C. S., Mercier, H., Moat, B. I., Perez, R. C., Piecuch, C. G., Rhein, M., Srokosz, M. A., Trenberth, K. E., Bacon, S., Forget, G., Goni, G., Kieke, D., Koelling, J., Lamont, T., McCarthy, G. D., Mertens, C., Send, U., Smeed, D. A., Speich, S., Berg, M. v. d., Volkov, D., and Wilson, C.: Atlantic Meridional Overturning Circulation: Observed Transport and Variability, Frontiers in Marine Science, 6, 260, https://doi.org/10.3389/fmars.2019.00260, 2019.

Fu, L.-L.: Ocean Circulation and Variability from Satellite Altimetry, in: Ocean Ciculation and Climate, edited by Siedler, G., Griffies, S. M., Gould, J., and Church, J. A., vol. 77 of *International Geophysics Series*, Academic Press, 2001.

Fukumori, I., Raghunath, R., and Fu, L. L.: Nature of global large-scale sea level variability in relation to atmospheric forcing: A modeling study, Journal of Geophysical Research: Solid Earth, 103, 5493–5512, https://doi.org/10.1029/97JC02907, 1998.

Fukumori, I., Wang, O., Llovel, W., Fenty, I., and Forget, G.: A near-uniform fluctuation of ocean bottom pressure and sea level across the deep ocean basins of the Arctic Ocean and the Nordic Seas, Progress in Oceanography, 134, 152–172, https://doi.org/10.1016/j.pocean.2015.01.013, 2015.

Fukumori, I., Wang, O., and Fenty, I.: Causal Mechanisms of Sea-level and Freshwater Content Change in the Beaufort Sea, Journal of Physical Oceanography, https://doi.org/10.1175/jpo-d-21-0069.1, 2021.

GCOS: The 2022 GCOS ECVs Requirements, Tech. rep., World Meteorological Organization, URL chrome-extension://efaidnbmnnnibpcajpcglclefindmkaj/https://library.wmo.int/doc_num.php?explnum_id=11318, 2022.

Giles, K. A., Laxon, S. W., Ridout, A. L., Wingham, D. J., and Bacon, S.: Western Arctic Ocean freshwater storage increased by wind-driven spin-up of the Beaufort Gyre, Nature Geoscience, 5, 194–197, https://doi.org/10.1038/ngeo1379, 2012.

Good, S., Fiedler, E., Mao, C., Martin, M. J., Maycock, A., Reid, R., Roberts-Jones, J., Searle, T., Waters, J., While, J., and Worsfold, M.: The Current Configuration of the OSTIA System for Operational Production of Foundation Sea Surface Temperature and Ice Concentration Analyses, Remote Sensing, 12, 720, https://doi.org/10.3390/rs12040720, 2020.

Greene, C. A., Thirumalai, K., Kearney, K. A., Delgado, J. M., Schwanghart, W., Wolfenbarger, N. S., Thyng, K. M., Gwyther, D. E., Gardner, A. S., and Blankenship, D. D.: The Climate Data Toolbox for MATLAB, Geochemistry, Geophysics, Geosystems, 20, 3774–3781, https://doi.org/10.1029/2019gc008392, 2019.

Gruber, T. and Willberg, M.: Signal and error assessment of GOCE-based high resolution gravity field models, Journal of Geodetic Science, 9, 71–86, https://doi.org/10.1515/jogs-2019-0008, 2019.

Haine, T. W., Curry, B., Gerdes, R., Hansen, E., Karcher, M., Lee, C., Rudels, B., Spreen, G., Steur, L. d., Stewart, K. D., and Woodgate, R.: Arctic freshwater export: Status, mechanisms, and prospects, Global and Planetary Change, 125, 13–35, https://doi.org/10.1016/j.gloplacha.2014.11.013, 2015.

Hakkinen, S., Proshutinsky, A., and Ashik, I.: Sea ice drift in the Arctic since the 1950s, Geophysical Research Letters, 35, 1 – 5, https://doi.org/10.1029/2008gl034791, 2008.

Haller, M., Brümmer, B., and Müller, G.: Atmosphere–ice forcing in the transpolar drift stream: results from the DAMOCLES ice-buoy campaigns 2007–2009, The Cryosphere, 8, 275–288, https://doi.org/10.5194/tc-8-275-2014, 2014.

Hattermann, T., Isachsen, P. E., von Appen, W.-J., and Sundfjord, A.: Eddy-driven recirculation of Atlantic Water in Fram Strait, Geophysical Research Letters, 43, 3406–3414, https://doi.org/10.1002/(ISSN)1944-8007, 2016.

Hendricks, S., Ricker, R., and Paul, S.: Product User Guide & Algorithm Specification: AWI CryoSat-2 Sea Ice Thickness (version 2.4), EPIC.awi.de, Alfred Wegener Institute Helmholtz Centre for Polar and Marine Research, URL https://epic.awi.de/id/eprint/54733/, 2021.

Heukamp, F. O., Aue, L., Wang, Q., Ionita, M., Kanzow, T., Wekerle, C., and Rinke, A.: Cyclones modulate the control of the North Atlantic Oscillation on transports into the Barents Sea, Communications Earth & Environment, 4, 324, https://doi.org/10.1038/s43247-023-00985-1, 2023.

Horwath, M., Gutknecht, B. D., Cazenave, A., Palanisamy, H. K., Marti, F., Marzeion, B., Paul, F., Bris, R. L., Hogg, A. E., Otosaka, I., Shepherd, A., Döll, P., Cáceres, D., Schmied, H. M., Johannessen, J. A., Nilsen, J. E. Ø., Raj, R. P., Forsberg, R., Sørensen, L. S., Barletta, V. R., Simonsen, S. B., Knudsen, P., Andersen, O. B.,

Ranndal, H., Rose, S. K., Merchant, C. J., Macintosh, C. R., Schuckmann, K. v., Novotny, K., Groh, A., Restano, M., and Benveniste, J.: Global sea-level budget and ocean-mass budget, with a focus on advanced data products and uncertainty characterisation, Earth System Science Data, 14, 411–447, https://doi.org/10.5194/essd-14-411-2022, 2022.

Hughes, C. W. and de Cuevas, B. A.: Why Western Boundary Currents in Realistic Oceans are Inviscid: A Link between Form Stress and Bottom Pressure Torques, Journal of Physical Oceanography, 31, 2871–2885, https://doi.org/10.1175/1520-0485(2001)031<2871:wwbcir>2.0.co;2, 2001.

Hunkins, K.: Ekman drift currents in the Arctic Ocean, Deep Sea Research and Oceanographic Abstracts, 13, 607–620, https://doi.org/10.1016/0011-7471(66)90592-4, 1966.

Ingvaldsen, R. B., Asplin, L., and Loeng, H.: Velocity field of the western entrance to the Barents Sea, Journal of Geophysical Research: Oceans, 109, https://doi.org/10.1029/2003jc001811, 2004.

Intergovernmental Panel on Climate Change: The Ocean and Cryosphere in a Changing Climate: Special Report of the Intergovernmental Panel on Climate Change, Cambridge University Press, https://doi.org/10.1017/9781009157964, 2022.

Iona, A., Theodorou, A., Watelet, S., Troupin, C., Beckers, J.-M., and Simoncelli, S.: Mediterranean Sea Hydrographic Atlas: towards optimal data analysis by including time-dependent statistical parameters, Earth System Science Data, 10, 1281–1300, https://doi.org/10.5194/essd-10-1281-2018, 2018.

Isachsen, P. E., LaCasce, J. H., Mauritzen, C., and Häkkinen, S.: Wind-Driven Variability of the Large-Scale Recirculating Flow in the Nordic Seas and Arctic Ocean, Journal of Physical Oceanography, 33, 2534 – 2550, https://doi.org/10.1175/1520-0485(2003)033<2534:WVOTLR>2.0.CO;2, 2003.

Ivanov, V. and Shapiro, G.: Formation of a dense water cascade in the marginal ice zone in the Barents Sea, Deep Sea Research Part I: Oceanographic Research Papers, 52, 1699–1717, https://doi.org/10.1016/j.dsr.2005.04.004, 2005.

Jackett, D. R. and Mcdougall, T. J.: Minimal Adjustment of Hydrographic Profiles to Achieve Static Stability, Journal of Atmospheric and Oceanic Technology, 12, 381–389, https://doi.org/10.1175/1520-0426(1995)012<0381:maohpt>2.0.co;2, 1995.

Jahn, A., Tremblay, L. B., Newton, R., Holland, M. M., Mysak, L. A., and Dmitrenko, I. A.: A tracer study of the Arctic Ocean's liquid freshwater export variability, Journal of Geophysical Research: Solid Earth, 115, 10 419, https://doi.org/10.1029/2009JC005873, 2010.

Jakobsson, M., Mayer, L., Coakley, B., Dowdeswell, J. A., Forbes, S., Fridman, B., Hodnesdal, H., Noormets, R., Pedersen, R., Rebesco, M., Schenke, H. W., Zarayskaya, Y., Accettella, D., Armstrong, A., Anderson, R. M., Bienhoff, P., Camerlenghi, A., Church, I., Edwards, M., Gardner, J. V., Hall, J. K., Hell, B., Hestvik, O., Kristoffersen, Y., Marcussen, C., Mohammad, R., Mosher, D., Nghiem, S. V., Pedrosa, M. T., Travaglini, P. G., and Weatherall, P.: The International Bathymetric Chart of the Arctic Ocean (IBCAO) Version 3.0, Geophysical Research Letters, 39, n/a–n/a, https://doi.org/10.1029/2012gl052219, 2012.

Janout, M. A., Aksenov, Y., Hölemann, J. A., Rabe, B., Schauer, U., Polyakov, I. V., Bacon, S., Coward, A. C., Karcher, M., Lenn, Y.-D., Kassens, H., and Timokhov, L.: Kara Sea freshwater transport through Vilkitsky Strait: Variability, forcing, and further pathways toward the western Arctic Ocean from a model and observations, Journal of Geophysical Research: Oceans, 120, 4925–4944, https://doi.org/10.1002/2014JC010635, 2015.

Johnson, H. L., Cornish, S. B., Kostov, Y., Beer, E., and Lique, C.: Arctic Ocean Freshwater Content and Its Decadal Memory of Sea-Level Pressure, Geophysical Research Letters, 45, 4991 – 5001, https://doi.org/10.1029/2017gl076870, 2018.

Karcher, M., Kauker, F., Gerdes, R., Hunke, E., and Zhang, J.: On the dynamics of Atlantic Water circulation in the Arctic Ocean, Journal of Geophysical Research: Solid Earth, 112, https://doi.org/10.1029/2006jc003630, 2007.

Kaur, S., Ehn, J. K., and Barber, D. G.: Pan-arctic winter drift speeds and changing patterns of sea ice motion: 1979–2015, Polar Record, 54, 303–311, https://doi.org/10.1017/S0032247418000566, 2018.

Kirillov, S. A., Dmitrenko, I. A., Ivanov, V. V., Aksenov, E. O., Makhotin, M. S., and Quevas, B. A. d.: The influence of atmospheric circulation on the dynamics of the intermediate water layer in the eastern part of the St. Anna Trough, Doklady Earth Sciences, 444, 630–633, https://doi.org/10.1134/s1028334x12050121, 2012.

Knudsen, P., Andersen, O., and Maximenko, N.: A new ocean mean dynamic topography model, derived from a combination of gravity, altimetry and drifter velocity data, Advances in Space Research, https://doi.org/10.1016/j.asr.2019.12.001, 2019.

Komjathy, A. and Born, G. H.: GPS-based ionospheric corrections for single frequency radar altimetry, Journal of Atmospheric and Solar-Terrestrial Physics, 61, 1197–1203, https://doi.org/10.1016/S1364-6826(99)00051-6, 1999.

Korhonen, M., Rudels, B., Marnela, M., Wisotzki, A., and Zhao, J.: Time and space variability of freshwater content, heat content and seasonal ice melt in the Arctic Ocean from 1991 to 2011, Ocean Science, 9, 1015–1055, https://doi.org/10.5194/os-9-1015-2013, 2013.

Kudryavtsev, V., Stokoz, A., and Khvorostovsky, K.: On Barotropic Response of Arctic Seas to Polar Lows: A Case Study in the Barents Sea, Remote Sensing, 15, 4239, https://doi.org/10.3390/rs15174239, 2023.

Kwok, R. and Morison, J.: Dynamic topography of the ice-covered Arctic Ocean from ICESat, Geophysical Research Letters, 38, 1–6, https://doi.org/10.1029/2010GL046063, 2011.

Kwok, R. and Morison, J.: Sea surface height and dynamic topography of the ice-covered oceans from CryoSat-2: 2011-2014, Journal of Geophysical Research: Oceans, 121, 674–692, https://doi.org/10.1002/2015JC011357, 2016.

Kwok, R., Spreen, G., and Pang, S.: Arctic sea ice circulation and drift speed: Decadal trends and ocean currents, Journal of Geophysical Research: Oceans, 118, 2408–2425, https://doi.org/10.1002/jgrc.20191, 2013.

Landy, J. C., Bouffard, J., Wilson, C., Rynders, S., Aksenov, Y., and Tsamados, M.: Improved Arctic Sea Ice Freeboard Retrieval From Satellite Altimetry Using Optimized Sea Surface Decorrelation Scales, Journal of Geophysical Research: Oceans, 126, https://doi.org/10.1029/2021jc017466, 2021.

Lauvset, S. K., Key, R. M., Olsen, A., Heuven, S. v., Velo, A., Lin, X., Schirnick, C., Kozyr, A., Tanhua, T., Hoppema, M., Jutterström, S., Steinfeldt, R., Jeansson, E., Ishii, M., Perez, F. F., Suzuki, T., and Watelet, S.: A new global interior ocean mapped climatology: the 1°×1° GLODAP version 2, Earth System Science Data, 8, 325 – 340, https://doi.org/10.5194/essd-8-325-2016, 2016.

Laxon, S. W.: Sea ice altimeter processing scheme at the EODC, International Journal of Remote Sensing, 15, 915–924, https://doi.org/10.1080/01431169408954124, 1994.

Le Bras, I. A. A., Straneo, F., Holte, J., and Holliday, N. P.: Seasonality of Freshwater in the East Greenland Current System From 2014 to 2016, Journal of Geophysical Research: Oceans, 123, 8828–8848, https://doi.org/10.1029/2018JC014511, 2018.

Lenartz, F., Troupin, C., and Lefebvre, W.: Air Pollution Modeling and its Application XXV, Springer Proceedings in Complexity, pp. 231–235, https://doi.org/10.1007/978-3-319-57645-9_37, 2017.

Lien, V. S., Vikebø, F. B., and Skagseth, Ø.: One mechanism contributing to co-variability of the Atlantic inflow branches to the Arctic, Nature Communications, 4, 1488, https://doi.org/10.1038/ncomms2505, 2013.

Liu, Y., Weisberg, R. H., Vignudelli, S., Roblou, L., and Merz, C. R.: Comparison of the X-TRACK altimetry estimated currents with moored ADCP and HF radar observations on the West Florida Shelf, Advances in Space Research, 50, 1085–1098, https://doi.org/10.1016/j.asr.2011.09.012, 2012.

Lyard, F., Lefevre, F., Letellier, T., and Francis, O.: Modelling the global ocean tides: modern insights from FES2004, Ocean Dynamics, 56, 394–415, https://doi.org/10.1007/s10236-006-0086-x, 2006.

Lyard, F. H., Allain, D. J., Cancet, M., Carrère, L., and Picot, N.: FES2014 global ocean tide atlas: design and performance, Ocean Science, 17, 615–649, https://doi.org/10.5194/os-17-615-2021, 2021.

Ma, B., Steele, M., and Lee, C. M.: Ekman circulation in the Arctic Ocean: Beyond the Beaufort Gyre, Journal of Geophysical Research: Oceans, 122, 3358–3374, https://doi.org/10.1002/2016JC012624, 2017.

Martin, T., Steele, M., and Zhang, J.: Seasonality and long-term trend of Arctic Ocean surface stress in a model, Journal of Geophysical Research: Oceans, 119, 1723–1738, https://doi.org/10.1002/2013jc009425, 2014.

Maslanik, J., Stroeve, J., Fowler, C., and Emery, W.: Distribution and trends in Arctic sea ice age through spring 2011, Geophysical Research Letters, 38, n/a–n/a, https://doi.org/10.1029/2011gl047735, 2011.

Mathis, J. T., Pickart, R. S., Hansell, D. A., Kadko, D., and Bates, N. R.: Eddy transport of organic carbon and nutrients from the Chukchi Shelf: Impact on the upper halocline of the western Arctic Ocean, Journal of Geophysical Research: Oceans, 112, https://doi.org/10.1029/2006jc003899, 2007.

McPhee, M.: Air-Ice-Ocean Interaction: Turbulent Ocean Boundary Layer Exchange Processes, Springer New York, NY, URL https://doi.org/10.1007/978-0-387-78335-2, 2008.

McPhee, M. G.: Turbulent heat flux in the upper ocean under sea ice, Journal of Geophysical Research: Oceans, 97, 5365–5379, https://doi.org/10.1029/92jc00239, 1992.

McPhee, M. G.: Intensification of Geostrophic Currents in the Canada Basin, Arctic Ocean, Journal of Climate, 26, 3130–3138, https://doi.org/10.1175/JCLI-D-12-00289.1, 2012.

Meneghello, G., Marshall, J., Timmermans, M.-L., and Scott, J.: Observations of Seasonal Upwelling and Downwelling in the Beaufort Sea Mediated by Sea Ice, Journal of Physical Oceanography, 48, 795 – 805, https://doi.org/10.1175/jpo-d-17-0188.1, 2018.

Min, L., Pickart, R. S., Spall, M. A., Weingartner, T. J., Lin, P., Moore, G. W. K., and Qi, Y.: Circulation of the Chukchi Sea shelfbreak and slope from moored timeseries, Progress in Oceanography, 172, 14–33, https://doi.org/10.1016/j.pocean.2019.01.002, 2019.

Mizobata, K., Watanabe, E., and Kimura, N.: Wintertime variability of the Beaufort gyre in the Arctic Ocean derived from CryoSat-2/SIRAL observations, Journal of Geophysical Research: Oceans, 121, 1685–1699, https://doi.org/10.1002/2015JC011218, 2016.

Morgan, P. and Pender, L.: CSIRO MATLAB seawater library., 2009.

Morison, J., Kwok, R., Peralta-Ferriz, C., Alkire, M., Rigor, I., Andersen, R., and Steele, M.: Changing Arctic Ocean freshwater pathways, Nature, 481, 66 – 70, https://doi.org/10.1038/nature10705, 2012.

Morison, J., Kwok, R., Dickinson, S., Morison, D., Peralta-Ferriz, C., and Andersen, R.: Sea State Bias of ICESat in the Subarctic Seas, IEEE Geoscience and Remote Sensing Letters, 15, 1144–1148, https://doi.org/10.1109/lgrs.2018.2834362, 2018.

Morison, J., Kwok, R., Dickinson, S., Andersen, R., Peralta-Ferriz, C., Morison, D., Rigor, I., Dewey, S., and Guthrie, J.: The Cyclonic Mode of Arctic Ocean Circulation, Journal of Physical Oceanography, 51, 1053 – 1075, https://doi.org/10.1175/jpo-d-20-0190.1, 2021.

Mudge, T., Fissel, D., Sadowy, D., Borg, K., Billenness, D., and Knox, K.: Analysis of ice and Metocean measurements, Chukchi Sea 2013-2014, for Shell. Project Report for Shell International Exporation and Production Inc., Houston, Texas by ASL Environmental Sciences Inc., Tech. rep., ASL Environmental Sciences Inc., Victoria, B.C. Canada, URL https://www.nodc.noaa.gov/archive/arc0111/0164964/1.1/data/0-data/Chukchi_IndustryMoorings_reports/reports_public/2013-14/Shell/ASL_Report_PR-862_Chukchi_Sea_Shell.pdf, 2015.

Mulet, S., Rio, M. H., Etienne, H., Artana, C., Cancet, M., Dibarboure, G., Feng, H., Husson, R., Picot, N., Provost, C., and Strub, P. T.: The new CNES-CLS18 Global Mean Dynamic Topography, Ocean Science, pp. 1–31, https://doi.org/10.5194/os-2020-117, 2021.

Munk, W. H.: ON THE WIND-DRIVEN OCEAN CIRCULATION, Journal of Meteorology, 7, 80–93, https://doi.org/10.1175/1520-0469(1950)007<0080:otwdoc>2.0.co;2, 1950.

Müller, F. L., Dettmering, D., Wekerle, C., Schwatke, C., Passaro, M., Bosch, W., and Seitz, F.: Geostrophic currents in the northern Nordic Seas from a combination of multi-mission satellite altimetry and ocean modeling, Earth System Science Data, 11, 1765 – 1781, https://doi.org/10.5194/essd-11-1765-2019, 2019a.

Müller, F. L., Wekerle, C., Dettmering, D., Passaro, M., Bosch, W., and Seitz, F.: Dynamic Ocean Topography of the Greenland Sea: A comparison between satellite altimetry and ocean modeling, The Cryosphere, p. 611–626, https://doi.org/10.5194/tc-13-611-2019, 2019b.

Nguyen, A. T., Pillar, H., Ocaña, V., Bigdeli, A., Smith, T. A., and Heimbach, P.: The Arctic Subpolar Gyre sTate Estimate: Description and Assessment of a Data-Constrained, Dynamically Consistent Ocean-Sea Ice Estimate for 2002–2017, Journal of Advances in Modeling Earth Systems, 13, https://doi.org/10.1029/2020ms002398, 2021.

Nøst, O. A. and Isachsen, P. E.: The large-scale time-mean ocean circulation in the Nordic Seas and Arctic Ocean estimated from simplified dynamics, Journal of Marine Research, 61, 175–210, https://doi.org/10.1357/002224003322005069, 2003.

Nurser, A. J. G. and Bacon, S.: The Rossby radius in the Arctic Ocean, Ocean Science, 10, 967–975, https://doi.org/10.5194/os-10-967-2014, 2014.

Osadchiev, A., Viting, K., Frey, D., Demeshko, D., Dzhamalova, A., Nurlibaeva, A., Gordey, A., Krechik, V., Spivak, E., Semiletov, I., and Stepanova, N.: Structure and Circulation of Atlantic Water Masses in the St. Anna Trough in the Kara Sea, Frontiers in Marine Science, 9, 915 674, https://doi.org/10.3389/fmars.2022.915674, 2022.

Osadchiev, A. A., Pisareva, M. N., Spivak, E. A., Shchuka, S. A., and Semiletov, I. P.: Freshwater transport between the Kara, Laptev, and East-Siberian seas, Scientific Reports, 10, 1–14, https://doi.org/10.1038/s41598-020-70096-w, 2020.

Overland, J. E. and Wang, M.: Resolving Future Arctic/Midlatitude Weather Connections, Earth's Future, 6, 1146–1152, https://doi.org/10.1029/2018ef000901, 2018.

Passaro, M., Cipollini, P., Vignudelli, S., Quartly, G. D., and Snaith, H. M.: ALES: A multi-mission adaptive subwaveform retracker for coastal and open ocean altimetry, Remote Sensing of Environment, 145, 173–189, https://doi.org/10.1016/j.rse.2014.02.008, 2014.

Passaro, M., Rose, S. K., Andersen, O. B., Boergens, E., Calafat, F. M., Dettmering, D., and Benveniste, J.: ALES+: Adapting a homogenous ocean retracker for satellite altimetry to sea ice leads, coastal and inland waters, Remote Sensing of Environment, 211, 456–471, https://doi.org/10.1016/j.rse.2018.02.074, 2018.

Pawlowicz, R., Beardsley, B., and Lentz, S.: Classical tidal harmonic analysis including error estimates in MATLAB using T_TIDE, Computers & Geosciences, 28, 929–937, https://doi.org/10.1016/S0098-3004(02)00013-4, 2002.

Peacock, N. R. and Laxon, S. W.: Sea surface height determination in the Arctic Ocean from ERS altimetry, Journal of Geophysical Research: Solid Earth, 109, 925, https://doi.org/10.1029/2001jc001026, 2004.

Peralta-Ferriz, C. and Morison, J.: Understanding the annual cycle of the Arctic Ocean bottom pressure, Geophysical Research Letters, 37, 1–6, https://doi.org/10.1029/2010GL042827, 2010.

Peralta-Ferriz, C. and Woodgate, R. A.: The Dominant Role of the East Siberian Sea in Driving the Oceanic Flow Through the Bering Strait—Conclusions From GRACE Ocean Mass Satellite Data and In Situ Mooring Observations Between 2002 and 2016, Geophysical Research Letters, 44, 11,472 – 11,481, https://doi.org/10.1002/2017gl075179, 2017.

Peralta-Ferriz, C., Morison, J. H., Wallace, J. M., and Zhang, J.: A basin-coherent mode of sub-monthly variability in Arctic Ocean bottom pressure, Geophysical Research Letters, 38, https://doi.org/10.1029/2011GL048142, 2011.

Peralta-Ferriz, C., Morison, J. H., Wallace, J. M., Bonin, J. A., and Zhang, J.: Arctic Ocean Circulation Patterns Revealed by GRACE, Journal of Climate, 27, 1445–1468, https://doi.org/10.1175/JCLI-D-13-00013.1, 2014.

Pérez Hernández, M. D., Pickart, R. S., Torres, D. J., Bahr, F., Sundfjord, A., Ingvaldsen, R., Renner, A. H. H., Möller, A. B., von Appen, W.-J., and Pavlov, V.: Structure, Transport, and Seasonality of the Atlantic Water Boundary Current North of Svalbard: Results From a Yearlong Mooring Array, Journal of Geophysical Research: Oceans, 124, 1679–1698, https://doi.org/10.1029/2018JC014759, 2019.

Peterson, A. K., Fer, I., McPhee, M. G., and Randelhoff, A.: Turbulent heat and momentum fluxes in the upper ocean under Arctic sea ice, Journal of Geophysical Research: Oceans, 122, 1439–1456, https://doi.org/10.1002/2016jc012283, 2017.

Piecuch, C. G., Fukumori, I., Ponte, R. M., Schindelegger, M., Wang, O., and Zhao, M.: Low-Frequency Dynamic Ocean Response to Barometric-Pressure Loading, Journal of Physical Oceanography, 52, 2627–2641, https://doi.org/10.1175/jpo-d-22-0090.1, 2022.

Pnyushkov, A. and Polyakov, I.: Nansen and Amundsen Basins Observational System (NABOS): Contributing to Understanding Changes in the Arctic, Oceanography, 35, https://doi.org/10.5670/oceanog.2022.104, 2022.

Pnyushkov, A. V., Polyakov, I. V., Ivanov, V. V., Aksenov, Y., Coward, A. C., Janout, M., and Rabe, B.: Structure and variability of the boundary current in the Eurasian Basin of the Arctic Ocean, Deep-Sea Research Part I, 101, 80–97, https://doi.org/10.1016/j.dsr.2015.03.001, 2015.

Pnyushkov, A. V., Polyakov, I. V., Padman, L., and Nguyen, A. T.: Structure and dynamics of mesoscale eddies over the Laptev Sea continental slope in the Arctic Ocean, Ocean Science, 14, 1329–1347, https://doi.org/10.5194/os-14-1329-2018, 2018.

Pnyushkov, A. V., Polyakov, I. V., Alekseev, G. V., Ashik, I. M., Baumann, T. M., Carmack, E. C., Ivanov, V. V., and Rember, R.: A Steady Regime of Volume and Heat Transports in the Eastern Arctic Ocean in the Early 21st Century, Frontiers in Marine Science, 8, 705 608, https://doi.org/10.3389/fmars.2021.705608, 2021.

Poisson, J.-C., Quartly, G. D., Kurekin, A. A., Thibaut, P., Hoang, D., and Nencioli, F.: Development of an ENVISAT Altimetry Processor Providing Sea Level Continuity Between Open Ocean and Arctic Leads, IEEE Transactions on Geoscience and Remote Sensing, 56, 5299–5319, https://doi.org/10.1109/tgrs.2018.2813061, 2018.

Polyakov, I. V.: NABOS II - ADCP Water Current Data 2013 - 2015., Arctic Data Center, https://doi.org/doi:10.18739/A28G8FJ3H, 2016.

Polyakov, I. V.: Acoustic Dopper Current Profiler (ADCP) from moorings taken in the Eurasian and Makarov basins, Arctic Ocean, 2015-2018. , https://doi.org/doi:10.18739/A2HT2GB80, 2019.

Polyakov, I. V. and Rembert, R.: Conductivity, Temperature, Pressure (CTD) measurements from Sea Bird Electronics SBE37 instruments taken in the Eurasian and Makarov basins, Arctic Ocean, 2015-2018., Arctic Data Center, https://doi.org/doi:10.18739/A2NK3652R, 2019.

Polyakov, I. V., Pnyushkov, A. V., Alkire, M. B., Ashik, I. M., Baumann, T. M., Carmack, E. C., Goszczko, I., Guthrie, J., Ivanov, V. V., Kanzow, T., Krishfield, R., Kwok, R., Sundfjord, A., Morison, J., Rember, R., and Yulin, A.: Greater role for Atlantic inflows on sea-ice loss in the Eurasian Basin of the Arctic Ocean, Science, 356, 285–291, https://doi.org/10.1126/science.aai8204, 2017.

Polyakov, I. V., Rippeth, T. P., Fer, I., Alkire, M. B., Baumann, T. M., Carmack, E. C., Ingvaldsen, R., Ivanov, V. V., Janout, M., Lind, S., Padman, L., Pnyushkov, A. V., and Rember, R.: Weakening of Cold Halocline Layer Exposes Sea Ice to Oceanic Heat in the Eastern Arctic Ocean, Journal of Climate, 33, 8107–8123, https://doi.org/10.1175/jcli-d-19-0976.1, 2020a.

Polyakov, I. V., Rippeth, T. P., Fer, I., Baumann, T. M., Carmack, E. C., Ivanov, V. V., Janout, M., Padman, L., Pnyushkov, A. V., and Rember, R.: Intensification of Near-Surface Currents and Shear in the Eastern Arctic Ocean, Geophysical Research Letters, 47, 11, https://doi.org/10.1029/2020gl089469, 2020b.

Ponte, R. M. and Gaspar, P.: Regional analysis of the inverted barometer effect over the global ocean using TOPEX/POSEIDON data and model results, Journal of Geophysical Research, 104, 15 587–15 601, https://doi.org/10.1029/1999JC900113, 1999.

Prandi, P., Poisson, J.-C., Faugère, Y., Guillot, A., and Dibarboure, G.: Arctic sea surface height maps from multi-altimeter combination, Earth System Science Data, 13, 5469–5482, https://doi.org/10.5194/essd-13-5469-2021, 2021.

Proshutinsky, A., Krishfield, R., Timmermans, M.-L., Toole, J., Carmack, E. C., McLaughlin, F., Williams, W. J., Zimmermann, S., Itoh, M., and Shimada, K.: Beaufort Gyre freshwater reservoir: State and variability from observations, Journal of Geophysical Research: Solid Earth, 114, 14 485, https://doi.org/10.1029/2008JC005104, 2009.

Proshutinsky, A., Dukhovskoy, D., Timmermans, M.-L., Krishfield, R., and Bamber, J. L.: Arctic circulation regimes, Philosophical Transactions of the Royal Society A: Mathematical, Physical and Engineering Sciences, 373, 1 – 18, https://doi.org/10.1098/rsta.2014.0160, 2015.

Proshutinsky, A., Krishfield, R., Toole, J. M., Timmermans, M., Williams, W., Zimmermann, S., Yamamoto-Kawai, M., Armitage, T. W. K., Dukhovskoy, D., Golubeva, E., Manucharyan, G. E., Platov, G., Watanabe, E., Kikuchi, T., Nishino, S., Itoh, M., Kang, S., Cho, K., Tateyama, K., and Zhao, J.: Analysis of the Beaufort Gyre Freshwater Content in 2003–2018, Journal of Geophysical Research: Oceans, 124, 9658–9689, https://doi.org/10.1029/2019jc015281, 2019.

Proshutinsky, A. Y. and Johnson, M. A.: Two circulation regimes of the wind-driven Arctic Ocean, Journal of Geophysical Research: Solid Earth, 102, 12 493–12 514, https://doi.org/10.1029/97JC00738, 1997.

Pujol, M. I., Dobricic, S., Pinardi, N., and Adani, M.: Impact of Multialtimeter Sea Level Assimilation in the Mediterranean Forecasting Model, Journal of Atmospheric and Oceanic Technology, 27, 2065 – 2082, https://doi.org/10.1175/2010jtecho715.1, 2010.

Pujol, M.-I., Faugère, Y., Taburet, G., Dupuy, S., Pelloquin, C., Ablain, M., and Picot, N.: DUACS DT2014: the new multi-mission altimeter data set reprocessed over 20 years, Ocean Science, 12, 1067 – 1090, URL https://www.ocean-sci.net/12/1067/2016/os-12-1067-2016.pdf, 2016.

Pujol, M.-I., Dupuy, S., Vergara, O., Román, A. S., Faugère, Y., Prandi, P., Dabat, M.-L., Dagneaux, Q., Lievin, M., Cadier, E., Dibarboure, G., and Picot, N.: Refining the Resolution of DUACS Along-Track Level-3 Sea Level Altimetry Products, Remote Sensing, 15, 793, https://doi.org/10.3390/rs15030793, 2023.

Quartly, G. D., Rinne, E., Passaro, M., Andersen, O. B., Dinardo, S., Fleury, S., Guillot, A., Hendricks, S., Kurekin, A. A., Müller, F. L., Ricker, R., Skourup, H., and Tsamados, M.: Retrieving Sea Level and Freeboard in the Arctic: A Review of Current Radar Altimetry Methodologies and Future Perspectives, Remote Sensing, 11, 881, https://doi.org/10.3390/rs11070881, 2019.

Quinn, K. J. and Ponte, R. M.: High frequency barotropic ocean variability observed by GRACE and satellite altimetry, Geophysical Research Letters, 39, 1–5, https://doi.org/10.1029/2012GL051301, 2012.

Rabe, B., Karcher, M., Schauer, U., Toole, J. M., Krishfield, R., Pisarev, S., Kauker, F., and Kikuchi, T.: An assessment of Arctic Ocean freshwater content changes from the 1990s to the 2006–2008 period, Deep-Sea Research Part I, 58, 173–185, https://doi.org/doi:10.1016/j.dsr.2010.12.002, 2011.

Rabe, B., Karcher, M., Kauker, F., Schauer, U., Toole, J. M., Krishfield, R. A., Pisarev, S., Kikuchi, T., and Su, J.: Arctic Ocean basin liquid freshwater storage trend 1992–2012, Geophysical Research Letters, 41, 961–968, https://doi.org/10.1002/2013gl058121, 2014.

Raj, R. P., Andersen, O. B., Johannessen, J. A., Gutknecht, B. D., Chatterjee, S., Rose, S. K., Bonaduce, A., Horwath, M., Ranndal, H., Richter, K., Palanisamy, H., Ludwigsen, C. A., Bertino, L., Nilsen, J. E. Ø., Knudsen, P., Hogg, A., Cazenave, A., and Benveniste, J.: Arctic Sea Level Budget Assessment during the GRACE/Argo Time Period, Remote Sensing, 12, 2837, https://doi.org/10.3390/rs12172837, 2020.

Rampal, P., Weiss, J., and Marsan, D.: Positive trend in the mean speed and deformation rate of Arctic sea ice, 1979–2007, Journal of Geophysical Research, 114, 3331 – 14, https://doi.org/10.1029/2008jc005066, 2009.

Regan, H. C., Lique, C., and Armitage, T. W. K.: The Beaufort Gyre Extent, Shape, and Location Between 2003 and 2014 From Satellite Observations, Journal of Geophysical Research: Oceans, 94, 14,485, https://doi.org/10.1029/2018JC014379, 2019.

Rhein, M., Steinfeldt, R., Huhn, O., Sültenfuß, J., and Breckenfelder, T.: Greenland Submarine Melt Water Observed in the Labrador and Irminger Sea, Geophysical Research Letters, 45, 10,570–10,578, https://doi.org/10.1029/2018gl079110, 2018.

Ricker, R., Hendricks, S., Helm, V., and Davidson, M.: Sensitivity of CryoSat-2 Arctic sea-ice freeboard and thickness on radar-waveform interpretation, The Cryosphere, 8, 1607–1622, https://doi.org/10.5194/tc-8-1607-2014, 2014.

Ricker, R., Hendricks, S., and Beckers, J.: The Impact of Geophysical Corrections on Sea-Ice Freeboard Retrieved from Satellite Altimetry, Remote Sensing, 8, 1–15, https://doi.org/10.3390/rs8040317, 2016.

Ricker, R., Girard-Ardhuin, F., Krumpen, T., and Lique, C.: Satellite-derived sea ice export and its impact on Arctic ice mass balance, The Cryosphere Discussions, 12, 3017 – 3032, https://doi.org/10.5194/tc-12-3017-2018, 2018.

Rio, M. H., Guinehut, S., and Larnicol, G.: New CNES-CLS09 global mean dynamic topography computed from the combination of GRACE data, altimetry, and in situ measurements, Journal of Geophysical Research, 116, C11 001–25, https://doi.org/10.1029/2010JC006505, 2011.

Rixen, M., Beckers, J. M., Brankart, J. M., and Brasseur, P.: A numerically efficient data analysis method with error map generation, Ocean Modelling, 2, 45 – 60, https://doi.org/10.1016/s1463-5003(00)00009-3, 2000.

Robbins, J. W., Neumann, T. A., Kwok, R., and Morison, J.: ICESat-2 Oceanic & Sea Ice Responses to Atmospheric Forcing, in: Conference Proceedings, 2016 Fall meeting, AGU, San Francisco, CA, 12-16 Dec., URL https://ui.adsabs.harvard.edu/abs/2016AGUFM.C11A0744R/abstract, 2016.

Rogge, A., Janout, M., Loginova, N., Trudnowska, E., Hörstmann, C., Wekerle, C., Oziel, L., Schourup-Kristensen, V., Ruiz-Castillo, E., Schulz, K., Povazhnyy, V. V., Iversen, M. H., and Waite, A. M.: Carbon dioxide sink in the Arctic Ocean from cross-shelf transport of dense Barents Sea water, Nature Geoscience, 16, 82–88, https://doi.org/10.1038/s41561-022-01069-z, 2023.

Rose, S. K., Andersen, O. B., Passaro, M., Ludwigsen, C. A., and Schwatke, C.: Arctic Ocean Sea Level Record from the Complete Radar Altimetry Era: 1991–2018, Remote Sensing, 11, 1672, https://doi.org/10.3390/rs11141672, 2019.

Rudels, B., Muench, R. D., Gunn, J., Schauer, U., and Friedrich, H. J.: Evolution of the Arctic Ocean boundary current north of the Siberian shelves, Journal of Marine Systems, 25, 77–99, https://doi.org/10.1016/s0924-7963(00)00009-9, 2000.

Ruiz-Castillo, E., Janout, M., Hölemann, J., Kanzow, T., Schulz, K., and Ivanov, V.: Structure and Seasonal Variability of the Arctic Boundary Current North of Severnaya Zemlya, Journal of Geophysical Research: Oceans, 128, https://doi.org/10.1029/2022jc018677, 2023.

Scharroo, R. and Lillibridge, J.: Non-Parametric Sea-State Bias Models and Their Relevance to Sea Level Change Studies, in: Envisat ERS Symposium, Salzburg, Austria, 2005.

Scharroo, R., Leuliette, E., Lillibridge, J., Byrne, D., Naeije, M., and Mitchum, G.: RADS: Consistent multi-mission products, in: Proc. of the Symposium on Years of Progress in Radar Altimetry, Venice, - September, Eur. Space Agency Spec. Publ., 2013.

Scharroo, Remko: RADS data manual., Tech. rep., Delft Institute for Earth-Oriented Space Research & NOAA Laboratory for Satellite Altimetry & EUMETSAT, URL https://usermanual.wiki/Document/rads4datamanual.1752171340/help, 2018.

Schauer, U., Loeng, H., Rudels, B., Ozhigin, V. K., and Dieck, W.: Atlantic Water flow through the Barents and Kara Seas , Deep-Sea Research Part I, https://doi.org/10.1016/S0967-0637(02)00125-5, 2002.

Schauer, U., Fahrbach, E., Osterhus, S., and Rohardt, G.: Arctic warming through the Fram Strait: Oceanic heat transport from 3 years of measurements, Journal of Geophysical Research, p. 11, https://doi.org/10.1029/2003jc001823, 2004.

Serreze, M. C., Barrett, A. P., Slater, A. G., Woodgate, R. A., Aagaard, K., Lammers, R. B., Steele, M., Moritz, R., Meredith, M., and Lee, C. M.: The large-scale freshwater cycle of the Arctic, Journal of Geophysical Research: Oceans, 111, https://doi.org/10.1029/2005jc003424, 2006.

Serreze, M. C., Barrett, A. P., Stroeve, J. C., Kindig, D. N., and Holland, M. M.: The emergence of surface-based Arctic amplification, The Cryosphere, 3, 11–19, https://doi.org/10.5194/tc-3-11-2009, 2009.

Siegismund, F., Johannessen, J., Drange, H., Mork, K. A., and Korablev, A.: Steric height variability in the Nordic Seas, Journal of Geophysical Research: Solid Earth, 112, 2733, https://doi.org/10.1029/2007JC004221, 2007.

Simpson, J. H. and Sharples, J.: Introduction to the physical and biological oceanography of shelf seas, Cambridge University Press, https://doi.org/10.1017/cbo9781139034098, 2012.

Smedsrud, L. H., Ingvaldsen, R., Nilsen, J. E. Ø., and Skagseth, Ø.: Heat in the Barents Sea: transport, storage, and surface fluxes, Ocean Science, 6, 219–234, https://doi.org/10.5194/os-6-219-2010, 2010.

Smedsrud, L. H., Esau, I., Ingvaldsen, R. B., Eldevik, T., Haugan, P. M., Li, C., Lien, V. S., Olsen, A., Omar, A. M., Otterå, O. H., Risebrobakken, B., Sandø, A. B., Semenov, V. A., and Sorokina, S. A.: THE ROLE OF THE BARENTS SEA IN THE ARCTIC CLIMATE SYSTEM, Reviews of Geophysics, 51, 415–449, https://doi.org/10.1002/rog.20017, 2013.

Solgaard, A. M., Rapp, D., Noël, B. P. Y., and Hvidberg, C. S.: Seasonal Patterns of Greenland Ice Velocity From Sentinel-1 SAR Data Linked to Runoff, Geophysical Research Letters, 49, https://doi.org/10.1029/2022gl100343, 2022.

Solomon, A., Heuzé, C., Rabe, B., Bacon, S., Bertino, L., Heimbach, P., Inoue, J., Iovino, D., Mottram, R., Zhang, X., Aksenov, Y., McAdam, R., Nguyen, A., Raj, R. P., and Tang, H.: Freshwater in the Arctic Ocean 2010–2019, Ocean Science, 17, 1081–1102, https://doi.org/10.5194/os-17-1081-2021, 2021.

Spall, M. A.: On the Circulation of Atlantic Water in the Arctic Ocean, Journal of Physical Oceanography, 43, 2352–2371, https://doi.org/10.1175/jpo-d-13-079.1, 2013.

Spreen, G., Kwok, R., and Menemenlis, D.: Trends in Arctic sea ice drift and role of wind forcing: 1992-2009, Geophysical Research Letters, 38, 1–6, https://doi.org/10.1029/2011GL048970, 2011.

Stammer, D., Wunsch, C., and Ponte, R. M.: De-aliasing of global high frequency barotropic motions in altimeter observations, Geophysical Research Letters, 27, 1175–1178, https://doi.org/10.1029/1999GL011263, 2000.

Stendardo, I., Rhein, M., and Steinfeldt, R.: The North Atlantic Current and its Volume and Freshwater Transports in the Subpolar North Atlantic, Time Period 1993–2016, Journal of Geophysical Research: Oceans, 125, https://doi.org/10.1029/2020jc016065, 2020.

Stommel, H.: The westward intensification of wind-driven ocean currents, Eos, Transactions American Geophysical Union, 29, 202–206, https://doi.org/10.1029/tr029i002p00202, 1948.

Sumata, H., Steur, L. d., Gerland, S., Divine, D. V., and Pavlova, O.: Unprecedented decline of Arctic sea ice outflow in 2018, Nature Communications, 13, 1747, https://doi.org/10.1038/s41467-022-29470-7, 2022.

Sverdrup, H. U.: Wind-Driven Currents in a Baroclinic Ocean; with Application to the Equatorial Currents of the Eastern Pacific*, Proceedings of the National Academy of Sciences, 33, 318–326, https://doi.org/10.1073/pnas.33.11.318, 1947.

Talley, L. D., Pickard, G. L., Emery, W. J., and Swift, J. H.: Chapter 7 - Dynamical Processes for Descriptive Ocean Circulation, in: Descriptive Physical Oceanography (Sixth Edition), edited by Talley, L. D., Pickard, G. L., Emery, W. J., and Swift, J. H., pp. 187–221, Academic Press, Boston, sixth edition edn., https://doi.org/https://doi.org/10.1016/B978-0-7506-4552-2.10007-1, 2011.

Team, I. A., Abdalla, S., Kolahchi, A. A., Ablain, M., Adusumilli, S., Bhowmick, S. A., Alou-Font, E., Amarouche, L., Andersen, O. B., Antich, H., Aouf, L., Arbic, B., Armitage, T., Arnault, S., Artana, C., Aulicino, G., Ayoub, N., Badulin, S., Baker, S., Banks, C., Bao, L., Barbetta, S., Barceló-Llull, B., Barlier, F., Basu, S., Bauer-Gottwein, P., Becker, M., Beckley, B., Bellefond, N., Belonenko, T., Benkiran, M., Benkouider, T., Bennartz, R., Benveniste, J., Bercher, N., Berge-Nguyen, M., Bettencourt, J., Blarel, F., Blazquez, A., Blumstein, D., Bonnefond, P., Borde, F., Bouffard, J., Boy, F., Boy, J.-P., Brachet, C., Brasseur, P., Braun, A., Brocca, L., Brockley, D., Brodeau, L., Brown, S., Bruinsma, S., Bulczak, A., Buzzard, S., Cahill, M., Calmant, S., Calzas, M., Camici, S., Cancet, M., Capdeville, H., Carabajal, C. C., Carrere, L., Cazenave, A., Chassignet, E. P., Chauhan, P., Cherchali, S., Chereskin, T., Cheymol, C., Ciani, D., Cipollini, P., Cirillo, F., Cosme, E., Coss, S., Cotroneo, Y., Cotton, D., Couhert, A., Coutin-Faye, S., Crétaux, J.-F., Cyr, F., d'Ovidio, F., Darrozes, J., David, C., Dayoub, N., Staerke, D. D., Deng, X., Desai, S., Desjonqueres, J.-D., Dettmering, D., Bella, A. D., Díaz-Barroso, L., Dibarboure, G., Dieng, H. B., Dinardo, S., Dobslaw, H., Dodet, G., Doglioli, A., Domeneghetti, A., Donahue, D., Dong, S., Donlon, C., Dorandeu, J., Drezen, C., Drinkwater, M., Penhoat, Y. D., Dushaw, B., Egido, A., Erofeeva, S., Escudier, P., Esselborn, S., Exertier, P., Fablet, R., Falco, C., Farrell, S. L., Faugere, Y., Femenias, P., Fenoglio, L., Fernandes, J., Fernández, J. G., Ferrage, P., Ferrari, R., Fichen, L., Filippucci, P., Flampouris, S., Fleury, S., Fornari, M., Forsberg, R., Frappart, F., Frery, M.-l., Garcia, P., Garcia-Mondejar, A., Gaudelli, J., Gaultier, L., Getirana, A., Gibert, F., Gil, A., Gilbert, L., Gille, S., Giulicchi, L., Gómez-Enri, J., Gómez-Navarro, L., Gommenginger, C., Gourdeau, L., Griffin, D., Groh, A., Guerin, A., Guerrero, R., Guinle, T., Gupta, P., Gutknecht, B. D., Hamon, M., Han, G., Hauser, D., Helm, V., Hendricks, S., Hernandez, F., Hogg, A., Horwath, M., Idžanović, M., Janssen, P., Jeansou, E., Jia, Y., Jia, Y., Jiang, L., Johannessen, J. A., Kamachi, M., Karimova, S., Kelly, K., Kim, S. Y., King, R., Kittel, C. M., Klein, P., Klos, A., Knudsen, P., Koenig, R., Kostianoy, A., Kouraev, A., Kumar, R., Labroue, S., Lago, L. S., Lambin, J., Lasson, L., Laurain, O., Laxenaire, R., Lázaro, C., Gac, S. L., Sommer, J. L., Traon, P.-Y. L., Lebedev, S., Léger, F., Legresy, B., Lemoine, F., Lenain, L., Leuliette, E., Levy, M., Lillibridge, J., Liu, J., Llovel, W., Lyard, F., Macintosh, C., Varona, E. M., Manfredi, C., Marin, F., Mason, E., Massari, C., Mavrocordatos, C., Maximenko, N., McMillan, M., Medina, T., Melet, A., Meloni, M., Mertikas, S., Metref, S., Meyssignac, B., Minster, J.-F., Moreau, T., Moreira, D., Morel, Y., Morrow, R., Moyard, J., Mulet, S., Naeije, M., Nerem, R. S., Ngodock, H., Nielsen, K., Nilsen, J. E. Ø., Niño, F., Loddo, C. N., Noûs, C., Obligis, E., Otosaka, I., Otten, M., Ozbahceci, B. O., Raj, R. P., Paiva, R., Paniagua, G., Paolo, F., Paris, A., Pascual, A., Passaro, M., Paul, S., Pavelsky, T., Pearson, C., Penduff, T., Peng, F., Perosanz, F., Picot, N., Piras, F., Poggiali, V., Poirier, E., León, S. P. d., Prants, S., Prigent, C., Provost, C., Pujol, M.-I., Qiu, B., Quilfen, Y., Rami, A., Raney, R. K., Raynal, M., Remy, E., Rémy, F., Restano, M., Richardson, A., Richardson, D., Ricker, R., Ricko, M., Rinne, E., Rose, S. K., Rosmorduc, V., Rudenko, S., Ruiz, S., Ryan, B. J., Salaün, C., Sanchez-Roman, A., Sørensen, L. S., Sandwell, D., Saraceno, M., Scagliola, M., Schaeffer, P., Scharffenberg, M. G., Scharroo, R., Schiller, A., Schneider, R., Schwatke, C., Scozzari, A., Ser-giacomi, E., Seyler, F., Shah, R., Sharma, R., Shaw, A., Shepherd, A., Shriver, J., Shum, C., Simons, W., Simonsen, S. B., Slater, T., Smith, W., Soares, S., Sokolovskiy,

M., Soudarin, L., Spatar, C., Speich, S., Srinivasan, M., Srokosz, M., Stanev, E., Staneva, J., Steunou, N., Stroeve, J., Su, B., Sulistioadi, Y. B., Swain, D., Sylvestre-baron, A., Taburet, N., Tailleux, R., Takayama, K., Tapley, B., Tarpanelli, A., Tavernier, G., Testut, L., Thakur, P. K., Thibaut, P., Thompson, L., Tintoré, J., Tison, C., Tourain, C., Tournadre, J., Townsend, B., Tran, N., Trilles, S., Tsamados, M., Tseng, K.-H., Ubelmann, C., Uebbing, B., Vergara, O., Verron, J., Vieira, T., Vignudelli, S., Shiffer, N. V., Visser, P., Vivier, F., Volkov, D., Schuckmann, K. v., Vuglinskii, V., Vuilleumier, P., Walter, B., Wang, J., Wang, C., Watson, C., Wilkin, J., Willis, J., Wilson, H., Woodworth, P., Yang, K., Yao, F., Zaharia, R., Zakharova, E., Zaron, E. D., Zhang, Y., Zhao, Z., Zinchenko, V., and Zlotnicki, V.: Altimetry for the future: Building on 25 years of progress, Advances in Space Research, 68, 319–363, https://doi.org/10.1016/j.asr.2021.01.022, 2021.

Thompson, A. F., Stewart, A. L., Spence, P., and Heywood, K. J.: The Antarctic Slope Current in a Changing Climate, Reviews of Geophysics, 56, 741–770, https://doi.org/10.1029/2018rg000624, 2018.

Tilling, R. L., Ridout, A., and Shepherd, A.: Estimating Arctic sea ice thickness and volume using CryoSat-2 radar altimeter data, Advances in Space Research, 62, 1203 – 1225, https://doi.org/10.1016/j.asr.2017.10.051, 2018.

Timmermann, R., Danilov, S., Schröter, J., Böning, C., Sidorenko, D., and Rollenhagen, K.: Ocean circulation and sea ice distribution in a finite element global sea ice–ocean model, Ocean Modelling, 27, 114–129, https://doi.org/10.1016/j.ocemod.2008.10.009, 2009.

Timmermans, M.-L. and Marshall, J.: Understanding Arctic Ocean Circulation: A Review of Ocean Dynamics in a Changing Climate, Journal of Geophysical Research: Oceans, 125, C04S02, https://doi.org/10.1029/2018jc014378, 2020.

Timmermans, M.-L., Proshutinsky, A., Krishfield, R. A., Perovich, D. K., Richter-Menge, J. A., Stanton, T. P., and Toole, J. M.: Surface freshening in the Arctic Ocean's Eurasian Basin: An apparent consequence of recent change in the wind-driven circulation, Journal of Geophysical Research, 116, 1 – 17, https://doi.org/10.1029/2011jc006975, 2011.

Traon, P. Y. L.: From satellite altimetry to Argo and operational oceanography: three revolutions in oceanography, Ocean Science, 9, 901 – 915, https://doi.org/10.5194/os-9-901-2013, 2013.

Troupin, C., Machín, F., Ouberdous, M., Sirjacobs, D., Barth, A., and Beckers, J. M.: High-resolution climatology of the northeast Atlantic using Data-Interpolating Variational Analysis (Diva), Journal of Geophysical Research: Solid Earth, 115, 455, https://doi.org/10.1029/2009jc005512, 2010.

Troupin, C., Barth, A., Sirjacobs, D., Ouberdous, M., Brankart, J. M., Brasseur, P., Rixen, M., Alvera-Azcárate, A., Belounis, M., Capet, A., Lenartz, F., Toussaint, M. E., and Beckers, J. M.: Generation of analysis and consistent error fields using the Data Interpolating Variational Analysis (DIVA), Ocean Modelling, 52-53, 90–101, https://doi.org/10.1016/j.ocemod.2012.05.002, 2012.

Tsubouchi, T., Appen, W.-J. v., Kanzow, T., and Steur, L. d.: Temporal variability of the overturning circulation in the Arctic Ocean and the associated heat and freshwater transports during 2004-2010, Journal of Physical Oceanography, https://doi.org/10.1175/jpo-d-23-0056.1, 2023.

Tsujino, H., Urakawa, S., Nakano, H., Small, R. J., Kim, W. M., Yeager, S. G., Danabasoglu, G., Suzuki, T., Bamber, J. L., Bentsen, M., Böning, C. W., Bozec, A., Chassignet, E. P., Curchitser, E., Boeira Dias, F., Durack, P. J., Griffies, S. M., Harada, Y., Ilicak, M., Josey, S. A., Kobayashi, C., Kobayashi, S., Komuro, Y., Large, W. G., Le Sommer, J., Marsland, S. J., Masina, S., Scheinert, M., Tomita, H., Valdivieso, M., and Yamazaki, D.: JRA-55 based surface dataset for driving ocean–sea-ice models (JRA55-do), Ocean Modelling, 130, 79–139, https://doi.org/https://doi.org/10.1016/j.ocemod.2018.07.002, 2018.

Tyberghein, L., Verbruggen, H., Pauly, K., Troupin, C., Mineur, F., and Clerck, O. D.: Bio-ORACLE: a global environmental dataset for marine species distribution modelling, Global Ecology and Biogeography, 21, 272 – 281, https://doi.org/10.1111/j.1466-8238.2011.00656.x, 2012.

Vinogradova, N. T., Ponte, R. M., and Stammer, D.: Relation between sea level and bottom pressure and the vertical dependence of oceanic variability, Geophysical Research Letters, 34, C03 010, https://doi.org/10.1029/2006GL028588, 2007.

Volkov, D. L. and Landerer, F. W.: Nonseasonal fluctuations of the Arctic Ocean mass observed by the GRACE satellites, Journal of Geophysical Research: Oceans, 118, 6451 – 6460, https://doi.org/10.1002/2013jc009341, 2013.

Volkov, D. L. and Pujol, M. I.: Quality assessment of a satellite altimetry data product in the Nordic, Barents, and Kara seas, Journal of Geophysical Research, 117, 1–12, https://doi.org/10.1029/2011JC007557, 2012.

Volkov, D. L., Landerer, F. W., and Kirillov, S. A.: The genesis of sea level variability in the Barents Sea, Continental Shelf Research, 66, 92–104, https://doi.org/10.1016/j.csr.2013.07.007, 2013.

von Appen, W.-J.: Physical oceanography and current meter data (including raw data) from FRAM moorings in the Fram Strait, 2016-2018, PANGAEA, https://doi.org/10.1594/PANGAEA.904565, 2019.

von Appen, W.-J., Schauer, U., Somavilla Cabrillo, R., Bauerfeind, E., and Beszczynska-Möller, A.: Physical oceanography during various cruises to the Fram Strait, 1998-2012, PANGAEA, https://doi.org/10.1594/PANGAEA.150007, in supplement to: von Appen, Wilken-Jon; Schauer, Ursula; Somavilla, Raquel; Bauerfeind, Eduard; Beszczynska-Möller, Agnieszka (2015): Exchange of warming deep waters across Fram Strait. Deep Sea Research Part I: Oceanographic Research Papers, 103, 86-100, https://doi.org/10.1016/j.dsr.2015.06.003, 2015.

von Appen, W.-J., Schauer, U., Hattermann, T., and Beszczynska-Möller, A.: Seasonal Cycle of Mesoscale Instability of the West Spitsbergen Current, Journal of Physical Oceanography, 46, 1231–1254, https://doi.org/10.1175/JPO-D-15-0184.1, 2016.

von Appen, W.-J., Beszczynska-Möller, A., Schauer, U., and Fahrbach, E.: Physical oceanography and current meter data from moorings F1-F14 and F15/F16 in the Fram Strait, 1997-2016, PANGAEA, https://doi.org/10.1594/PANGAEA.900883, 2019.

Wahr, J. M.: Deformation induced by polar motion, Journal of Geophysical Research: Solid Earth, 90, 9363–9368, https://doi.org/10.1029/JB090iB11p09363, 1985.

Wang, Q., Danilov, S., and Schröter, J.: Finite element ocean circulation model based on triangular prismatic elements, with application in studying the effect of topography representation, Journal of Geophysical Research: Oceans, 113, https://doi.org/10.1029/2007jc004482, 2008.

Wang, Q., Wekerle, C., Danilov, S., Koldunov, N., Sidorenko, D., Sein, D., Rabe, B., and Jung, T.: Arctic Sea Ice Decline Significantly Contributed to the Unprecedented Liquid Freshwater Accumulation in the Beaufort Gyre of the Arctic Ocean, Geophysical Research Letters, 45, 4956 – 4964, https://doi.org/10.1029/2018gl077901, 2018a.

Wang, Q., Wekerle, C., Danilov, S., Wang, X., and Jung, T.: A 4.5 km resolution Arctic Ocean simulation with the global multi-resolution model FESOM 1.4, Geoscientific Model Development, 11, 1229–1255, https://doi.org/10.5194/gmd-11-1229-2018, 2018b.

Wang, Q., Wekerle, C., Danilov, S., Sidorenko, D., Koldunov, N., Sein, D., Rabe, B., and Jung, T.: Recent Sea Ice Decline Did Not Significantly Increase the Total Liquid Freshwater Content of the Arctic Ocean, Journal of Climate, 32, 15–32, https://doi.org/10.1175/JCLI-D-18-0237.1, 2019.

Wang, Q., Wekerle, C., Wang, X., Danilov, S., Koldunov, N., Sein, D., Sidorenko, D., von Appen, W.-J., and Jung, T.: Intensification of the Atlantic Water Supply to the Arctic Ocean Through Fram Strait Induced by Arctic Sea Ice Decline, Geophysical Research Letters, 47, 2016, https://doi.org/10.1029/2019GL086682, 2020.

Watelet, S., Skagseth, Ø., Lien, V. S., Sagen, H., Østensen, Ø., Ivshin, V., and Beckers, J.-M.: A volumetric census of the Barents Sea in a changing climate, Earth System Science Data, 12, 2447 – 2457, https://doi.org/10.5194/essd-12-2447-2020, 2020.

Watkins, M. M., Wiese, D. N., Yuan, D., Boening, C., and Landerer, F. W.: Improved methods for observing Earth's time variable mass distribution with GRACE using spherical cap mascons, Journal of Geophysical Research: Solid Earth, 120, 2648–2671, https://doi.org/10.1002/2014jb011547, 2015.

Wiese, D. N., Landerer, F. W., and Watkins, M. M.: Quantifying and reducing leakage errors in the JPL RL05M GRACE mascon solution, Water Resources Research, 52, 7490–7502, https://doi.org/10.1002/2016wr019344, 2016.

Willmes, S. and Heinemann, G.: Sea-Ice Wintertime Lead Frequencies and Regional Characteristics in the Arctic, 2003–2015, Remote Sensing, 8, 4, https://doi.org/10.3390/rs8010004, 2016.

Wingham, D. J., Francis, C. R., Baker, S., Bouzinac, C., Brockley, D., Cullen, R., de Chateau-Thierry, P., Laxon, S. W., Mallow, U., Mavrocordatos, C., Phalippou, L., Ratier, G., Rey, L., Rostan, F., Viau, P., and Wallis, D. W.: CryoSat: A mission to determine the fluctuations in Earth's land and marine ice fields , Advances in Space Research, 37, 841–871, https://doi.org/10.1016/j.asr.2005.07.027, 2006.

Witze, A.: Russia's war in Ukraine forces Arctic climate projects to pivot, Nature, 607, 432–432, https://doi.org/10.1038/d41586-022-01868-9, 2022.

Woodgate, R. A., Aagaard, K., and Weingartner, T. J.: A year in the physical oceanography of the Chukchi Sea: Moored measurements from autumn 1990–1991, Deep Sea Research Part II: Topical Studies in Oceanography, 52, 3116 – 3149, https://doi.org/10.1016/j.dsr2.2005.10.016, 2005.

Wunsch, C., Ponte, R. M., and Heimbach, P.: Decadal Trends in Sea Level Patterns: 1993–2004, Journal of Climate, 20, 5889–5911, https://doi.org/10.1175/2007jcli1840.1, 2007.

Xiao, K., Chen, M., Wang, Q., Wang, X., and Zhang, W.: Low-frequency sea level variability and impact of recent sea ice decline on the sea level trend in the Arctic Ocean from a high-resolution simulation, Ocean Dynamics, 70, 787 – 802, https://doi.org/10.1007/s10236-020-01373-5, 2020.

Zhang, J., Lindsay, R., Steele, M., and Schweiger, A.: What drove the dramatic retreat of arctic sea ice during summer 2007?, Geophysical Research Letters, 35, L18 504, https://doi.org/10.1029/2008gl034005, 2008.

Zhao, M., Timmermans, M., Cole, S., Krishfield, R., and Toole, J.: Evolution of the eddy field in the Arctic Ocean's Canada Basin, 2005–2015, Geophysical Research Letters, 43, 8106–8114, https://doi.org/10.1002/2016gl069671, 2016.

Chapter 6

Declaration — Erklärung

first page

I herewith declare, that I

1. have formulated the thesis myself and without the help of others,
2. have not used sources and tools other than those indicated nor aids other than those permissible,
3. have marked the literal or textual taken part of the used works.

I hereby declare that I have not qualified or applied for a doctorate procedure in the past.

I agree to the reviewing of the doctoral thesis with qualified software during the investigation of the pretence of plagiarism.

Hiermit versichere ich, dass ich

1. die Arbeit ohne unerlaubte fremde Hilfe angefertigt habe,
2. keine anderen als die von mir angegebenen Quellen und Hilfsmittel benutzt habe,
3. die, den benutzten Werken wörtlich oder inhaltlich entnommenen Stellen als solche kenntlich gemacht habe.

Hiermit versichere ich, dass ich mich bisher keinem Promotionsverfahren unterzogen bzw. ein solches beantragt habe.

Ich bin damit einverstanden, dass eine Überprüfung der Dissertation mit qualifizierter Software im Rahmen der Untersuchung von Plagiatsvorwürfen gestattet ist.

Bremerhaven, 05.10.2023 Francesca Doglioni